Dual Functional Theranostic Nanoparticles for Rhabdomyosarcoma Treatment

A thesis submitted for the degree of
DPhil in Women's & Reproductive Health

Chengchen Duan

Supervisor: Prof. Helen Townley,
Second Supervisor: Dr. Kevin Coward

Wolfson College

Nuffield Department of Women's & Reproductive Health

University of Oxford

May 2022

Abstract

Rhabdomyosarcoma (RMS) is one of the most common soft tissue sarcomas and is extremely aggressive and highly malignant. The majority of cases occur in children, and most commonly appear in the arms or legs. Currently, RMS is treated with aggressive chemotherapy, as well as surgery and/or radiation in many cases. The aggressive treatments often cause long term after-effects, and can even cause permanent life-altering disabilities. Alternative treatment modalities are urgently needed.

The aim of this work is to build a dual-functional therapy/near-infrared (NIR) imaging nanoparticle, which could perform gene therapy with specific RMS gene knock-down regulated by pH-activated-release, and monitor the effects on tumour size with delivered near-infrared (NIR) dye. The nanoparticle will be surface functionalized with novel aptamers for improved targeting. The design can therefore be separated into four parts from outside to inside: aptamer-based targeting system, a pH-responsive charge reversible coating layer, nanoparticle-based NIR non-invasive imaging, and nanoparticle transfected siRNA for alveolar RMS (aRMS) specific gene knockdown.

Aptamers were chosen as the targeting ligand for the nanosystem since compared to antibodies, they are much smaller, have higher affinity and specificity, and lower immunogenicity. Furthermore, they are easier and cheaper to manufacture. The binding target for aptamer generation was Neural EGF-Like 1 (NELL1) chosen based on validation results which suggested overexpression on the surface of the target aRMS cells. Oligos were isolated, and their binding affinity was quantified using Surface Plasmon Resonance (SPR). The selected NELL1 aptamer could locate and firmly bind to the NELL1 on the surface of aRMS cells, which could therefore potentially minimize off-target effects.

The aptamer was attached to a synthesized pH-activated charge reversible PMPC-PDPA@PEG-

b-PAMA/DMMA copolymer layer. The PEG-*b*-PAMA/DMMA within the copolymer was able to efficiently convert the charge from negative (under physiological pH) to positive (under acidic pH), and the PMPC-PDPA could revert from a hydrophilic to a hydrophobic state after being activated by the acidic environment of tumours and subcellular organelles (endosomes & lysosomes). The enhanced tissue accumulation and cellular uptake could be achieved with increased adsorption onto negatively charged cellular membranes.

For NIR imaging, IR820 NIR dye was loaded into the mesoporous silica nanoparticles core to enable non-invasive monitoring of the uptake and accumulation of the nanosystem during treatment. Compared with free IR820 dye which could only rely on passive diffusion, the IR820-loaded MSNPs were found to have significant improvements from the perspectives of cellular uptake, accumulation amount and penetration depth within both 2D and 3D cell models.

Two siRNA targeting options were selected and validated for aRMS gene therapy: (i) Human αB-crystallin (CRYAB) & Heat Shock Protein Family B (Small) Member 2 (HSPB2) double knockout, and (ii) Keratin 17 (KRT17) knockdown.

Through linking the validated siRNAs onto the MSNPs surface with the disulfide bound which could only be cleavaged by the high concentration of GSH within RMS cells, it has been found to have a high degree of RNase I degradation prevention, and a significant enhanced transfection efficiency. The total GSH levels within RD and RH30 cells were found to be 5.08 and 9.28 times higher than that of control fibroblast cells. Compared with the commercially available DharmaFect transfection reagent, the nanoparticles transfected siRNA has shown a similar or better level of gene knockdown; with a significant suppression of aRMS cells proliferation and mobility.

Overall, the constructed nanosystem could provide another route for tackling aRMS in a more effective way, with fewer side-effects.

Keywords: Nanoparticles, Gene Therapy, Sarcoma, Aptamer, NIR Imaging

Table of Contents

Abbreviation

3′-UTR	3′-untranslated region
AA	acetic acid
AChR	acetylcholine receptor
AFM	Atomic force microscope
AMA	Aminoethyl methacrylate hydrochloride
AptN	anti-NELL1 aptamers
aRMS	alveolar RMS
ATP	adenosine-5'-triphosphate
ATRP	Atom transfer radical polymerization
AuNPs	Gold nanoparticles
AuNTs	gold nanotriangles
AXT	axitinib
BBB	blood-brain barrier
BTB	blood tumour barrier
CAFs	cancer-associated fibroblasts
Ce6(Mn)	paclitaxel
CRYAB	Human αB-crystallin
CST	celastrol
CTAC	exadecyltrimethylammonium Chloride
DCA	1,2-dicarboxylic-cyclohexene anhydride
DCM	Dichloromethane
DDMON	degradable dendritic mesoporous organosilica nanoparticle
DKO	double knockout
DLS	Dynamic Light Scattering
DMEM	Dulbecco's Modified Eagle's Medium
DMMA	2,3-dimethylmaleic anhydride
DMONs	dendritic mesoporous organosilica nanoparticles
DMSO	dimethyl sulfoxide
DSPE-PEG	1,2-distearoyl-sn-glycero-3-phosphoethanolamine-N-[biotinyl(polyethylene glycol)-2000
DTT	dithiothreitol
ECM	specific extracellular matrix
EEO	electroendoosmotic
EPR	Enhanced permeability and retention
eRMS	embryonic RMS
FBS	Fetal Bovine Serum
FDA	Food and Drug Administration
FGF2	fibroblast growth factor 2
GCV	ganciclovir
GFP	Green fluorescent protein
GSH	glutathione
GSSG	dimeric oxidised form GSH

HIF1α	hypoxia-inducible factor 1α
HSPB2	Heat Shock Protein Family B (Small) Member 2
HSV-TK	herpes simplex thymidine kinase
HTAMNs	hierarchical tumour acidity-responsive magnetic nanobomb
ICG	indocyanine green
KRAS	Kirsten rat sarcoma viral oncogene
KRT17	Keratin 17
MDR1	Multidrug resistance-1
MFI	Median fluorescence intensity
miRNAs	microRNAs
MMPs	matrix metalloproteinases
MPTES	3-mercaptopropyl triethoxysilane
mRNA	messenger RNA
MSNPs	mesoporous silica nanoparticles
MTT	3-(4,5-Dimethylthiazol-2-yl)-2,5-Diphenyltetrazolium Bromide
MyoD1	Myogenic Differentiation 1
NaN3	sodium azide
NELL1	Neural epidermal growth factor–like (EGFL)-like protein
NIH	National Institutes of Health
NIR-II	second near-infrared spectral region
NMR	Nuclear Magnetic Resonance
NV	nanovalves
OXPHOS	oxidative phosphorylation
PAMA	poly(2-aminoethyl methacrylate)
PAX	encoding paired box protein
PDPA-*b*-PAMA	Poly(2-diisopropylaminoethyl methacrylate)-*b*-poly(2-aminoethyl methacrylate hydrochloride)
PEG	polyethylene glycol
PEG-*b*-PAMA	poly(ethylene glycol)-*b*-poly(2-aminoethyl methacrylate hydrochloride
PLGA	poly(D,L-lactide-co-glycolide
PLL	poly(L-lysine)
PMNT	iron oxide nanotubes
PPK2	polyphosphate kinase 2
PTX	paclitaxel
PTZ	phenothiazine
R.U.	response unit
RES	reticuloendothelial system
RISC	RNA-induced silencing complex
RMS	rhabdomyosarcoma
RNAi	RNA interference
ROS	reactive oxygen species
RT-PCR	reverse transcription polymerase chain reaction
SD	standard deviation
SERS	Surface Enhanced Raman Spectroscopy
sgRNA	single guide RNA
SpCas9	Streptoccocus pyogenes

STS	soft tissue sarcoma
TALEN	transcription activator-like effector nucleases
TEA	Triethylamine
TEM	Transmission electron microscopy
TEOS	Tetraethyl orthosilicate
TGA	Thermogravimetric analysis
THF	Tetrahydrofuran
TM	tetramethyl succinic anhydride
TME	tumour microenvironment
TMS	tetramethylsilane
TNAs	therapeutic nucleic acids
USM	unconventional secretory machinery
VEGF	vascular endothelial growth factor
ZFN	Zinc finger nucleases
α-CD	α-cyclodextrin

List of Figures & Tables

Statement of the Change of Planned Research Work due to COVID-19 Pandemic

Work was planned to complete before university buildings were closed to non-Covid-19 research:

The aim of this research was to build a dual-functional theranostic nanoparticle with a pH-activated-release therapeutic core. RMS specific designed siRNA, which works as the therapeutic reagent, was designed to be delivered into tumour cells and the therapeutic effects monitored through non-invasive near infrared (NIR) signals. The synthesized dual-functional nanosystem could target the release of the siRNA and suppress the growth of the cancer cells, and the NIR signal should decrease as the tumour shrinks. This research was designed to set up the foundation of an efficient dual functional nanosystem which could be clinically applied in the future. Based on the planned work, two types of nanoparticles based on silica and gold should be synthesized as the core of the system. The surface of both types of nanoparticles was functionalised with thiol bonds in order to carry, and enable targeted-release of siRNA. The characterization, link & releasing, and anti-degradation works was planned to be finished after the synthesis. Based on the plan, a specific aptamer targeting NELL1 should be chosen as the targeting ligand for our nanosystem.

How the pandemic affected this research:

Due to the COVID-19 pandemic, lab has been shut down for most of the time in 2020, the project progress has been serious disrupted. Even though the lab has been reopened in late 2020, the research time has been strictly limited due to social distancing and lab capacity requirement. However, thanks to the nine months of extension granted by the University, most of the planned work has been successfully completed including evaluating the constructed system within multiple cell models.

Acknowledgements

If I get a chance to time travel and tell myself in 2018 what has happened in the past four years, I will definitely believe I went crazy. Now the magical journey is coming to an end, I really want to appreciate everyone who has helped me.

First, I would like to express my most sincere appreciation to my supervisor, Prof. Helen Townley. To me, Helen is not only a supervisor who kindly offered me an opportunity to come to Oxford to explore the topic which I am interested. She is also a mentor who is always willing to share her experience, and guide me out of the jungle of research when I got lost. She has always inspired me with her wisdom and knowledge. More than that, she is also a good friend who would like to sit together with us during lunch. No matter what happened, I know I could always get support from her. It is my greatest honour to have Helen as my DPhil supervisor. Thank you, Helen.

I also would like to thank my second supervisor, Dr Kevin Coward, for teaching me to stay optimistic, every catchup with him was always a joyful memory during my past four years. Besides, I also would like to acknowledge the help from Dr Karl Morten, Mrs Celine Jones, Dr Neil Young for kindly offering me support during my research.

I particularly wish to thank Mr Ben White, my best friend, I will never forget every pint we had together and all the fantastic bro memories. I also want to thank Hakmin, Nahla, Molly, Laura, Morgan, Xiaoyu(Jack), Jiabao, Rob, Joe, Jochem, Reza, Simona, Fariza, Calvin, Abi, Boon, Yutong and all other colleagues in Helen's lab, Begbroke and NDWRH who has kindly offered me help during my DPhil research.

I also want to thank all the friends I met in Oxford: Shiyan, Andy, Yaqiong, Bin, Monica, Steven, Yiwen. Without your encouragement and support, I wouldn't have lived such a happy life in the past four years.

I would like to acknowledge all the sponsors for supporting my scholarship and research: University of Oxford, China Scholarship Council and Williams Fund. I wouldn't have this opportunity to come here without your support.

Finally, I would like to express my deepest and special appreciation to my parents. My mom and dad have always tried their best to offer me the help, I would not achieve any of these without their unconditional love and support. Although we did not get to meet in the past three years, I know they are always there waiting for me. Especially thanks to my love, Miss Yexuan Yang and her parents, for all the encouragement, company and delicious food. Thank you for always believing in me, meeting you is the best thing happened during my DPhil study.

Publications

Chapter 2 have been published on:

Chengchen Duan and Helen E Townley.

Isolation of NELL 1 Aptamers for Rhabdomyosarcoma Targeting. *Bioengineering*, 2022; 9(4):174.

Parts of Chapter 3 and Chapter 5 have been published:

Benjamin D White, Chengchen Duan **[Joint First Author],** Helen E Townley.

Nanoparticle Activation Methods in Cancer Treatment.

Biomolecules, 2019; 9(5):202.

Parts of Chapter 4 and Chapter 5 have been ready for submission:

Chengchen Duan, Helen E Townley.

Exploitation of high tumour GSH levels for targetted siRNA delivery in rhabdomyosarcoma cells.

Manuscript in preparation

Also co-authored:

Duan, C., Evison, A., Taylor, L., Onur, S., Morten, K., & Townley, H.

The common diabetes drug metformin can diminish the action of citral against Rhabdomyosarcoma cells in vitro.

Phytotherapy Research, 2021, 35(3), 1378-1388.

Duan, C., & Townley, H. E.

Nanoparticles as Vectors to Tackle Cancer.

Biomolecules, 2021, 11(11), 1729.

Chapter 1

Background

1.1 Cancer

As the second-highest cause of death globally which accounted for near 10 million deaths (2020; WHO), cancer is of major concern, especially in the developed countries (Sung et al., 2021). Efforts have focussed on overcoming the obstacles to early diagnosis and efficient treatment (Chakraborty & Rahman, 2012). Data from Cancer Research UK indicated that as a consequence the one-year, five-year and ten-year survival rates have significantly improved (Cancer Research UK, 2019). The ten-year survival rate of cancer patients in England and Wales, for example, has increased to over 50 % which doubled from 24 % from four decades ago (Cancer Research UK, 2019). Although different cancers are normally triggered by different factors, there are two most common reasons: genetic instability and mutation, and a pro-inflammatory environment (Grivennikov et al., 2010). Despite improvements in identifying and treating cancer, the death rate of cancer patients remains unacceptably high in the UK compared with other western European countries, such as Sweden or Netherlands, especially in some of the more aggressive tumour patients such as liver cancer, pancreatic cancer and lung cancer (Nur et al., 2015).

Cancers cells are normally characterised as genetically altered autogenic cells (Stratton et al., 2009). They have specific physiologic characteristics compared with normal body cells (Chakraborty & Rahman, 2012; Grivennikov et al., 2010; Stratton et al., 2009). They are normally found to lose or alter some of their metabolism activity from the genetic level, which leads to full or partial suppression of the genetic error repairing ability (Stratton et al., 2009). The downregulation of certain gene suppressor genes, such as PTEN or p53, can lead to the accumulation of the inherited genetic errors (Armaghany et al., 2012). Conversely, a large number of oncogenes which should be muted can be

upregulated and cause cancer (Stratton et al., 2009). To date, efforts have been made to develop the most efficient way to diagnosis and treat cancer as early as possible, based on the physiological and genetic features of cancer cells, without damaging healthy tissues (Chakraborty & Rahman, 2012; Pucci et al., 2019).

Cell growth and proliferation are carefully controlled with limited cycles in all normal healthy cells, except stem cells (Moolgavkar, 1993).With the help of a variety of growth and signalling factors, the number and function of normal cells is precisely managed and balanced (Sears & Nevins, 2002). However, cancer cells have been found to proliferate at a high and sustained rate (Laird, 1964). The self-stimulatory proliferation signals and deregulation of the anti-proliferative signals results in disrupted homeostasis in cancer cells (Witsch et al., 2010). At the same time, the cellular apoptosis mechanisms for cancer cells are also altered or lost (Laird, 1964; Okada & Mak, 2004). Thus, cancer cells are generally found to grow in an uncontrollable manner both *in vivo* and *in vitro* (Laird, 1964).

As a result of dysfunction and misregulation in mitochondrial signalling pathways, cancer cells have a changed and abnormal metabolism (Jones & Thompson, 2009). The Warburg effect has been recognized as one of the most distinctive characteristics of cancer's metabolic derivation (Potter et al., 2016). Generally, oxidative phosphorylation (OXPHOS) in normal cells is considered as the main mechanism of respiration for generating adenosine-5'-triphosphate (ATP) which acts as the carrier for energy (Smeitink et al., 2001; Warburg, 1956; Warburg et al., 1927). Compared with glycolysis, OXPHOS is more efficient and consumes more oxygen (du Plessis et al., 2015; Smeitink et al., 2001). Nevertheless, it has been discovered that most cancer cells still choose to produce energy primarily by glycolysis rather than OXPHOS even when adequate oxygen is available in the cytoplasm (Smeitink et al., 2001; Warburg, 1956; Warburg et al., 1927). This phenomenon was concluded as the Warburg effect to represent the metabolic derivation

which causes inadequate energy production in cancer cells (Warburg, 1956; Warburg et al., 1927). However, there have been studies contesting the established Warburg effects. For example, it has been discovered that the Warburg effects may actually be a result of cancer cells adapting to the damaged mitochondria (Lopez-Lazaro, 2008). It has also been hypothesized that the altered gene regulation including downregulation of suppressor genes and upregulation of oncogenes may directly or indirectly induce glycolysis as the energy source (Schiliro & Firestein, 2021). Therefore, the mechanism of the Warburg effect is not completely understood at the moment.

In order to develop quickly, most types of cancer cells aggregate and form clusters (Deisboeck et al., 2001). This form of solid tumour structure absorbs an excessive amount of oxygen and nutrients (Deisboeck et al., 2001). For the transportation, angiogenesis (the signalling of development of new blood vessels) is boosted by vascular endothelial growth factor (VEGF) produced by cancer cells (Sherwood et al., 1971).

As a result of angiogenesis, the cancer cells within the solid tumour are able to overcome the limits imposed by passive nutrition transport from nearby blood vessels(Fang et al., 2011). However, the rapidly grown blood vessels surrounding tumours are normally made up of poorly aligned defective endothelial cells without sufficient support from the smooth muscle layer. This causes large fenestrations and an enhanced permeability of tumour blood vessels (Fang et al., 2011). Furthermore, as the lymphatic system is poorly linked to the tumour area large molecules or nanoparticles are retained (Nakamura et al., 2016). This further enhances the permeability effect. In general, EPR effect has been considered as an important and fundamental theory for the delivery of anti-tumour nanocarriers(Matsumura & Maeda, 1986).

In addition to the fundamental complexity of cancer cells, solid tumours are normally formed of multiple layers of one or more types of cancer cells, and could build a special

and complex tumour microenvironment (TME) which is associated with tumour intra-heterogeneity (Quail & Joyce, 2013). Moreover, hypoxia has been found in the core of solid tumours due to the insufficient supply of nutrients and oxygen, and altered metabolic pathways (aerobic glycolysis) (Krock et al., 2011). This process creates an acidic microenvironment (pH 6.5) inside the tumour through the accumulation of the acidic metabolic products (Quail & Joyce, 2013; Trédan et al., 2007).

The TME has also been found to link with abnormal proliferation signalling, cell apoptosis resistance, upregulated invasion, and metastasis (Quail & Joyce, 2013; Trédan et al., 2007). In addition to the cancer cells within the TME, there are also several other types of supporting cell types, such as the cancer-associated fibroblasts (CAFs) (Liu et al., 2019), TME specific extracellular matrix (ECM), and immune-related cells (T cells, B cells, macrophages and NK cells) (Rossi et al., 2020). Therapies that target the TME are urgently needed, as a powerful enhancement of other current cellular-level targeting therapies which were developed only focusing on the molecular level of cancer cells (Pucci et al., 2019; Trédan et al., 2007).

The TME is directly associated with the resistance against many cancer therapies, especially in the delivery of the therapeutic reagents into the inner core of solid tumours (Khawar et al., 2015).

Metastasis has long been thought to be a key indicator of whether a tumour is benign or malignant (Cancer Research UK, 2019; Koten et al., 1993), and as the most lethal aspect of cancer (Liotta et al., 1991).

It has been found that the cell-to-cell attachment or adhesion is inhibited in the development of various types of aggressive cancers (Guan, 2015). This can directly lead to enhanced cellular mobility and invasion, which is also shown directly as tumour metastasis (Liotta et al., 1991; Weidner et al., 2010).

Cancer cells can migrate away from the solid tumour into surrounding tissues, or even distant organs through the circulatory and lymphatic systems (Guan, 2015; Quail & Joyce, 2013). The main cause is the deregulated cell-to-cell attachment or adhesion which leads to the escape of cancer cells into the outer circulatory system (Berx & van Roy, 2009; Janiszewska et al., 2020; Su et al., 2017).

1.2 Rhabdomyosarcoma

Soft tissue sarcomas (STS) are one of the most common paediatrics cancers, and account for nearly 10 % of all cancer cases in children (Skapek et al., 2019; Ward et al., 2014). Furthermore, half of all childhood STS cases are rhabdomyosarcoma (RMS) (Skapek et al., 2019; Ward et al., 2014). RMS is a type of cancer which is directly linked to the propensity for myogenic differentiation (Chen et al., 2019; Skapek et al., 2019). There are two main subtypes of RMS; alveolar RMS (aRMS) and embryonic RMS (eRMS). Both of the subtypes have different orientation and fundamental differences in cell metabolism (Davicioni et al., 2009).

1.2.1 Molecular fundamentals of RMS

Both aRMS and eRMS were found to originate from immature skeletal myoblast-like cells (Davicioni et al., 2009; Skapek et al., 2019). Cytogenetics has shown that the development of RMS is normally associated with chromosomal translocations of chromosomes 1 or 2 and chromosome 13 (referred as t(1;13) and t(2;13)) (Xia et al., 2002). However, a small percentage of aRMS patients do not have any of these translocations (Wang, 2012). Clinically, tumours from these patients are physiologically equivalent to those with eRMS (Skapek et al., 2019; Wang, 2012).

aRMS, eRMS, and pleomorphic RMS are the three histological subtypes of RMS described by the WHO, with aRMS and eRMS being the most common in children and teenagers (Parham & Barr, 2013; Rudzinski et al., 2015). Spindle cell & sclerosing RMS is now also recognised as a new subtype by the WHO (Rudzinski et al., 2015). The shape of RMS cells is very varied: spherical, ovoid, 'tadpole-shape', spindle-shaped, or similar to normal myoblasts (Parham & Barr, 2013).

A further method to enhance the classification of RMS subtypes relates to the difference between 'fusion-positive' (FPRMS) and 'fusion-negative' (FNRMS) RMS subtypes (Davicioni et al., 2009; Parham & Barr, 2013). Most aRMS-associated genome translocations could lead to the production of novel fusion proteins such as the encoding paired box protein (PAX) 3 or PAX 7 based on Next Generation DNA & RNA sequencing (Shern et al., 2014).

For the diagnosis of RMS, tumour tissue is collected by incisional, excisional or core needle biopsy. Biopsy samples are then sent for histo-immunology or pathology examinations (Parham & Barr, 2013; Rudzinski et al., 2015).

1.2.2 Development of RMS treatment methods

Currently, most of the patients rely on intensive and invasive treatment methods, such as chemotherapy, ionizing radiotherapy, surgery, or combinations (Chen et al., 2019; Skapek et al., 2019). These aggressive treatments can lead to unavoidable life-long side effects. Moreover, metastatic RMS cases which are diagnosed late due to the lack of early diagnostic methods have a very low survival rate of less than 30 % with the traditional treatment methods (Hoffmeier et al., 2014; Skapek et al., 2019). However, there have been collaborative RMS-related clinical trials worldwide, which enabled a dramatic improvement in survival rate in the last few decades (Chen et al., 2019). Furthermore,

knowledge of RMS at a more precise molecular level for more sensitive diagnosis methods, and targeted therapy with lower/no side effects, has advanced treatment methods in recent years (Arruebo et al., 2011; Fordham et al., 2021).

Although there have been significant advances in the treatment of RMS, children with RMS metastasis and relapse have an extremely low rate of survival (Heske & Mascarenhas, 2021; Wang, 2012). Furthermore, patients are subjected to months of various intensive treatment methods, such as the surgery combined with long-term chemotherapy and/or radiotherapy. These can all lead to immediate life-threatening toxicity and potentially life-long side effects (Chen et al., 2019).

1.2.3 Epidemiology of RMS

1.2.3.1 Age and sex

RMS can be caused by numerous factors; which are different for various subtypes and individuals. Based on the current data, it has been found that eRMS is more frequent than aRMS within the young population (Wang, 2012).

One main factor which affects the incidence rate of RMS is the patient's age. RMS is the most prevalent soft tissue sarcoma in children, despite being a rare disease (Egas-Bejar & Huh, 2014; Skapek et al., 2019). Within the population younger than 20, the total RMS incidence rate is around 5 per million people (Egas-Bejar & Huh, 2014; Skapek et al., 2019). This rate is even higher for the population younger than 15 which is around 6.5 per million people, according to a study in Sweden in 2016 (Lychou et al., 2016; Skapek et al., 2019). While aRMS has a constant incidence rate throughout the childhood and adolescence period, eRMS is found to have much higher frequency in the early stages of adolescence rather than childhood (Egas-Bejar & Huh, 2014; Ognjanovic et al., 2009).

Different kinds of the PAX-FOXO-positive abnormal fusions may also affect the average

age of RMS. For example, the average age of the PAX3-FOXO1-positive cases were found to be greater than the PAX7-FOXO1-positive cases (Shern et al., 2014).

In addition, gender has also been found to be associated with the RMS incidence rate. It has been found that males are more likely than females to have eRMS with a near 50 % higher incidence rate (Ognjanovic et al., 2009; Skapek et al., 2019).

While RMS incidence rate has been widely considered as not to be linked with patient ethnicity, surprisingly, the prevalence of RMS seems to be lower in Asia, with just a few instances per million seen in Japanese, Indian, and Chinese populations which may indicate there may be still some linkage between ethnicity and incidence rate (Egas-Bejar & Huh, 2014; Ognjanovic et al., 2009; Skapek et al., 2019).

Based on historical data, it has been indicated that the incidence rate of less aggressive eRMS has remained stable in the past few decades since 1970s (Ognjanovic et al., 2009). Nevertheless, a constantly increasing of incidence rate of more aggressive aRMS with a significantly increase of 4.2 % within the same period has raised concern (Ognjanovic et al., 2009; Ward et al., 2014). Some research suggested that it may due to diagnosis methods with higher sensitivity, or changes in the diagnostic criteria of aRMS (Parham & Barr, 2013; Skapek et al., 2019; Wang, 2012).

1.2.3.2 Factors of RMS development

In contrast to other types of sarcomas (e.g. Ewing sarcoma, osteosarcoma) which also have high incidence rates in adolescence, no detailed genomic analysis has been performed for RMS (Skapek et al., 2019). Finding the right mutation point in the genome from the whole-genome or exome sequence is crucial for finding the right cure for RMS. Currently, the exact genetic mutation causing the disease has not been identified. Still, there is a large amount of evidence showing that both genetic mutations and environmental factors play

an important role in RMS development (Davicioni et al., 2009; Egas-Bejar & Huh, 2014; Fordham et al., 2021; Wang, 2012; Xia et al., 2002).

In addition, it has been suggested that the development of RMS may have a strong correlation with other genetic diseases. For example, it has been found that the eRMS is more likely to develop within the population which has the neurofibromatosis type I (linked with deletion of NF1 gene) (Ars et al., 2003; Crucis et al., 2015), Li–Fraumeni syndrome (linked with germline TP53 mutations) (Magnusson et al., 2012) or Costello syndrome (linked with HRAS gene mutation) (Kerr et al., 2006; Skapek et al., 2019).

Moreover, like other cancers, environmental factors have also been found to correlate with the development of RMS, such as water and air pollution, and ionising radiation (Cancer Research UK, 2019; Sung et al., 2021). Detailed research has shown that children and teenagers who are exposed to much higher volumes of environmental hazard factors, have a much higher RMS incidence rate (Egas-Bejar & Huh, 2014).

1.2.4 Diagnosis & prevention of RMS

As RMS has become a worldwide concern, correct diagnosis and prevention are extremely important.

1.2.4.1 Clinical diagnosis

Unlike most cancers which mainly focus on one or few organs, RMS may affect almost any region of the body (Skapek et al., 2019). However, there are still some preferences for the subtypes of RMS. For example, it has been discovered that aRMS normally locates in the extremities of patients, with very few cases in the head and neck (Parham & Barr, 2013; Wang, 2012). eRMS normally showed in an opposite way with most cases locating in the head and neck (Parham & Barr, 2013; Wang, 2012).

It was even more serious that more than one-fifth of children may show distant metastasis

during the first diagnosis based on the clinical test results (Koscielniak et al., 1992). As discussed above, metastases mainly develop through the haematogenous or lymphatic pathways, and expand to the bone and bone marrow, and lungs (Egas-Bejar & Huh, 2014; Koscielniak et al., 1992).

The research on the early signs and symptoms of RMS has been quite limited, especially in the young population. RMS commonly starts as a painless solid mass located in the head and neck, or arms and legs. Some early signs may also be found in the tissue of surrounding organs or nearby neurovasculature (Egas-Bejar & Huh, 2014; Rudzinski et al., 2015; Skapek et al., 2019; Wang, 2012).

Although it can be difficult to identify RMS due to the vagueness of early signs and symptoms, recent advances allow more sensitive methods to diagnose the RMS accurately through a tiny amount of RMS specific biomarkers within the peripheral blood sample (Chen et al., 2019). However, this method is not sufficient for the correct diagnosis of the subtype of the RMS and the proteins could also be produced by other tumours, such as the malignant triton tumour and Wilms tumour (Chen et al., 2019; Egas-Bejar & Huh, 2014). Further validation of cellular characteristics is also needed for accurate diagnosis.

More sensitive techniques have also been applied for better and earlier detection of RMS. For example, the reverse transcription polymerase chain reaction (RT-PCR) was used for tracing RMS with very limited amounts of sample (peripheral blood or bone marrow). The RMS could be detected through measurement of RMS related gene expressions, such as the Myogenic Differentiation 1 (MyoD1) and acetylcholine receptor (AChR) (Gallego et al., 2006; Thomson et al., 1999).

1.2.4.2 Prevention

Similar to other childhood cancers which are hard to be diagnosed early with no clear

hazard factors, preventative measures are not clear for most the RMS patients (Wang, 2012). However, it is advisable for certain high-risk groups to perform regular blood tests with RT-PCR to trace the possible RMS which could help early diagnosis, and prevent potential life-threatening metastases (Chen et al., 2019; Gallego et al., 2006; Thomson et al., 1999)

1.2.5 Treatment of RMS

Over the last several decades, the 5-year overall survival rate of RMS in the young population has significantly increased to over 70 % (Egas-Bejar & Huh, 2014; Ward et al., 2014).

Numerous factors contribute to this improved survival, including the use of multimodal therapies, which typically include surgical removal of the primary solid tumour, ionising radiation to the primary tumour site, and intensive chemotherapy (Chen et al., 2019).

1.2.5.1 Surgical removal

Surgery works most effectively if the tumour site can be clearly identified and localized. It is also worth noting that surgery is only successful before the metastases of the tumour (Sullivan et al., 2015).

Surgical treatments and procedures have improved for tumour removal. With new techniques (like gamma knife), the tumour site could be removed with less harm to the patients, even in some metastasis instances (Flannery et al., 2010). However, surgery has its own disadvantages. Not all tumours could be fully removed, especially in inoperable sites which may lead to permanent harm to the patient (Chen et al., 2019). Moreover, a high relapse rate has been recorded for patients in which tumour tissue is not fully removed, or where there are hidden metastases (Chen et al., 2019; Heske & Mascarenhas, 2021).

Due to the limitation of the surgical methods, although it is still the most widely applied

for RMS treatment, combination use of chemotherapy and/or radiotherapy has become usual for current clinical treatment (Chen et al., 2019; Egas-Bejar & Huh, 2014).

1.2.5.2 Chemotherapy

Chemotherapy has been used for many decades, and involves the application of specific chemical compounds to eliminate tumour growth (Chabner & Roberts, 2005). The three main types of chemotherapeutics are hormonal compounds, cytotoxic compounds, and molecularly targeted compounds (Chabner & Roberts, 2005; Chen et al., 2019). To date, the most widely applied type for cancer treatments are cytotoxic compounds (Chabner & Roberts, 2005). The fundamental ethos of cytotoxic chemotherapy is to injure and kill rapidly dividing and growing cells by interfering with DNA synthesis or preventing mitosis (Chabner & Roberts, 2005). Currently, the chemotherapy drugs which are most widely used clinically are Doxorubicin, Paclitaxel and Camptothecin which could affect the mitosis and/or the DNA ligation enzyme activity inside cells. This further leads to permanent DNA damage and cellular apoptosis (Chabner & Roberts, 2005; Hsiang et al., 1985).

These drugs may be successful in specifically killing cancer cells because most cancer cells proliferate at a much faster rate than healthy cells. However, some healthy cells such as the blood stem cells in bone marrow also proliferate quickly and can be significantly affected. As a result, severe side effects such as decreased blood cell production, hair loss, and infertility are common in patients using chemotherapy (Chabner & Roberts, 2005).

1.2.5.3 Radiotherapy

As another frequently used treatment methods, radiotherapy is normally applied together with surgery to remove the tumour tissue (Symonds, 2001). It works by applying ionising radiation to the tissue to cause the DNA damage and cell death in the exposed area

(Symonds, 2001). Similar to the fundamentals of the chemotherapy, cancer cells normally grow at a much faster speed than healthy cells, and consequently, are more greatly affected (Chakraborty & Rahman, 2012; Stratton et al., 2009). Furthermore, DNA damage repair is normally restricted in the cancer cells. Therefore, once the cells are damaged by ionising radiation, the DNA could not be repaired effectively, leading to decreased proliferation and apoptosis (Llen et al., 2009; Symonds, 2001). Besides, as the normal cells have a functional DNA damage repair system, they will recover from the radiation or be removed by the immune system. This method can be used to treat a wide range of cancers, including haematological cancers (blood cancers that do not form solid tumours), and it can also be used to prevent recurrence following surgery (Symonds, 2001).

The limitations of radiation, however, continue to hamper its use in cancer treatment. Radiotherapy has the potential to inflict irreversible damage to healthy tissues in the surrounding areas, leading to long-term complications such as tissue fibrosis, hair loss, and infertility (Gordon & McMillan, 1997; Symonds, 2001).

1.3 Gene Therapy & Nanovectors

Gene therapy is used as a means to bring exogenous nucleic acids into cells. Commonly applied gene therapy molecules include gene segments, siRNAs, miRNAs, and oligonucleotides. The main goals of gene therapy are editing target genes, regulating expression, or expressing an exogenous protein (Kamimura et al., 2019; Li et al., 2019; Roma-Rodrigues et al., 2020; Senapati et al., 2019; Shao et al., 2019).

Tumour gene therapy has been achieved using both *ex vivo* and/or *in vivo* gene transfer of the therapeutic nucleic acids (TNAs) (Amer, 2014). *Ex vivo* approaches gather patient-derived tumour cells, grow them as 2D monolayers, modify them genetically, and then

reintroduce them into the host (Amer, 2014). For *in vivo* delivery of TNAs into the tumour cells, the TNAs could be transported through nasal, oral, transdermal or intravenous routes (Amer, 2014; van Haasteren et al., 2018; Zylberberg et al., 2017).

1.3.1 Cancer gene therapy at molecular biology level

Previous work has shown that TNAs, such as genes, oligonucleotides, miRNAs, or siRNAs, can be delivered to tumours and eliminate cancer cells by suppressing oncogenes or restoring tumour suppressor gene expression (Kamimura et al., 2019; Li et al., 2019; Roma-Rodrigues et al., 2020; Senapati et al., 2019; Shao et al., 2019). The fundamental aim of these methods, such as RNA interference (RNAi), gene editing therapy and antisense therapy, is to change or modulate gene expression (Fernandes & Baptista, 2017; Roma-Rodrigues et al., 2014; Roma-Rodrigues et al., 2020). In addition to targeting the tumour cells, similar methods can be used to target the TME *via* angiogenesis (Chen, Mangala, et al., 2019; de Palma et al., 2017; Sherwood et al., 1971).

1.3.2 Different types of gene therapy

1.3.2.1 siRNA mediated gene silencing

Gene silencing is a mechanism in which nucleic acids are introduced into tumour cells, causing specific genes to be downregulated (Jain et al., 2018; Roma-Rodrigues et al., 2020; Xin et al., 2017). The siRNA is normally delivered as a longer version of double-stranded RNA with the 3'-end nucleotides overhang before cleavage and processing with the intracellular RNase III-like enzyme into small siRNA. The functional complex which is known as the RISC (RNA-induced silencing complex) can bind the processed siRNAs and keep the more stable strand within the complex for the guiding of the target messenger RNA (mRNA). The targeted mRNA is then cleaved by the specific catalytic RISC (Dana et al., 2017; Jain et al., 2018; Roma-Rodrigues et al., 2020; Xin et al., 2017). Introducing

siRNA into tumour cells to target a specific complementary sequence on a gene's mRNA, either causing its death or limiting protein creation, is a common method of gene silencing therapy. The target for the siRNA gene silencing could be commonly applied to oncogenes such as KRAS (Kirsten rat sarcoma viral oncogene), or the drug resistance gene MDR1 (Multidrug resistance-1) (Mehta et al., 2019; Shao et al., 2019; Strand et al., 2019; Zhang et al., 2019). Upregulated-gene related to the proliferation of cells could also be specifically selected as the target, for example the EWS-FLI1 gene for the Ewing sarcoma (Hu-Lieskovan et al., 2005). Target selectivity, avoiding of off-target effect, short circulation time, cellular internalisation, and endosomal escape are all issues that siRNA-based approaches have to deal with before they can be approved for wide use in the clinic (Setten et al., 2019). There are numerous studies focusing on how to get around these limits, such as computational simulation for better siRNA design, nanoparticle encapsulation, and chemical modification (Devi, 2006; Shao et al., 2019; Singh et al., 2018).

1.3.2.2 Gene Replacement

Gene replacement could be used for the preservation of the gene's stability and full expression, or the restoration of mutated genes to their wild-type form (Yamamoto & Gerbi, 2018). As gene suppressor genes, such as the P21, TP53, and PTEN, have been found to be fully (or near fully) silenced in most cancer cell types (el Sharkawi et al., 2017; Ibnat et al., 2019; Moore et al., 2018). The P53 protein which expression level was controlled by the TP53 gene, for example, has been found to play a critical role in cell cycle control, apoptosis, and/or autophagy. There have been many studies applying TP53 gene as a potential target for gene replacement cancer therapy (Valente et al., 2018).

Gene replacement therapy is normally achieved by delivering the exogenous DNA into the cell nucleus. To facilitate this process, strategies such as nuclear-targeted delivery have been proposed (Durymanov & Reineke, 2018). However, gene replacement therapy is

more complex than just delivering the DNA into nucleus; other processes include activation of certain upstream pathways. Thus, to date suppressor gene replacement application to cancer therapeutics is limited (Roma-Rodrigues et al., 2020).

1.3.2.3 MicroRNA-Specific Therapeutics

As a kind of non-coding RNA which has been found to significantly affect expression of specific genes in the cytoplasm, certain microRNAs (miRNAs) which support the tumour formation are overexpressed in cancer. Other miRNAs are downregulated, bypassing inhibitory control of oncogenes or regulation of cell differentiation and death (Tan et al., 2018). miRNA targeted treatment works by regulating the miRNA levels inside cells. While miRNA uses the same mechanism as RNAi, the former is a complementary (or semi-complementary) sequence to the 3′ untranslated region (3′-UTR) of a single messenger RNA (mRNA) target to interfere with a particular cellular function (Senapati et al., 2019).

The miRNA levels that change within abnormal cancer cells may be restored to normal physiological levels utilising miRNA-duplexes to replace under-expressed miRNAs complementary to the sequence of the miRNA of interest (Tan et al., 2018). Numerous studies proposed miRNA repositioning for cancer therapy, for example, to upregulate the miR181a/miR212 miRNAs combination to tackle the anti-myogenic features of FNRMS. This significantly decreased the proliferation rate of the targeted cells (Pozzo et al., 2021). However, there are still many issues around the application of miRNAs such as circulatory degradation, off-target effects, cellular-toxicity, and inadequate transportation (Roma-Rodrigues et al., 2020; Xue et al., 2017).

1.3.2.4 Genome Editing

As one of the hot topics nowadays, genome editing treatment has great potential to become the next generation method for gene therapy. Genome editing treatment, including specific

insertion, deletion, replacement, or integration within the genome, is performed with genome editing tools such as the Zinc finger nucleases (ZFN), CRISPR/Cas9 system, transcription activator-like effector nucleases (TALEN) (Maeder & Gersbach, 2016).

Selection of the potential site for DNA cleavage and avoiding any possible collateral damage to the expression of other gene expression is crucial for whole genome editing treatment. In general, the most efficient tool for current genome editing treatment is the CRISPR/Cas9 system which has been proven to be stable in editing the selected mutation associated with the tumour proliferation and metastases (Moon et al., 2019; Xing & Meng, 2020; Yeh et al., 2019; Yin et al., 2019).

CRISPR/Cas9 system applies *Streptoccocus pyogenes* (SpCas9) to recognize the specific sequence for guiding. The whole system is guided by the Cas 9 single guide RNA (sgRNA) which is customized based on the targeted region within the genome (Tong et al., 2019). However, although CRISPR/Cas9 system has been considered as system with high specificity, the amount of CRISPR/Cas9 within the normal tissues other than the tumour area still needs to be minimized to avoid off-target effects (Roma-Rodrigues et al., 2020).

1.3.2.5 Suicide Genes

As a conversional way of gene therapy, the suicide gene therapy includes two main routes for treatment: the first way is direct suicide gene delivery & therapy, which mainly focuses on delivering a gene encoding one or multiple cytotoxic proteins and expressing it/them inside the cancer cells. The second way is to deliver an enzyme-coding gene which could convert a non-toxic prodrug into cytotoxic compounds (Abenhamar Navarro et al., 2016; Roma-Rodrigues et al., 2020). The main goal of both routes is eliminating the cancer cells through the generation of cytotoxic molecules that induced cell death.

There are currently multiple clinical trials focusing on different tumours, such as liver and

colon tumours (Abenhamar Navarro et al., 2016). The possibility of applying suicide gene therapy for RMS treatment has been investigated: herpes simplex thymidine kinase (HSV-TK) gene was induced for gene therapy of RH30 cells. The induced HSV-TK could efficiently convert the non-toxic prodrug ganciclovir (GCV) into cytotoxic molecules which lead to cell apoptosis through interruption of DNA synthesis and the induction of mitochondrial damage (Konieczny et al., 2017).

One difficulty in suicide gene therapy is that the selected and delivered suicide gene needs a high expression within tumours, which is essential to be under the control of tumour-specific promoters (Duzgunes, 2019; Konieczny et al., 2017).

1.3.2.6 Angiogenesis Targeted Gene Therapy

TME targeted gene therapy has become of increasing interest in recent years (de Palma et al., 2017; Sherwood et al., 1971). It is well known that hypoxia generated by uncontrolled tumour cell proliferation induces the release of angiogenesis signals to ensure sufficient delivery of nutrition and oxygen into the tumour (Krock et al., 2011; Lugano et al., 2020). Common angiogenesis signals include the vascular endothelial growth factor (VEGF), and angiopoietins (Lugano et al., 2020). To combat tumour angiogenesis, gene therapy is mainly applied for re-adjusting essential gene regulation related to angiogenesis (Sherwood et al., 1971). For example, pro-angiogenic genes like VEGF could be down regulated and anti-angiogenic factors like endostatin could be upregulated through proper induction of therapeutic genes (Sun et al., 2019). The potential for angiogenesis targeting in cancer therapy is now restricted by our current limited knowledge around the TME abnormal gene expressions. Moreover, sole regulation of certain angiogenic genes may result in the activation of alternative pathways which may offset the therapeutic effects (Lugano et al., 2020; Roma-Rodrigues et al., 2020).

1.3.3 Nanovectors for gene therapy

There are several obstacles for the administration of naked TNAs which has limited the widely application of gene therapy (Chen et al., 2016).

Although TNAs has been considered as having great potential in oncology treatment, there are still many barriers blocking the clinical application of TNAs in vivo, such as nucleases degradation, non-specific binding with serum proteins and kidney filtration (H. J. Kim et al., 2016; Tatiparti et al., 2017). TNAs have been used clinically, but mostly only in some specific areas such as eyes or skin which are on the surface. In addition, the anionic charge of both the phosphate backbone and cell membranes increases the difficulty of passive diffusion of TNAs into cells (J. Wang et al., 2010) (Figure 1.1). Furthermore, bare TNAs (such as mRNA or siRNA) has no targeting ability which may lead to severe side effects in normal cells. Nanoparticles made of a variety of materials have been assessed for the protection of TNAs (Du et al., 2014; H. J. Kim et al., 2016; J. Wang et al., 2010). Moreover, one of the major advantages of the gene-editing nanoparticles carrying the TNAs is that it significantly decreases the possibilities of being cleared by the immune system and the percentage of off-target effects compared with the traditional retrovirus system or bare TNAs (H. J. Kim et al., 2016).

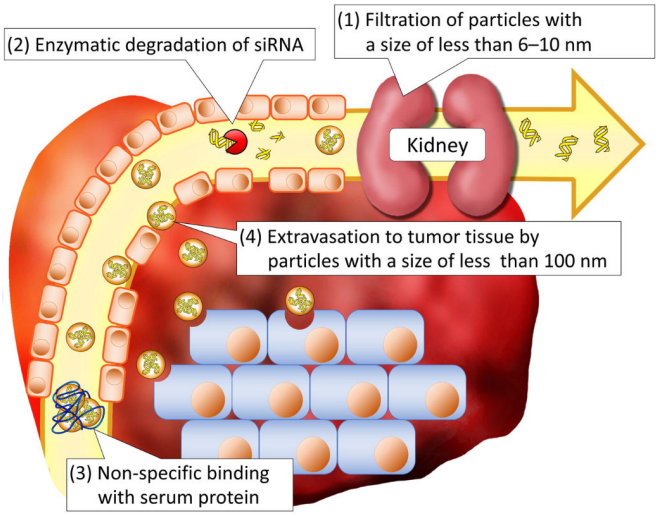

Figure 1.1 Obstacles of siRNA delivery in vivo, image was modified from literature (H. J. Kim et al.,

2016)

Thus, it is necessary to use stable vectors that protect the TNA cargos and efficiently deliver them into tumour cells (van Haasteren et al., 2018). In addition to overcoming the transfection or delivery obstacles for both *in vitro* therapeutic cells preparation and *in vivo* gene therapy, suitable delivery carriers could also improve efficiency (Jain et al., 2018; McNeish et al., 2004; Singh et al., 2018; van Haasteren et al., 2018). The successful cancer gene therapy vectors should be safe, effective, and controllable based on the actual patients' conditions (Sun et al., 2019).

The first TNA delivery vectors were based on a viral platform, such as adenovirus or lentivirus (Lundstrom, 2018). Viral vectors have many advantages in delivering TNA based on their fundamental characteristics of penetration into cells and expression of carried nucleic acids. There are many studies and clinical trials proving the efficiency of viral vectors in gene therapy (Lundstrom, 2018; N. Yang, 2015).

Nevertheless, there is no perfect system when considering the advantages and limitations of the whole carrier. Viral vectors have been found to have many shortcomings especially regarding safety issues (Lundstrom, 2018). For example, clinical trials have shown that viral vectors were associated with potential immunogenicity, blood clotting risk, and cancer risk. Furthermore, the packaging capacity of viral vectors, especially for large TNA, has been restricted by viral vector size and technical engineering limitations compared to totally synthetic nanoparticles (Grieger & Samulski, 2005; Kaiser, 2020; Singh et al., 2018). Thus, to overcome all the shortcomings of viral vectors, researchers have focused more on the development of fully-synthesized nanoparticles which can be customized for TNA delivery.

To improve upon viral vectors, nanosystems are often required to be effective and

biocompatible for delivery. Similar to other vectors, typical TNAs delivered by nanoparticles are DNA, siRNA, miRNA, or more complex system like CRISPR/Cas9 (Patil et al., 2019; Roma-Rodrigues et al., 2020; N. Yang, 2015).

Nanoparticles are considered to be particles which are of 1-100 nm in size (*ISO - ISO/TS 80004-2:2015 - Nanotechnologies — Vocabulary — Part 2: Nano-Objects*, n.d.). Nanoparticles can be made with inorganic (e.g. silica (Ma et al., 2010), iron oxide (Stanley et al., 2012), carbon (Ray et al., 2009)) or organic materials (e.g. liposomes (L. Feng et al., 2017)). As the nano-scale could provide significantly higher surface area, nanoparticles are applied in many different areas like catalysts and innovative therapeutics. In clinical areas, nanoparticles have been widely applied for delivering different classes of therapeutic reagents and diagnostic probes (Shi et al., 2017). In the delivery process, nanoparticles can passively accumulate in the tumour area due to enhanced permeability and retention (EPR) effects. This is the result of a wider fenestration of blood vessel of blood vessel endothelial cells in tumour than normal tissues (Manchun et al., 2012). In addition to passive accumulation in the tumour, active targeting of nanoparticles can be achieved through grafting targeting molecules onto the surface, such as antibodies (Liu et al., 1998), peptides (Hu et al., 2012), or aptamers (Sivakumar et al., 2018). Through surface functionalization, the nanoparticles could significantly improve the transfection efficiency of delivered plasmids and siRNA compared to traditional viral vectors. The functionalization could also provide nanoparticles with better biocompatibility to avoid *in vivo* clearance during delivery (Patil et al., 2019).

In addition, compared with viral vectors, many functionalized nanoparticles have a better penetration of tumours and cells, and have shorter endosomal escape time to protect the carried TNAs (Chen et al., 2016; van Haasteren et al., 2018).

The TME introduces significant obstacles for delivery into the core of solid tumours;

including little or no vascularization, thick layers of ECM, and low interstitial fluid pressure (Deng et al., 2018; Y.-L. Su & Hu, 2018). To overcome these obstacles, the synthesized nanoparticles should be specifically designed and tested accordingly. For example, through conjugating the ECM specific linker onto polymetric micelles which could sensitively cleave the matrix metalloproteinases (MMPs), the delivery efficiency of paclitaxel into tumour tissues was significantly increased by 2.5 times compared to the control group (Roma-Rodrigues et al., 2020; Su & Hu, 2018; Zhu et al., 2013).

The design of smart nanoparticles requires regulating the release of carried TNAs under the right conditions and environment. Release can be controlled extrinsically or regulated by variations between malignant and normal cells (White et al., 2019). Intrinsic activation methods include pH, enzymatic and concentration-dependent changes as a result of altered cancer cell metabolism. Extrinsic activation conditions are also commonly applied, such as ultrasonic, magnetic, light, and X-ray activation (White et al., 2019).

1.3.3.1 Inorganic Based Materials – Silica Nanoparticles

Following the introduction of mesoporous silica materials in the last century (Kresge et al., 1992; Yanagisawa et al., 2006), several different applications in various fields have been reported, including catalytic chemistry, adsorption of chemical and biomolecules, sensors of molecule concentration or pH changes, and biomedical materials for controlled drug delivery. Current, all routes for synthesising the mesoporous material are based on a bottom-up strategy: Mesoporous silica nanoparticles (MSNPs) are synthesised using a sol-gel system and subsequent template removal. The characteristics including the diameter and shape of the nanoparticles, the mesopores, and all other physical characteristics can be adjusted by changing the synthesis condition and templates (Nandiyanto et al., 2009; Suteewong et al., 2010).

There are multiple synthesis protocols for different type of silica nanoparticles which have

been proven to be reliable and repeatable. However, some limitation still exists for the synthesis, for example, the selection of sol-gel templates for porous structure formation which are normally surfactants are quite limited (Putz et al., 2015). Moreover, insufficient removal of surfactants normally leads to strong cytotoxicity and immunogenicity (Huang et al., 2014).

For the last two decades, MSNPs have widely applied in biomedical research due to their excellent biocompatibility, stability, ease of functionalization, and high loading capacity (Vallet-Regi et al., 2000). The loading capacity of MSNPs could be maximized through engineering the formation of mesopores during synthesis, for example, Hexagonal-symmetry MSNPs (HMSNPs) with a diameter of 105.66 ± 23.11 nm has been found to have a large surface area of 1110.89 ± 1.73 m^2/g (Huang et al., 2014). In addition, several studies have indicated that the MSNPs could be safe within the circulation *in vivo*, and enter the cells *via* endocytosis with no immunogenicity, if appropriately functionalized with, for example, polyethylene glycol (PEG) (Tang et al., 2012).

Loading of TNAs onto MSNPs can be accomplished by several different methods: (1) the cargo could be adsorbed onto the surface and the mesopores which could be pre-functionalized into positive charged surface for obtaining the maximum loading amount of negatively charged TNAs, (2) The TNAs could be functionalized accordingly and linked to the MSNPs surface and mesoporous through chemical conjugation (Tang et al., 2012). The conjugation method is currently most widely used for its maximized loading capacity, stability and activated releasing.

Recent work has shown that MSNPs could facilitate gene transfections in selected cell lines *in vitro*. MSNPs were shown to efficiently deliver carried DNA into human embryonic kidney 293T and monkey kidney fibroblast-like COS7 cell models with low cytotoxicity (Bhakta et al., 2011). A further study showed that MSNPs may invoke toxicity and

proinflammatory side effects through macrophage activation *in vivo* when tested in the animal models (Murugadoss et al., 2017).

In summary, more research needs to be performed before the full clinical application of MSNPs as a drug carrier.

1.3.3.2 Inorganic Based Materials – Gold Nanoparticles

Gold is one of the noble metals with unique functionalities, and has been widely applied for biomedical applications. Gold nanoparticles (AuNPs) have excellent biocompability, and anti-infectious and anti-inflammatory properties (Yeo et al., 2018). Most synthesis routes for AuNPs start with the reduction of chloroauric acid ($HAuCl_4$). Different $HAuCl_4$ concentrations, reaction conditions or surfactants significantly change the physical properties, such as the shape and size (Ding et al., 2014; Peng & Liang, 2019). Moreover, additional functionalization can be performed on the outer surface of the AuNPs which permits further conjugation and labelling, better internalization, and optimized optical characteristics (Ding et al., 2014; Peng & Liang, 2019).

Multiple studies have been conducted with AuNPs as the carrier for TNAs, especially in the field of gene therapy. AuNPs have been demonstrated to efficiently deliver genes and antimicrobial peptides into stem cells (Peng et al., 2016). Moreover, rather than just delivery of TNAs (siRNA, miRNA, shRNA) into the cells, AuNPs could prevent the degradation of cargo from by intracellular nuclease by steric protection (Peng & Liang, 2019). Previous research has successfully employed AuNPs to deliver β-catenin targeting RNA aptamers into the nucleus region of cancer cells. Compared with free RNA aptamers which were easily degraded by the RNase within the cytoplasm, the effective protection by the AuNPs greatly decreased the intracellular activity of β-catenin which then led to apoptosis of the targeted lung cancer cells (Ryou et al., 2011).

Notably, the surface of AuNPs can bind strongly to thiol and amine groups. Therefore, AuNPs can be easily functionalized with other molecules, such as proteins that contain cysteine or lysine residues, or lipid or polymers with the amine group (Artiga et al., 2019). This has been exploited to product a layer-by-layer siRNA delivery nanosystem. The efficiency of delivery and gene silencing was significantly improved compared to bare AuNPs vector (Elbakry et al., 2009).

In addition to spherical AuNPs, other shapes can also be obtained through controlling the synthesis procedures, such as rods (Villar-Alvarez et al., 2018) or triangles (Scarabelli et al., 2014). Different shapes of AuNPs have been used in the biomedical field for different purposes based on their unique shape-associated stability, cellular uptake rate, biocompability, surface area, and optical features (Chithrani et al., 2006; Dewi et al., 2014; Guo et al., 2018; Xie et al., 2017). For example, gold nanorods have been synthesized to deliver siRNA into brain cells for adjusting regulation of the dopamine signalling pathway (Lee et al., 2013; Roma-Rodrigues et al., 2020).

1.3.3.3 Inorganic Based Materials – Iron Oxide Nanoparticles

Over the past several decades, the clinical applications of iron oxide nanoparticles have grown dramatically due to the low cost of synthesis, stability, large surface area, and unique magnetic properties (McBain et al., 2008; Peng et al., 2008). Large scale manufacturing processes have been applied for synthesizing iron oxide nanoparticles at a much lower cost, using techniques such as vapour condensation and reverse micelle synthesis (McBain et al., 2008).

The unique magnetic functionality enables the control of nanoparticles using an external magnetic field. Previous research has already indicated that bare iron oxide nanoparticles successfully delivered the coated DNA and transfected selected cells (Magro et al., 2017). Furthermore, with the help of a magnetic field, the transfection efficiency could be further

improved (Magro et al., 2017). The impact of magnetism could also enhance cellular apoptosis through inducing targeted gene regulation with high-efficiency TNAs (Magro et al., 2017).

Iron oxide nanoparticles can also undergo magnetic hyperthermia which can heat the surrounding tissues significantly above the normal temperature to induce cytotoxic hyperthermia and cell apoptosis (Altanerova et al., 2017). Suicide genes have been successfully loaded with iron oxide nanoparticles for effective transfection of proliferation inhibition genes and prodrug treatment in tumour cells. At the same time, the nanosystem could induce hypothermia with external magnetic fields thus enhancing cancer cells death (Altanerova et al., 2017).

1.3.3.4 Inorganic Based Materials – Carbon Nanoparticles

There are currently two main types of carbon-based nanomaterials applied in biomedicine, spherical graphene nanoparticles and carbon nanotubes.

In addition to the outstanding electrical and thermal functionalities of carbon materials, carbon has great flexibility for materials synthesis. For example, as a two-dimensional crystal within the carbon family, graphene can be made into nanoparticles with a hexagonal monolayer structure (Francis & Devasena, 2018).

Spherical graphene nanoparticles can bind to TNAs through adsorption or chemical conjugation with the help of a coated polymer (like mPEG). Polymer coatings may also enhance the biocompability of the graphene nanoparticles. siRNA has been shown to be conjugated onto PEI coated graphene nanoparticles, and the targeted protein expression level was significantly reduced in MDA-MB-231 breast cancer cells (Huang et al., 2016). Although spherical graphene nanoparticles have shown promising inhibition of tumour growth, several issues also limit their widespread biomedical application, such as poor

stability and high toxicity at both cellular and organ levels, potentially causing severe inflammatory (Ou et al., 2016).

In addition to spherical graphene nanoparticles, carbon nanotubes have also been widely used in multiple fields including clinical applications. The hollow tube structure defined by carbon monolayers can both increase the surface area to 900–1000 m^2/g, and protect the cargo within the structure (Bacsa et al., 2000; Xu et al., 2006). In contrast to other types of nanomaterials, carbon nanotubes are commonly synthesized with the help of laser and ultrasound. Carbon nanotubes at a length within 0.5–2 μm and diameter of 20–30 nm were seen to actively accumulate in cells through the membrane (Al-Jamal et al., 2011; Xu et al., 2006). The positive surface potential of the carbon nanotubes further improved the cellular uptake rate, which significantly enhanced the suppression level of caspase-3 protein expression inside rat brain cells through delivered siRNAs within nanotubes (Al-Jamal et al., 2011).

However, the applications of carbon nanotubes are limited due to their significant cytotoxicity. In recent years, many studies have managed to decrease the cytotoxicity by external functionalization and the coating of outer layers (Fahrenholtz et al., 2016).

1.3.3.5 Organic Based Materials – Polymeric Nanoparticles

Polymeric nanoparticles are one of the most widely applied materials in nanomedicines (Dizaj et al., 2014; Roma-Rodrigues et al., 2020). In addition to chemically synthesized polymers, there are also many natural polymer materials, including starch, gelatine, and cellulose, which have attracted attention due to their similar (or improved) release profiles and biocompability (El-Say & El-Sawy, 2017; Fialho et al., 2021; Mohan et al., 2016). Due to the cationic functionality of most polymers, TNAs cargo could be stably and easily linked to the nanoparticles for delivery. Due to their superb biodegradability, biocompatibility, and immunogenicity, polymeric nanoparticles have been applied in the

delivery of therapeutics for cancer therapy and tested in clinical trials since decades ago (Nitta & Numata, 2013). There are many examples of applying polymeric nanoparticles to carry TNAs. For example, polymeric nanoparticles based on poly(2-aminoethyl methacrylate) (PAMA) was used to deliver TNAs into COS-7 and HepG2 cells (Santo et al., 2019). Moreover, polymers like phosphatidylcholine-modified PEI could form a non-covalent complex with TNAs. It has been shown that siRNA-PEI complexes could efficiently penetrate cancer cell membranes and knockdown the selected miR1246 and mrR155 genes within the targeted cells (Navarro et al., 2012).

1.3.3.6 Organic Based Materials – Lipid Based Nanoparticles

Lipid nanosystem, including liposomes, solid lipid nanoparticles, and lipid coating layers for nanoparticles, have become the primary choice for almost all the current delivery design of TNAs. Because of their amphiphilic functionality, lipid nanoparticles can easily attach to the cellular membrane and deliver cargoes into cells. The delivery efficiency is highly related to the particular lipid, as well as the surface functionalization (Garcia-Pinel et al., 2019; Roma-Rodrigues et al., 2020; Yonezawa et al., 2020).

Pure lipid shells that form a nanostructure are normally called liposomes. As the lipid molecule which forms the lipid layer has both hydrophilic (“water-loving”) and hydrophobic (“water-fearing”) tails, therapeutic chemicals or TNAs could be loaded or linked onto either side of the lipid layer according to their specific functionalities (Eloy et al., 2018). As liposomes have outstanding commercialization value, most current liposome formulation and synthesis methods have been patented (Sheoran et al., 2019). The size of the liposomes can be adjusted during the synthesis process. They can therefore be tailored to fit the carried cargo, and to maximize the EPR effect which is fundamental for nanoparticle penetration into the tumour (Nakamura et al., 2016). Furthermore, the lipid could also be chemically functionalized before or during the synthesis to add specific

functions (such as targeting) to the liposomes. For example, folic acid has been mixed with cholesterol phospholipids before the liposome synthesis. The synthesized liposome would then be able to target those cancer cells with overexpression of folic acid receptors (Kumar et al., 2019).

For TNA delivery, there are also numerous liposome applications. For example, conjugating liposomes with folic acid and loading DNA plasmids containing tumour-suppressing p53 gene, the p53 proteins could be successfully expressed within tumour cells after transfection. Using this construct, the proliferation of targeted breast tumour cells was eliminated within both *in vitro* and *in vivo* models (Chen, Zhu, et al., 2019). Similar results have also been validated in ovarian cancer cells model using liposomes designed with a similar strategy (Zuo et al., 2019).

Liposomes may also be used for therapeutic RNA delivery. Through a combination of the chemotherapy compound docetaxel together with targeting the TMPRSS2/ERG mRNA within a PEG modified liposome, the viability of prostate cancer cells was dramatically suppressed after the transfection (Shao et al., 2020).

Moreover, liposomes are also one of the most popular choices for delivery of the CRISPR/Cas9 system. Cholesterol-based liposomes have been used to deliver customized sgRNA for the CRISPR/Cas9 system transfection. The transfection efficiency was validated in HEK293 cells lines resulting in 39% of knockout of targeted GFP (Green fluorescent protein) reporter. Results indicated that the liposomes could effectively transfect the targeted cells with loaded CRISPR/Cas9 system with no significant cytotoxicity (Hosseini et al., 2019). In the near future, liposomes have great potential to replace the currently applied viral vectors which have many hidden issues, as previously discussed (Li et al., 2018; Xu et al., 2019).

Solid lipid nanoparticles may also be synthesized but these are not widely applied clinically.

The positively charged solid lipid nanoparticles can protect the carried cargo from degradation. Through encapsulating the carried TNAs into solid lipid nanoparticles, the complex can efficiently deliver the cargo to the targeted area. To date, scientists have successfully tested solid lipid nanoparticles to treat eye diseases and cancers (lung, liver, prostate and ovarian cancer) (del Pozo-Rodriguez et al., 2016; Wang et al., 2015). However, it is also worth noting that due to the presence of surfactants during synthesis, biocompability is normally quite limited although some modifications, such as N-carboxymethyl chitosan coating, can offset the effect (Baek & Cho, 2017; Mishra et al., 2018).

In summary, lipid-based nanoparticles have promise for clinical applications delivering TNAs to the tumour area.

1.3.3.7 Organic Based Materials – Exosomes

In contrast to the previously discussed nanoparticles, exosomes are naturally formed. Exosomes are produced by cells as a communication vector among the cells. These nanosized vesicles have the same membrane structure as the cells and usually contain specific proteins and nucleic acids for exchange among cells. The content is directly decided by the source of the exosomes (Gilligan & Dwyer, 2017; Mashouri et al., 2019). In recent years, the potential for applications of exosomes in cancer therapy has been explored. Since the cancer cell derived exosomes have the same membrane structure and formulation as the cancer cell membrane, the internalization of exosomes could be significantly easier compared with other nanocarriers (which may need different internalization pathways) or normal cells derived exosomes (Franzen et al., 2014). Moreover, compared to other vectors, cancer cell derived exosomes could have better immune escape functionality (Roma-Rodrigues et al., 2014; Roma-Rodrigues et al., 2020).

Exosomes are also natural and biodegradable which avoids unnecessary cytotoxicity (Gilligan & Dwyer, 2017). For cancer therapy, exosomes could be derived from cells pre-engineered to express the targeting ligand on the surface (Limoni et al., 2019). It has been previously reported that HER2 targeting exosomes were successfully produced in engineered HEK293T cells. Specific TPD52 knockdown siRNA was encapsulated within the derived engineered exosomes and incubated with the target SKBR3 cells. In this way, gene expression was significantly suppressed by 70 % after successful transfection with the exosomes (Limoni et al., 2019).

Table 1.1 Comparison of the advantages and disadvantages among different nanomaterials

General Types	Material	Advantages	Disadvantages
Inorganic based materials	**Silica**	1. Widely applied in different biomedical areas	1. Selection of templates for porous structure formation are quite limited
		2. Various kinds of well-proven reliable synthesising routes under different conditions	2. Insufficient removal of synthesis surfactants may lead to strong cytotoxicity and immunogenicity
		3. Great biocompability, stability, ease of functionalization, and	

		high loading capacity	
	Gold	1. Excellent biocompability, and anti-infectious and anti-inflammatory properties	1. Unstable compared with other materials
		2. Efficiently deliver genes and prevention of nuclease degradation	2. Unable to remove the synthesis surfactants which may lead to cytotoxicity
		3. Surface could be easily functionalised with groups like thiol and amine groups	3. Relatively expensive to synthesize
		4. Unique optical feature	
	Iron Oxide	1. Unique magnetic functionality	1. Unable to do surface functionalisation without help of coated polymers
		2. Could induce magnetic	

		hyperthermia	
		3. Low cost of synthesis, stability, large surface area,	
	Carbon	1. Outstanding electrical and thermal functionalities	1. Significant cytotoxicity
		2. Large surface area for carbon nanotubes	2. Unable to do surface functionalisation without help of coated polymers
Organic Based Materials	**Polymer**	1. One of the most widely applied materials in nanomedicines	1. Functionalities and biocompatibility highly rely on the synthesis method
		2. Various routes of synthesis including natural polymer and chemical synthesis	2. Could bring in unremovable chemical residues which may lead to cytotoxicity
		3. Stable and easy functionalisation	3. Synthesis often require extreme conditions and toxic chemicals

		4. Superb biodegradability, biocompatibility, and immunogenicity	
	Lipid	1. Could easily attach to the cellular membrane due to amphiphilic functionality	1. Original raw materials are all very costly
		2. Great biocompability and most popular choices of commercialised nanocarriers	2. Most of the current liposomes have already been patented
		3. Easy to be tailored for the delivery of specific cargos	
	Exosomes	1. Have the same membrane structure as the cells and usually contain specific proteins and nucleic acids for exchange among cells	1. Hard and costly to produce the right size and enough amount of exosomes for nanomedicine purpose
		2. Natural and biodegradable which	2. Impossible to keep the consistency of

		avoids unnecessary cytotoxicity	quality

1.4 Aims and Objectives

The aim of this thesis is to build a dual-functional nanoparticle, which could perform gene therapy with specific RMS gene knock-down regulated by pH-activated-release, and monitor the size of tumour with delivered NIR dye. The nanoparticle will be surface functionalized with novel aptamers for improved targeting.

My specific aims are as follows:

(1) To synthesize, characterise and optimize nanoparticles for carrying the therapeutic siRNA. Maximize the biocompability and delivery efficiency of the whole nanosystem.

(2) To select aptamers which could bind NELL1.

(3) Synthesize a copolymer for the specific release of the cargo under low pH environments found in tumours.

(4) Select an siRNA with the potential for maximizing therapeutic outcomes within the aRMS cell models.

(5) To determine the therapeutic effect of the nanosystem in two-dimensional (2D) and three-dimensional (3D) tumour models compared to naked siRNA.

(6) To determine the real-time monitoring of NIR probe, the penetration depth and signal strength with the help of the whole designed nanosystem.

(7) Establish and validate the successful construction of the whole nanosystem to ensure that it is functional and stable.

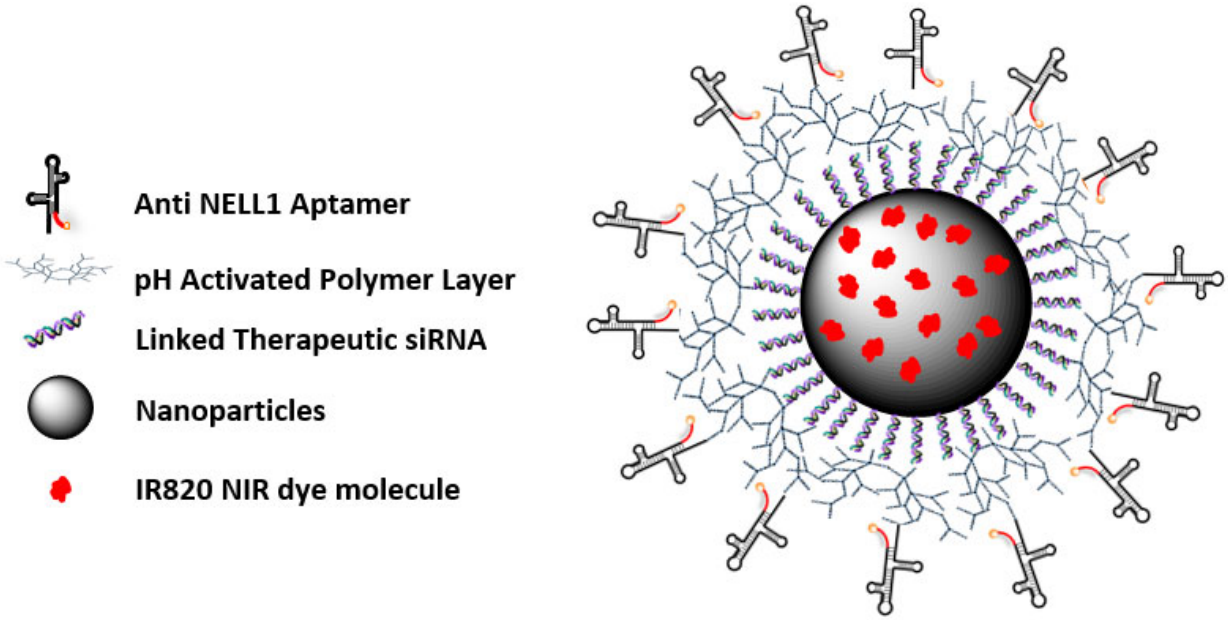

Figure 1.2 Schematic diagram of the designed nanosystem

Chapter 2

Active Targeting System

NELL1 (Neural epidermal growth factor–like (EGFL)-like protein) is an important biomarker associated with tissue and bone development and regeneration. NELL1 upregulation has been linked with metastasis and negative prognosis in rhabdomyosarcoma (RMS). Furthermore, multiple recent studies have also shown the importance of NELL1 in inflammatory bowel disease and membranous nephropathy, amongst other diseases. In this study, several anti-NELL1 DNA aptamers were selected from a randomized ssDNA pool using a fluorescence guided method and evaluated for their binding affinity and selectivity. Several other methods such as a metabolic assay and confocal microscopy were also applied for the evaluation of selected aptamers. The top three candidates were evaluated further and AptNCan3 was shown to have a binding affinity up to 959.2 nM. Selectivity was examined in RH30 RMS cells which over-expressed NELL1. Both AptNCan2 and AptNCan3 could significantly suppress metabolic activity in RMS cells. AptNCan3 was found to locate on the cell membrane, and also on intracellular vesicles, which matched the location of NELL1 shown by antibodies in previous research (Pang et al., 2015). These results indicate that the selected anti-NELL1 aptamer showed strong, and highly specific, binding to NELL1, and therefore has potential to be used for *in vitro* or *in vivo* studies and treatments.

2.1 Introduction

Neural epidermal growth factor–like (EGFL)-like protein (NELL1) has previously been shown to have an important role in enhancing or repairing tissues and bones during development and regeneration (Cowan et al., 2007; Kuroda et al., 1999; W. Li et al., 2011). NELL1 was also found to directly or indirectly act as an important biomarker for many diseases, such as osteoporosis (James et al., 2015; Karasik et al., 2010), metabolic diseases (James et al., 2011; Shen et al., 2016), neuro-related diseases including bipolar or depression (Lin et al., 2018; Mathieu et al., 2015), inflammatory bowel disease (Franke et al., 2007), and tumour or tumour-related membranous nephropathy (Caza et al., 2021; Rapa et al., 2012; Tombolan et al., 2017; Cheng et al., 2021). Moreover, as a biomarker that was often seen to be upregulated with further disease progression, NELL1 shows potential beyond simply a disease indicator (Tombolan et al., 2017). Previous research has shown that NELL1 was significantly upregulated in the more metastatic alveolar RMS, whilst only low levels were seen in the embryonal form (Rapa et al., 2012). NELL1 expression levels were also found to be directly linked to a negative prognosis (Tombolan et al., 2017). NELL1 overexpression promoted tumour invasion, implying that NELL1 may function as an oncogene and play an important role in cancer progression (Rapa et al., 2012; Tombolan et al., 2017). Furthermore, as NELL1 was also found to act as a signalling molecule for important cell functions, previous research has discovered that binding to certain region of NELL1 could block and affect the NELL1 mediated cell adhesion (Hasebe et al., 2012). Herein, we have focussed on the paediatric disease rhabdomyosarcoma (RMS). Current treatment of RMS highly relies on invasive surgery, chemotherapy and/or radiotherapy methods, these treatments do not have any targeting functionality and normally lead to extremely strong off-targeting side effects (Pappo et al., 1997).

Recently, the concept of applying aptamers as a target antigen for therapeutic purposes has gained momentum (Caza et al., 2021). Compared to antibodies which are commonly used, aptamers are much smaller, and can have higher affinity and specificity, and lower immunogenicity (J. Zhou & Rossi, 2017). In addition, it has also been indicated that binding of an aptamer to important cellular signalling molecules could affect the intracellular metabolism with a relatively low IC50 (Shum et al., 2011). Furthermore, it is easier and cheaper to manufacture aptamers compared to antibodies (Lauridsen et al., 2012).

In this study, DNA aptamers that targeted NELL1 were screened and evaluated. NELL1 had been identified in previous microarray and microscopy studies which suggested that it is overexpressed on the surface of target rhabdomyosarcoma cells (Rapa et al., 2012). RMS and control fibroblast cell lines were used for validation of the binding affinity and specificity of the selected anti-NELL1 aptamers (AptN). Herein, we present both multiple anti-NELL1 aptamers with good affinity and selectivity, and also a robust and optimized aptamer selection protocol.

2.2 Materials and Methods

2.2.1 Cell lines

This study tested four different cell lines, which included a normal fibroblast control cell line, and three other immortalized human cancer cell lines. RH30 (American Type Tissue Culture Collection (ATCC) no. CRL-2061), was originally obtained and derived from a 17-year-old male's bone marrow metastasis, and was chosen to represent the alveolar RMS (aRMS). RD (ATCC no. CRL-7763) was originally obtained and derived from a 7-year-old female's muscle carcinoma, and was chosen to represent the embryonal RMS (eRMS). U-87MG (ATCC no. HTB-14), was derived from a human glioblastoma, and chosen as a non-RMS control cancer cell line. RH30, RD and U-87MG were all acquired

from the ATCC (Manassas; VA, US). The fibroblast cell line was kindly provided by Dr Jo Poulton from the Nuffield Department of Women's & Reproductive Health, University of Oxford.

2.2.2 Cell culture

All cells were incubated in high-glucose Dulbecco's Modified Eagle's Medium (DMEM) [Sigma- Aldrich, Poole, UK] with 10 % (v/v) Fetal Bovine Serum (FBS) [Sigma- Aldrich, Poole, UK], 2 mM L-glutamine [Gibco, Life Technologies Ltd, Renfrew, UK], penicillin (100 U/mL) and streptomycin (100 g/mL) [Gibco, Life Technologies Ltd, Renfrew, UK]. T75 Tissue Culture Treated Flasks [Nunc, Thermofisher Scientific, Renfrew, UK] were used to culture the cells in a humidified 5 % CO_2 incubator at 37°C. Cells were detached from the flask surface using 0.25 % (w/v) trypsin containing 0.02 % (w/v) EDTA [Sigma-Aldrich, Poole, UK].

2.2.3 Cell survival assay (Crystal violet assay)

After treatment, cells were washed with cold PBS three times, before 30 minutes fixation in a 1 % (v/v) glutaraldehyde solution. The crystal violet solution (1 % (w/v) crystal violet [Sigma-Aldrich, Poole, UK] mixed in a 4:1:5 (v/v/v) combination of H_2O, glacial acetic acid, and methanol) was applied to the fixed cells for 1 hour at room temperature. After staining, excess supernatant was removed. The cells were then thoroughly washed and rinsed with water until all excess crystal violet staining solution was removed. The microplate was then left to dry at room temperature for 2 days before the next step. Prior to reading, dye in each well was resuspended vigorously with 100 µL of solubiliser (1 % (w/v) SDS in 10 % (v/v) glacial acetic acid). The absorbance was measured at 540 nm with a plate reader [Tecan Infinite® 200 PRO, Reading, UK].

2.2.4 Cell metabolic assay (MTT)

Cell proliferation and metabolic activity was measured using a colourimetric MTT assay

(3-(4,5-Dimethylthiazol-2-yl)-2,5-Diphenyltetrazolium Bromide). After treatment the medium was discarded from the microplate well. MTT medium solution (100 µL of growth medium containing 0.5 mg/mL of MTT) was then added into each well for 3 hours incubation at 37 oC. Purple formazan crystals formed inside cells, and was confirmed before the next step. All supernatant was thoroughly removed, and each well was re-suspended vigorously with 100 µL of dimethyl sulfoxide (DMSO) to dissolve the formazan. Prior to reading, the microplate was incubated for 20 minutes and shaken for 2 minutes. The absorbance was then measured at 575 nm with a plate reader [Tecan Infinite® 200 PRO, Reading, UK].

2.2.5 Flow cytometry

In order to validate the location of NELL1 on the cell surface, cells were incubated with antibody and analysed using FACS. Cells were detached from the flasks and collected by several rounds of centrifugation and PBS washing. The cells were then resuspended to a final concentration of $1x10^7$ cells/mL with flow cytometry staining buffer (PBS, 5 % (v/v) FBS, 0.1 % (w/v) NaN_3 (sodium azide)). The cells were subsequently incubated with 1:500 anti-NELL1 primary antibody [Abcam, Cambridge, UK] for 30 min, and 1:500 Cy3-labelled anti-Rabbit IgG (H+L) cross-absorbed secondary antibody [Thermofisher Scientific, Renfrew, UK] for 60 min. The excess antibody was washed away through multiple washings after every antibody incubation step.

To validate the specific binding of the anti-NELL1 aptamers with the cell surface NELL1 protein, the anti-NELL1 antibody was labelled with a fluorescent tag using Mix-n-Stain CF555 labelling kits [Biotium, CA, US]. The selected anti-NELL1 aptamers were synthesized with a 5'-biotin tag [Sigma-Aldrich, Poole, UK] and labelled with PE-Streptavidin [BioLegend, CA, US]. Cells were separately incubated overnight with free PE-streptavidin, 1:200 CF555-labelled anti-NELL1 primary antibody [Abcam,

Cambridge, UK] or 500 nM PE-labelled anti-NELL1 aptamers at 37 ºC. The excess dye or binding ligand was washed away through multiple PBS washing after the incubation step. The whole process was conducted on ice in a dark environment. All groups of cells were fixed with 4 % (v/v) PFA solution prior to testing. All cells were analysed and compared with the FACS Calibur flow cytometer [Becton Dickinson, Wokingham, UK]. The experiment was performed in replicates on three independent occasions.

2.2.6 Western blotting

Detached cells were collected using multiple rounds of centrifugation and PBS washing. Freshly made cell lysis buffer (50 mM Tris-HCl, pH 7.4, 150 mM NaCl, 0.01 % (v/v) Triton X-100) was prepared. Directly before use, 10 µL protease inhibitor and EDTA [Life Technologies Ltd, Renfrew, UK] was added per 1 mL of lysis buffer. The cells were resuspended and lysed for 30 minutes on ice. The supernatant was collected with high-speed centrifugation at 4 °C and transferred into sterile 1.5 mL tubes (Eppendorf, Loughborough, UK). A Bradford Assay [Pierce™, Bio-rad, Watford, UK] was then used to determine the amount of protein in the cell lysate.

Lysates (10 µg of protein) from each cell line were separated using Novex® NuPAGE® SDS-PAGE Gel [Thermofisher Scientific, Renfrew, UK] in BupH Tris-HEPES-SES Running buffer [Thermofisher Scientific, Renfrew, UK], at 180 V for 1 hour. The gel transfer was performed using a Wet/Tank Blotting Transfer system [Bio-rad, Watford, UK] and a PVDF blotting membrane [Amersham GE, Buckinghamshire, UK] in ice-cold transfer buffer (200 mM Glycine, 25 mM Tris, 20 % (v/v) Methanol) at 100 V for 1 hour. Ponceau S solution (0.1 % (w/v) Ponceau S in 5 % (v/v) acetic acid) was applied to the membrane in order to visualize and confirm successful transfer of the protein bands. The PVDF membrane was then de-stained using distilled water. Freshly made TBST buffer (10 mM Tris-HCl, 150 mM NaCl, 0.05 % (v/v) Tween-20) containing 5 % (w/v) non-fat

milk was used to block the membrane at room temperature for 2 hours. The blocked membrane was then cut based on the ladder and incubated separately with 1:200 anti-Beta Actin antibody [Santa Cruz, CA, US] or 1:1000 Anti-NELL1 antibody [Abcam, Cambridge, UK] in 1 % (w/v) BSA in TBST overnight at 4 °C. The 1:1000 diluted goat anti-rabbit HRP conjugated secondary antibody [Santa Cruz, CA, US] was added to the membrane and incubated for 2 hours after three rounds of TBST washing. This was followed by three rounds of washing with TBST buffer. Pierce ECL Western Blotting Substrate [Thermofisher Scientific, Renfrew, UK] was used to visualize the protein bands in G:Box [Syngene, Cambridge, UK].

2.2.7 Selection of anti-NELL1 aptamers

PEG-NHS-functionalized coverslips were prepared following the protocol from Chandradoss et al., with slight modification (Chandradoss et al., 2014). The glass coverslips were treated with Milli-Q H_2O, 1 M KOH, and piranha solution, separately for 2 hours with sonication to fully remove any possible contaminants from the surface. A mixture of APTES and methanol (1:10 v/v) was applied to allow amino bond conjugation on the coverslip surface. Biotin-PEG (2 mg) and mPEG-NHS (40 mg) [Lysanbio, AL, US] were dissolved in 140 µL PEG buffer (100 mM of sodium bicarbonate buffer, pH 8.0) for 2 pairs of coverslips. After 3 h incubation, T50 buffer (10 mM Tris-HCl, 50mM NaCl, 1 % (v/v) Tween-20; pH 8.0) was used to wash off excess mPEG. The functionalized coverslips were stored separately at -20 °C before use.

The NELL1 protein coating and some of the aptamer selection steps were optimized from the work of Lauridsen et al (Lauridsen et al., 2012). NELL1 protein stock solution (25 µL @ 125 µM) [R&D Systems, MN, US] was dissolved in 30 µL PBS with 10 % (v/v) glycerol. The protein solution was then applied dropwise to the PEG-NHS-functionalized coverslips on a flat clean surface. The treated coverslips were then incubated for 40 min

in a 24 °C humidifying environment before washing three times with PBST. Unreacted NHS groups were then blocked with 300 µL of 800 µM ethanolamine for 35 min in the humidifying chamber. Two more rounds of PBST washing were performed before the oligo selection step.

The 40-nucleotide random FAM labelled oligo library [Integrated DNA Technologies, IA, US] was synthesized following the sequencing: 5'-GGACAGGACCACACCCAGCG (40 random bases) GGCTCCTGTGTGTCGCTTTGT/36-FAM/-3'. For the negative selection of the oligo library, the treated PEG-NHS-functionalized coverslip was fully deactivated with 300 µL ethanolamine. Negative selected nucleic acid library (100 µL) was then transferred to the NELL1 coated coverslip. The coverslip was then incubated in the clean humidifying environment overnight, and washed with 800 µL PBST washing buffer and gently dried with nitrogen gas. The selection process was monitored using a Motic 101M microscope with a Moticam 2500 camera and MHG 100B laser [Motic, Xiamen, China]. The washing processes were repeated until there were only very few fluorescent dots on the whole coverslip.

The selected oligos were eluted by crushing the glass coverslip in Milli-Q H_2O at 90°C for 20 minutes. The resulting mixture was then centrifuged at 14,000 rpm to remove the supernatant which contained the oligos. An 18-cycle PCR was then performed with the Q5 HF Polymerase Mastermix [Thermofisher Scientific, Renfrew, UK] following the optimized protocol: denaturation at 98 °C for 30 sec, 18 rounds of extension at 98 °C for 10 sec, final extension at 72 °C for 10 mins, then hold at 12 °C until finish. The forward primer was designed as 5'-GGACAGGACCACACCCAGCG-3', and the reverse primer was designed as 3'-ACAAAGCGACACACAGGAGCC-5'. Quality control of the PCR product was performed using 4 % (w/v) agarose gel electrophoresis. The PCR product

was stored at -20 °C before the next step.

The PCR products were extracted and purified with the Monarch® DNA gel extraction kit [New England Biolabs, MA, US]. After quantification with NanoQuant Infinite 200 Pro [Tecan, Reading, UK], 5.33 ng of PCR fragment was used for phosphorylation and blunt-end plasmid ligation following the manufacturer's instructions [NZYTech, Lisboa, Portugal]. The ligated plasmid was quantified again before transformation. The ligated vector was then transformed into the JM109 competent *E. coli* cells following the manufacturer's instructions [NZYTech, Lisaboa, Portugal]. Blue/White screening was performed using 100 μg/mL X-Gal [Promega, Wis, US]/ 0.5 mM IPTG [Sigma- Aldrich, Poole, UK] in agar plates containing 100 μg/mL carbenicillin. Positive colonies were picked and grown in LB media, and then the plasmids extracted using aMonarch® Plasmid Miniprep Kit [New England Biolabs, MA, US]. An extra round of validation of ligation product using PCR was performed with the same forward and reverse primer under the same conditions. After gel electrophoresis, only those ligated plasmids with amplification bands at the right size were selected. The selected plasmids were quantified, and the transformed cells were stored in 25 % (v/v) glycerol in a -80°C freezer.

After quantification, 10 μL of purified plasmids which contained more than 200 ng of DNA was transferred to a separate microcentrifuge tube. A T7 promoter sequencing primer (5'-(TAATACGACTCACTATAGGG)-3') was used for sequencing. The product was then sent for DNA Sanger Sequencing [Eurofins Genomics, Wolverhampton, UK]. The sequencing results were analysed using the Addgene software [Addgene, MA, US]. The potential secondary structure and binding affinity were predicted with the DNA folding platform from the mfold web server (Zuker, 2003).

2.2.8 Surface Plasmon Resonance (SPR) analysis

Aptamer candidates were selected from the sequencing results based on the predicted

potential binding affinity. These sequences were sent off for re-synthesis with 5' biotin tags [Sigma- Aldrich, Poole, UK]. Surface Plasmon Resonance Biacore T200 [GE healthcare, IL, US] was used to quantify the selected aptamers at 37°C. PBS was used as the running buffer to simulate an *in vivo* environment. A streptavidin immobilized sensor chip Series S CAP [GE healthcare, IL, US] was used for aptamer quantification. The 5′-biotinylated anti-NELL1 aptamer candidates were immobilized on the chip surface following the manufacturer's instructions at a flow rate of 100 µL/min after the chip surface regeneration. Different concentrations of NELL1 recombinant protein solutions (30 nM, 300 nM, 750 nM, and 1500 nM) were injected and passed through the chip at a flow rate of 30 µL/min for 60 sec.

The binding affinity (Kd) values were calculated through a non-linear fitting model using the Biacore Evaluation software and GraphPad Prism Pro fitting function. In general, the quantified binding and dissociate signals were exported from the sensorgrams from the Biacore Evaluation software. The numbers were then fitted through the analyse-nonlinerar regression fitting function building the GraphPad Prism. The Kd is calculated as the ratio of the dissociation rate (Koff), to the binding rate (kon) of the evaluated ligand. Through the binding function within the Nonlinear regression (curve fit), the Kd values were separated calculated for each tested samples.

2.2.9 Confocal imaging of anti-NELL1 aptamers specific binding

Cells were seeded into glass-bottom imaging Petri dishes [ibidi GmbH, Martinsried, Germany] at a density of $1x10^5$ cells per well in DMEM growth media and left 24 hours in a tissue culture incubator to allow the cells to adhere to the surface. Cells were separately incubated overnight with free PE-streptavidin (RH30 only), 1:200 diluted CF555-labelled anti-NELL1 primary antibody (RH30 only) [Abcam, Cambridge, UK], or 500 nM PE-labelled anti-NELL1 aptamers (all cell lines) at 37 ºC. After incubation,

the cells were washed three times with cold PBS. The whole process was conducted in a dark environment. The cells were then kept in warm PBS and stained with 0.1 μg/mL DAPI [Thermofisher Scientific, Renfrew, UK] and 1:200 diluted CellBrite™ Green Cytoplasmic Membrane Dye [Biotium, CA, US] for 15 mins separately before imaging. The cells were then thoroughly washed three times with cold PBS before fixation with 4 % (v/v) Paraformaldehyde solution [Bio-rad, Watford, UK] prior to imaging. The imaging was conducted with a Leica SP8 confocal microscope. [Leica Biosystems, Nussloch, Germany]

2.2.10 Statistical analysis

All statistical analysis of experimental data was performed using Microsoft™ Excel [Microsoft, NM, US]. GraphPad Prism 8.0.2 [GraphPad Prism, La Jolla, CA, US] was applied for graph plotting and non-linear simulation. All results were presented as mean ± SD. When the p values were less than 0.05, the difference was considered significant and shown. When two or more groups were compared, the two-tailed homoscedastic Student's t-test and one-way ANOVA were applied for statistical analysis.

2.2.11 Other software

Flow cytometry data was analysed and compared using FlowJo VX [FlowJo, LLC, Ashland, OR, US]. The Leica Application Suite X (LAS X) was used for all relevant analysis and measurement of confocal images. ImageJ 1.53 [National Institutes of Health (NIH), Bethesda, MD, US] was used to quantify Western blots, which were then standardised against the data from the control groups for plotting. The illustration for the Biacore chip principle was drawn with the BioRender platform [BioRender, Toronto, Canada].

2.2.12 Experimental methodology

The researcher did not randomize or blind any experimental groups during this research.

As a negative control, all samples were compared to cells cultured with the appropriate vehicle solvent.

2.3 Results

2.3.1 Cell surface NELL1 validation and comparison of expression

While previous microarray studies suggested that NELL1 is overexpressed on the surface of aRMS cells, flow cytometry experiments were undertaken for further confirmation (Rapa et al., 2012). To validate the location of the NELL1 protein as the cellular outer-membrane, cells were incubated with anti-NELL1 antibody and Cy3 conjugated secondary antibody. Cells were kept alive during the whole process so the antibodies could not penetrate cell membranes. PBS control and secondary antibody-only incubation groups were applied as a control for removing the background and non-specific binding fluorescence. Fibroblasts were chosen as being representative of normal cells. RD and RH30 were selected as being representatives of eRMS and aRMS, respectively. FACS data for fibroblasts, RD, and RH30 cells, with different incubations are shown (Figure 2.1A). RH30 cells can be seen to have a significant peak shift (orange) compared with the 'no antibody' (red) and 'secondary antibody only' (blue) control groups (Figure 2.1A(iii)). Conversely, there was almost no peak shift observed in the fibroblasts (Figure 2.1A i) and RD sarcoma cells (Figure 2.1A ii). In order to compare the difference more clearly, Median fluorescence intensity (MFI) of all flow cytometry measured events was applied for quantification (Figure 2.1B). The data showed that a considerable amount of NELL1 was expressed on the metastatic RH30 cell membrane with a significant increase in signal compared with the control groups. However, there was almost no NELL1 found on the fibroblasts and RD cell membranes.

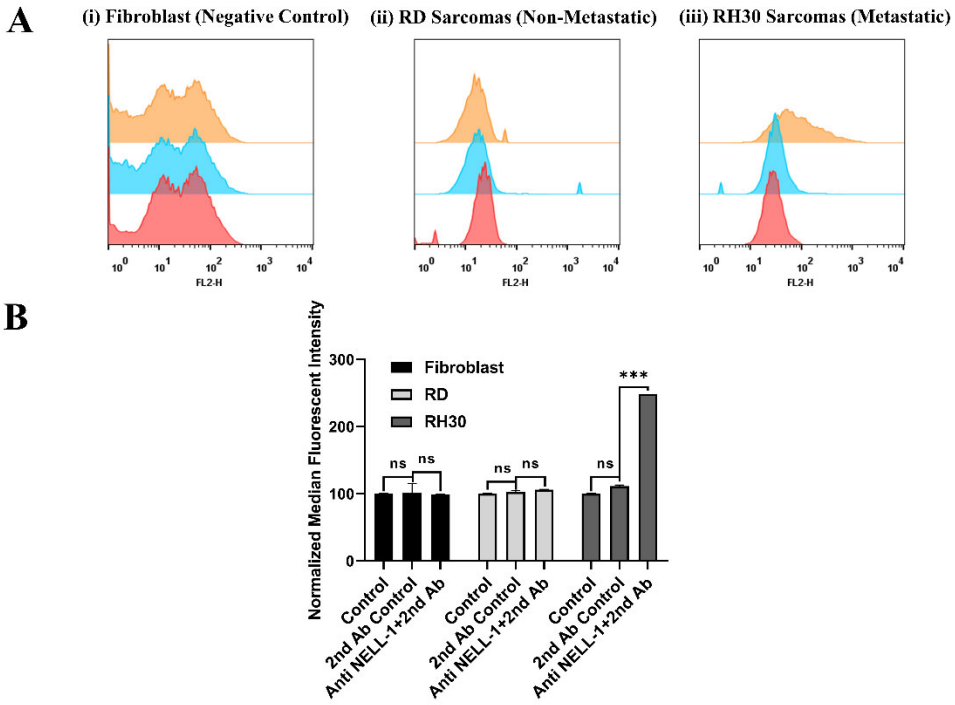

Figure 2.1 Validation of NELL1 on cell surface measured by flow cytometry.

(A) Representative flow cytometry histogram result for fibroblasts, RD and RH30 sarcoma cells. Cells were incubated with either PBS (Red), Cy3-labelled anti-Rabbit secondary antibody only (Blue), or anti-NELL1 primary antibody and Cy3-labelled anti-Rabbit secondary antibody (Orange). (B) Results from the normalized median fluorescence intensity of flow cytometry results for Fibroblast, RD and RH30 sarcoma cells. Cells were incubated with different incubation in the PBS (control), Cy3-labelled anti-Rabbit secondary antibody only (2nd Ab control), or anti-NELL1 primary antibody and Cy3-labelled anti-Rabbit secondary antibody (Anti NELL1 and 2nd Ab). Data is presented as mean±SD for each individual cell line (n=3 independent experiments of triplicates). Significance was tested using a two tailed t-test compared to the untreated cells for each cell line (***P≤0.005, ns=not significant)

As the NELL1 was shown to be localized on the outer cell membrane of RH30 (Figure 2.1), the expression level was then confirmed and compared by Western Blotting. β-Actin was used as a housekeeping gene since it remains at a steady level in most kinds of mammalian cells (Figure 2.2A, S3) (Hunter & Garrels, 1977). Similar to the observed FACs results, RH30 sarcomas showed a nearly three-fold higher expression level than RD cells (Figure 2.2B). In addition, fibroblasts were monitored as they represented normal cells in the body which might lead to false targeting if they had a high NELL1 expression (Grinnell, 1994). U-87MG was chosen as a further negative control as it has

been shown to have very low NELL1 expression in previous studies (Maeda et al., 2001). Based on the normalized quantification blotting signal, both of the negative controls (Fibroblast and U-87MG) have shown a significantly lower level of NELL1 expression compared with RH30 cells (Figure S1, S4; Table S1, S2).

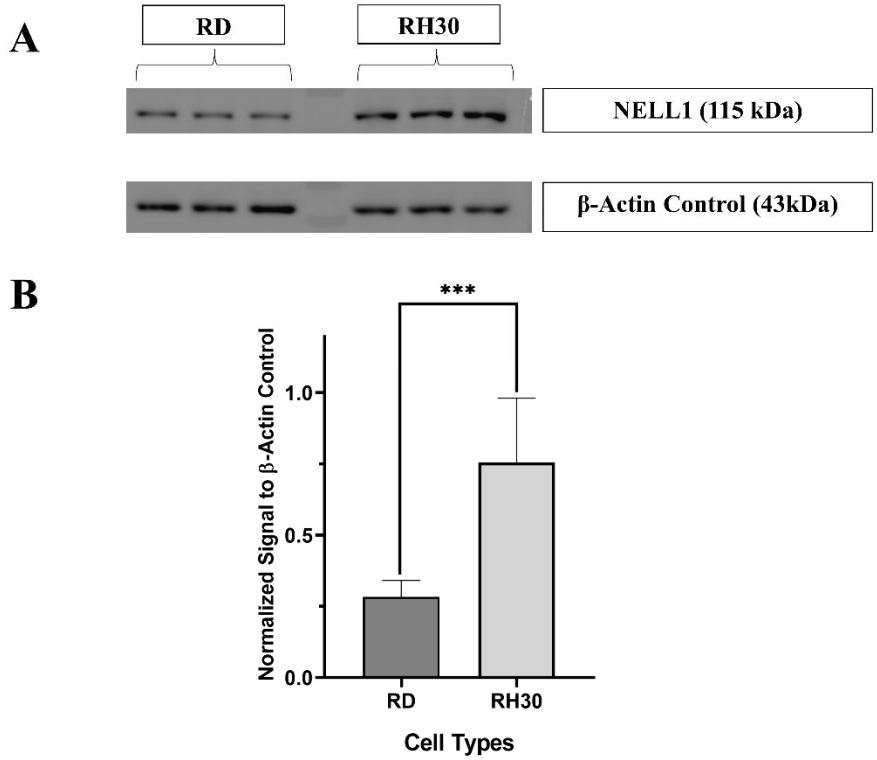

Figure 2.2 Measurement of NELL1 expression level with Western Blotting.

(A) Representative cropped Western blot comparing NELL1 expression in RD and RH30 sarcoma cells. β-Actin was applied as housekeeping gene control. The densitometry readings of each band (Table S1, S2) and uncropped blot (Figure S3) were included in the supplementary materials (n = 3) (B) Quantification of Western blotting showing the β-Actin normalized NELL1 expression level of different cell lines. Data are presented as mean ±SD for each individual cell line (n = 3). Significance was tested using a two tailed t-test compared to the untreated cells for each cell line (*** $p \leq 0.005$).

2.3.2 Anti-NELL1 aptamers selection

After the NELL1 had been confirmed to have potential as the targeting protein, a FAM labelled oligo library was used to screen for an anti-NELL1 aptamer. As the NELL1 protein was immobilized on the functionalized coverslip surface, multiple oligos remained on the coverslip after the incubation process. Several rounds of washing were

conducted to remove those oligos which had no or lower binding affinities to NELL1 protein. Under the fluorescent microscope, the selection process could be monitored with the green fluorescence decreasing with increasing numbers of washing rounds. This indicated a decreasing number of the oligos remaining on the surface (Figure S2). The remaining oligos were obtained after several rounds of intensive washing. The selected oligos were extracted from the coverslip and used as the template for PCR. The right size product was then purified and ligated into blunt end linearized plasmids and amplified in competent *E. coli* for storage and sequencing purpose.

2.3.3 Evaluation of selected anti-NELL1 aptamers candidates

The secondary structure of the aptamer sequences was predicted with the mFold platform for the next step of the evaluation study (Zuker, 2003). Three candidates with the highest potential binding affinity, named AptNCan1, AptNCan2 and AptNCan3, were chosen based on their functional region within the secondary structure, e.g. hairpin loops (Figure 2.3). At least two hairpin loops were found in the variable region of each candidate. It is noteworthy that AptNCan3 shows a multi-hairpin loop which is often considered as a region likely to have a high binding affinity due to the ability to form a more complex 3D binding structure (Dunn et al., 2017).

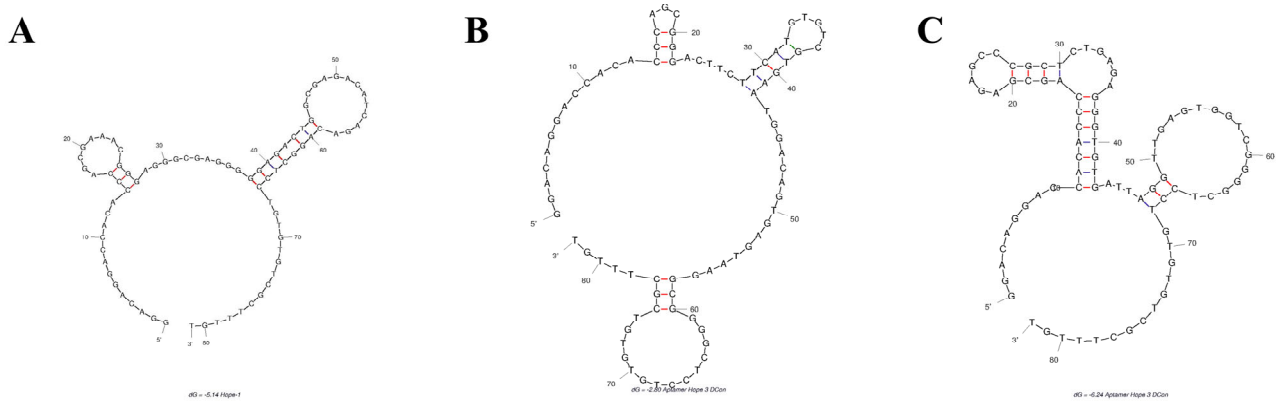

Figure 2.3 Predicted 2D Structure of anti-NELL1 Aptamer Candidates.

The 2D structure of the aptamer candidates was predicted from the sequencing data and the ssDNA folding function of mFold web server. Figures showed the three candidates with highest potential binding affinity. (A) AptNCan1, (B) AptNCan2, (C) AptNCan3.

Table 2.1 Predicted potential 2D Structures and ΔG Folding Energy Values of anti-NELL1 Aptamer Candidates based on their sequences.

Name	Sequence	Predicted 2D Structure	ΔG folding energy (The lower, the better)
AptNCan-1	5'-GGACAGGACCACACCCAGCGAAACGGGAGGGCGAGGGGGAGACTGGCGAGACATCAGACAGGCTCCTGTGTCGCTTTGT-3'	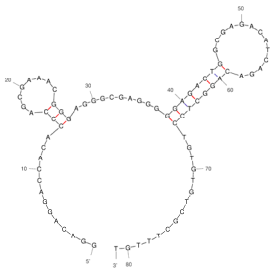	-5.14 kcal/mol
		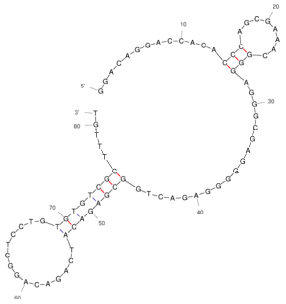	-4.90 kcal/mol
		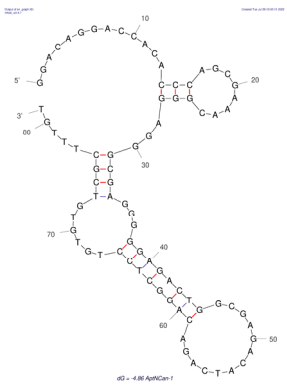	-4.86 kcal/mol
AptNCan-2	5'-GGACAGGACCACACCCAGCGGGACTTCTTCATGTGTCGTGAATGGACAGTGAGTAAGGCGGGGCTCCTGTGTGTCGCTTTGT-3'	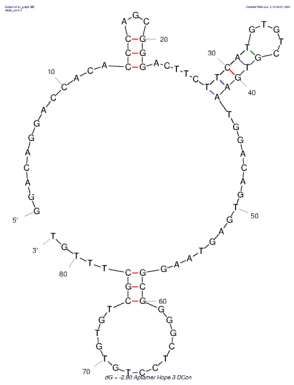	-3.02 kcal/mol

		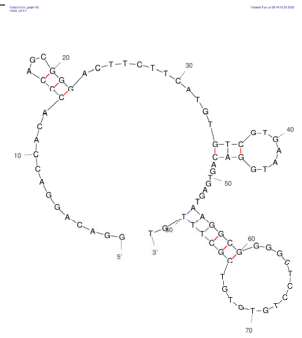	-2.66 kcal/mol
		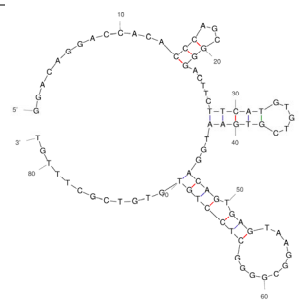	-2.37 kcal/mol
AptNCan-3	5'-GGACAGGACCACACCCAGCGAGAGCCCGCTCTGAGAGGGTGTGATTAGGTTGAGTGGTCGGGGCTCCTGTGTGTCGCTTTGT-3'	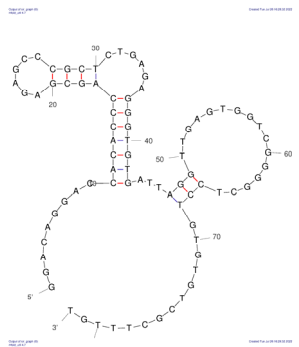	-6.79 kcal/mol
		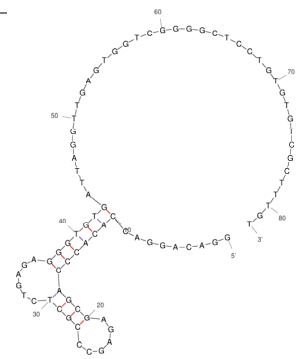	-6.53 kcal/mol
		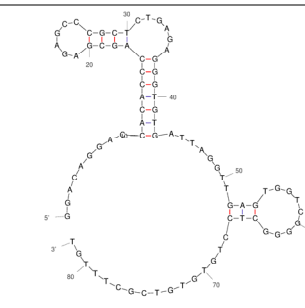	-6.25 kcal/mol

With the help of SPR, the binding affinity of each selected aptamer candidate could be precisely quantified. Through a biotin-streptavidin linkage, the 5'-biotinylated aptamer candidates could be fixed onto the surface of Biacore CAP chips for affinity quantification with different concentrations of recombinant NELL1 protein (Figure 2.4A). By deducting the baseline response unit (R.U.) value of different concentrations of NELL1 protein, the absolute R.U. values were calculated for each candidate.

There were mainly two reasons why we did not reverse the SPR experiment which immobilised the NELL1 protein onto the surface of CAP chips and injected different concentrations of the aptamer candidates. The first reason was the large molecular weight (molecular size) differences between the NELL1 protein and the aptamer candidates which was only 81 nt, which would lead to a significant higher background signal from the protein and a hardly noticeable signal change during the binding and dissociation of the aptamer candidates. It could further affect the calculation of Kd values. Moreover, immobilisation process needs the biotin residue to combine with the CAP chip surface which means extra functionalisation steps for the prepared NELL1 protein solution. It could also significantly affect the binding affinity evaluation process. Thus, the reverse SPR experiment was unlikely to work.

The extent to which a single molecule binds to its ligand is known as affinity. The equilibrium dissociation constant value (which is normally known as Kd), was commonly used to assess and quantify the strength of bimolecular interactions. Kd values which represent the binding affinity were calculated through a non-linear fitting function. AptNCan1 demonstrated the highest binding affinity with a Kd of 135.1 nM. The other two candidates (AptNCan2 and AptNCan3) also showed good binding to the NELL1 protein, with binding limits all lower than 1 μM, i.e. Kd of 491.8 and 959.2 nM, respectively (Figure 2.4B).

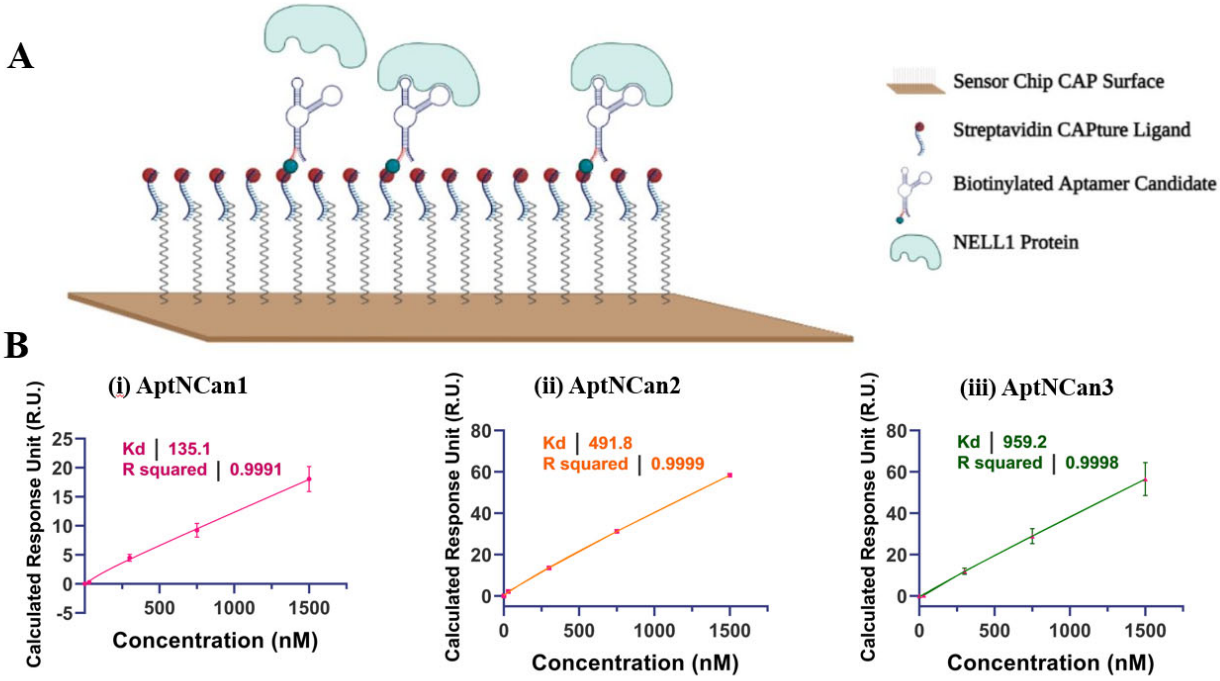

Figure 2.4 Quantification of the binding between NELL1 protein and aptamer candidates.

(A) Illustration of the principle of using Biacore CAP microfluidic chip for the quantification of anti-NELL1 aptamer candidate to NELL1 protein analyte. Modified from Laboratory Guideline Biacore System, 28-9615-80 AB, 11/2011, GE Healthcare Bio-Sciences AB. www.gelifesciences.com/biacore. (B) Representative quantification of binding affinity Kd of different aptamer candidates fit from the SPR binding data. Data is presented at mean±SD for each individual candidate binding (n=3).

2.3.4 Evaluation of selected candidates *in vitro*

Once binding had been confirmed, further work was performed to determine the effects of the anti-NELL1 aptamers on cell proliferation and metabolism. As in the initial validation experiments, fibroblasts were chosen as being representative of normal cells. RD cells which have very limited expression of NELL1 protein were used as a negative control. Cells were incubated with a series of concentrations of anti-NELL1 aptamers ranging from 1~1000 nM for 24hrs. The rates of proliferation were assessed using crystal violet staining, and metabolic activity with an MTT assay. There were no significant differences in the rate of proliferation between fibroblasts, RD, or RH30 cells (Figure 2.5A). Metabolic activity was also not affected in fibroblast cells in the presence of the

anti-NELL1 aptamers. However, the metabolic activity was reduced in both RD and RH30 cells, in the presence of AptNCan2 and AptNCan3. Incubation with 1000 nM AptNCan3 showed a highly significant difference between RH30 cells (12.2 % decrease in metabolic rate) and RD cells (7.7 % decrease in metabolic rate) (Figure 2.5B).

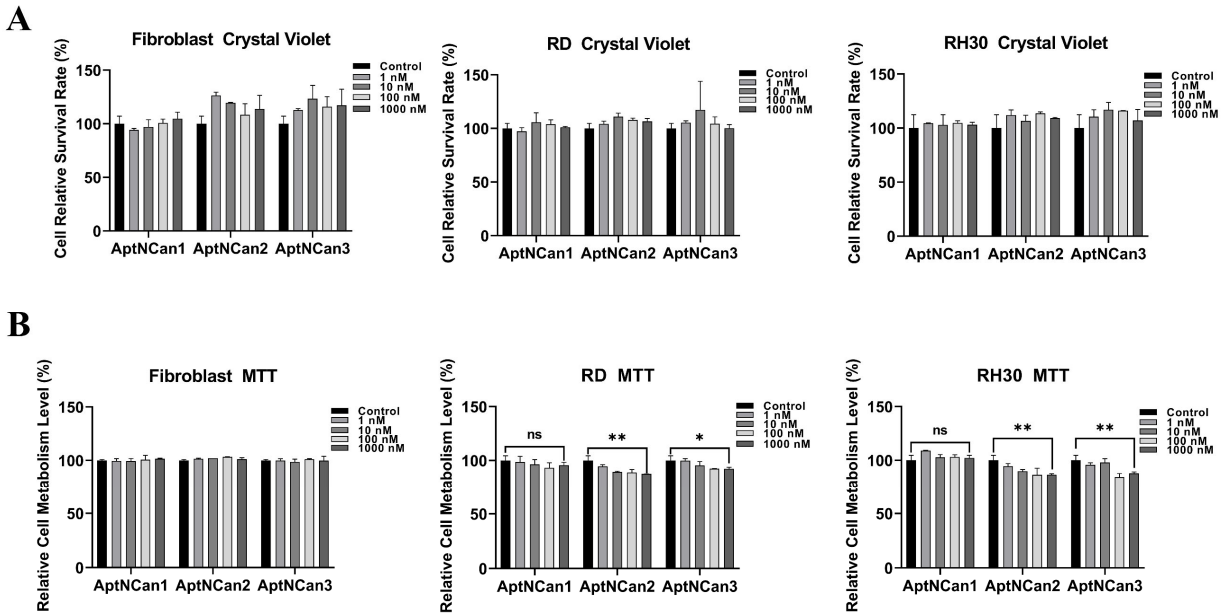

Figure 2.5 Measurement of anti-NELL1 aptamers' potential effects on cell proliferation.

(A) Crystal violet assay results comparing the cell relative survival rate of fibroblast, RD and RH30 sarcoma cells after treated with different concentration of anti-NELL1 aptamer candidates for 24hrs. (n=6) (B) MTT assay results comparing the cell relative metabolism level of fibroblast, RD and RH30 sarcoma cells after treated with different concentration of anti-NELL1 aptamer candidates for 24hrs. (n=6) Data is presented as mean ±SD for each individual cell line (n=3). Significance was tested using a two tailed t-test compared to the untreated cells for each cell line (*P≤0.05, **P≤0.01)

Despite the fact that AptNCan1 showed the highest theoretical binding affinity, there was no statistically significant effect on the metabolism in either RD or RH30 cells.

Based on the results of cell viability and metabolism assay, AptNCan2 and AptCan3 were chosen for the next steps of specificity evaluation. Both AptNCan2 and AptNCan3 were prelabelled with 5'biotin and PE-streptavidin was coupled onto the 5'ends for visualization and evaluation. To investigate the binding specificity of the NELL1

aptamers *in vitro*, PBS only, free PE-streptavidin and CF555 labelled anti-NELL1 antibodies were applied as control groups. The fibroblast negative control cell line did not show any binding with either the anti-NELL1 antibody or the aptamers AptaNCan2 or 3 (Figure 2.6A(i)). RD cells showed a significant peak shift only with AptNCan2 (Figure 2.6A(ii)). Both AptNCan2 and AptaNCan3 showed significant peak shifts in RH30 cells, with the latter being much greater (Figure 2.6A (iii)). The selectivity of both candidates for RMS cells which expressed NELL1 were proven. But it also revealed that AptaNCan3 had significant better specificity compared with AptNCan2 (Figure 2.6A).

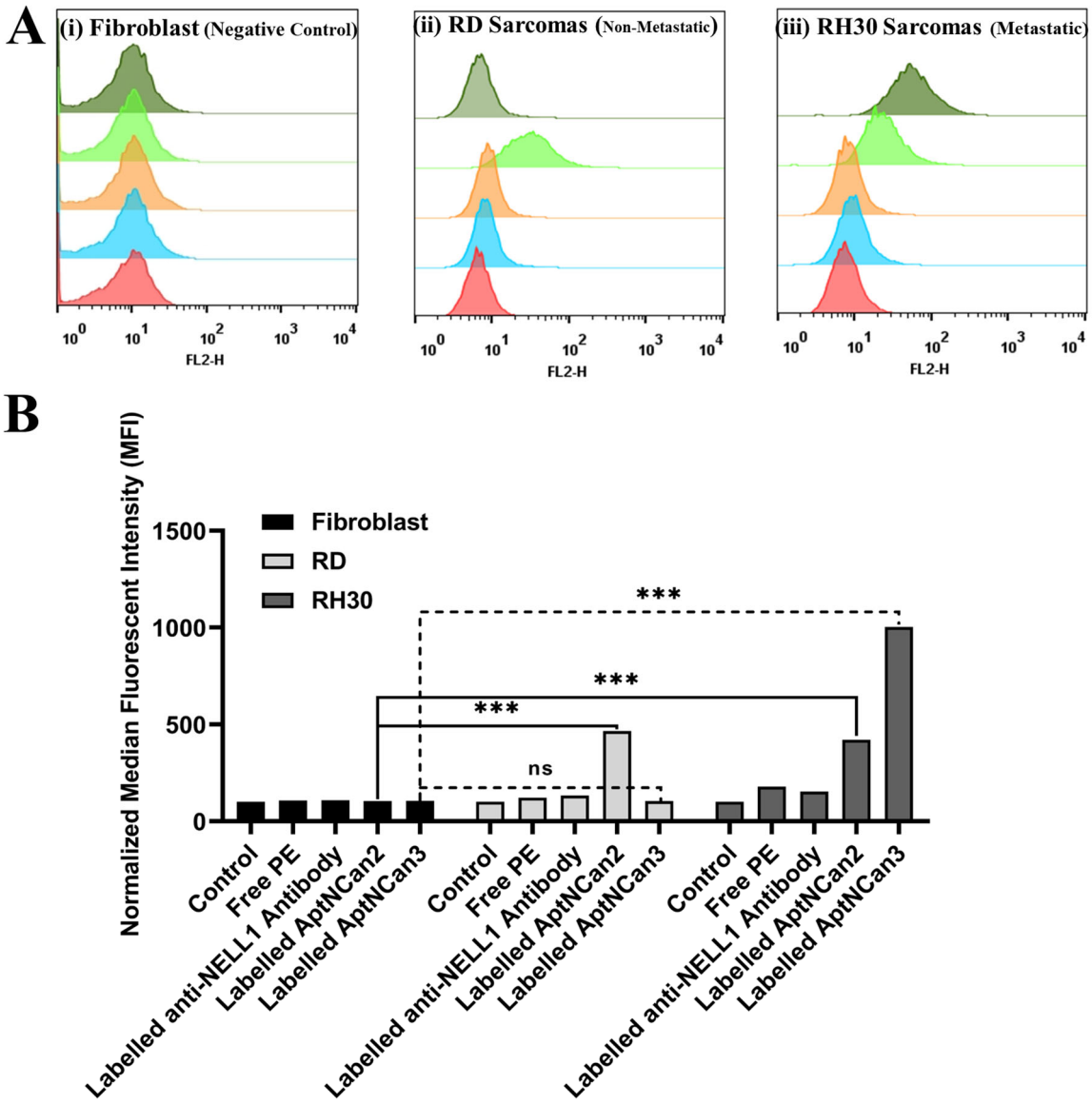

Figure 2.6 Validation of anti-NELL1 aptamers specific binding measured by flow cytometry.

(A) Representative flow cytometry histogram result for fibroblasts, RD and RH30 sarcoma cells. Cells were incubated with either PBS (Red), free PE staining (Blue), CF555-labelled anti-NELL1 antibody only (Orange), PE-labelled AptNCan2 (Light green) and PE-labelled AptNCan3 (Dark green). (B) Results from the normalized median fluorescence intensity of flow cytometry results for Fibroblast, RD and RH30 sarcoma cells. Cells were incubated with different incubation in the PBS (control), free PE staining, CF555-labelled anti-NELL1 antibody and PE-labelled anti-NELL1 aptamer 1&2. Data is presented as mean ±SD for each individual cell line (n=3 independent experiments of triplicates). Error bars were too small to be shown. Significance was tested using a two tailed t-test compared to the untreated cells for each cell line (***P≤0.005, ns=not significant)

The MFI data of each event (Figure 2.6A) was collected and the quantitative data illustrated in Figure 2.6B. All the data was normalized to the PBS control group for comparison. AptNCan2 showed significant specific binding in both RD and RH30 cells. AptNCan3 showed specific binding in RH30 cells, and the signal strength was more than twice that seen for AptNCan2. Since the number of fluorescent groups coupled to the aptamer corresponds directly to the amount of the aptamer, the MFI value was directly linked with the amount of the bound aptamer on the cell surface. Although free PE fluorophore could easily penetrate the cell membrane, it could be observed that only a very limited amount of PE signal was left after sufficient wash cycles and cell fixation (Figure 2.6B). This confirmed that the signal was specific to the binding of anti-NELL1 aptamers with RMS cells. Similar to the cell surface NELL1 validation data (Figure 2.1), the MFI of anti-NELL1 antibody still showed a similar trend for three groups, i.e. the MFI signal was greater in RH30 compared with fibroblast and RD groups. Although the significance among antibody-incubated groups was similar to comparable data in Figure 2.1, the much higher affinity of aptamer-incubated groups greatly extended the scale and minimized the apparent difference among antibody-incubated groups (Figure 2.6B). Based on the flow cytometry binding specificity evaluation, the AptNCan3 aptamer was used in subsequent experiments. *In vitro* localization experiments were performed using

confocal microscopy after incubation of live RMS cells with the anti-NELL1 aptamer. Negative controls included unlabelled aptamer (Figure 7A) and unbound PE fluorophore (Figure 2.7C). Signal was only seen in the PE channel for labelled anti-NELL 1 antibody (Figure 2.7B) and labelled anti-NELL1 AptNCan3 aptamer (Figure 2.7D), as would be expected. Since PE-streptavidin could freely penetrate the cell membrane, all non-specific PE signals inside cells would be removed by washing and fixation. Cell membrane staining and DAPI cell nucleus staining were also used, and the images show that all bound signal from the PE channel was within the cytoplasm, but outside the nucleus (Figure 2.7). The anti-NELL1 AptNCan3 aptamer (Figure 2.7D) also showed a much stronger fluorescence signal compared with the antibody (Figure 2.7B) which also corresponded to the flow cytometry MFI data (Figure 2.6B).

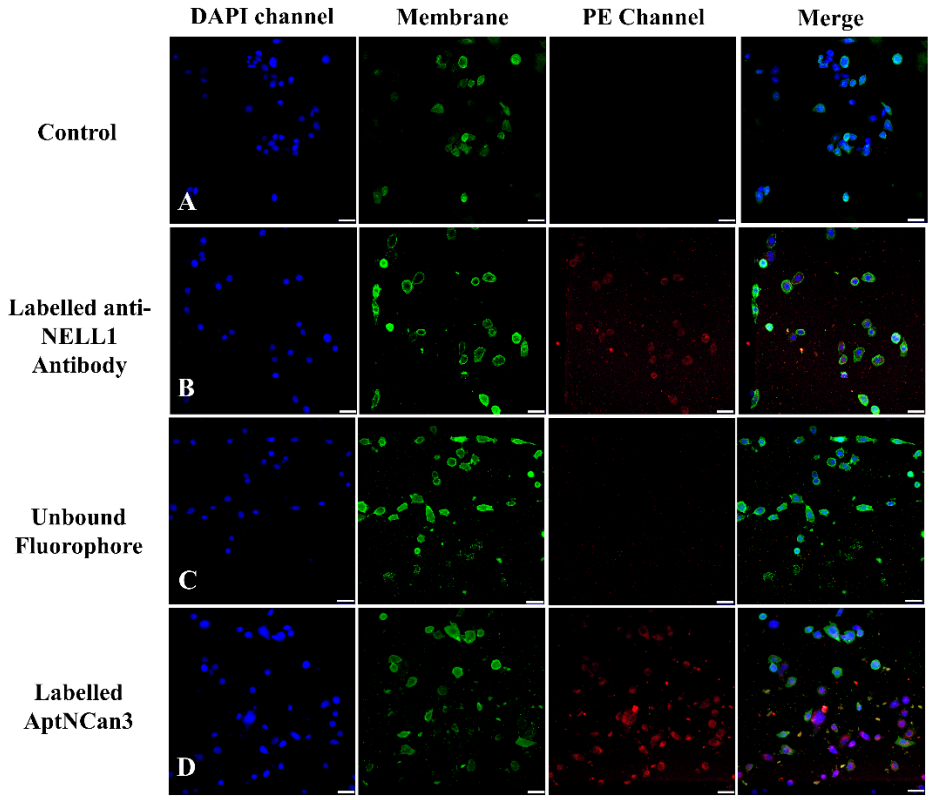

Figure 2.7 Fluorescence confocal imaging of anti-NELL1 aptamers specific binding in RH30 sarcoma cells.

The RH30 sarcoma cells were incubated overnight with (A) non-labelled AptNCan3; (B) CF555-labelled anti-NELL1 antibody; (C) Unbound PE staining and (D) PE-labelled AptNCan3. The cells were then thoroughly washed and fixed with 4 % PFA. Scale bar, 50 µm.

Imaging was repeated with all three cell types (Figure 2.8). As seen in the flow cytometry data (Figure 2.6), confocal imaging showed that AptNCan3 has a strong binding affinity for RH30 cells, but shows almost no binding with fibroblasts or RD cells (Figure 2.8).

To further investigate the cellular localization of AptNCan3, cells were imaged at a higher magnification (83x). The PE labelling of aptamers could clearly help to localize the aptamers (Figure 2.9A). CellBrite™ green cytoplasmic membrane staining indicated that the aptamer signal was present in the intracellular area (Figure 2.9C, 2.9D). Instead of evenly spreading among the cytoplasm which most small molecules or fluorophores did, the aptamer signals showed specifically overlapping with parts of the membrane signal (Figure 2.9E). The punctate structures indicate accumulation within a subcellular structure e.g. lysosome (Figure 2.9B). Due to the multiple times of washing and length of incubation, most of the aptamer signals were detected inside the cells, but some were still visible on the membrane surface (Figure 2.9E). No NELL1 signal was observed in the nucleus or on the nuclear membrane indicating that this was not non-specific binding (Figure 2.9F).

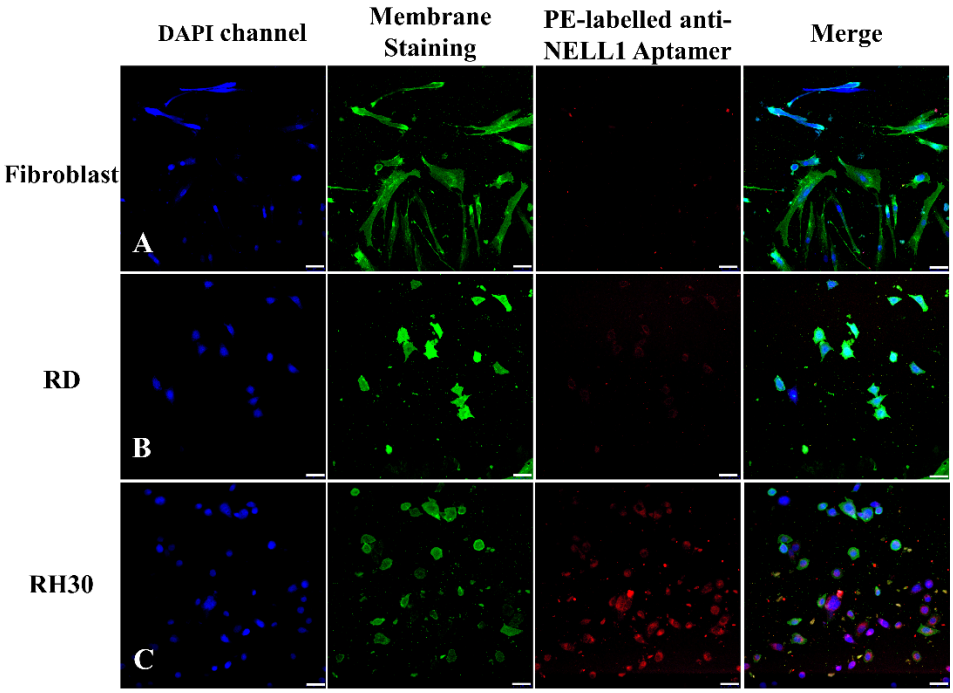

Figure 2.8 Fluorescence confocal imaging of anti-NELL1 aptamers cell specific binding.

The PE-labelled anti-NELL1 aptamer AptNCan3 were incubated overnight with (A) Fibroblast; (B) RD sarcomas; (C) RH30 sarcomas. The cells were then thoroughly washed and fixed with 4 % PFA. Scale bar, 50 µm.

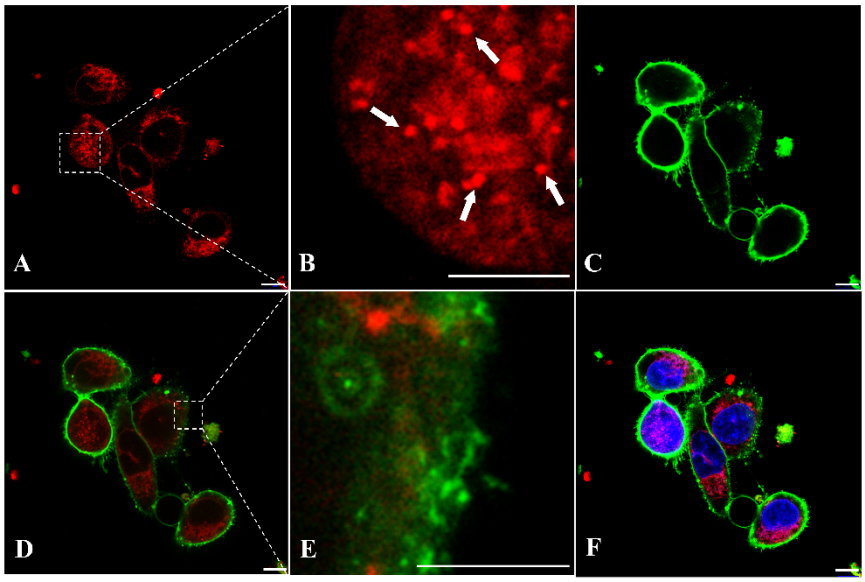

Figure 2.9 Fluorescence confocal imaging of anti-NELL1 aptamers specific binding in RH30 sarcoma cells for binding colocalization analysis.

The RH30 sarcoma cells were incubated with (A) PE-labelled AptNCan3 for overnight, (B) magnified image of the region of interest (ROI) box in A, arrows showing the small punctate structures, followed by (C) staining with CellBrite® green Membrane Staining. (D) merged images of A and C, (E) magnified image of the region of interest (ROI) box in D, (F) merged images of D and the nucleus stained with DAPI.The cells were then thoroughly washed and fixed with 4 % PFA before imaging. Scale bar, 10 µm.

2.4 Discussion

2.4.1 NELL1 as a biomarker for targeting

Historically, NELL1 was recognized only as a protein with a role in osteogenic stimulation. However, more recently, NELL1 has been found to have abnormal expression levels in a number of diseases. The paediatric cancer, RMS, shows significantly higher expression levels within the metastatic alveolar RMS (aRMS) form than the embryonal form (eRMS) (Rapa et al., 2012). Moreover, it was discovered that high expression levels of NELL1 are normally linked with negative outcomes in some types of sarcoma (Tombolan et al., 2017). Targeting NELL1 could therefore prove useful in the fight against cancer (Caza et al., 2021).

To be useful as a specific targeting molecule, the biomarker needs to be found on the outer surface of the cell membrane and also to be differentially expressed in cells or tissues. Although NELL1 has been identified as a secreted exocrine protein, previous studies have demonstrated that NELL1 was persistently localized in a specific way similar to a membrane protein on the outside of the cell membrane; described as unconventional secretory machinery (USM). Through USM, NELL1 was normally transported and accumulated on the cell membrane before secretion. This is similar to some other secreted proteins such as fibroblast growth factor 2 (FGF2), or interleukin 1β (Crisan et al., 2008; Keller et al., 2008; Pang et al., 2015). To confirm the location of NELL1 as the outer-membrane of aRMS cells we performed flow cytometry (Figure 2.1). Furthermore, GFP-labelled NELL1 has previously been shown to be located on the cell outer-membrane which supported our results and provided the evidence for selecting NELL1 as a target (Pang et al., 2015).

2.4.2 Binding of NELL1 aptamer can affect cellular metabolism

Several previous studies have directly demonstrated a relationship between NELL1 and

the proliferation and metastasis of cancer cells, particularly in RMS (Pang et al., 2015; Rapa et al., 2012; Tombolan et al., 2017). While our study indicated that NELL1 binding by aptamers affected cell metabolism as shown by the MTT assay (Figure 2.5B) no similar studies have reported effects on cell metabolism, although a previous study showed successful pathway blockage which linked suppression of metabolism to the binding of an aptamer to polyphosphate kinase 2 (PPK2). The results showed that inorganic polyphosphate intracellular metabolism was significantly inhibited upon aptamer binding with an IC50 of 40 nM (Shum et al., 2011). Furthermore, as NELL1 was also found to act as a signalling molecule for important cell functions, previous research has discovered that binding to certain region of NELL1 could block and affect the NELL1 mediated cell adhesion (Hasebe et al., 2012). A scratch assay has also been performed with the selected aptamer and aptamer conjugation which showed the significant inhibitory effect of NELL1 aptamer in the growth and mobility of RH30 cells through affecting its metabolism.

2.4.3 NELL1 aptamer specificity

The applied aptamer screening method was optimized from a protocol based on fluorescence-guided screening to immobilized NELL1 protein from a randomized library (Chandradoss et al., 2014). This method ensured our selected aptamers had high affinities to NELL1. However, the specific point on the protein to which the aptamer candidates bind cannot be pre-determined. Our data (Figure 2.5B) showed that both AptNCan2 and AptNCan3 could both affect the metabolism of NELL1 expressed RMS cells, but despite having the highest binding affinity AptNCan1 did not have any effect on cell metabolism (Figure 2.5B). This may be directly linked to the site of the aptamer binding on the NELL1 protein. It was also found that AptCan2 had a very similar binding for RD and RH30 cells (Figure 2.6), considering that both cell lines could secrete NELL1 but with a

significantly different level, as shown in our study and in peer studies (Rapa et al., 2012; Tombolan et al., 2017). This suggested that AptNCan2 was likely to bind to another protein with a similar structure to NELL1, e.g. an isoform, given the high similarities within the NEL families. NELL2, for example, is an isoform within the NEL family which is approximately 55 % identical to NELL1. Some cell lines with relatively low NELL1 expression levels have been discovered to have a high level of NELL2 expression (Kuroda et al., 1999; Maeda et al., 2001). AptNCan3 was further assessed using confocal imaging, and comparison with commercially anti-NELL1 antibody confirmed the specificity of the aptamer to RH30 cells compared to other cell lines (Figure 2.6, 2.7).

2.4.4 The aggregation of NELL1 in intracellular vesicles was strongly linked to the properties of NELL1

This study, and others (Kuroda et al., 1999; Pang et al., 2015) showed that a large amount of NELL1 aggregated on the cell membrane, although it should be noted that NELL1 is a secreted protein rather than a membrane protein. NELL1 is normally transported to the membrane via exocytotic vesicles. This corresponds with our confocal imaging results, where the signal which corresponded to NELL1 binding ligands (red PE channel) remained within the cell membrane signal area (green), regardless of whether a NELL1-specific aptamer or the antibody was used (Figure 2.6, 2.7, 2.8, 2.9). Under higher magnification, it was discovered that instead of binding non-specifically or passively diffusing into the cytosol which normally led to uniformly distribution within the cytoplasm, the ssDNA-based aptamer was specifically clustered in punctate (vesicle) structures, which was also directly associated with the properties of NELL1 and its transport mechanism (Figure 2.9B). The specific distribution of NELL1 protein and the specific high-affinity binding of the aptamer led to the concentration of the intracellular signal in the vesicles. This hypothesis was also supported by fluorescence and immunohistochemical results in other studies, where NELL1 showed a directional

aggregation and translocation within the cytosol (Kuroda et al., 1999; Pang et al., 2015).

2.5 Conclusions

In conclusion, after successful validation of NELL1 expression and membrane location, several anti-NELL1 DNA aptamers were successfully screened through the optimized robust quick selection protocol. Evaluation of affinity and selectivity were performed step-by-step for a further selection of screened aptamers. All three candidates were measured to have a relatively high binding affinity with calculated Kd under 1000 nM. Two of the three candidates also showed suppression of metabolic activity in NELL1 expressing cell lines. Among those, AptNCan3 was evaluated as the best candidate which has the best balance of affinity and cell specificity. It was shown to accumulate on the membrane and in punctate structures within cells. The identification of these aptamers can permit easy, cheap and quick manufacture of targeting moieties towards NELL1 expressing cells; often those involved in cancer or other pathologies.

In this chapter, one of the anti-NELL1 aptamer candidates (AptNCan3) has been successfully selected due to its great balance between binding affinity and cell specificity. Following this study, our research moved on to the next important construct, pH-responsive polymer layer, which worked as an important linkage between the targeting aptamer and the therapy core.

Chapter 3

pH-Responsive Charge Reversible Layer

Stimuli-responsive materials have been found to significantly enhance the accumulation and uptake of delivered therapeutic reagents. Through activation by the acidic environment of tumours and subcellular organelles (endosomes & lysosomes), the synthesized pH-activated PMPC-PDPA@PEG-*b*-PAMA/DMMA copolymer layer could efficiently convert charge, and revert from a hydrophilic to hydrophobic state with the decrease in pH of the surrounding environment. The copolymer can remain neutral or negatively charged in a normal physiological environment (pH 7.4), avoiding rapid clearance and non-specific binding. Conversion to a positive charge in the tumour microenvironment (pH 6.8) facilitates tissue accumulation and cellular uptake through enhanced adsorption onto the negatively charged cellular membranes.

The copolymer layer was critical to the overall design of the nanosystem, since it was used to coat the NIR-siRNA-linked core nanoparticle, and also linked with the selected DNA aptamers.

3.1 Introduction

3.1.1 Stimuli-Responsive Materials

Stimuli-responsive synthesized materials may be used for a wide variety of applications but have more recently been used for drug delivery in clinical applications. *In vivo* drug delivery normally includes several steps: passing from intravenous blood or body fluid circulation to tissue accumulation and cellular uptake. During the delivery process, the carriers must overcome obstacles to be able to precisely send cargo to the required location. Such barriers include macrophage clearance, non-specific binding with serum proteins, kidney filtration and enzymatic degradation (Mura et al., 2013).

One of the most important factors affecting the efficacy of the delivery of nanocarriers is surface charge. It has been shown that negatively charged groups on the cell surface (such as sialic acid) could be applied as a useful tool for enhancing the deliveries of nanocarriers (Verma & Stellacci, 2010). Positively charged nanocarriers, for example, could enhance the cellular uptake due to stronger attraction to the negatively charged cellular membrane (Verma & Stellacci, 2010). In the previous study, atomic force microscopy (AFM) was used to quantify the force between (poly(D,L-lactide-co-glycolide) (PLGA) nanoparticles functionalized with PLL nanoparticles and cell membranes. The stronger adsorption has been validated through the tighter binding distance and forces (Vasir & Labhasetwar, 2008). Circulation time and bioavailability may be decreased due to the formation of serum protein coronas and non-specific binding. Due to the efficiency of positively charged nanoparticles in penetrating cell membranes and internalising cells, they are the most commonly used synthetic carriers for medication and gene delivery (Fröhlich, 2012; Verma & Stellacci, 2010).

Charge-reversal delivery may enable more efficient delivery of cargo. Generally, charge

convertible carriers are designed to remain neutral or negatively charged under normal physiological conditions, but can convert to a positive charge in response to specific stimuli such as pH, temperature, or reactive oxygen species (ROS) levels (Zhang et al., 2022). This could significantly prolong the circulation time and increase tissue accumulation and cellular uptake.

3.1.2 pH-activated nanocarriers

It has been long established that pH is different among organs, tissues, and various subcellular organelles. Endosomes and lysosomes, for example, are subcellular organelles which are acidic with pH ranges of 5.5–6.0 and 4.5–5.0, respectively. The acidic pH (pH 6.5–6.8) within the tumour environment compared with the normal environment (pH 7.2–7.4) has led to their use as stimuli for tumour targeted delivery (Wu et al., 2018). The pH of the cytoplasm in cancer cells is higher than that of healthy cells. However, within the cells the lysosomal compartments behave differently. Lysosomes in normal cells maintain an acidic environment in the range 4.5–6.5, whereas lysosomes in malignant cells can be below pH 4.5. In highly metabolic cells the lysosomes can be in the range pH 3.8–4.7 (Glunde et al., 2003). The difference between lysosomes in healthy and malignant cells makes them a good target for responsive release (Griset et al., 2009).

pH-sensitive polymers, metals, and lipid-based nanomaterials have become the most popular materials for the intracellular release of treatment compounds. In addition to controlling release, the coating materials can also act as protection for the cargo, such as RNAi which can easily be degraded within the lysosome (Xu et al., 2016). pH-sensitive nanovalves (NV) have been applied for sealing the cargo inside the pores of mesoporous silica nanoparticles (MSNs) prior to delivery. The NV was composed of α-cyclodextrin (α-CD) complexed with an aniline-based stalk on the surface of MSNs. After entering cells, the lysosomal acidic pH activates the nanovalves by decreasing the bond between the stalk

and α-CD and leads to the responsive release of anti-cancer drugs. Doxorubicin loaded NV-MSNs have shown good cellular toxicity by killing over 80 % of MIA PaCa-2 pancreatic cancer cells compared with the same concentration of empty control NV-MSNs (Hwang et al., 2015).

Similarly, Muniswamy and collaborators developed a system comprising a DOX-loaded PLGA nanoparticle core and a dendrimer-cationised-albumin outer layer (dCatAlb-pDNP). The PLGA degraded at the mid to late endosomal pH (4.5–5.5) in cancer cells and released the DOX. Furthermore, the system was able to penetrate the blood-brain barrier (BBB) and blood tumour barrier (BTB). Cell experiments with U-87 MG glioblastoma cells showed a 5.5-fold increase in tumour cell death due to increasing the expression levels of caspase-3 gene which mediates cellular apoptosis (Muniswamy et al., 2019)

pH-activated release systems can also deliver cargo other than chemotherapeutics, such as nucleic acids for gene therapy techniques. Xu and collaborators reported an innovative pH-activated polymer (Meo-PEG-*b*-P(DPA-co-GMA-TEPA-C14))-based system for delivering siRNA into tumour cells efficiently. Endosomal swelling was induced by the buffering effect of PDPA degradation. This greatly decreased the escape time of siRNA and increased its silencing efficiency. *In vitro* experimental results revealed that the viability of PC3 prostate cancer cells was decreased over 5-times with the use of controlled release, and iRGD (amino acid cyclic peptide: CRGDKGPDC) polymer, which enhanced membrane penetration (Xu et al., 2016).

In addition to various kinds of polymers, many pH-responsive metallic nanomaterials have also been widely applied in tumour treatment. Titanium peroxide (TiOx) and titanium dioxide (TiO2) have been broadly used in biomedicine due to its biocompatibility and optical functionalities. Dai and collaborators reported a dual-stimuli-responsive TiOx/ DOX nanodrug system which was applied to lung cancer models. Titania nanosheets were

synthesized and DOX loaded onto the surface of the sheets. Due to the exceptional pH-responsive release profile, the DOX could be preserved in the TiOx perfectly at neutral pH (releasing less than 10 % over 48 h). However, the DOX could be rapidly released from the TiOx nanosheets at acidic pH, i.e. more than 50 % drug release in less than 24 h. As a result, the TiOx/DOX system killed 88.45 ± 0.91 % of A549 lung cancer cells with a DOX concentration of 10 μg mL−1 after 48h (Dai et al., 2018).

Iron oxide nanomaterials have been very promising pH-triggered release anti-cancer reagent carriers for a long time. Yue and collaborators applied iron oxide nanotubes (PMNTs) for pH-activated release of paclitaxel (PTX), which has low water solubility. The activation pH was set as 4.5, which would greatly enhance PTX release in carcinoma cells and decrease the possibility of non-specific release in normal cells. In the stimulation test, nearly 80 % of the loaded PTX was released when the pH was at 4.5, compared with less than 40 % when the pH was at 7.4. At the same time, the rod-like shape of the nanotubes further accelerated the uptake rate of the system. The MTT (3-(4,5-Dimethylthiazol-2-yl)-2,5-Diphenyltetrazolium Bromide) assay results showed that 100 μg mL-1 of the PTX-PMNTs killed over 70 % of the A549 cells within 24 h, illustrating the high efficiency of the system (Yue et al., 2011).

Calcium-based materials, such as calcium phosphate (CaP) (Mi et al., 2016), and calcium carbonate ($CaCO_3$), have also been widely applied in tumour diagnosis and therapy. Dong and collaborators (2016) prepared mono-dispersed $CaCO_3$ nanoparticles which were coated with PEG, and carried the photosensitizer Mn^{2+}-chelated chlorin e6 (Ce6(Mn)) and the chemotherapeutic DOX. While stable under physiological pH (7.4), it was demonstrated that the DOX was released in an acidic environment (pH = 5.5) due to the rapid degradation of the particles. Furthermore, *in vitro* experiments using 4T1 murine breast cancer cells showed that over 80 % of cells were killed after incubation with 5 μg mL^{-1} DOX for 24 h.

Furthermore, the release of Ce6(Mn) from the particles enhanced T1-contrast under magnetic resonance imaging. These particles are therefore suitable for photodynamic and chemotherapeutic therapy, in addition to real time monitoring. This was proven in 4T1 tumour bearing mice, in which over 25 % of the T1 MRI signal came directly from the tumour, and the tumours were significantly smaller than in control groups (Dong et al., 2016).

pH-activated lipid-based nanomaterials have also showed promise in cancer treatments due to good biocompatibility and membrane penetrating functions. Choi and collaborators designed a nanosystem using the compound 1,2-distearoyl-sn-glycero-3-phosphoethanolamine-N-[biotinyl(polyethylene glycol)-2000] (DSPE-PEG) for coating MSNs with axitinib (AXT) and celastrol (CST) as cargo. *In vitro* drug release test results showed that the release of AXT and CST both significantly increased at pH 5.0 compared to pH 7.4. The results from these systems revealed that the lipid outer layer significantly increased the efficacy of mitochondrial-based cell apoptosis. When the system was applied to SCC7 carcinoma, tumour bearing mice models tumour inhibition was over 64 % compared to the control groups (Choi et al., 2016).

3.1.3 pH-activated Charge Convertible Polymer

Currently, two main primary routes have been followed for designing pH-activated charge convertible polymers i.e. the protonation/deprotonation of surface chemical groups, and acid-labile bond breakage (Zhang et al., 2022).

Charge convertible copolymers based on acid-labile bond dissociation are the most commonly used. Acid sensitive covalent bonds are found within the polymer structure, such as amide, oxime, ether, or hydrazine bonds. Upon bond breakage, the physicochemical characteristics of the copolymer change accordingly (Kim et al., 2018; Zhang et al., 2022). With the help of primary amine groups which enable the charge convertible functionality,

2,3-dimethylmaleic anhydride (DMMA) has been used and validated multiple times in pH activated charge convertible polymers. Compared with other functional groups which were also based on the primary amine group, such as the 1,2-dicarboxylic-cyclohexene anhydride (DCA) or tetramethyl succinic anhydride (TM), the DMMA based copolymer has demonstrated a stable and quick charge reverse response with the change of pH. At pH 6 the DMMA based polymer poly(L-lysine) (PLL)-DMMA successfully converted its surface potential within only minutes compared to 7.5 hours or more for other polymers. The gap was even more significant at a lower pH when DMMA-based polymers were seen to change instantaneously (Zhou et al., 2009). In addition, the combination of a DMMA based monomer with iron oxide magnetic nanoparticles was used to form a hierarchical tumour acidity-responsive magnetic nanobomb (dubbed HTAMNs) which could be used for tumour diagnosis and treatment. The DMMA functional group could rapidly reverse the whole nanosystem charge from negative to positive after exposure to the acidic pH which greatly enhanced the imaging sensitivity and therapeutic efficacy, plus a significantly higher cellular uptake (Yang et al., 2019).

3.1.4 Hydrophilic-Hydrophobic Reversion Function

Nanoparticle hydrophobicity and hydrophilicity are also critical parameters for delivery. Whereas hydrophilic nanoparticles are normally stable *in vivo*, a hydrophobic surface significantly restricts circulation around the body. However, an improved cellular uptake was also observed for the hydrophobic nanoparticles, mainly through the cellular absorption of the hydrophobic chains interaction with the lipophilic cell membrane which directly led to the enhanced uptake of hydrophobic layer coated nanoparticles (Nam et al., 2009). Copolymers that have both hydrophilic and hydrophobic tails have been designed to maximise drug bioavailability while minimising pharmacological adver(Gil & Hudson, 2004). Micelles for hydrophilic-hydrophobic pH-activation have been synthesized using

Poly(2-diisopropylaminoethyl methacrylate)-*b*-poly(2-aminoethyl methacrylate hydrochloride) (PDPA-*b*-PAMA). Due to the hydrophilic and hydrophobic tails within the same copolymer, the polymer micelle could stay hydrophilic within the normal environment yet reverse to a hydrophobic state after entering the low pH tumour environment (Lomas et al., 2010).

To fulfil the functionalities of both charge conversion and hydrophilic-hydrophobic reversion, a combination of pH activated polymers were applied by absorbing the commercially available positive charged poly(2-(methacryloyloxy)ethyl phosphorylcholine)–poly(2-(diisopropylamino)ethyl methacrylate) (PMPC-PDPA) (Pegoraro et al., 2013) onto the surface of the DMMA modified poly(ethylene glycol)-*b*-poly(2-aminoethyl methacrylate hydrochloride) (PEG-*b*-PAMA) (Lomas et al., 2010) with strong electrostatic interactions at neutral pH. The PMPC-PDPA@PEG-*b*-PAMA/DMMA copolymer could convert both the surface charge and perform hydrophilic-hydrophobic reversion based on the change in pH. Due to the negative surface potential shielding, the *in vivo* circulation could be greatly extended. At the sample time, stable circulation also ensured enough time for the EPR effect which could further improve tumour accumulation (Torchilin, 2011). Through conversion to a positive charge in an acidic environment, it has been proven that cellular internalisation could be greatly enhanced.

3.2 Materials and Methods

3.2.1 Preparation of the mPEG-Br macroinitiator of polymerization

The synthesis protocol of mPEG-Br macroinitiator was adapted from Nizardo and collaborators (2018). A mixture of 200 g of toluene [Sigma- Aldrich, Poole, UK] and 4.0 g (2 mmol) of dried mPEG (Mn=2000 g/mol, flake) [Sigma- Aldrich, Poole, UK] was purged with nitrogen gas for 20 min to remove oxygen. Triethylamine (TEA) (0.40 g)

[Sigma- Aldrich, Poole, UK] was added dropwise into the mixture under a nitrogen environment and magnetically stirred at 200 rpm for 30 mins. Subsequently, 0.5 mL of alpha-bromoisobutyryl bromide [Sigma- Aldrich, Poole, UK] was added dropwise over 1 hour, at 5-minute intervals. Since alpha-bromoisobutyryl was particularly sensitive to moisture and oxygen, it was split into 5 or more 1.5 mL Eppendorf tubes in case of moisture exposure. The reaction flask was then tightly sealed with parafilm [Bemis, WI, US] to prevent any possible exposure to oxygen and moisture. The whole mixture was left to react for 48 h at room temperature. The mPEG-Br was extracted from toluene by vigorously mixing the reaction mixture with an equal amount of distilled water. Dichloromethane (DCM) [Sigma- Aldrich, Poole, UK] was applied three times for 50 mL per time to fully extract mPEG-Br from water. The extracted product in the organic phase was then washed with distilled water several times to remove any water-soluble contaminants. The product was then dried with $MgSO_4$ [Sigma- Aldrich, Poole, UK] and filtered through glass-fibre filter paper [Sigma- Aldrich, Poole, UK]. The majority of the organic phase was evaporated until the appearance of a white crude viscous product. Diethyl ether [Sigma- Aldrich, Poole, UK] was then used to reprecipitate the product. After filtering, the final colourless solid product was obtained. This was then vacuum-dried overnight to eliminate any remaining solvent.

3.2.2 Removal of the phenothiazine (PTZ) inhibitor from purchased 2-aminoethyl methacrylate hydrochloride (AMA) monomers

The removal process of PTZ inhibitor from purchased AMA (90 %, contains ~500 ppm phenothiazine as a stabilizer) monomer [Sigma- Aldrich, Poole, UK] was adapted from the method published by Panzarasa and collaborators (2015) (Panzarasa et al., 2015). The AMA monomer with stabilizer was mixed with tetrahydrofuran (THF) [Sigma- Aldrich, Poole, UK] in a 1:20 m/v ratio (e.g. 1g AMA per 20 mL THF). Subsequently, the entire

mixture was kept in the dark for two hours under constant stirring. Glass-fibre filter paper was then used to collect the pure AMA. The product was then vacuum-dried for two days. The final dry form of product was then sealed to prevent oxidation, and kept at room temperature until the next step of synthesis.

3.2.3 Synthesis of PEG-*b*-PAMA via atom transfer radical polymerization (ATRP)

Synthesis of PEG-*b*-PAMA *via* ATRP was done by optimising the method of Li and collaborators (2016). To start the reaction, 1.325 g of AMA monomer were dissolved in 5 mL of 4:1 (v/v) isopropanol-H_2O mixture, and the mixture was purged constantly with nitrogen for at least 20 minutes while stirring to remove dissolved oxygen. Under a nitrogen environment, 400 mg PEG-Br macroinitiator and 62.48 mg 2,2′-bipyridine (bpy) were applied into the reaction. Following the addition of 19.8 mg of CuCl the reaction was kept under nitrogen atmosphere for the whole reaction process. The flask was sealed and stirred at 60°C for the next 24 h. The reaction was terminated by exposing the Cu^+ catalyst to air by opening the flask. To fully remove the by-product (Cu^{2+} ions), the final reaction solution was diluted into an appropriate amount of distilled water and dialysed for 3 days with Spectra Por Dialysis Tubing (molecular weight cut-off: 1000 Da) [Repligen, MA, US]. The clear aqueous solution was then freeze-dried. The synthesized PEG-*b*-PAMA was then sent for validation with H1 500 MHz Bruker Nuclear Magnetic Resonance (NMR) instrument [Bruker, Karlsruhe, Germany].

3.2.4 Synthesis of pH-responsive PEG-*b*-PAMA/DMMA

Synthesis of PEG-*b*-PAMA/DMMA was done by optimising the method published by Li and collaborators (2016). To start the reaction, 465 mg of synthesized and validated PEG-*b*-PAMA (Mn = 4650) was dissolved in 10 mL of DMSO. Under vigorous stirring, 2.62 mg of bpy and 1.8 mL of TEA were added into the reaction. Following the fully

dissolving and mixing of the reaction, an excess amount of 2,3-dimethylmaleic anhydride (DMMA) (more than 605 mg, this method used 1g) was added. The reaction flask was then sealed and stirred at 40 °C for 24 h. To fully remove the excess of DMMA, the final reaction solution was diluted into an appropriate amount of distilled water and dialysed in water for 3 days with Spectra Por Dialysis Tubing (molecular weight cut-off: 1000 Da) [Repligen, MA, US]. The clear aqueous solution was then freeze-dried. The synthesized PEG-*b*-PAMA/DMMA was then sent for the validation with H^1 500 MHz Bruker Nuclear Magnetic Resonance (NMR) spectrometre [Bruker, Karlsruhe, Germany].

3.2.5 Preparation of pH activated PMPC-PDPA@PEG-*b*-PAMA/DMMA co-polymer layer

The overall pH-responsive polymer layer potential was adjusted using PMPC-PDPA (supplied by Prof. Giuseppe Battaglia, University of Sheffield) (Pegoraro et al., 2013). Based on the provided information from the collaborator, the PMPC100-PDPA120 was synthesised at the condition of number average weight Mn (measured with Gel permeation chromatography) of 62,000 and polydispersity of 1.38 (Pegoraro et al., 2013). Before the preparation of PMPC-PDPA@PEG-*b*-PAMA/DMMA micelles, the PMPC-PDPA co-polymer solutions were prepared in 1xPBS at a concentration of 5 mg/mL. The solution pH was then adjusted to 5.0 using 0.1 M HCl. 1 mg/mL PMPC-PDPA solutions were prepared by dilution with pH 5.0 PBS solution.

After this, the synthesized and validated PEG-*b*-PAMA/DMMA was dissolved in the phosphates buffer solution which the pH has been pre-adjusted to 10.0 which was for speeding up the dissolving process. The resulting PEG-*b*-PAMA/DMMA solution was then added to 1 mg/mL or 5 mg/mL PMPC-PDPA co-polymer solutions, dropwise. The mixture was allowed to stir at room temperature for 1 hour. The pH of the reacted co-

polymer solution was then adjusted back to neutral with 2M NaOH. The PMPC-PDPA@PEG-*b*-PAMA/DMMA solution was shaken for 15 minutes and sonicated for 5 minutes in a water bath.

3.2.6 Validation of pH-responsive functionality of PEG-*b*-PAMA/DMMA and PMPC-PDPA@PEG-*b*-PAMA/DMMA

Surface charge was determined under a series of different acidities/ alkalinities. HEPES buffers (25 mM) was prepared with pH ranging from 1.0 to 9.0 by adjusting with 1 M NaOH and HCl. The PEG-*b*-PAMA (1mg/mL), PEG-*b*-PAMA/DMMA (1mg/mL) and PMPC-PDPA@PEG-*b*-PAMA/DMMA (1mg/mL by DMMA) polymer solutions were prepared, ultrasonicated and filtrated with 0.22 μm syringe driven filters before measurement. The polymer solution was then mixed with HEPES solutions of different pH (pH ranging from 1.0 to 9.0) solution in a ratio of 1:9 by pipetting and transferred to the sample cuvettes. Using a DLS instrument [Zetasizer Nano, Malvern, UK] with a He–Ne laser (= 633 nm), the surface charge (zeta potential, mV) of PEG-*b*-PAMA, PEG-*b*-PAMA/DMMA and PMPC-PDPA@PEG-*b*-PAMA/DMMA at different pH conditions were measured. The samples were measured at 37 ℃ with a scattering angle of 90 degrees. Zeta potentials were calculated after readings of 100 runs per sample.

3.2.7 Coating of PMPC-PDPA@PEG-*b*-PAMA/DMMA onto the outer surface of gold NanoTriangles (AuNTs)

Prior to the coating, gold nanotriangles (AuNTs) were prepared following the protocol detailed in Chapter 4. The AuNTs were re-suspended in 1xPBS, then transferred into 98 % ethanol to remove the surface coating of CTAC which acted as a stabilizer. The particles were then collected by ultra-high speed centrifugation, and re-suspended in RNase-free 1xPBS [Sigma- Aldrich, Poole, UK] at a concentration of 5 mg/mL. PMPC-PDPA@PEG-*b*-PAMA/DMMA (5 mg/mL; pH 7.4) were ultrasonicated and filtered with a 0.22 μm

syringe driven filters. The resulting AuNTs suspension (100 μL) was added dropwise to 1 mL pH-responsive co-polymer solution. During the addition of the AuNTs suspension, the mixture was constantly vortexed. The solution was kept at pH 7 for the whole process. The nanoparticles were subsequently centrifuged at 10,000 rpm for 5 min and washed twice with 1xPBS before collection.

3.2.8 Characterization

The H^1 Bruker NMR spectra of mPEG-Br, PEG-*b*-PAMA and PEG-*b*-PAMA/DMMA were acquired at 500 MHz using a Bruker Avance spectrometer [Bruker, Karlsruhe, Germany] with tetramethylsilane (TMS) [Sigma- Aldrich, Poole, UK] as an internal standard after dissolving in D_2O and DCl [Sigma- Aldrich, Poole, UK]. The JEOL-2100 TEM [JEOL, Tokyo, Japan] was used to obtain the TEM images of PMPC-PDPA@PEG-*b*-PAMA/DMMA micelles and PMPC-PDPA@PEG-*b*-PAMA/DMMA coated AuNTs operating at 200 kV. The sample grid [Agar Scientific, Stansted, UK] was negatively stained with 1 % (w/v) phosphotungstic acid [Sigma- Aldrich, Poole, UK] before adding the sample on top of it. The grid was thoroughly air-dried before being inserted into the TEM. The Gatan 3 microscopy suite software [Gatan, Inc., CA, US] was used for TEM images analysis.

3.2.9 Data analysis and statistic test

All statistical analysis of experimental data was performed using Microsoft™ Excel [Microsoft, NM, US]. GraphPad Prism 8.0.2 [GraphPad Prism, La Jolla, CA, US] was used for graph plotting and non-linear stimulation. All results were presented as mean ± SD. When the p values (probability values from statistical significance testing) were less than 0.05, the difference was considered significant and shown. When two or more groups were compared, the two-tailed homoscedastic Student's t-test and one-way ANOVA were

applied for statistical analysis.

3.3 Results

3.3.1 Synthesis and characterization of pH-responsive charge reversible PEG-*b*-PAMA/DMMA

ATRP is often used to synthesize polymers with unique functionalities and characteristics (Li et al., 2016; Matyjaszewski & Xia, 2001) In this chapter, a PEG-*b*-PAMA/DMMA copolymer was made through ATRP following a optimisation of a two-step protocol. Confirmation of the structure of the copolymer was attained using H^1 NMR. mPEG was used as the raw material for the synthesis of the mPEG-Br macroinitiator (Figure 3.1) which was then confirmed by NMR (Figure 3.2) with H^1 (δ [ppm] in D_2O): 1.94 (6H, –$C(CH_3)_2Br$), 3.38 (3H, –O–CH_3), 3.5–4.0 (4H, –CH_2–CH_2–O–), 4.4 (2H, –$COOCH_2$-).

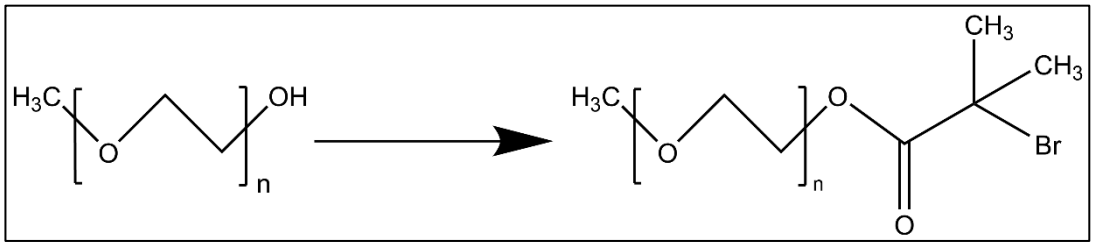

Figure 3.1 Schematic diagram of the synthesis process from mPEG to mPEG-Br

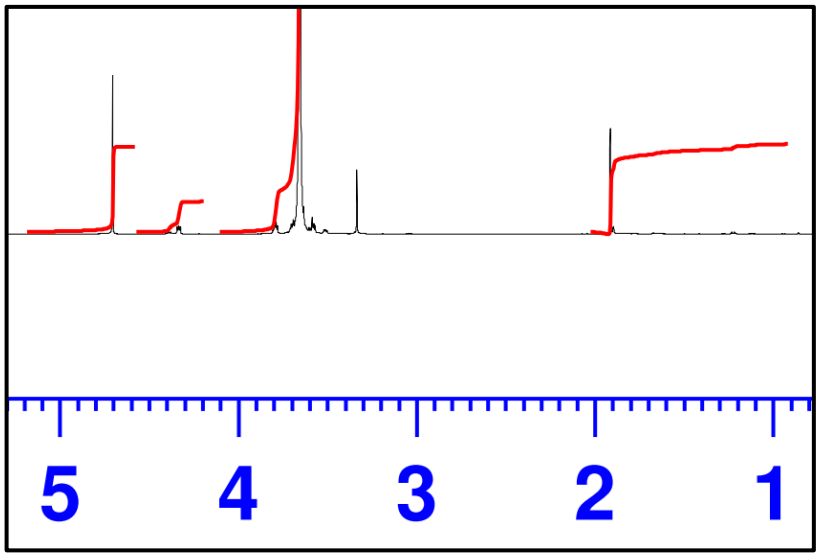

Figure 3.2 H1-NMR spectrum confirmed the chemical synthesis of mPEG-Br

Following the successful synthesis and validation of mPEG-Br macroinitiator for ATRP polymerization, the synthesis of PEG-*b*-PAMA was performed within an anaerobic chamber with precise temperature control. The synthesized PEG-*b*-PAMA was dialyzed to remove excess Cu^{2+} ions and freeze-dried until a white powder form of the copolymer was obtained. PEG-*b*-PAMA (490.6 mg) was obtained from the synthesis, with the yield percentage at around 37.4 %. H1 NMR data further validated the structure of the synthesized PEG-PAMA copolymer. As shown in Figure. 3.3, the typical H1 NMR spectrum of PEG-*b*-PAMA revealed two peaks at δ = 4.253 and 3.314 ppm, respectively, which were attributed to the resonance of $–OCH_2CH_2–$ and $–OCH_2CH_2–$ of the side chain, demonstrating the presence of the PAMA block.

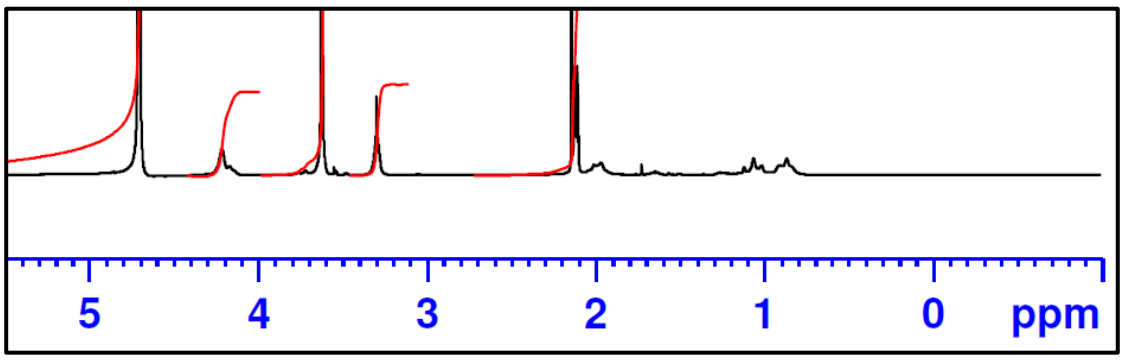

Figure 3.3 H^1-NMR spectrum of synthesized PEG-*b*-PAMA (Note: δ = 4.253 and 3.314 ppm)

In total of 465 mg of PEG-*b*-PAMA was applied as the raw material for the synthesis of PEG-b-PAMA/DMMA . The obtained PEG-*b*-PAMA/DMMA was dialysed for 48 hours to remove the unreacted DMMA with H^1 NMR data further demonstrated the successful addition of DMMA to the PEG-PAMA block after the reaction. The appearance of a new peak at = 1.804 ppm in the 1H NMR spectra of PEG-*b*-PAMA/DMMA (Figure.3.4), which was induced by the resonance of $–C(CH_3)=C(CH_3)–$, indicating the successful addition of the DMMA group (Figure 3.5). The whole synthesis process starting from mPEG to the final product PEG-*b*-PAMA/DMMA has been concluded as Figure 3.6.

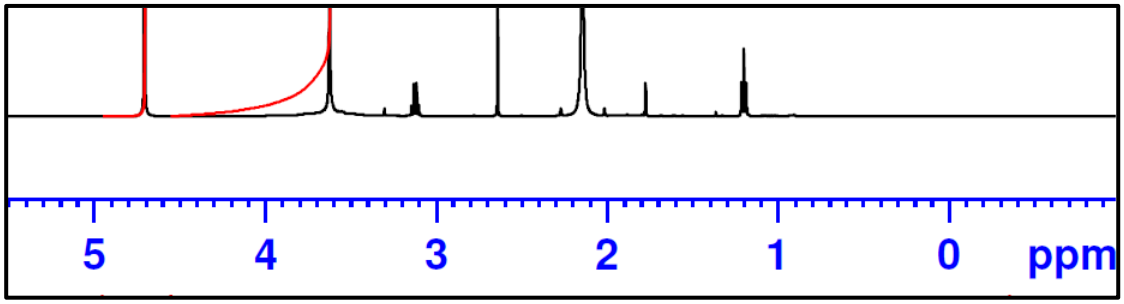

Figure 3.4 H^1-NMR spectrum of PEG-*b*-PAMA/DMMA sample (Note:δ = 1.804 ppm)

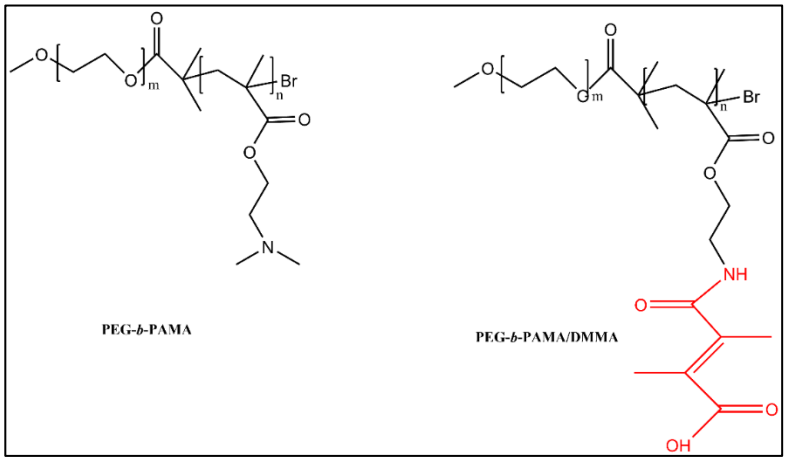

Figure 3.5 Schematic diagram of the synthesized PEG-*b*-PAMA and PEG-*b*-PAMA/DMMA

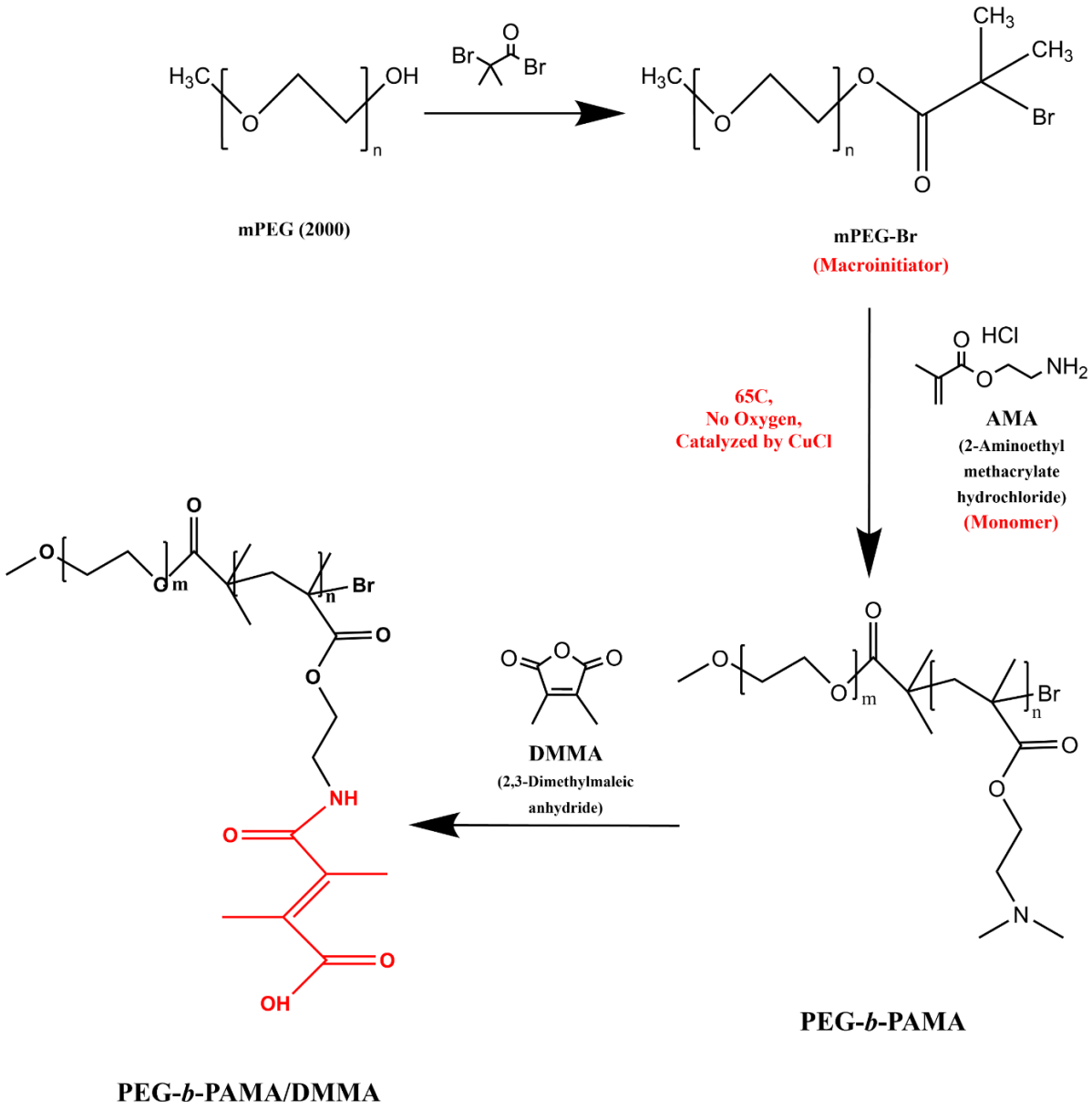

Figure 3.6 Schematic diagram of the whole synthesis process of PEG-*b*-PAMA/DMMA

3.3.2 PMPC-PDPA coating for charge neutral point adjustment

Following the synthesis and validation of PEG-*b*-PAMA/DMMA, the pH-responsive charge-reversible functionality was tested in 25 mM HEPES buffers at 37 ℃. The PEG-*b*-PAMA backbone was applied as the control. The zeta potential results demonstrated that the charge of the PEG-*b*-PAMA backbone copolymer stayed stable between 10-15 mV within the pH range 1.0 to 8.0. When the pH was neutral, the zeta potential of the

copolymer was at 14.77 ± 1.00 mV (Figure 3.7).

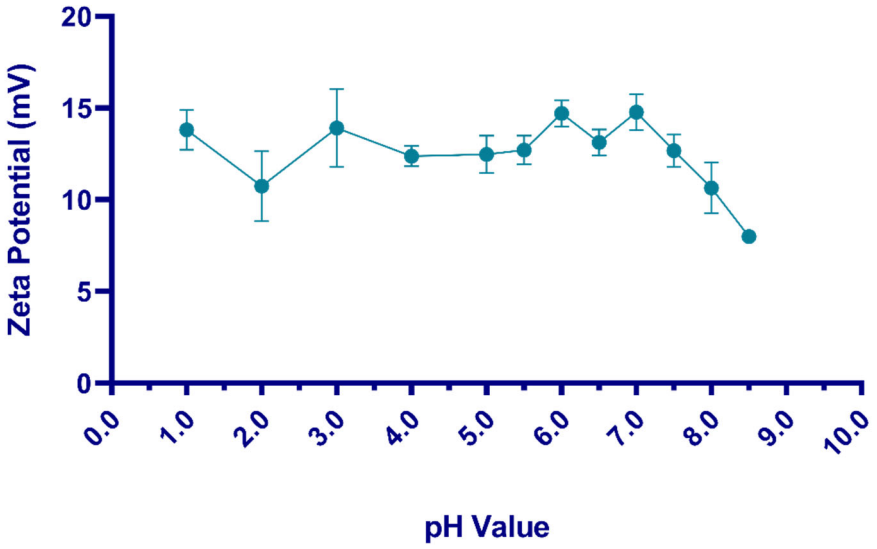

Figure 3.7 Quantified Zeta Potential of PEG-*b*-PAMA under different pH conditions. Data is presented at mean ±SD for each individual candidate binding (n=3).

Different from the PEG-*b*-PAMA backbone, the addition of DMMA to the copolymer structure conferred pH-responsive charge-reversible functionality to the whole copolymer. As demonstrated in the measured zeta potentials from buffers of different pH, the charge of PEG-*b*-PAMA/DMMA copolymer remained positive when pH was lower than 3.0. The overall trend of the copolymer charge was shown to decrease with an increase of pH value. The overall zeta potential of copolymer at pH 6.0, 6.5, 7.0 was -1.92 ± 0.73 mV, -2.11 ± 0.04 mV and -3.62 ± 0.54 mV, respectively. Although there was a slight jump at pH 7.5 to -1.44 ± 0.61 mV, the potential was still following the decline trend after this point from pH 8.0 to 9.0 (Figure 3.8).

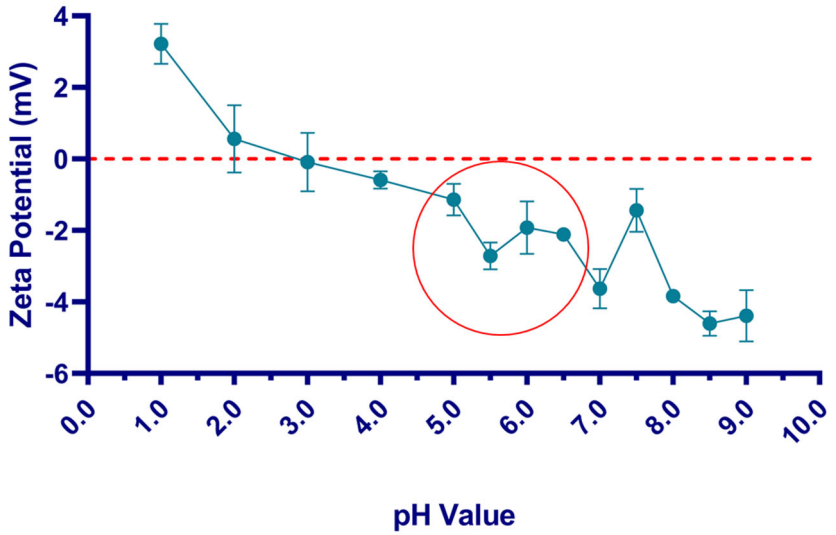

Figure 3.8 Quantified Zeta Potential of PEG-*b*-PAMA/DMMA under different pH conditions. Data is presented at mean ±SD for each individual candidate binding (n=3).

For the next step after the validation of pH-responsive charge-reversible functionality, commercially available constantly positive charged PMPC-PDPA coating was applied for charge neutral point adjustment. It was essential to validate the ideal mass ratio of PEG-*b*-PAMA/DMMA to PMPC-PDPA in tests in order to construct adequate PMPC-PDPA @PEG-*b*-PAMA/DMMA layers which could reverse their potential at the right pH. Different quantities of PMPC-PDPA (1 & 5 mg/mL) were mixed with the prepared 1mg/mL PMPC-PDPA@PEG-*b*-PAMA/DMMA copolymer solutions under stirring conditions in the process of generating a PMPC-PDPA @PEG-*b*-PAMA/DMMA mixture with a stable zeta potential. In a pH changing environment, the PEG-*b*-PAMA/DMMA copolymer could exhibit a negative-to-positive charge conversion. The control sample, the PEG-*b*-PAMA block backbone, could only show has a large positive charge regardless of the pH setting.

Subsequently, zeta potential measurements were used to characterise the resultant PMPC-PDPA @PEG-*b*-PAMA/DMMA polymer mixture solutions, as shown in Figure 3.8. It was shown that compared to the bare PEG-*b*-PAMA/DMMA, which had an initial charge

of around -2 mV from pH 6.5 to 7.5, the addition of positively charged PMPC-PDPA could significantly adjust the overall zeta potential. When 5 mg/mL PMPC-PDPA was added, the charge of PMPC-PDPA @PEG-*b*-PAMA/DMMA had a constant positive charge; 1.38 ± 0.49 mV and 0.18± 0.91 mV, at pH 6.5 and 7.4, respectively (Figure 3.9). It also indicated the success in mixing and coating of positively charged PMPC-PDPA on the surface of PEG-*b*-PAMA/DMMA. When the amount of added PMPC-PDPA was decreased to 1 mg/mL, an increase in overall charge could still be seen, but to a lesser extent. The overall zeta potential increased to -1.62 ± 0.37 mV and -0.95 ± 0.11 mV, at pH 6.5 and 7.4, respectively (Figure 3.9). In general, it revealed that the right amount of PMPC-PDPA coating could help to adjust charge neutral pH into the designed proper range.

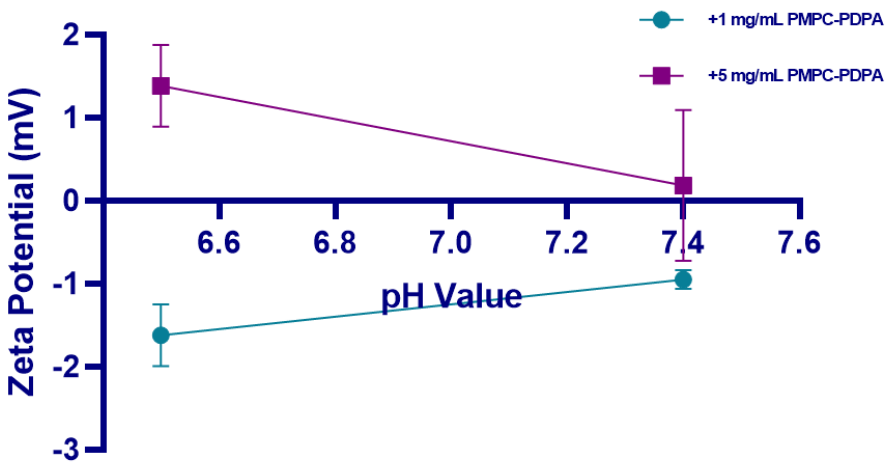

Figure 3.9 Quantified Zeta Potential of 1 mg/mL and 5 mg/mL of PMPC-PDPA mixed with PEG-*b*-PAMA/DMMA under different pH conditions. Data is presented at mean ±SD for each individual candidate binding (n=3).

3.3.3 PMPC-PDPA@PEG-*b*-PAMA/DMMA coating and validation

After successful validation of using different concentrations of PMPC-PDPA to adjust the pH-related charge neutral point for the copolymer, PMPC-PDPA@PEG-*b*-

PAMA/DMMA was treated as a whole copolymer system. TEM was applied to analyse the morphology of pure PMPC-PDPA@PEG-*b*-PAMA/DMMA and copolymer coated nanoparticles (Figure 3.10 & 3.11). The AuNTs were synthesized following the established protocol, and then coated with 1mg/mL PMPC-PDPA@PEG-*b*-PAMA/DMMA. From the TEM images, although both the pure PMPC-PDPA@PEG-*b*-PAMA/DMMA and copolymer coated nanoparticles could be able to self-assemble into spherical structures or spherical coating (Figure 3.10), the pure copolymer micelles did not seem to be stable, independent or clearly homogeneous in size. On the contrary, with the inner structural support provided by the solid nanoparticles, the copolymer coated AuNTs showed a much better uniformity than that of the blank copolymer micelles (Figure 3.11). The copolymer coating (1 mg/mL) did not significantly affect the diameter of the nanoparticles based on the TEM images. Therefore, the TEM results clearly demonstrated that PMPC-PDPA@PEG-*b*-PAMA/DMMA copolymer could encapsulate the nanoparticles.

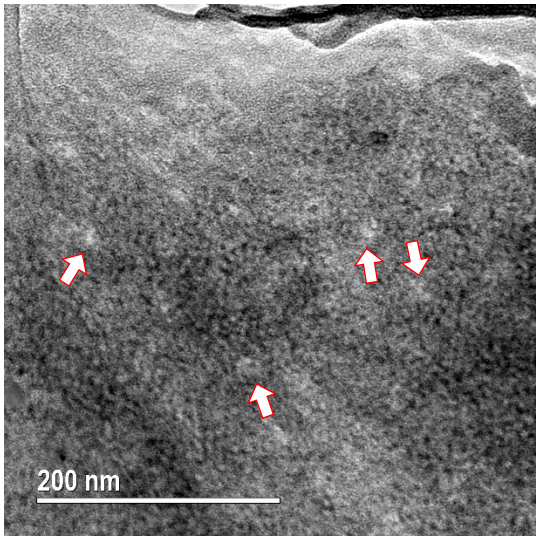

Figure 3.10 PMPC-PDPA@PEG-*b*-PAMA/DMMA copolymer micelles under negative staining (Selected small white spherical structures shown by white arrows, more micelles in this image, average size around 10 nm)**.**

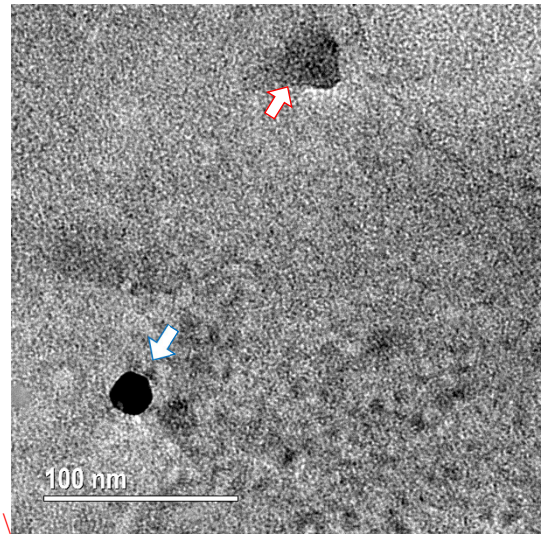

Figure 3.11 TEM Images of PMPC-PDPA@PEG-*b*-PAMA/DMMA copolymer coated AuNTs (upper right, red arrow) compared with uncoated AuNTs (lower left, blue arrow)

3.4 Discussion

3.4.1 Charge conversion with DMMA group

ATRP is a widely used technique in the synthesis of polymers with unique functionalities and structures, and was used here for the synthesis of PEG-*b*-PAMA/DMMA copolymer (Li et al., 2016; Matyjaszewski & Xia, 2001). As a block polymer with hydrophilic PAMA tails, the PEG-*b*-PAMA backbone was not able to self-assemble into micelles. DMMA does not have any of the pH activated functions until it was added into the tail of the PEG-*b*-PAMA backbone. As shown in Figure 3.8, the PEG-*b*-PAMA/DMMA could effectively reverse its potential from positive to negative with increasing pH with the help of the DMMA block compared to the PEG-*b*-PAMA backbone. Through H^1 NMR validation, it could be confirmed that the successful synthesis of PEG-*b*-PAMA copolymer backbone and the linkage of DMMA under the specific synthesis condition (no oxygen, specific temperature etc). However, the current PEG-*b*-PAMA/DMMA reversed potential from positive to negative between pH 2.0 and 3.0 did not fit the requirements for reversal between the pH of normal tissue (pH 7.4) and tumour tissue (pH 6.5) (Figure 3.8).

As an amphiphilic block copolymer, the pH-sensitive block copolymer PMPC-PDPA has both hydrophilic and hydrophobic tails. As previously demonstrated, the pH could effectively change the solubility of PMPC-PDPA (Pegoraro et al., 2013). When the surrounding pH was below 6.4, the amine groups on the copolymer chains were protonated. This led directly to the increase of solubility of the co-hydrophilic polymer features. However, when the pH was greater than 6.4, the tertiary amine groups of PDPA were deprotonated, resulting in the hydrophobicity and insolubility of the whole PMPC-PDPA copolymer. At physiological pH, PDPA can interact with the negatively charged sugar-phosphate backbone of a nucleic acid. As shown here, the PMPC-PDPA@PEG-*b*-

PAMA/DMMA copolymer could also help to cap the DNA based targeting aptamer on the outer surface of the nanosystem with high efficiency (Lomas et al., 2010).

3.4.2 PMPC-PDPA adjustment of whole copolymer system

The commercially available pH-activated polymer PMPC-PDPA, which has a constant positive charge in all pH, was used to modify the PEG-*b*-PAMA/DMMA copolymer system. Two different concentrations were assessed (1mg/mL and 5mg/mL) and showed different content of charge reversing which was directly correlated with the amount of mixed PMPC-PDPA. Data showed that adding 1 mg/mL PMPC-PDPA was not enough to fully reverse the zeta potential in the 6.5 to 7.4 range to be positive. Conversely, the 5 mg/mL addition could successfully help the co-polymer to meet the designed aim with a positive charge at acidic tumour pH while remaining neutral or negative within the normal body environment. The charge convertible functionality enables a very important feature of the whole nanosystem: it could keep the nanosystem outer layer charge constantly negative which could significantly reduce the possibility of off-target accumulation by normal cells. It would also prolong circulation due to the strong electrostatic repulsion with the negatively-charged cell membrane or blood serum proteins (Zhang et al., 2022). The reduced probability of forming a serum protein corona could also limit the possibility of being cleared by the reticuloendothelial system (RES) (Li et al., 2016; Zhang et al., 2022).

Furthermore, the PMPC-PDPA@PEG-*b*-PAMA/DMMA copolymer could self-assemble into small micelles or easily coat the nanoparticles with its amphiphilic functionality which was supported by the hydrophilic PAMA and hydrophobic PDPA. Even after long time of sample preparation and storage at room temperature, clear indication of micelles and stable coatings around the nanoparticles showed that the great

and stable functionality of the synthesized co-polymer working as a carrier from the TEM results (Figure 3.10 & 3.11).

3.4.3 Issues concerning PMPC-PDPA

Despite the excellent functionality the co-polymer has shown, some problems still remain with the selected PMPC-PDPA. As a widely applied pH activated release polymer that was also commercially available, PMPC-PDPA was selected to adjust the pH charge neutral point for the co-polymer system. However, some issues remained especially around the cargo-releasing of the PMPC-PDPA polymer. Previous research has found that the release profile of PMPC-PDPA was fully-dependent to the pH. When the pH was at 6.4 which was common for most tumour environments, it would normally take 10 hours to release less than 10 % of the cargo which was too slow for the design (Gouveia et al., 2019). During the synthesis and testing steps within the experiments, it has also been noticed that the PMPC-PDPA was unexpectedly stable within the acidic environment. However, the PMPC-PDPA part could be easily upgraded and replaced with a similar positive-charged polymer that has a better release profile, which also facilitated the design and function of our current nanosystem.

3.5 Conclusion

In conclusion, the pH-activated PMPC-PDPA@PEG-*b*-PAMA/DMMA copolymer layer, which has both charge conversion and hydrophilic-hydrophobic reversion functionalities, was successfully synthesized and evaluated. As validated within this study and previous research, the PEG-*b*-PAMA/DMMA could convert its surface charge from negative to positive accordingly to the decrease in environmental pH. Through mixing with the right amount of positively charged PMPC-PDPA, the copolymer

remained neutral or negatively charged under a normal environment (pH 7.4) which helps to avoid the quick clearance and non-specific binding, and conversion to a positive charge in the tumour microenvironment (pH 6.8) which enables enhanced tissue accumulation and cellular uptake. The following validation with TEM results around the bare micelles and nanoparticles' coating further confirmed the copolymer has the potential to self-assemble into nanomicelles or coat the nanoparticles without massively changing its size. The copolymer layer formed a very important construct of the whole designed nanosystem, which could protect the coated therapy core and enhance the delivery efficiency at the same time.

In summary, the PMPC-PDPA@PEG-*b*-PAMA/DMMA copolymer layer has been successfully synthesized and evaluated. It was constructed into the nanosystem to coat the nanoparticle-based therapy core and linked with the selected DNA aptamers. The NIR dye-loaded siRNA-linked therapy core is detailed and discussed in Chapter 4 and 5.

Chapter 4

Nanoparticle-based NIR Non-Invasive Reporting System

Nanoparticles could help to deliver, protect, target, and enhance penetration. The addition of NIR dyes to nanosystem which delivers the therapeutic reagent can enable monitoring of uptake and accumulation during treatment non-invasively. Two types of nanoparticles based on silica and gold were synthesized. The MSNPs were loaded with IR820 dye, and the delivery efficacy was evaluated using spheroid models. In this chapter, the IR820-loaded MSNPs were analysed from the perspectives of cellular uptake, degree of accumulation, and penetration depth to evaluate the NIR imaging function of the synthesized nanosystem.

4.1 Introduction

4.1.1 Nanoparticle core

Delivery of a drug to the right location is crucial for effective cancer treatment. However, many obstacles may prevent sufficient amount of therapeutic molecules to accumulate in a tumour. These include non-specific binding with serum proteins, immune system clearance, and kidney filtration (Kim et al., 2016; Tatiparti et al., 2017). Moreover, negatively charged molecules or drugs, such as siRNA or mRNA, are not able to passively diffuse through cellular membranes into the cytoplasm (Wang et al., 2010). In addition, off-target effects may significantly increase the possibility of severe side effects due to the unspecific uptake of normal cells.

Nanoparticles made of a variety of materials have been assessed for the effective protection and delivery of cancer therapeutic agents, including inorganic (e.g. silica (Ma et al., 2010), iron oxide (Stanley et al., 2012), carbon (Ray et al., 2009)) and organic materials (e.g. liposomes (Feng et al., 2017)) (Du et al., 2014; Kim et al., 2016; Wang et al., 2010). Nanoparticles can passively accumulate in a tumour area *via* the enhanced permeability and retention (EPR) effect (Torchilin, 2011). This couples fenestrations in the blood vessel endothelial cells in the tumour tissues with inadequate lymphatic drainage. Nanoparticle delivery of therapeutic molecules could significantly decrease the possibility of being cleared by the immune system, and reduces off-target effects compared with a traditional retrovirus system or bare siRNA (Kim et al., 2016). In addition to passive accumulation in the tumour, active targeting of nanoparticles could be achieved through grafting targeting molecules onto the surface, such as antibodies (Liu et al., 1998), peptides (Pan et al., 2012), or aptamers (Sivakumar et al., 2018).

In this study, thiol functionalized mesoporous silica nanoparticles (SH-MSNPs) and gold nanotriangles (AuNTs) were synthesized. Silica nanoparticles have been widely used in

various biomedical studies with well-established methods for controlling the size, shape and morphology (Slowing et al., 2008). In addition to the useful functionalities of silica nanoparticles, gold nanoparticles (AuNPs) have also been found to have unique optical functionality, excellent biocompability, and anti-infectious and anti-inflammatory properties (Yeo et al., 2018). Moreover, AuNTs have also been validated with the highest cell uptake rate among all different shapes of AuNPs (Xie et al., 2017).

4.1.2 IR820 dye – nanoparticle conjugation as a NIR reporting system

The wavelength range from 900 to 1700 nm is commonly defined as the second near-infrared spectral region (NIR-II). Compared with the traditional NIR-I which ranges from 780 to 900 nm, the NIR-II range is more suitable for non-invasive biomedical sensing due to decreased tissue scattering, better imaging resolution and penetration depth (Feng et al., 2019; Qiu et al., 2018). Decreased tissue scattering could also prevent the issue of low signal-to-noise ratio due to the high tissue background noise (Feng et al., 2019). The addition of a NIR dye to the nanoparticle would enable tracking both *in vitro* and *in vivo* through penetration across the skin and centimetre depth, within a transparency window so that blood does not interfere with the signal. (Xia et al., 2016)

As one of the most widely applied NIR dyes which have superb biocompability and the analog and better alternative of the only Food and Drug Administration (FDA) approved NIR dye indocyanine green (ICG), IR820 is a small molecule NIR dye that covers both the NIR-I and NIR-II with a broad emission range from 700-1300 nm. Moreover, it allows high penetration depth NIR signalling, and could also be potentially used for photothermal and photodynamic therapy (Xia et al., 2016). In addition, it has also been discovered that encapsulation with the nanoparticles could further enhance the biocompatibility and stability of the IR820 dye (Xia et al., 2016).

Therefore, in this chapter, different classes of nanoparticles have been successfully synthesized, characterised and evaluated.

4.2 Methods

4.2.1 Cell lines & Tissue Culture

The cell lines were prepared and cultured following the methods described in Chapter 2.2.1 and 2.2.2.

4.2.2 Synthesis of thiol functionalized MSNPs (SH-MSNPs)

The SH-MSNP synthesis method was modified and optimized from a published protocol (Pan et al., 2012). Hexadecyltrimethylammonium Chloride (2g; CTAC) [Sigma- Aldrich, Poole, UK] and Triethylamine (0.06g; TEA) [Sigma- Aldrich, Poole, UK] were dissolved and added into 20 mL of 95°C distilled water under intensive stirring. After 1h of stirring, Tetraethyl orthosilicate (1.5 mL; TEOS) [Sigma- Aldrich, Poole, UK] was added dropwise into the mixture. After a further 1h, 200 µL of a 1:1 mixture of TEOS and 3-mercaptopropyl triethoxysilane (MPTES) [Sigma- Aldrich, Poole, UK] was added into the reaction. The synthesized nanoparticles were collected by high-speed centrifugation and washed with 99 % ethanol three times. The obtained SH-MSNPs were vacuum dried and stored at room temperature.

4.2.3 Synthesis of Gold Nanotriangles (AuNTs)

Gold nano-seeds were prepared by adding 25 µL of 0.05 M $HAuCl_4$ solution into 4.7 mL of 0.1M CTAC solution under intensive staining at 600 rpm. 300 µL of freshly made 0.01M $NaBH_4$ solution was added directly into the mixture. The reaction mixture was kept stirring for more than 2 h at room temperature for consuming the excess of borohydride.

For preparation of the gold nanotriangles, two solutions were pre-made before the synthesis:

Solution A: 1.6 mL of 0.1 M CTAC, 40 μL of 0.05 M $HAuCl_4$, and 15 μL of 0.01 M NaI solution were mixed in 8 mL of distilled water. 40 μL of 0.1 M acetic acid (AA) solution was added immediately before use.

Solution B: 500 μL of 0.05 M $HAuCl_4$ solution and 300 μL of 0.01 M NaI solution was mixed in 40 mL of distilled water. 400 μL of 0.1 M AA solution was added right before use.

100 μL of 10x diluted synthesized gold nano-seeds was added into the solution A. After a briefly stirring for less than 10 sec, 3.2 mL of reaction solution A was immediately transferred into solution B. The reaction of solution B was kept in an anaerobic environment overnight for the growing of nanotriangles. The synthesized gold nanotriangles were obtained by freeze-dry and stored at -20°C.

4.2.4 Nanoparticles Characterization

For the preparation of specimens for transmission electron microscopy (TEM), the synthesized SH-MSNPs or AuNTs were dispersed in ethanol and dropped onto holey carbon-coated TEM grids [Agar Scientific, Stansted, UK] until fully dried. A JEOL-2100 TEM [JEOL, Tokyo, Japan] was used for TEM imaging, operating at 200kV. Gatan 3 microscopy suite software [Gatan, Inc., CA, US] was used for TEM image analysis.

Dynamic Light Scattering (DLS) and particle surface ζ (zeta) potential was measured with a Zetasizer Nano ZS90 [Malvern Panalytical, Malvern UK]. The SH-MSNPs were suspended in 1 x PBS buffer (pH=7.4) prior to the measurement to quantify the surface charge for particles in a colloidal suspension. For calculating electrophoretic mobility, zeta potential, and zeta potential distribution, 100 runs were read for every sample.

Thermogravimetric analysis (TGA) [Perkin Elmer TGA7, US] was used to analyse

nanoparticles from 110°C to 800°C at a rate of 10°C per minute under a nitrogen atmosphere.

For validation of surface thiol bonds, the Raman spectra of SH-MSNPs were read using a confocal Horiba Jobin-Yvon Raman microscope [Horiba, Glasgow, UK] equipped with a 532-nm neodymium-yttrium aluminium garnet laser. The laser power on samples was 12 mW after attenuation by neutral density filters.

4.2.5 IR820 NPs Loading in siRNA-linked MSNPs

To load NIR dye IR820 [Sigma- Aldrich, Poole, UK] into the siRNA-linked MSNPs, 200 μL of IR820 stock solution (84.90 mg/mL) was prepared by dissolving IR820 in DMSO. The stock solution was then diluted 1000 times with RNase free water. Diluted IR820 solution (4mL) was then mixed with siRNA-linked MSNPs (Full description in Chapter 5) with shaking at room temperature for 24 h in a dark environment. The particles were washed with RNase free water and collected by ultrahigh-speed centrifugation (20,000 rpm, 10 min); this was repeated several times until all impurities were essentially removed. The final product (IR820-loaded siRNA-MSNPs) was stored in RNase free PBS buffer at 4 °C.

4.2.6 3D Spheroid Generation and treatment

The 3D RMS spheroids were grown on 1 % (w/v) agarose-coated 96-well plate. To prepare the plate, powder form low electroendosmotic (EEO) agarose [Sigma Aldrich, Poole, UK] was fully dissolved in 1xPBS with very mild heating until the formation of a clear solution [Sigma Aldrich, Poole, UK]. Warm agarose solution (100 μL) was carefully added to a flat-bottom 96-well plate ensuring that no bubbles were present. The plate was left to dry, and sterilized under UV for 2 h at room temperature. A flat solid agarose layer could be seen to form in the well after this step. RMS cells from culture were washed with DMEM

medium and seeded at a density of 100,000 cells per well onto the agarose-coated plate without hurting the agarose layer. The plate was then cultured at 37 °C with 5 % CO_2 in a tissue culture incubator for 4 days. The growth of the spheroids was monitored every day, and after 4 days they were transferred into a normal 96 well plate for experiments.

The RMS spheroids were incubated for 72 h with either (i) PBS, (ii) the same concentration of free IR820 NIR dye, or (iii) IR820-loaded siRNA-linked MSNPs.

4.2.7 Flow cytometry for IR820 delivery evaluation

In order to validate the IR820 NIR signal penetration rate, RH30 cell spheroids were prepared before incubation for 24h with either (i) PBS, (ii) the same concentration of free IR820 NIR dye, or (iii) IR820-loaded siRNA-linked MSNPs.

Likewise, for comparing the penetration speed the same experiment was performed over a periods of 0~24 hours.

Similar to the apoptosis/necrosis assay, the treated RH30 spheroids were collected and dissociated into single cells by trypsin treatment and centrifugation. The cells were then washed three times with 500 µL of cold 1 x PBS to remove any non-specific binding dye or particles. All the collected cells were fixed with a 4 % (v/v) PFA solution [Bio-rad, Watford, UK] prior to the next step of flow cytometry analysis. Flow cytometry was performed using a BD FACS Calibur and evaluated in the FL4-H channel. The amount of IR820 signal was quantified by normalized median fluorescence intensity. The entire procedure was carried out on ice in darkness. The experiment was repeated in duplicate on three separate occasions.

4.2.8 Confocal imaging of IR820 cell penetration delivered with MSNPs

Cells were seeded at a density of $1x10^5$ cells per well in complete DMEM medium which was pre-added with 2 mM L-glutamine [Gibco, Life Technologies Ltd, Renfrew, UK],

penicillin (100 U/mL) and streptomycin (100 g/mL) [Gibco, Life Technologies Ltd, Renfrew, UK] and 10 % (v/v) Fetal Bovine Serum (FBS) [Sigma Aldrich, Poole, UK], in glass-bottom imaging petri dishes [ibidi GmbH, Germany] and allowed to adhere to the surface for 24 hours in a 37 ºC tissue culture incubator. RH30 sarcoma cells were incubated overnight with the same concentration of either free IR820 or IR820-loaded siRNA-linked MSNPs, respectively. The cells were washed three times with cold PBS after incubation to remove any non-specific binding. The entire procedure was carried out in complete darkness. Before imaging, the cells were maintained in warm PBS and stained for 15 minutes with 0.1 g/mL DAPI [Thermofisher Scientific, Renfrew, UK] and 1:200 diluted CellBriteTM Green Cytoplasmic Membrane Dye [Biotium, CA, US]. All samples were then fixed with a 4 % (v/v) PFA solution. A Leica SP8 confocal microscope was used for imaging. [Leica Biosystems, Germany]

4.2.9 Statistics and reproducibility

All statistical analysis of experimental data was performed using Microsoft™ Excel [Microsoft, NM, US]. GraphPad Prism 8.0.2 [GraphPad Prism, La Jolla, CA, US] was used for graph plotting. Error bars in the experiments indicate standard deviation (SD). The difference was considered significant and shown when the p values were less than 0.05. The figure legends included information on the number of events and independent experiments, as well as statistical data and methodologies.

4.2.10 Other software

FlowJo VX [FlowJo, LLC, OR, US] was used to analyse and compare flow cytometry data. For all confocal image analysis and measurement, the Leica Application Suite X (LAS X) was employed.

4.3 Results

4.3.1 Thiol-Functionalized Mesoporous Silica Nanoparticles (SH-MSNPs)

Nanoparticles based on mesoporous silica were synthesized as the core of the system. The surface of the nanoparticles was functionalized with thiol bonds for attachment and targeted release of the siRNA (Pan et al., 2012). The diameter of these SH-MSNPs was monitored by multiple methods. The hydrodynamic diameter was determined to be 73.57± 17.12 nm by dynamic light scattering (DLS) (Figure S8). TEM images of the SH-MSNPs indicated a spherical shape with a mesoporous surface. The diameters of irregular mesopores on the surface appeared to be around 1-2 nm by randomly measuring 100 mesopores from the TEM image (Figure 4.1A). Furthermore, a very thin 1 nm surface layer was observed on the SH-MSNPs which could be considered as evidence of a thiol bond layer (Figure 4.1A). The average diameter was calculated as 42.59 ± 4.24 nm through randomly counting 100 nanoparticles from images. All measured diameters were grouped, and Gaussian fitted and all particle diameters were well distributed in a very narrow range and the mean value was 42.11± 4.12 nm. This showed a uniform distribution of particle diameter (Figure 4.1B). In a neutral pH, the surface potential of SH-MSNPs was determined to be -23.3 ± 7.50 mV (Figure S9). The strong surface potential could keep the nanoparticles moderately stable in an aqueous environment.

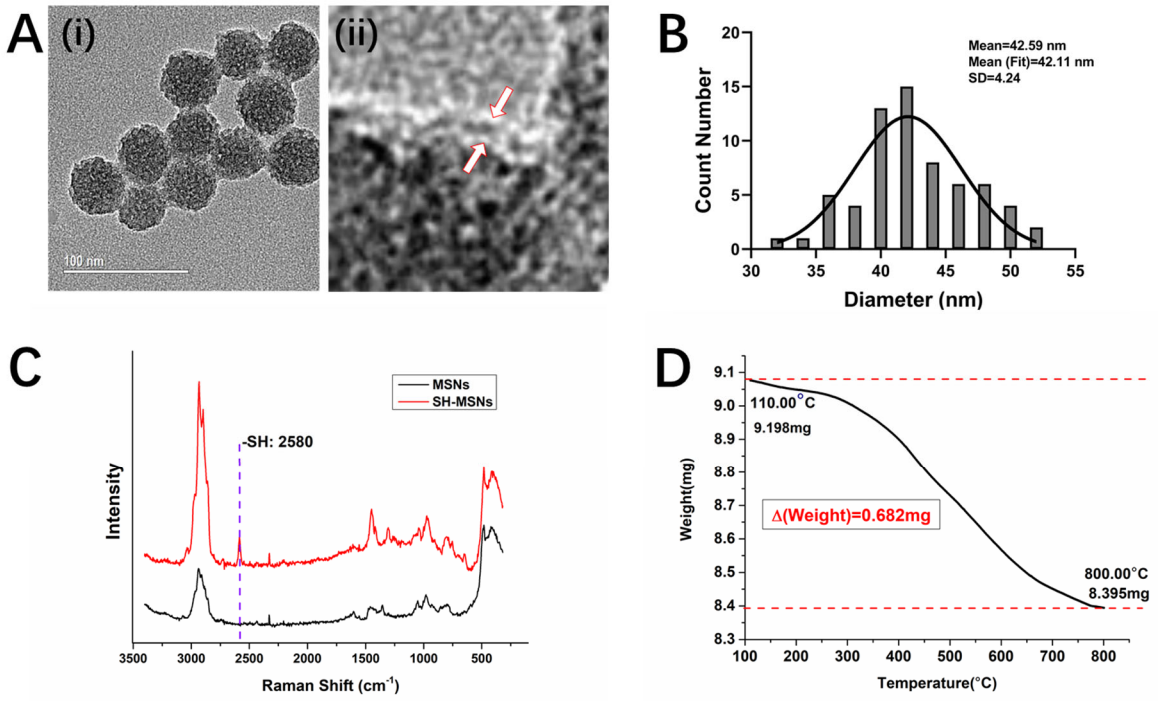

Figure 4.1 Characterization of Synthesized SH-MSNPs and Thiol Bonds on the Particle Surface

A: TEM images of (i) synthesized 50 nm SH-MSNPs, (ii) Enlarged surface thiol bond layer of SH-MSNPs (layer indicated by arrows). B: Gaussian Distribution of SH-MSNPs Diameter Measured from the TEM images. C: Thiol bond was detected using Raman Spectroscopy. A unique 2580 cm^{-1} peak was shown in SH-MSNPs, but not in MSNPs. D: The amount of functionalized thiol bond was quantified using TGA from 110 °C to 800 °C in nitrogen environment.

Raman Spectroscopy was used to compare the synthesized SH-MSNPs with bare MSNPs for further validation of the surface thiol bonds. SH-MSNPs showed a very strong peak at 2580 cm^{-1} which was absent from bare MSNPs. This peak is a fingerprint peak for the thiol group (Sokolova & Epple, 2008). Moreover, the thiol bond was linked to the silica network through $–CH_2-CH_2-CH_2-SH$. Raman fingerprints of —C at 1305 cm^{-1} and C—S at 653 cm^{-1} were also observed from the comparison (Figure 4.1C) (Xiong et al., 2018). Subsequently, the surface thiol groups were quantified by Thermal Gravimetric Analysis (TGA). From the weight decrease, the amount of thiol groups on the surface was calculated as 0.065 mol per 1 mol SH-MSNPs. This amount would dictate the amount of siRNA the particle could carry (Figure 4.1D).

4.3.2 Gold NanoTriangles (AuNTs)

In addition to the mesoporous silica nanoparticles, gold nanotriangles were also synthesized due to the intrinsic thiol bonds on surface which could be useful for further surface functionalization (Scarabelli et al., 2014). The diameter of the synthesized gold nanotriangles was also monitored through multiple methods, such as CPS disk centrifuge and ZetaSizer. The hydrodynamic diameter of Au NTs were measured as 28.3 ± 7.25 nm from CPS (Figure S10) and 33.48 ± 1.8 nm from DLS (Figure S11). TEM images were obtained for confirmation of the diameter and morphology of the AuNTs. It could be observed that the AuNTs were equilateral triangle shaped with a smooth surface (Figure 4.2A). After measuring 155 Au NTs from the obtained TEM images, the average width was measured as 26.21 ± 3.13 nm (Figure 4.2A). The Gaussian fitting was applied for all measured width. The fitted average diameter of width was 26.10 ± 2.25 nm which was almost the same as the measured width and the R-square value was 0.97 which indicated a very uniform diameter distribution (Figure 4.2B).

The surface potential of the Au NTs was opposite from that of SH-MSNPs in that the AuNTs had very strong positive surface charge of 44.3 ± 1.35 mV. It was also worth noting that the surface charge mainly came from the surfactant remaining on the surface of the AuNTs which prevented the NTs from aggregating.

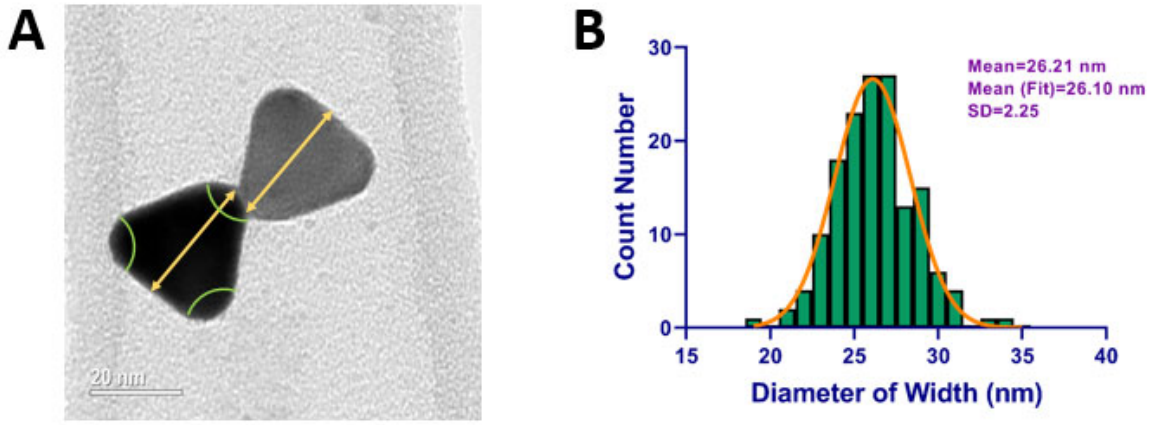

Figure 4.2 Characterization of Synthesized AuNTs

A: TEM image of two 26 nm Au NTs. B: Gaussian Distribution of Au NTs Diameter Measured from the TEM images

4.3.3 Cellular Uptake of IR820-loaded MSNPs Evaluation with Flow Cytometry

IR820 NIR dye was loaded into the siRNA-MSNPs prior to incubation with RH30 spheroids. The cellular uptake of IR820 was monitored using flow cytometry on dissociated cells from spheroids after 24 h of incubation. The IR820-loaded siRNA-MSNPs group showed a significant peak shift, indicating a much higher amount of dye per cell compared to incubation with free IR820 dye (Figure 4.3A(i)). The IR820 content was then quantified with the Median Fluorescence Intensity (MFI) data from flow cytometry. As it was shown in Figure 4.3A(ii), the MFI only reached 572 ± 39.42 with the free IR820 penetration. However, the IR820-loaded siRNA-MSNPs group showed an over two-fold increase with MFI levels reaching 1194 ± 33.54 after 24 h incubation.

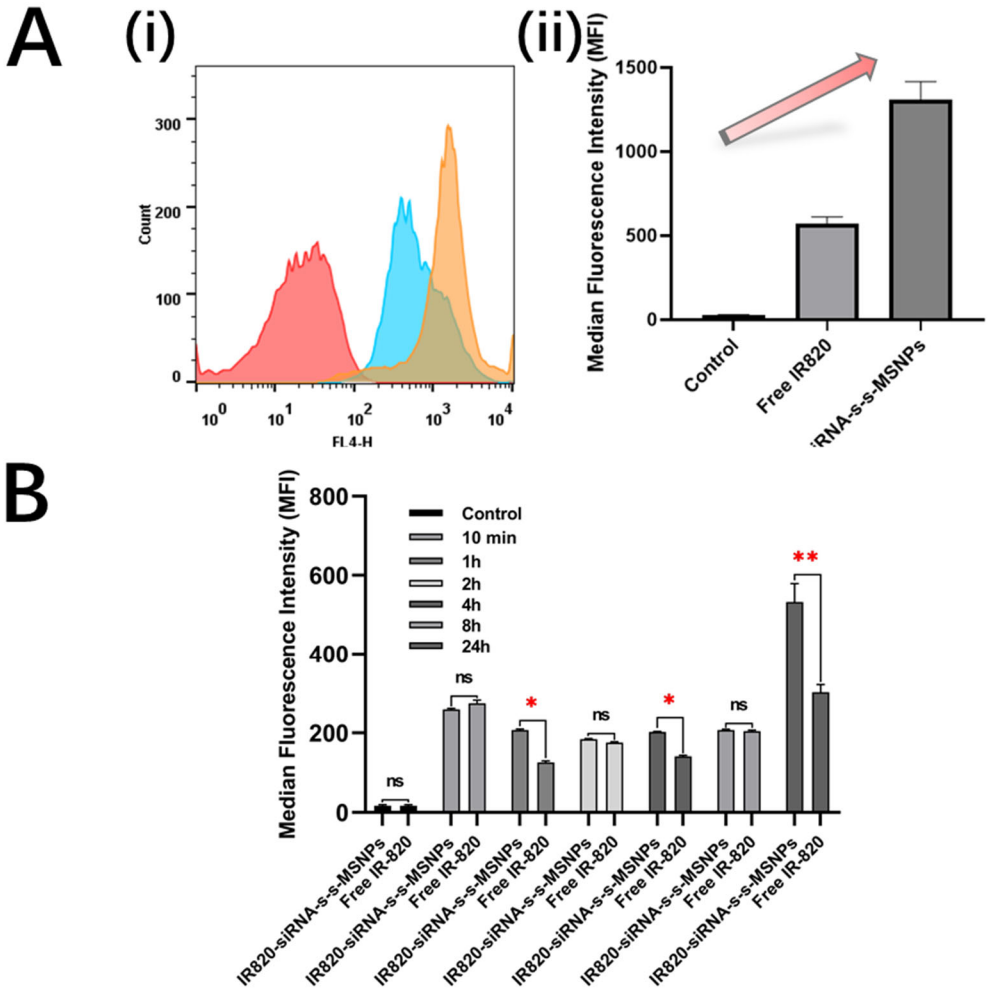

Figure 4.3 Evaluation of IR820 NIR signal penetration rate in RH30 sarcoma spheroids measured by flow cytometry

A: (i) Representative flow cytometry histogram of single cells from breaking RH30 sarcoma spheroids. Cells were incubated with either PBS (Red), free IR820 NIR dye(Blue), or IR820 NIR dye-loaded siRNA-linked MSNPs (Orange) for 24h. (ii) Results from the normalized median fluorescence intensity of flow cytometry of single cells from breaking RH30 sarcoma spheroids. Cells were incubated with either PBS, free IR820 NIR dye, or IR820 NIR dye-loaded siRNA-linked MSNPs for 24h . Data is presented as mean±SD for each individual cell line (n=3 independent triplicate experiments). B: Results from the normalized median fluorescence intensity of flow cytometry of single cells from breaking RH30 sarcoma spheroids. Cells were incubated with either free IR820 NIR dye, or IR820 NIR dye-loaded siRNA-s-s-MSNPs for different period of times ranging from 0~24h. Data is presented as mean±SD for each individual cell line (n=3 independent triplicate experiments). Significance was tested using a two tailed t-test compared to the cells with only buffers for each cell line (ns: not significant, *P≤0.05, **P≤0.01)

To further investigate the penetration and uptake speed within RH30 spheroids, time-dependent intracellular MFI was monitored from 10 min to 24 h. It was found that the signal was higher in IR820-loaded siRNA-MSNPs groups after 1 h and 4 h of incubation

compared to free IR820 groups. However, this trend wasn't constant enough for all groups under 8 h. It could be noticed that for the 10 min, 2 h, and 8 h incubation groups, the difference between free IR820 group and IR820-loaded siRNA-linked MSNPs group was statistically insignificant. Thus, a 24 h group was set up which was considered long enough for all free IR820 or IR820-loaded siRNA-MSNPs to reach deep penetration within the spheroids structure. It was observed that the MFI of IR820-loaded siRNA-MSNPs incubation was significantly higher than free IR820, with 532 ± 47 compared with 302 ± 20, respectively (Figure 4.3B).

4.3.4 Cellular Uptake of IR820-loaded MSNPs Evaluation with Confocal Microscopy

Cellular localization of siRNA-IR820-MSNPs was investigated using confocal microscopy. CellBrite™ green cytoplasmic membrane staining and DAPI nucleus staining indicated that the IR820 signal was present in the cytoplasm, but outside the nucleus. The sensor of confocal microscopy wasn't as sensitive as the flow cytometry which required higher amount of IR820 intracellular to show visible signals. From the images, it could be seen that the unbound IR820 group didn't show any signal after overnight incubation under the confocal microscope, which indicated relatively low delivery or penetration efficiency (Figure 4.4A). Nevertheless, the IR820-loaded siRNA-linked MSNPs group showed significantly visible signals in the IR820 channel under the confocal microscope, which indicated that the MSNPs could deliver a significantly higher amount of IR820 into the cells with a very limited concentration of nanoparticles applied for the spheroids incubation (Figure 4.4B). This result also corresponded to the flow cytometry result which the IR820-loaded siRNA-linked MSNPs group delivered a significant higher average amount of IR820 into cells than the free IR820 group (Figure 4.3).

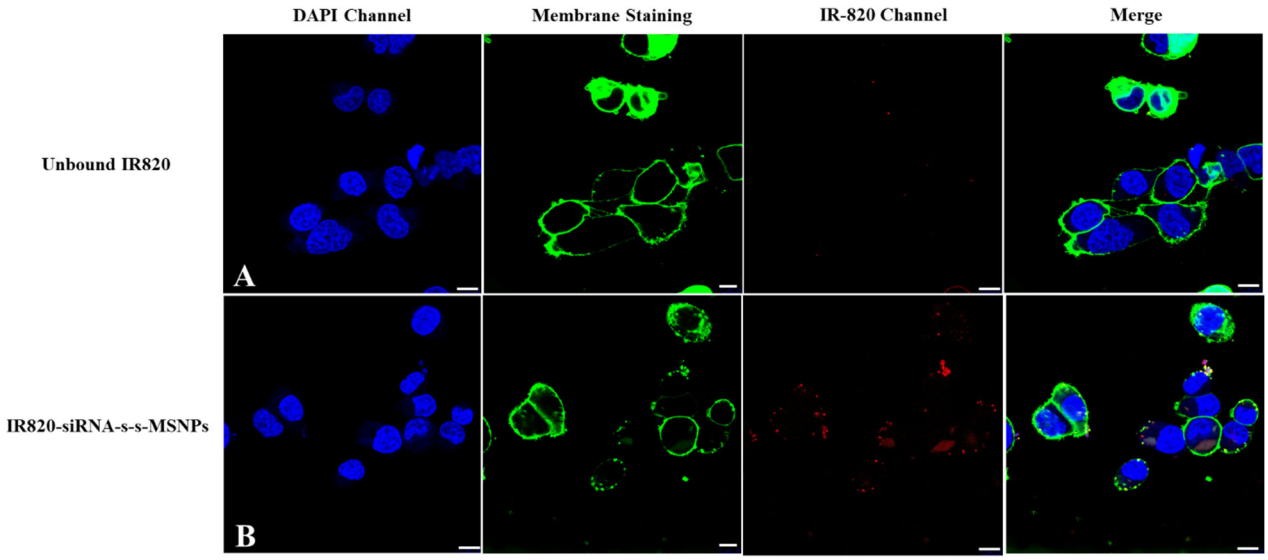

Figure 4.4 Fluorescence confocal imaging of efficient IR820 cell penetration delivered with MSNPs comparing to unbound staining.

The RH30 sarcoma cells were incubated overnight with A: Unbound IR820; B: IR820-loaded siRNA-linked MSNPs. The cells were then thoroughly washed and fixed with 4 % PFA. Scale bar, 10 μm.

4.4 Discussion

4.4.1 MSNPs can enhance the penetration of the loaded IR820 dye into 3D spheroids

Our system combined IR820 NIR signalling with MSNPs-delivered siRNA for knockdown. To our knowledge, there have been no similar studies in RMS cells. The loading of amphiphilic IR820 dye has been validated by other studies (Lei et al., 2014; Thapa et al., 2017), and could be effectively loaded into MSNPs with a relatively good capacity of 10.0 ± 0.8 % through hydrophobic–hydrophobic interactions (Thapa et al., 2017). Furthermore, it has also been shown that MSNPs could enhance the stability and energy conversion efficiency of loaded IR820 (Lei et al., 2014; Thapa et al., 2017). In our study, the amount of delivered IR820 was compared with free IR820. In contrast to the free dye which relies on passive diffusion, the endocytosis of MSNPs could greatly

improve the uptake of loaded IR820 (Tang et al., 2012). Moreover, the significant enhancement of penetration ability by the nanosystem was further revealed through the 3D spheroids model which has a much more complex structure and a concentration gradient from outside to inside (Figure 4.3B). The enhancement of penetration ability was validated by the clear peak shift and over a two-fold increase of MFI from flow cytometry experiments (Figure 4.3A). The penetration depth enhancement was further confirmed with the confocal images which showed signals with clear and stable IR820 signal for IR820-loaded siRNA-linked MSNPs group. The uptaken IR820 was kept within the endosomes. On the contrary, the free IR820 group showed no signal at all due to low uptake and diffusion out of the cells after fixation (Figure 4.4). For the time-dependent uptake evaluation with RH30 sarcoma spheroids, the trend between free IR820 and loaded IR820 was not clear for the first few hours. However, the ultimate significant MFI difference after 24 h demonstrated a deeper penetration assisted by MSNPs.

4.4.2 The nanoparticles core could be replaced or further functionalised

The SH-MSNPs surface will be further functionalized to reverse the surface potential to positive, e.g. through the incorporation of amino groups (amino functionalisation) (Pan et al., 2012). Moreover, SH-MSNPs are not the only option for the nanoparticle core. Indeed, as an alternative, AuNTs were synthesized and characterised as one of the candidates to act as the nanoparticle core for the designed nanosystem. As introduced before, AuNPs have several advantages, such as excellent biocompability, optical functionalities (photothermal and photodynamic functionalities), anti-infectious against bacteria and anti-inflammatory properties (Yeo et al., 2018). Furthermore, the reasons why the triangle shape were trialled were that: A(1) Triangle gold nanoparticles have been proven as the shape of AuNPs with the highest cell uptake rate (Xie et al., 2017), and (2) The edge of

the AuNTs has the potential to be applied for Surface Enhanced Raman Spectroscopy (SERS) which has now been widely used in the diagnostic field (Alvarez-Puebla & Liz-Marzán, 2010; Moisoiu et al., 2021). However, during this study it was found that the AuNTs which were synthesised could be oxidized very quickly. As some of the functionality, such as AuNTs need to keep a specific morphology for an enhanced uptake rate or SERS study, the rapid oxidation would directly affect the further development of the AuNTs within our design. It was therefore decided not to proceed with these nanoparticles.

4.5 Conclusion

In conclusion, MSNPs and AuNTs have been successfully synthesised. Both silica and gold-based nanoparticles were characterised from the perspectives of size, surface potential, morphology and other functionalities such as their surface pore sizes, quantification of surface bonds and so on. Gold materials have a great potential for future applications. However, they also showed to be easily oxidized, thus changing their morphology. With good encapsulation functionality due to the surface mesopores, the IR820 dye was easily loaded into synthesized MSNPs. Considering the total design of the nanosystem which considered siRNA linkage, the MSNPs were functionalized with surface thiol bonds during their synthesis. Dye loaded into particles showed a better uptake rate, accumulation, and penetration depth in cells compared with unloaded free dye, from flow cytometry and confocal imaging results. IR820 NIR monitoring could provide another route for tackling aRMS in a more efficient and non-invasive way. In Chapter 5, the successful combination of siRNA onto the conjugate, and the validation of the whole theranostic system as a whole will be discussed.

Chapter 5

Identification of siRNA for RMS treatment, and Validation of the Whole Constructed Nanosystem

Metastatic alveolar rhabdomyosarcoma (aRMS) is an aggressive paediatric cancer with a poor prognosis. Downregulation of critical tumour genes using targeted siRNA has the potential to improve patient outcomes. However, the delivery of siRNA remains an obstacle, and association with nanoparticles could help to deliver, protect, target, and enhance penetration. In this study, two siRNA targeting options were selected and validated: (i) Human αB-crystallin (CRYAB) & Heat Shock Protein Family B (Small) Member 2 (HSPB2), and (ii) Keratin 17 (KRT17). A mesoporous silica nanoparticle was loaded with IR820 dye and linked to the siRNA *via* disulfide bonds. The system was characterised and evaluated for transfection efficiency and knockdown. In addition, the metabolic effects and cell proliferation were monitored in 2D

culture and also in 3D spheroid models. The nanoparticles were found to maintain a strong bond with the siRNA molecules, and showed a high degree of protection, preventing degradation with RNase I during a 24 h incubation. The siRNA was effectively delivered and transfected into the aRMS cells by the nanoparticles with a significant suppression of viability; 53.21 ± 23.40 % for CRYAB & HSPB2 siRNA, and 88.06 ± 17.28 % for KRT17 siRNA. The cause of cellular proliferation suppression was discovered with over 50 % cell apoptosis and necrosis within the RH30 spheroids after 72 h. Total GSH levels within RD and RH30 cells were found to be 5.08 and 9.28 times higher than that of fibroblast cells. Since the selected siRNAs were bound onto the MSNPs surface with disulfide bonds which could be specifically cleaved by GSH, this was a good indicator that stimuli-activation could be used for specifically releasing the siRNA into the RMS cells. Furthermore, the PE-labelled aptamer (Sequence Selected from Chapter 2) was shown to firmly bind to the polymer layer on the surface of the nanoparticles. Therefore, a combined system of copolymer coated MSNPs with RMS targeting aptamers, specific siRNA treatment, and IR820 NIR monitoring was developed. This may help to pave the way for less invasive and more effective treatment of aRMS.

5.1 Introduction

5.1.1 Rhabdomyosarcoma

As one of the most common and aggressive paediatric cancers, Rhabdomyosarcoma (RMS) is believed to originate from skeletal muscle cells. There are two identified histological forms of RMS: embryonic RMS (eRMS) and alveolar RMS (aRMS) (Koscielniak et al., 1992). It has been shown that aRMS is more metastatic than the eRMS subtype, which normally leads to a poor prognosis (Marshall & Grosveld, 2012). Currently, most patients are treated with standard chemotherapy, radiotherapy, surgery or combinations. These aggressive treatments normally lead to unavoidable life-long side effects, which is particularly poignant in paediatric patients. Combined with the lack of early diagnostic methods which leads to advanced metastasis, aRMS has a very low survival rate of less than 30 % (Huang & Townley, 2016).

5.1.2 siRNA and delivery

The discovery of siRNA technologies has been hailed as having great potential for improved oncology treatment. Two sets of targets for the effective gene knockout in aRMS cells were assessed (i) Human αB-crystallin (CRYAB) & Heat Shock Protein Family B (Small) Member 2 (HSPB2), and (ii) Keratin 17 (KRT17). Both genes were found to be significantly upregulated in aRMS compared to eRMS or normal cells (Rapa et al., 2012). CRYAB & HSPB2 are closely linked and co-regulated by p53 (Tan et al., 2019). Furthermore, CRYAB overexpression has been shown to be tightly associated with the migration and invasion of gastric cancer cells (Chen et al., 2018). Double knockout (DKO) of CRYAB and HSPB2, has been shown to lead to cell apoptosis and necrosis. This was due to a decrease in ATP production-related calcium-dependent respiration and metabolism, and a reduction in superoxide production (Benjamin et al., 2007). KRT17, a

type I keratin, was first found to relate to the growth of the human epithelium (Yang et al., 2019). It has also been found to facilitate the development of cancers of the skin (Depianto et al., 2010), colon and breast (Li et al., 2020). Knockout of KRT17 using targeting siRNA could efficiently suppress cancer cell proliferation by inhibiting the AKT/mTOR/HIF1α pathway.

However, there are still many barriers blocking the clinical application of siRNA *in vivo*, such as nuclease degradation, non-specific binding to serum proteins, and kidney filtration (Kim et al., 2016; Tatiparti et al., 2017). In addition, the repulsion effect between the phosphate backbone of RNA and cell membranes which are both negatively charged increases the difficulty of passive diffusion of siRNAs into cells (Wang et al., 2010). Furthermore, bare siRNA has no targeting ability which may lead to severe side effects in normal cells. Consequently, siRNA has only been used for limited clinical treatment, such as eyes or skin which are externally accessed. Nanoparticle delivery of siRNA significantly decreases the possibility of being cleared by the immune system, and reduces off-target effects compared with a traditional retrovirus system or bare siRNA (Kim et al., 2016).

5.1.3 SH-MSNPs and GSH-activated siRNA release

In this study, thiol functionalized mesoporous silica nanoparticles (SH-MSNPs) were chosen as the delivery core for the nanosystem. The siRNA was synthesized with a 5' thiol functional group and formed a stable disulfide bond link with the SH-MSNPs core. The bond is expected to remain stable until entering the high glutathione (GSH) environment of cancer cells (Estrela et al., 2008). The GSH has been demonstrated as one of the special molecules in biological pathway regulation. The reducing and detoxifying functionalities of GSH are enabled by one of the key functional groups with thiol group (-SH) of the cysteine residue. GSH is kept in the reduced form the majority of the time, before being

transformed into the dimeric oxidised form GSH (GSSG) upon oxidative stress signalling. Thus, the GSH/GSSG ratio is a good indicator for the intracellular stress level; directly associated with cellular malfunction or multiple diseases. The GSH signalling molecule is also involved in metabolic activities, such as gene expression regulation, enzyme function, and protein synthesis. Intracellular glutathione (GSH) is more concentrated inside cells than extracellularly. Furthermore, the intracellular GSH concentration of cancerous cells is normally 1.7–7 fold higher than in normal cells (Mura et al., 2013; White et al., 2019). High concentration of GSH could efficiently break the disulfide bond linkage and allows for targeted release within the cancer cells.

In this study, the GSH concentration of RMS cells have been measured as the fundamental for the GSH-activated release. Moreover, the theranostic nanosystem which specifically releases nanoparticle bound siRNA in the high GSH environment of tumours, can be tracked with IR820 dye, has been developed and evaluated from several different perspectives. The build-up of the system as a whole has also been validated.

5.2 Methods

5.2.1 Cell lines & Tissue Culture

The cell lines were prepared and cultured as described in Chapter 2.2.1 and 2.2.2.

5.2.2 Cell viability & metabolic assay (MTT)

The cells were seeded, and the assay was performed following the same methods as in Chapter 2.2.4, except for the following detailed steps:

The cells were treated with one of the following: (i) buffer alone, (ii) free thiol functionalized siRNA, (iii) SH-MSNPs, (iv) siRNA with DharmaFect transfection reagent [Dharmacon, Lafayette, CO, USA], or (v) purified siRNA-linked MSNPs. The aliquoted

siRNA stock solution (20 μM in 1x siRNA buffer (60 mM KCl, 6 mM HEPES-pH 7.5, 0.2 mM $MgCl_2$)) [Horizon Discovery, Cambridge, UK] was prepared and applied for transfection. For DharmaFect induced transfection, the reaction was prepared from two tubes: Tube 1 containing siRNA and serum-free DMEM mixed at a 1:19 ratio, and tube 2 containing DharmaFect & serum-free DMEM mixed at a 1:49 ratio. Enough solution was prepared for at least 100 μL for each well. After 5 min, the two tubes were thoroughly mixed and incubated for 20 min at room temperature. Before transfection, the cells were washed once with PBS and antibiotic-free medium.

After the selected cell lines were treated with set concentrations of siRNA or siRNA-linked MSNPs for a defined period of time, the medium was discarded from the microplate well. Subsequently, MTT medium solution (100 mL of growth media with 0.5 mg/mL of MTT) was added into each well followed by 3 hours incubation at 37 ºC to allow the formation of purple formazan crystals within the cells. The formation of crystals was then validated before moving on to the next stage. All supernatant was carefully discarded and 100 μL dimethyl sulfoxide (DMSO) [Sigma- Aldrich, Poole, UK] was added into each well to solubilize the formazan. The microplate was incubated for 20 minutes and then shaken for 2 minutes before measurement. The absorbance was read at 575 nm using the plate reader following incubation [Tecan Infinite® 200 PRO, Reading, UK].

5.2.3 Scratch Assay

A scratch test was performed to assess cell migration and invasion. RMS cells were cultivated in a 12-well sterile microplate at a density of $3x10^5$ per well. Cells were allowed to grow, spread, and form a confluent monolayer for 48 h. A 1 mL pipette tip was used as a pin tool to scratch through the cell layer and remove the scratched cells, resulting in the formation of a cross-like cell-free zone in each well with a constant width.

After incubation with different concentrations of siRNA or siRNA-linked MSNPs, cells

would migrate inward to the scratched area at different speeds. For comparison of cell mobilities, images of scratches were taken before and after the incubation for different wells. The average width of the scratched cross was measured twice across the horizontal and vertical scratches near the centre of the cross. The cell mobilities were quantified using the difference in scratch width before and after incubation.

5.2.4 siRNA linkage with SH-MSNPs and validation of binding

Thiol functionalized siRNA was custom synthesized by Merck [Merck, Haverhill, UK]. The sequences of the siRNA targeted to **CRYAB mRNA** were:

5′-[ThiC6]CUGUGAAUGGACCAAGGAA[dT][dT]-3′ (sense strand)

and

5′-[ThiC6]UUCCUUGGUCCAUUCACAG[dT][dT]-3′ (antisense strand).

The sequence of the siRNA targeted to **HSPB2 mRNA** was:

5′-[ThiC6]CUCCCAUGAUGGCAUCUUA[dT][dT]-3′ (sense strand)

and

5′-[ThiC6]UAAGAUGCCAUCAUGGGAG[dT][dT]-3′ (antisense strand).

The sequence of the siRNA targeted to **KRT17 mRNA** was:

5′- [ThiC6]CCAGUACUACAGGACAAUU[dT][dT]-3′ (sense strand)

and

5′-[ThiC6]AAUUGUCCUGUAGUACUGG[dT][dT]-3′ (antisense strand).

siRNA was re-suspended in 1x siRNA buffer which contained 30 mM HEPES-pH 7.4, 300 mM KCl, 1.0 mM $MgCl_2$ and RNase-free water [Dharmacon, Lafayette, CO, USA].

The solubilized siRNA samples were then aliquoted into several tubes containing 50 µL of 20 µM siRNA stock suspension within the RNase free environment.

Prior to the linkage, all 5'-thiol functionalized siRNA was obtained in a disulfide form for stability. In order to reduce the disulfide bond of the thiol-modified 5' end to an active sulfhydryl form, 100 mM dithiothreitol (DTT) solution was added to 100 mM sodium phosphate buffer (pH 8.3 - 8.5). Aliquoted siRNA stock solution (50 µL) was mixed with 125 µL of the DTT solution, followed by incubation for 1h at room temperature. The by-product was carefully removed using a NAP-10 column and 100 mM sodium phosphate buffer (pH 6.0) following the manufacturer's protocol [GE Healthcare, Illinois, US]. The final activated product was eluted with 200 µL of sodium phosphate buffer (pH 6.0). All buffers were prepared with RNase-free water. The concentration of activated siRNA was measured with NanoQuant Plate™ using Infinite® 200 PRO plate reader dsRNA reading function [Tecan, Reading, UK].

Immediately after the activation and concentration reading, thiol functionalised siRNA (CRYAB & HSPB2, or KRT17) was mixed with 1 mg of SH-MSNPs dispersed in 1 mL of sodium phosphate buffer (pH=7.4). The binding reaction was kept for 8h within an RNase free environment at room temperature. siRNA-linked MSNPs were collected by centrifugation at 15,000 rpm for 30 min. The same amount of RNase free buffer was then added for re-dispersion of collected siRNA-linked MSNPs. The re-dispersion and centrifugation process was repeated four times, and all supernatant was collected for the reading of remaining free siRNA with NanoQuant Plate™.

For validation of siRNA linkage with SH-MSNPs, the purified siRNA-linked MSNPs and free siRNA samples were electrophoresed on a 2 % (w/v) native agarose gel for 1 h at 100 V. The gel was prepared in 0.5× TBE buffer supplemented with 0.005 % (v/v) EtBr and 10 mM $MgCl_2$.

5.2.5 Validation of RNase I Protection

For validation of the protective-effect of MSNPs to the linked siRNA, the siRNA-linked MSNPs or free siRNA targeting different mRNAs were incubated separately with 0.25 % (w/v) RNase I [Sigma- Aldrich, Poole, UK] for different periods of time ranging from 15 min to 4 h (for free siRNA) or even longer until 24 h. Gel electrophoresis was used to assess degradation as above. As previously, 2 % (w/v) native agarose gel electrophoresis was used to assess degradation for 1 h at 100 V. The gel was prepared under the same conditions.

5.2.6 APC Annexin V/PI Assay

Pure SH-MSNPs or siRNA-MSNPs treated RH30 spheroids were collected and dissociated into single cells by trypsin treatment and centrifugation. The cells were then washed three times with 200 µL of cold 1x PBS and Annexin V binding buffer [BioLegend, CA, US]. The washed cells were then incubated with 50 µL of Annexin V binding buffer which was pre-mixed with 2.5 µL of PI and 5 µL of APC Annexin V [BioLegend, CA, US] at room temperature for 15 min. The cells were then collected by centrifugation and resuspended in 400 µL of Annexin V binding buffer for flow cytometry evaluation. Flow cytometry was performed using a BD FACSCalibur [BD, NJ, US] and evaluated in both the FL3-H and FL4-H channels.

5.2.7 3D Spheroids Generation & Growth

The cell lines and spheroids were prepared and cultured following the same methods as in Chapter 4.2.6.

5.2.8 Measurement of intracellular GSH/GSSG level

A Promega GSH/GSSG-GloTM Assay was used to quantify the intracellular concentration

of total GSH and GSSG [Promega, Madison, WI, US]. In 96-well plates, normal cells (fibroblasts) and RMS cells were plated at a concentration of $1x10^4$ cells per well. The cells were allowed to adhere to the wells overnight incubation, and the assay was carried out according to the manufacturer's instructions. The medium was then discarded, and the cells were collected accordingly. The collected cells were then treated with either total glutathione lysis reagent or oxidised glutathione lysis reagent within the kit [Promega, Madison, WI, US]. Both plates were maintained at room temperature for 30 minutes before adding the luciferin production reagent. The plates were briefly shaken inside the plate reader [Tecan Infinite® 200 PRO, Reading, UK] before being allowed to equilibrate for 15 minutes at room temperature.

The Luminescence was then measured using a plate reader luminescence function [Tecan Infinite® 200 PRO, Reading, UK], and the GSH and GSSG amount was calculated according to the standard curve generated by the standard samples tested in plate at the same time. The following equation was used to compute GSH/GSSG ratios:

$$GSH/GSSG = [Total\ GSH-(2\ GSSG)]/GSSG.$$

5.2.9 Validation of construction of the designed nanosystem

The whole designed nanosystem could be separated into three parts: IR820-loaded siRNA-linked MSNPs core, pH- activated polymer layer, and targeting aptamers. For constructing the whole nanosystem, the prepared IR820-loaded siRNA-linked MSNPs core (5 mg/mL) was quickly sonicated in a sonicating water bath. Similar to the process described in Chapter 3.2.7, PMPC-PDPA@PEG-*b*-PAMA/DMMA (5 mg/mL; pH 7.4) were ultrasonicated and filtered with a 0.22 μm syringe driven filter. MSNP suspension (100 μL) was added dropwise into 1 mL pH-responsive co-polymer solution. During the addition, the mixture was constantly vortexed. The solution was kept at pH 7 for the whole process. It was then kept at room temperature for an addition 15 minutes to maximize the

coating. The nanoparticles were centrifuged at 10,000 rpm for 5 min then washed twice with 1x PBS before collection. The PE-labelled anti-NELL1 aptamers (500 nM) were added into the acquired mixture dropwisely. Similarly, it was then kept at room temperature for an addition 15 minutes for maximizing the coating. The nanoparticles were centrifuged at 10,000 rpm for 5 min then washed twice with same volume of 1x PBS before collection. To confirm the successful construction of the whole system, a similar process was also performed for IR820-loaded siRNA-linked MSNPs only, and polymer only with same amount of PE-labelled aptamers. All groups, including controls, were validated with the plate reader fluorescence function in the PE channel [Tecan Infinite® 200 PRO, Reading, UK].

5.2.10 Statistics and reproducibility

All statistical analysis of experimental data was performed using Microsoft™ Excel [Microsoft, NM, US]. GraphPad Prism 8.0.2 [GraphPad Prism, La Jolla, CA, US] was used for graph plotting. Error bars in the experiments indicate standard deviation (SD). The difference was considered significant and shown when the p values were less than 0.05. The figure legends included information on the number of events and independent experiments, as well as statistical data and methodologies.

5.2.11 Other software

FlowJo VX [FlowJo, LLC, OR, US] was used to analyse and compare flow cytometry data. For all confocal image analysis and measurement, the Leica Application Suite X (LAS X) was employed.

5.3 Results

5.3.1 Evaluation of Selected siRNAs

The genes CRYAB & HSPB2, and KRT17 were investigated as candidates for knockout in aRMS cells. RH30 cells (aRMS) were used for investigations, and compared with RD cells (eRMS). Both cell lines were transfected with CRYAB & HSPB2, or KRT17 siRNA, ranging from 12.5 nM to 50 nM. The eRMS cell line showed no significant reduction in proliferation rate compared with the control (Figure 5.1A(i)). Conversely, the cell viability and metabolism of the aRMS cell line (RH30) were both significantly suppressed. Cell growth was decreased to lower than 50 %, 24 h after transfection (Figure 5.1A(ii)). For the CRYAB & HSPB2 DKO using targeting siRNA, the cell viability of RH30 cells was suppressed to 39.92 %, 46.68 % and 44.68 % for 12.5 nM, 25nM, and 50 nM of both siRNAs, respectively. Similarly, after the KRT17 knockout, the cell viability of RH30 cells decreased to 47.74 %, 39.31 % and 42.35 % for 12.5 nM, 25nM, and 50 nM of siRNA, respectively. For the three concentrations applied, although they all showed significantly suppression compared to both cell control and the buffer control, there was no significant difference among various concentration or siRNA groups with viabilities all around 45 %.

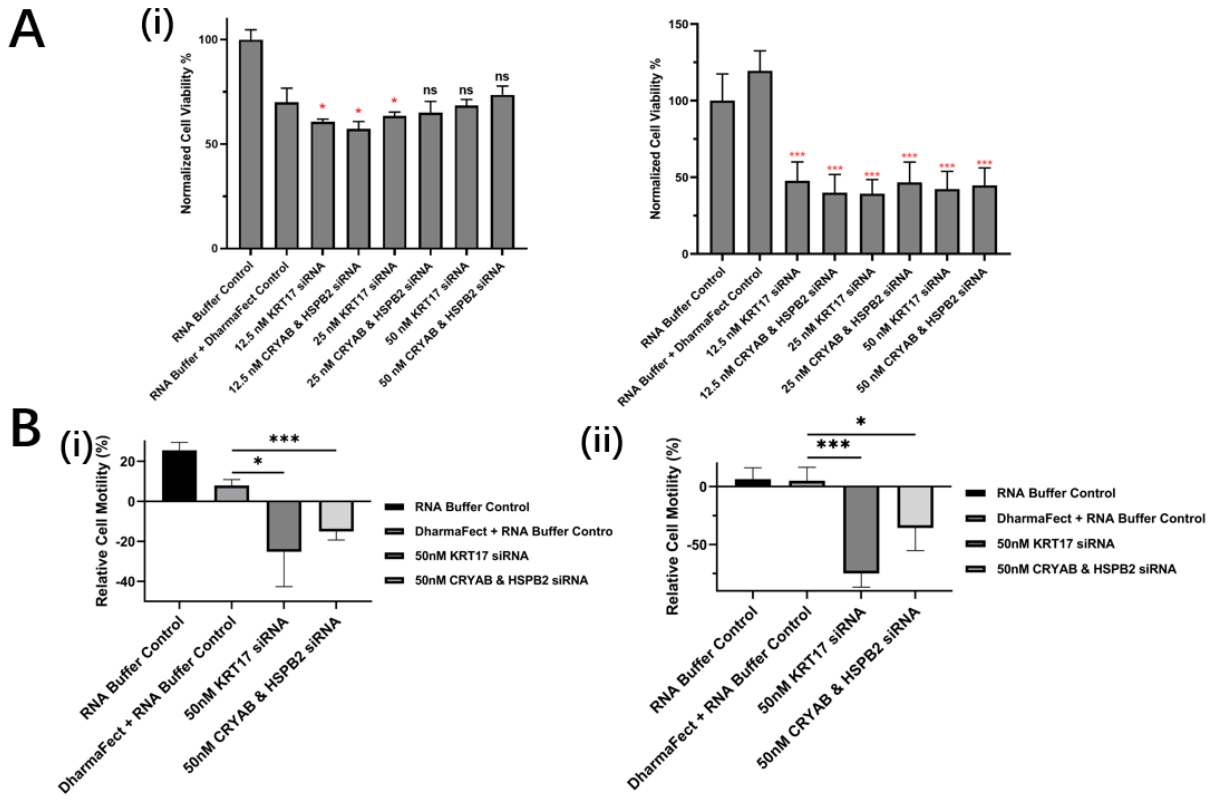

Figure 5.1 Measurement of chosen siRNAs' effects on cell proliferation & mobilities

(A) MTT results comparing the cell relative survival rate & metabolism level of (i) RD and (ii) RH30 sarcoma cells after knockout with different concentration of KRT17-targeting siRNA, or CRYAB & HSPB2-targeting siRNA using DharmaFect as transfection reagent for 24hrs (n=6), significance statistic all compared to the DharmaFect Control group. (B) Scratch assay results comparing the cell relative mobility of (i) RD and (ii) RH30 sarcoma cells after treated with 50 nM of KRT17-targeting siRNA, or CRYAB & HSPB2-targeting siRNA using DharmaFect as transfection reagent for 24hrs. Data is presented as mean ±SD for each individual cell line (n=3). Significance was tested using a two tailed t-test compared to the cells with only buffers for each cell line (ns: not significant, *P≤0.05, ***P≤0.001)

While cell viability was only affected in RH30 cells after the siRNA transfection for both CRYAB & HSPB2 DKO and KRT17 knockout using corresponded siRNA, cell invasion, as determined by the scratch test, showed significant inhibition in both RD and RH30 cells, albeit to different degrees. After transfection with 50 nM siRNA, RD cells showed a decrease in mobility of 25.17 % with KRT17 siRNA, and 15.08 % after with CRYAB & HSPB2 (Figure 5.1B(i)). However, much greater inhibition was seen in RH30 cells, with 74.95 % decrease with KRT17 siRNA and 35.79 % decrease with CRYAB & HSPB2 siRNA (Figure 5.1B(ii)).

5.3.2 Linkage and protection of siRNAs on the SH-MSNPs surface

The binding rates of siRNA onto the MSNPs surface were quantified as 51.41 % and 49.46 % for the linkage of CRYAB & HSPB2 siRNA, and KRT17 siRNA, respectively (Table S3). In order to further validate the stable linkage between siRNA and MSNPs, both the CRYAB & HSPB2 and KRT17 siRNA-linked MSNPs were examined by agarose electrophoresis. While free siRNA (or ladder) could move freely within the agarose gel, the stable linkage with MSNPs prevented any electrophoretic migration i.e. the fluorescent signal remained in the wells. No visible amounts of siRNA release could be detected by electrophoresis from the siRNA-linked MSNPs, demonstrating that the siRNA was strongly attached to the surface of the MSNPs *via* disulfide bonds (Figure 5.2).

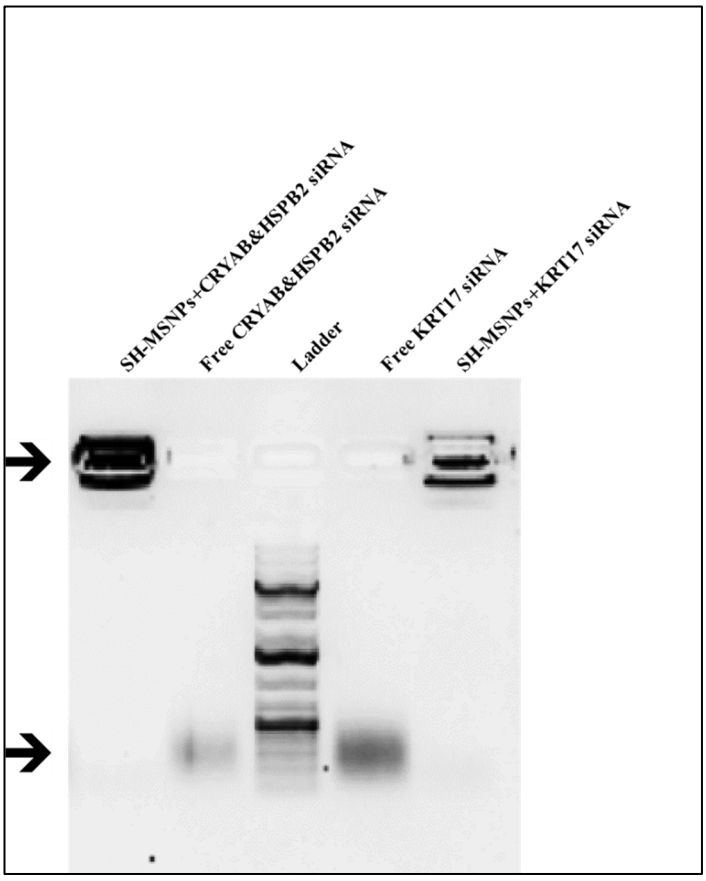

Figure 5.2 Validation of siRNA Linkage onto the surface of SH-MSNPs

Electrophoresis gel (1% agarose gel in TBA buffer) image of both free CRYAB & HSPB2-

targeting siRNA, or KRT17-targeting siRNA and siRNA-linked SH-MSNPs for the validation of disulfide bond linkage, cropped gel image. The ladder applied was ThermoFisher GeneRuler 1kb ladder, only for running validation, not for size reference.

In addition, samples were incubated with RNase I, an enzyme which could easily degrade unbound RNA. As shown in Figure 5.3A, 5 nM of free siRNA, irrespective of the sequence, was fully degraded by the RNase I in 15 min. However, the MSNPs were seen to protect the bound siRNAs from degradation; with a significant amount of siRNA visualised after electrophoresis after 2 h, 4 h, or 24 h incubation with RNase I (Figure 5.3B).

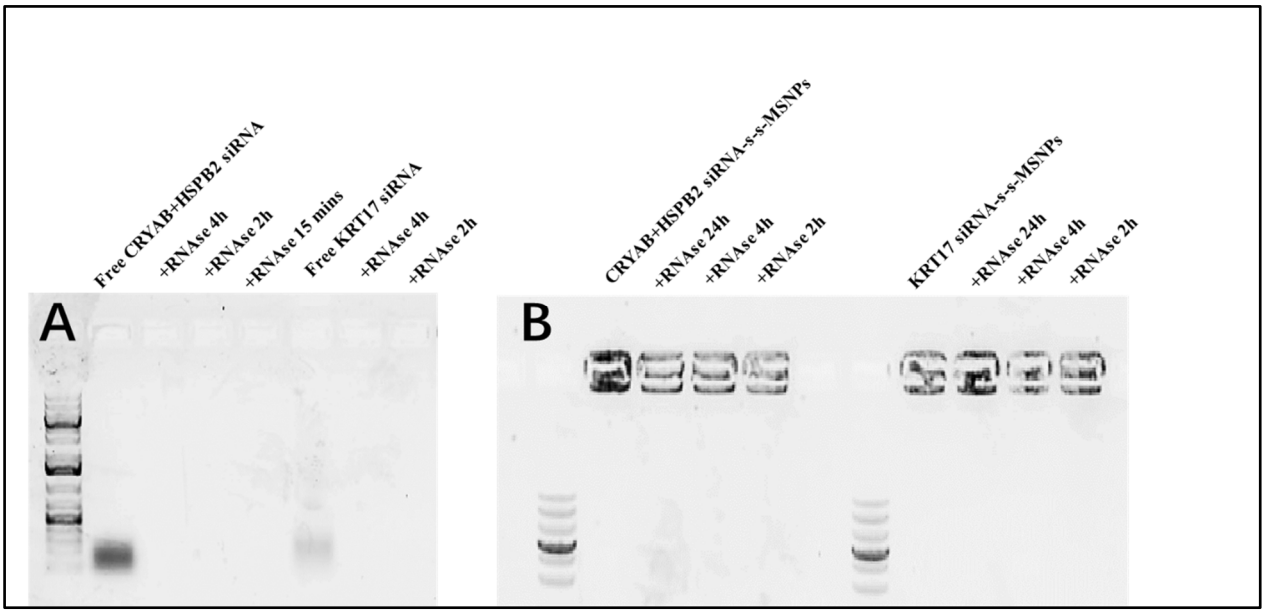

Figure 5.3 Evaluation of siRNA protection after linked onto the surface of SH-MSNPs

Electrophoresis gel image of (A) free CRYAB & HSPB2-targeting siRNA, or KRT17-targeting siRNA and (B) siRNA-linked SH-MSNPs, treated with same concentration of RNase for different periods of time at 37℃ for the evaluation of degradation prevention after linkage to SH-MSNPs. Cropped gel image. The ladder applied was GeneRuler 1kb ladder, only for running validation, not for size reference.

5.3.3 siRNA-linked MSNPs effects on cell proliferation & mobilities

The effects on aRMS cells proliferation and metabolism after incubation with siRNA-linked MSNPs were evaluated in comparison with the standard lipid transfection reagent

DharmaFect™. After 24 h of incubation, it was found that the carrier only (SH-MSNPs) control did not affect either RD or RH30 cells. Similarly, free siRNAs did not affect either RD or RH30 cells with regards to their proliferation or metabolic rate. However, when it came to transfection using DharmaFect or MSNPs carriers, RD and RH30 reacted differently at the same concentration of siRNAs. After siRNA transfection with DharmaFect, the RD cells showed very little difference in the viability level compared to the control group, except for the 5 nM KRT17 siRNA knockout group. The viability decreased to 60.75 ± 1.79 % after 24 h of transfection (Figure 5.4A(i)).

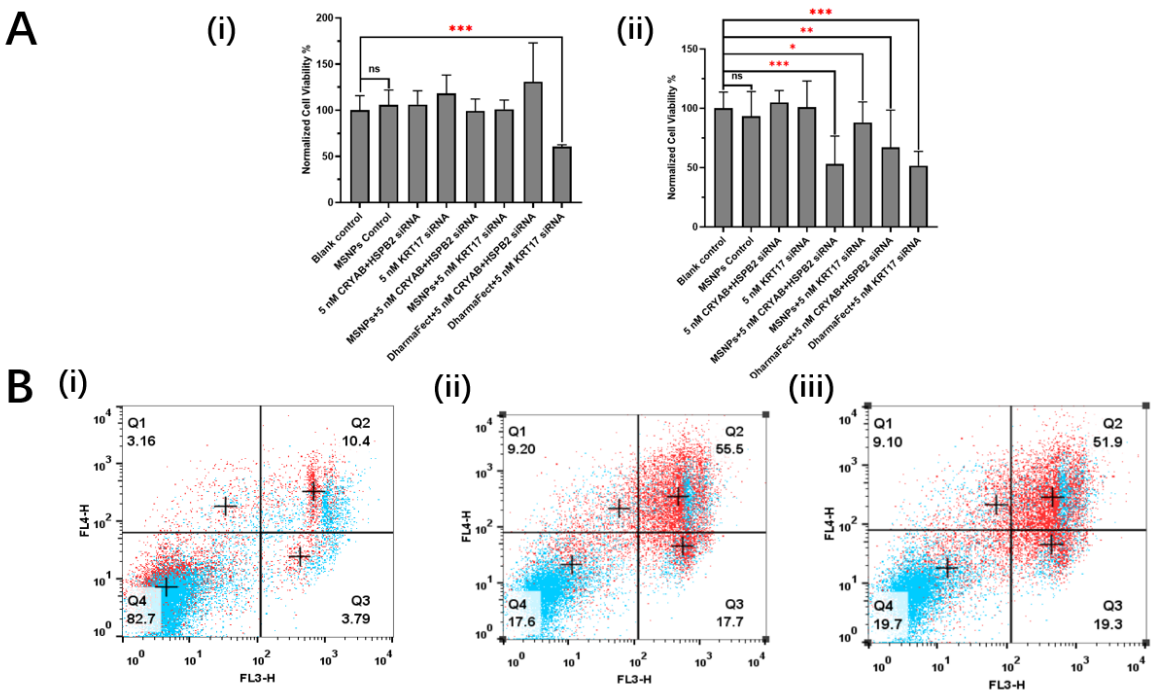

Figure 5.4 Measurement of siRNA-linked MSNPs effects on cell proliferation & mobilities

(A) MTT results comparing the relative cell survival rate & metabolism level of (i) RD and (ii) RH30 sarcoma cells after knockout with 5 nM of free CRYAB & HSPB2-targeting siRNA only, or KRT17-targeting siRNA only, or same concentration transfected by DharmaFect or MSNPs for 24hrs (n=6). Data is presented as mean ±SD for each individual cell line (n=3). Significance was tested using a two tailed t-test compared to the cells with only buffers for each cell line (ns: not significant, *P≤0.05, **P≤0.01, ***P≤0.001) (B) APC-Annexin V and PI assay results measuring the cell apoptosis and necrosis RH30 sarcoma cell spheroids after 72 hrs with (i), SH-MSNPs control (ii) 50 nM of CRYAB & HSPB2-target siRNA-linked MSNPs and (iii) 50 nM of KRT17-target siRNA-linked MSNPs. (Blue) Control groups (Red) Knockout groups.

Nevertheless, RH30 cells, which has a much higher expression for all targeted mRNA, were all very sensitive to the transfection. Following transfection of 5 nM siRNA with

DharmaFect, the viability of RH30 cells were significantly decreased to 67.16 ± 37.17 % for CRYAB & HSPB2 DKO using targeting siRNAs, and 51.64 ± 12.04 % for KRT17 knockout using targeting siRNA (Figure 5.4A(ii)).

Similar or better outcomes were shown in the MSNPs transfection groups. With the same amount of transfected siRNA, the viability of RH30 cells were significantly decreased to 53.21 ± 23.40 % for CRYAB & HSPB2 DKO using targeting siRNAs, and 88.06 ± 17.28 % for KRT17 knockout using targeting siRNA (Figure 5A(ii)).

In addition to 2D cultures, knockout effects were examined in 3D spheroid models. After incubation with 50 nM KRT17, or CRYAB & HSPB2 siRNA-linked MSNPs an APC-Annexin V/PI assay was used to evaluate cell apoptosis and necrosis after 72h. After incubation of RH30 cell spheroids with SH-MSNPs carrier control only 3.16 % and 10.4 % of cells were found to be in the early/ late apoptosis and necrosis stage, respectively (Figure 5.4B(i)). However, SH-MSNPs conjugated with CRYAB & HSPB2 showed 9.20 % of cells in early/ late apoptosis, and 55.5 % of cells in necrosis stage (Figure 5.4B(ii)). Similar results were seen after KRT17 knockout using targeting siRNA; 9.10 % in early/ late apoptosis and 51.9 % in necrosis (Figure 5.4B(iii)).

5.3.4 Effects on cell proliferation of IR820-loaded siRNA-linked MSNPs

Any negative effects of IR820 on cell growth and proliferation, or the functioning of knockout siRNA were examined. siRNA-IR820-MSNPs were incubated with RH30 spheroids and compared with PBS controls, free IR820 dye, and SH-MSNPs control. The size of spheroids was monitored at t=0 and 24h, 48h and 72 h. After 72 hours, spheroids incubated with free IR820 had increased by 48.15 ± 25.22 % compared to spheroids in the PBS control which grew 45.90 ± 29.46 %. Incubation of the spheroids with SH-MSNPs showed a slightly slower growth rate with 39.01 ± 15.82 %, although this was not

statistically different from the PBS control.

Incubation with siRNA-IR820-MSNPs showed a clear suppression in the growth rate. The spheroids grew much more slowely and the growth almost ceased after 48 h; between 48 h to 72 h, cells incubated with NPs loaded with CRYAB & HSPB2 only grew 2.89 %. Furthermore, the KRT17 siRNA-IR820-MSNPs showed signs of shrinkage and collapse in treated RH30 spheroids after 48 h; the relative size change was suppressed from 31.67 ± 7.53 % to 18.29 ± 11.06 % after 72 h incubation after the siRNA transfection (Figure 5.5).

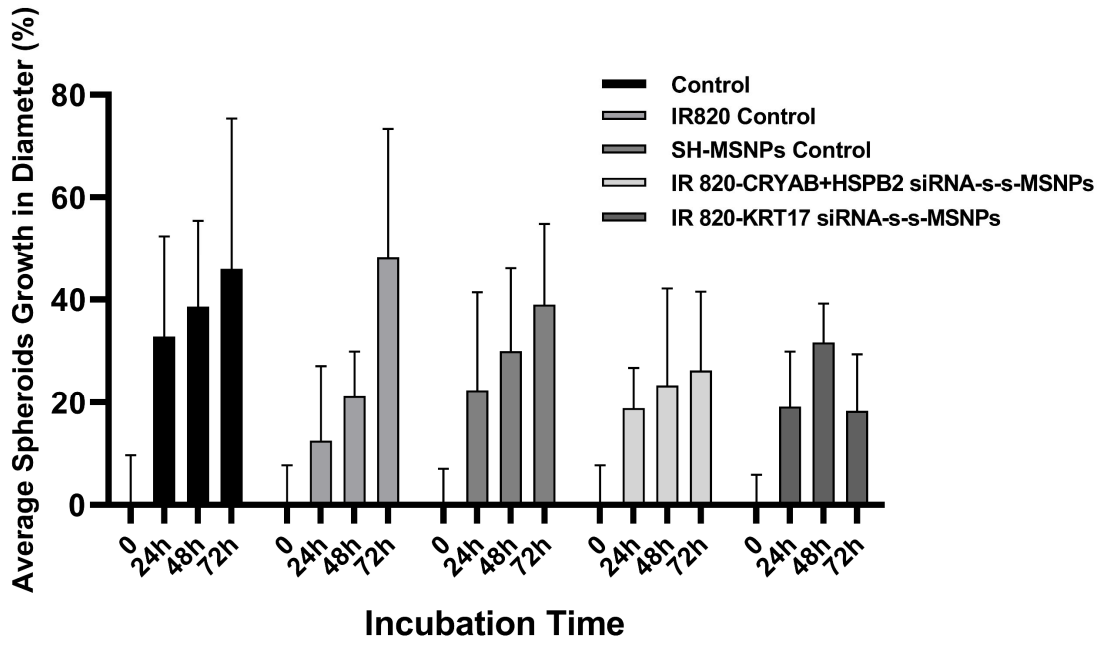

Figure 5.5 Measurement of IR820-loaded siRNA-linked MSNPs effects on cell proliferation

Average spheroid growth in diameter relevant to the RH30 sarcoma cells viability after treated with: PBS, unbound IR820, SH-MSNPs, CRYAB & HSPB2-targetted siRNA-linked IR820-loaded MSNPs, or KRT17-targetted siRNA-linked IR820-loaded MSNPs, for different period of times ranging from 0 - 72h (n=6). Data is presented as mean ±SD for each individual cell line.

Similar experiments were performed for the RD spheroids with the same incubation groups. The spheroids in all groups grew around 30 % in diameter after 72 h which showed no influence from the siRNA knockout for either CRYAB HSPB2 DKO or KRT17 using corresponded siRNAs (Figure S12). Thus, showing the specificity of these genes towards

aRMS cells.

5.3.5 Measurement of RMS intracellular GSH/GSSG level

Experiments were performed to validate that RMS cells, especially the targeted aRMS RH30 cells, have significantly higher levels of GSH than normal cells. A luminescence method was used for the assessment. Eight standards of known concentration of GSH were used to generate a standard curve (Figure 5.6A). The high correlation of the standard curve r=0.9966 further reassured the accuracy of the methods. All three cell lines were seen to have a total GSH level in the micromolar range; fibroblasts 0.25 ± 0.06 μM, RD cells 1.27 ± 0.07 μM, and RH30 cells 2.33 ± 0.14 μM (Figure 5.6B). Compared to fibroblasts, the two RMS cells lines showed a several-fold increase in the total GSH intracellular amount, i.e. 5.08 and 9.28 times higher for RD and RH30 cells, respectively.

The GSSG levels were also measured at the same time. As most of the intracellular GSH is normally kept in the reduced form, the GSSG levels were relatively low: fibroblasts 0.0045 ± 0.0005 μM, RD cells 0.0997 ± 0.0071 μM, and RH30 cells 0.1137 ± 0.0067 μM (Figure 5.6C). The ratios showed a different trend as the fibroblasts had the highest GSH/GSSG ratio; fibroblasts 57.59 ± 19.60, RD cells 12.83 ± 1.04, and RH30 cells 20.46 ± 0.32. Although there was a significant difference between RD and RH30 cell groups, the GSH/GSSG ratio decreased more than two-fold for both groups compared to normal fibroblast cells (Figure 5.6D).

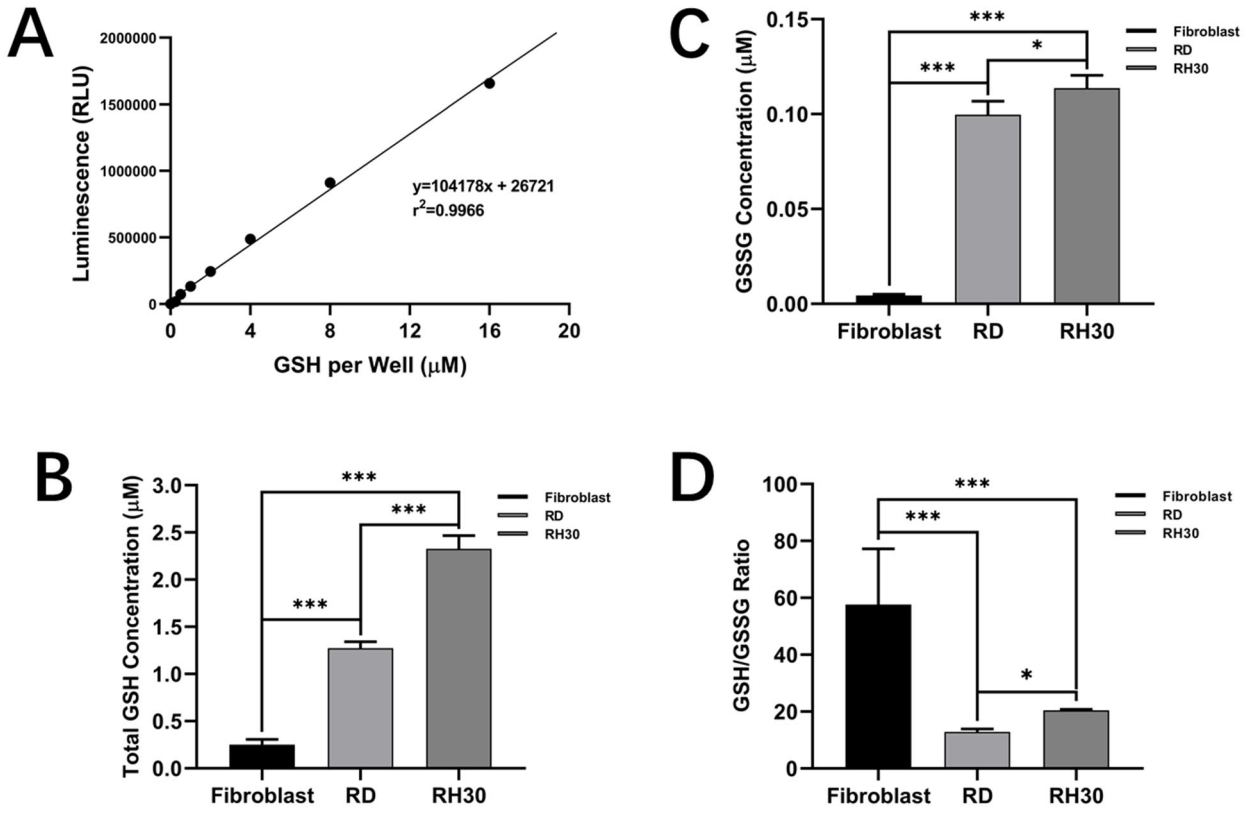

Figure 5.6 Quantification of intracellular GSG and GSSH concentration and GSH/GSSG ratio

(A) Standard curve plotted from eight standards (concentration ranging from 0.25 to 16 μM) which were treated under the same condition as the test samples, (B) Quantification of total GSH levels in fibroblasts, RD and RH30 cells under the same conditions, (C) Quantification of GSSG levels in fibroblasts, RD and RH30 cells under the same conditions, (D) GSH/GSSG ratio in fibroblasts, RD and RH30 cells under the same condition (n=6). Data is presented as mean ±SD for each individual cell line.

5.3.6 Validation of anti-NELL1 aptamers binding to PMPC-PDPA@PEG-*b*-PAMA/DMMA coated IR820-loaded siRNA-linked MSNPs

To validate the final construction of the designed nanosystem, especially the binding of anti-NELL1 aptamers described in Chapter 2, the same amount of PE-labelled anti-NELL1 aptamers was incubated with MSNPs, PMPC-PDPA@PEG-*b*-PAMA/DMMA only, or PMPC-PDPA@PEG-*b*-PAMA/DMMA-coated IR820-loaded siRNA-linked MSNPs. The emission fluorescence signal from the PE-labelled aptamers was used for quantification of the conjugation amount of aptamers. Both the pure PMPC-PDPA@PEG-*b*-

PAMA/DMMA and PMPC-PDPA@PEG-*b*-PAMA/DMMA-coated IR820-loaded siRNA-linked MSNPs group showed a significant increase in the fluorescent signal (Figure 5.7). On the contrary, the IR820-MSNPs linked with siRNAs did not show a significant increase in fluorescence signal after the incubation with aptamer compared to the PBS control (Figure 5.7). Due to the visible pink colour of PE, both the PMPC-PDPA@PEG-*b*-PAMA/DMMA group and PMPC-PDPA@PEG-*b*-PAMA/DMMA coated IR820-loaded siRNA-linked MSNPs group showed a significant colour change compared with the pure IR820-loaded siRNA-linked MSNPs group which remained of a white colour (Figure S13).

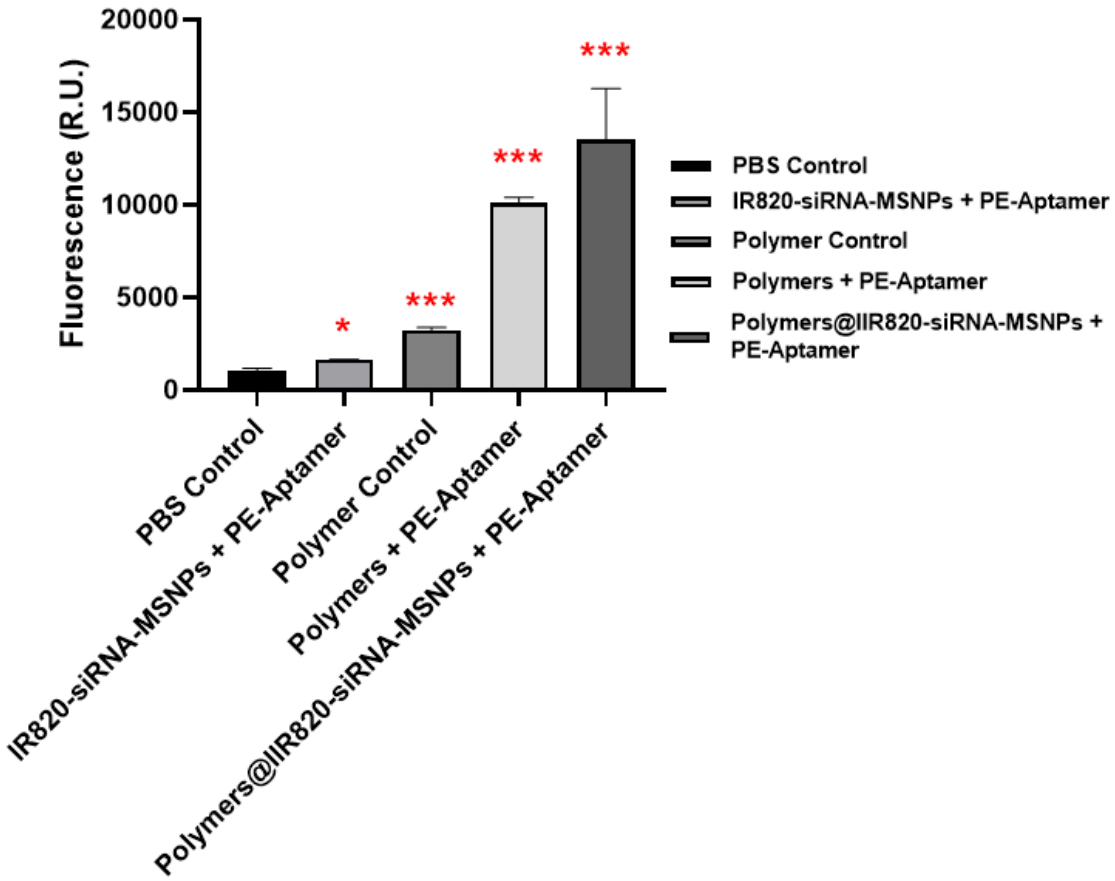

Figure 5.7 Measurement of the bound amount of PE-labelled aptamers after incubation using emission fluorescence signals

Average PE emission fluorescence after incubation with 500 nM PE-labelled anti-NELL1 aptamer.

Control groups (no incubation): PBS Control, PMPC-PDPA@PEG-*b*-PAMA/DMMA polymer control; Experimental groups (incubated with PE-labelled aptamers): IR820-loaded siRNA-linked MSNPs, PMPC-PDPA@PEG-*b*-PAMA/DMMA polymer, PMPC-PDPA@PEG-*b*-PAMA/DMMA coated IR820-loaded siRNA-linked MSNPs (n=6). Data is presented as mean ± SD for each individual cell line, statistic analysis all compared with PBS control group.

5.4 Discussion

5.4.1 The selected siRNAs could efficiently suppress aRMS growth

Previous studies in other cancer cell lines, such as the human breast adenocarcinoma cancer cells MCF7 (HTB-22) and human cervix adenocarcinoma cancer cells HeLa, have shown that the CRYAB & HSPB2 double knockout (DKO) using targeting siRNA can play an important role in inducing cell apoptosis and necrosis (Liu et al., 2014). Moreover, it has been shown that the CRYAB & HSPB2 gene expression level was related to human renal carcinogenesis through direct regulation of cell ROS levels and the Warburg effect (Liu et al., 2014). HSPB2 has specific interactions to regulate the Ca^{2+} inflow with the outer mitochondrial membrane in an unknown manner. However, one of the recent studies has figured out that one of the important interaction partner on the mitochondrial membrane was the glyceraldehyde 3-phosphate dehydrogenase (Grose et al., 2015). It directly affects the mitochondrial functionality after CRYAB & HSPB2 DKO through changing the mitochondrial membrane permeability (Weiss et al., 2003). By affecting the mitochondrial permeability transition and subsequent Ca^{2+} overload, CRYAB & HSPB2 DKO using targeting siRNAs could directly lead to necrotic and apoptotic cell death (Weiss et al., 2003). Herein it has been shown that the reduction of RH30 cell viability and mobility was mainly due to apoptosis and necrosis i.e. a 50 % reduction of the population after 72 h of transfection (Figure 5.5B), which further indicated that mitochondrial permeability could be the main cause of siRNA gene knockout-related viability suppression.

Expression level studies have previously shown that both CRYAB & HSPB2 are abnormally upregulated in aRMS compared with eRMS. In microarray evaluation of gene expression, CRYAB and HSPB2 were seen to be upregulated 13.52-fold and 12-fold, in RH30 and RD cells, respectively (Rapa et al., 2012). In fact, these genes showed two of the most significantly upregulated expression levels (Rapa et al., 2012).

Therefore, it has been further validated in our study that both viability (Figure 5.1A(ii) and mobility (Figure 5.1B) of aRMS cells was significantly suppressed after CRYAB & HSPB2 DKO transfected with targeting siRNAs concentrations as low as 12.5 nM after 24 h. Only small differences were seen in the eRMS groups due to the significantly lower initial level of expression of both genes.

Similarly, upregulation of KRT17 has been used as a diagnostic marker for several cancers, such as breast (van de Rijn et al., 2002), ovarian (Wang et al., 2013) and skin squamous carcinoma (Moll et al., 2008; Chivu-Economescu et al., 2017). KRT17 knockout using targeting siRNA has been shown to significantly suppress gastric cancer cell proliferation (42.36 ± 3.2 %) and migration (37.2 ± 6.2 %) through the AKT/mTOR pathway (Chivu-Economescu et al., 2017). The KRT17 gene has also been shown to be critical for proliferation of osteosarcoma (Yan et al., 2020), and for cellular adhesion and oncogenic transformation in Ewing's sarcoma (Sankar et al., 2013). Knockout of KRT17 using targeting siRNA may also decrease the viability and Warburg effect of osteosarcoma cells by significantly affecting the AKT/mTOR/hypoxia-inducible factor 1α (HIF1α) pathway and interrupting the expression of relevant genes (Yan et al., 2020). However, the effects of knockout of KRT17 using targeting siRNA in aRMS cells has not been previously demonstrated. The experimental results demonstrated that the knockout of KRT17 using targeting siRNA could efficiently decrease aRMS cell viability (Figure 5.1A(ii)), and mobility which may affect the AKT/mTOR pathway, a feature that has been confirmed in

other types of sarcoma (Figure 5.1B) (Yan et al., 2020).

5.4.2 MSNPs can deliver the targeting siRNA safely and effectively

This study aimed to synthesize a nanoparticle to deliver siRNA in a controlled and targeted manner. DharmaFect™ is a frequently used commercial RNA transfection reagent based on a cationic lipid. However, it results in cellular toxicity (Basu et al., 2008; Santos-Carballal et al., 2015), is unstable, expensive, and cannot be directly applied *in vivo* (Santos-Carballal et al., 2015). In contrast, MSNPs have excellent stability and biocompatibility, and are promising candidates for siRNA delivery (Möller et al., 2016; Na et al., 2012; Ngamcherdtrakul et al., 2015) In our study, thiol-functionalized siRNA was bound to SH-MSNPs through the formation of disulfide bonds. The disulfide bonds ensured stable and reliable binding before controlled release of the siRNA (Zhao et al., 2017). The stability of the complex was validated using gel electrophoresis with no visible leakiness (Figure 5.2).

In vivo RNase is an obstacle for siRNA-based gene therapy (Wang et al., 2010). There are different routes proposed to solve this issue. For example, 2'-O-methyl (2'-OMe) and 2'-deoxy-2'-fluoro (2'-F) modifications of siRNA have shown better potency and stability *in vitro* (Allerson et al., 2005), and numerous lipid-based carriers for siRNA delivery have been trialled including the commercially approved Patisiran (ONPATTRO™) (Yonezawa et al., 2020). The siRNA in our study was 21bp, and could therefore be easily degraded completely within 15 minutes (Figure 5.3A) which was in agreement with the short half-life of 6 min for siRNA clearance seen in other studies (Shen et al., 2014). MSNPs showed strong protective functionality of the carried siRNA, as also seen in other publications (Shen et al., 2014). The protection by MSNPs was mainly due to: (1) **Electrostatic repulsion**: the MSNPs were negatively charged (Figure S11), and the siRNA linked by the disulfide bonds increased the negative surface charge, leading to a strong repulsive

effect on RNase I, which itself has been proved to have an initial negative charge (Mitkevich et al., 2014), and (2) **Steric protection**: the silica nanoparticle core was mesoporous and a large proportion of the siRNAs were linked and contained within small pores. The RNase I, which is a large molecule was unable to access and degrade the siRNAs.

Compared with the DharmaFect transfection group, the siRNA-MSNP group showed similar or greater knockout efficacy evidenced by significant apoptosis and necrosis of the cell population (Figure 5.5).

5.4.3 GSH within aRMS cells could be applied for targeted release of siRNA

Several studies have indicated that GSH could be used as an intracellular stimuli response factor for active release of specific drugs into cells, especially in cancer cells. Yang and collaborators reported a cancer cell-specific degradable dendritic mesoporous organosilica nanoparticle (DDMON) which used the differences in GSH concentration for selective release. The release mechanism was based on the disulfide bonds (-S-S-) incorporation in the DDMONs. The high concentration of GSH in the cytoplasm of cancer cells would lead to the disintegration of the NP structure by the reduction of the disulphide bonds, and the release of encapsulated therapeutic agents. The DDMONs generated carried the cancer therapeutic PEI/RnNase (Polyethylenimine/Ribonuclease A) A-Aco-FITC (cis-aconitic acid- Fluorescein isothiocyanate) complex. Incubation of the complex in melanoma (B16F0) cell lines, resulted in significantly higher cell death compared to the same amount of the loaded non-biodegradable dendritic mesoporous organosilica nanoparticles (DMONs). As a control the constructs were tested in normal HEK293t cells, and viability was higher after treatment with DDMONs than DMONs. This confirmed the selectivity of the system based on the GSH concentration, thereby providing protection for healthy cells

(White et al., 2019; Yang et al., 2016). The GSH levels we found in aRMS cells were nearly 10 times higher than that of normal fibroblast cells (Figure 5.5). This further indicated that the GSH within RH30 cells could be applied for targeted release of nanoparticle associated siRNA.

5.4.4 PE-labelled aptamer binding to the outer surface of copolymer coated nanoparticle core

In addition to adjusting the charge-neutral pH for the copolymer system (Chapter 3.3.2), PMPC-PDPA also has a superb ability to bind to DNA molecules. It has been previously shown that PMPC-PDPA could effectively encapsulate significant amounts of plasmid DNA (Lomas et al., 2010).

Here, it has been shown that large amounts of PE-labelled anti-NELL1 aptamer could firmly bind to the copolymer or copolymer coated therapy core, which further validates the theory that the aptamer was bound through electrostatic interaction with the PMPC-PDPA on the outer surface. Even after several rounds of washing, the whole nanosystem could stay firmly as a nanosystem combining the discoveries from Chapters 3.3.3 and 5.3.6 (Diagram of the constructed nanosystem shown in Chapter 1).

5.5 Conclusion:

After successful validation knockout of selected targets (CRYAB & HSPB2, and KRT17) for aRMS suppression, the targeting siRNA was successfully linked to the surface of SH-MSNPs with disulfide bonds. The MSNPs were proven to successfully deliver, transfect and protect the siRNA. Compared with the transfection group using commercially available DharmaFect, all siRNAs delivered and transfected by the designed nanosystem were found to have a similar or better transfection efficiency with significant suppression

of viability and mobility within both 2D and 3D RH30 cell models. On the contrary, no change of viability or mobility was observed for the RD cell spheroid model after transfection. The siRNA was protected from RNase I degradation for over 24 h, compared with free siRNA which was degraded within a few minutes. Subsequently, IR820 dye was loaded into the siRNA-linked MSNPs to allow imaging of the nanoconstruct *in vivo*. The GSH and GSSG levels were precisely quantified for fibroblasts, RD and RH30 cells which indicated that the GSH levels within RH30 cells were sufficient for targeted release from the nanoparticle core. Moreover, the successful construction of the whole designed nanosystem was validated through the binding test of PE-labelled aptamer onto the copolymer coated core.

The successful building of the theranostic nanosystem which combines the targeting aptamers, aRMS-specific siRNAs therapy, and NIR monitoring could provide another route for tackling the aRMS in a more efficient and non-invasive way.

Chapter 6

Conclusion and Future

6.1 Summary of findings and limitation of work

As one of the most aggressive common soft tissue sarcoma, RMS is highly malignant. Most cases occur in children, and commonly appear in the arms or legs. Currently, RMS treatment mainly relies on aggressive chemotherapy, as well as surgery and/or radiation. The aggressive treatments often cause long-term after-effects, and can even cause permanent life-altering disabilities. Innovative treatment methods with better efficacy and fewer side effects are urgently needed.

The goal of this research was to create a pH-activated-release dual-functional theranostic nanoparticle system which could specifically target the aRMS cancer cells. The therapeutic effects of siRNA could be monitored using non-invasive NIR signals once it is administered to tumour cells. The stimuli-responsive release of the carried therapeutic molecules to maximise the tumour accumulation and minimize the off-targeting has been proven to be important for the nanosystem design.

The whole project could be separated into four parts: active targeting aptamer system; pH-responsive charge-reversible layer; nanoparticle-based NIR non-invasive reporting system; and siRNA for gene knockout.

In this thesis, it has been demonstrated that:

The NELL1 expression and membrane location has been successfully validated using Western blotting and flow cytometry. An improved, robust, rapid selection process was used to effectively screen a library of potential anti-NELL1 DNA aptamers. The selected aptamers were further investigated for affinity and cell-specific selectivity. With computed Kd < 1 μM, all three anti-NELL1 aptamer candidates were shown to have a significantly strong binding affinity. In NELL1-expressing cell lines, two of the three candidates demonstrated metabolic activity suppression. AptNCan3 was chosen as the best option

because it had the best combination of affinity and cell specificity. It was shown that AptNCan3 accumulated on cell membranes and in punctate structures in the cytoplasm. The identification of these aptamer sequences could lead to simple, low-cost, and rapid production of targeting moieties for NELL1-expressing cells, which are frequently seen in cancers and other diseases.

The pH-activated PMPC-PDPA@PEG-*b*-PAMA/DMMA copolymer layer was effectively synthesised and analysed, and shown to exhibit both charge conversion and hydrophilic-hydrophobic reversion functions. The PEG-*b*-PAMA/DMMA alters its surface charge from negative to positive in response to a reduction in environmental pH, as demonstrated in this work and earlier studies. The copolymer remained neutral or negatively charged in a normal environment (pH 7.4) after mixing with the right amount of positively charged PMPC-PDPA. This helped to avoid rapid clearance and non-specific binding, and conversion to a positive charge in the tumour microenvironment (pH 6.8) which enabled enhanced tissue accumulation and cellular uptake. The ability of the copolymer to self-assemble into nanomicelles or coat nanoparticles without significantly increasing its size was proven with TEM images.

The SH-MSNPs and AuNTs were successfully synthesised following the optimization of the protocol. Both types of nanoparticles were characterised in terms of size, surface potential and shape. The SH-MSNPs were chosen for loading the IR820 dye because of its high encapsulation capacity and strong loading stability. Compared with the unloaded free NIR dye, the combined IR820 dye nanosystem delivery system showed a significantly higher uptake rate, accumulation, and penetration depth in cells, according to flow cytometry and confocal microscopy imaging data.

However, it was noticed that the alternative core of synthesized AuNTs could be oxidized very quickly under ambient conditions. As some of the functionality, such as the enhanced

uptake rate or SERS study, would need the AuNTs to keep the specific morphology, it directly affected the further development of the AuNTs within our design. Thus, after coming up with these findings and careful consideration, we decided to change the route and used a more stable and well-proven materials: mesoporous silica. Although we have decided not to proceed with AuNTs for the remained of the experiments, it still provided valuable data and a new direction with great potentials for the future studies.

Finally, the targeting siRNA was effectively attached to the surface of SH-MSNPs using disulfide bonds following successful validation knockout of chosen targets (CRYAB & HSPB2, and KRT17) for aRMS suppression. The MSNPs were shown to transport, transfect, and preserve siRNA effectively. Compared with the transfection group using commercially available DharmaFect, all siRNAs delivered and transfected by the designed nanosystem showed a similar or better transfection efficiency with significant suppression of viability and mobility within both 2D and 3D RH30 cell models. The RD cell spheroid model, on the other hand, showed no change in viability after transfection with the siRNA indicating that the effect was specific to the aRMS cell type. When compared to free siRNA, which was degraded within minutes, the linked siRNA was highly protected against destruction by RNase I for over 24 hours. Subsequntly, IR820 dye was loaded into siRNA-coupled MSNPs to enable concurrent imaging. The quantities of GSH and GSSG in fibroblasts, RD, and RH30 cells were quantified, indicating that GSH inside RH30 cells could be used for targeted release of the linked siRNA. The binding of PE-labelled aptamers onto the copolymer coated MSNPs further demonstrated that the complete nanosystem was successfully assembled. The successful development of a theranostic nanosystem that combines targeting aptamers, controlled release, effective aRMS-specific siRNA treatment, and IR820 NIR monitoring may open up a new era for treating aRMS in a more efficient and non-invasive way.

6.2 Future work

The designed nanosystem was proven to be stable and effective, however, future improvement could be made. These are summarised as follows:

With regards to the selection of aptamers, it could be beneficial to further optimize the current selection process, especially since the PCR steps may lose a large percentage of good candidates due to their strong secondary structure. Further optimisation around the PCR amplification conditions (number of cycles, polymerase with higher proof-reading activity especially against potential secondary structure, annealing temperature) could be beneficial for generating aptamer candidates with better structure and binding affinities. Moreover, in addition to the DNA randomized library which was applied in this research, it could be considered using an RNA library which has more flexibility in forming different 3D structures for a higher binding affinity and specificity. Furthermore, some common proteins (such as bovine serum albumins or human serum albumins) could be applied as controls during the evaluation to exclude the candidates with bad selectivity.

For copolymer design, it has been discovered in this work that the current pH-activated charge conversion range was too narrow which was within $\pm$ 5 mV range. For optimizing this parameter, a better backbone could be designed to hold more DMMA molecules and enhance the charge convertibility. Moreover, it was also been found that the PMPC-PDPA did not show low solubility which significantly restricted the concentration of applied copolymer for the subsequent experiments. In the future, PMPC-PDPA could be replaced with other polymers of similar functionality (positively-charged & pH-activated deprotonation), but better hydro-solubility.

For the nanoparticle core, it was found that the synthesized AuNTs could be oxidized

very quickly without keeping it under extreme conditions of low temperature and no oxygen. Despite all the disadvantages, AuNTs still have potential due to properties such as the enhanced uptake rate or SERS. Hence, the optimization of AuNTs synthesis to maximize its stability under ambient conditions could be one of the main aims for future work. After ensuring the stability AuNTs' SERS functionality could help to build a label-free nanosystem which could also induce photodynamic therapy at the same time of delivering therapeutic reagents into the tumour area.

For the loaded NIR dye, IR820 was selected in this study and proven to have better accumulation and penetration after being loaded within the nanosystem. However, simple loading does not prevent potential leakage from the nanoparticles. In addition to NIR imaging, IR820 is widely used in photothermal therapies that convert NIR light into heat. For future work, it could be considered replacing IR820 with other novel NIR fluorescent molecules which could be easier to be functionalized and linked onto the nanoparticles. In addition, the whole constructed nanosystem could perform the photothermal therapy related study at the same time with controlled NIR laser activation.

For the siRNAs selected in this study, it was noticed that some of them had already been applied for the treatment of other types of cancers. In the future, it will be beneficial to test the current designed siRNA-linked nanoparticles in other cancer cell lines (such as gastric or pancreatic cancer) to broaden the range of applications of the designed system. For the evaluation of the constructed nanosystem, animal studies would be important and essential as the next step in the future. Although multiple spheroids testing was performed in this study, it cannot replace an *in vivo* evaluation of the nanosystem where it would face more complex organ accumulation, degradation environments, immune system clearance, before their actual functionalisation within the tumour area. Only after the validation studies in animals could the whole designed nanosystem be robust enough for

future clinical trials; and confirm its potential for saving more cancer patient lives with significantly higher efficacy and fewer side-effects.

Appendix

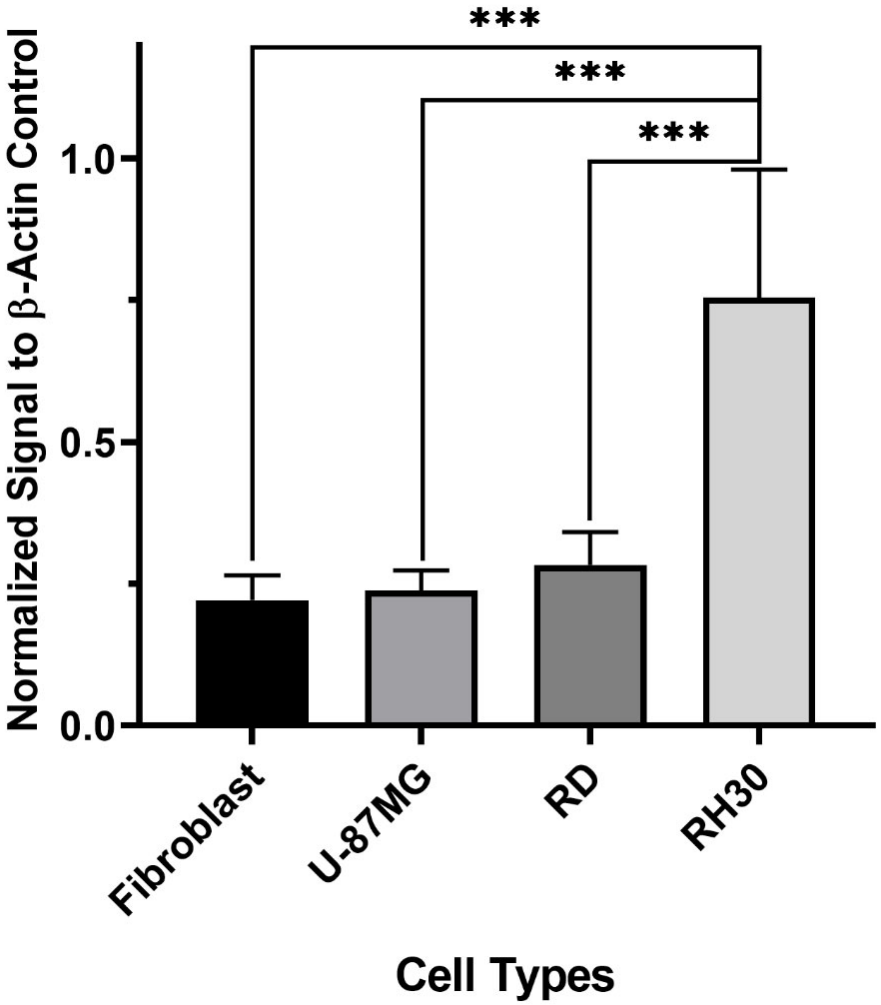

Figure S1 Measurement of NELL1 expression level with densitometry analysis of Western Blotting membrane of several other cell lines

Quantification of Western blotting showing the β-Actin normalized NELL1 expression level of different cell lines. Data is presented at mean ±SD for each individual cell line (n=3). Significance was tested using a two tailed t-test compared to the untreated cells for each cell line (*P≤0.05, **P≤0.01, ***P≤0.005)

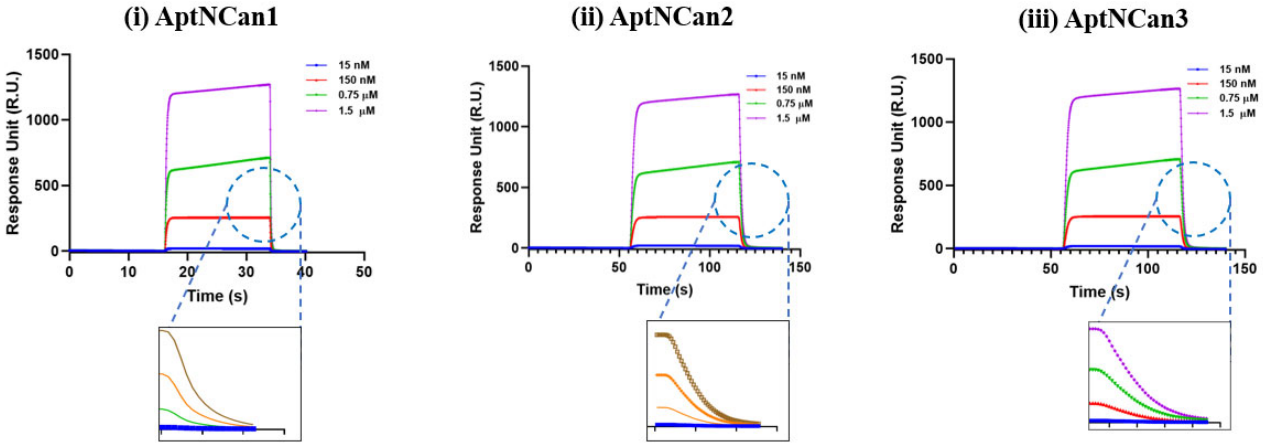

Figure S2 Representative quantified sensorgrams signals with different concentration of NELL-1 protein with anti-NELL1 aptamer candidates

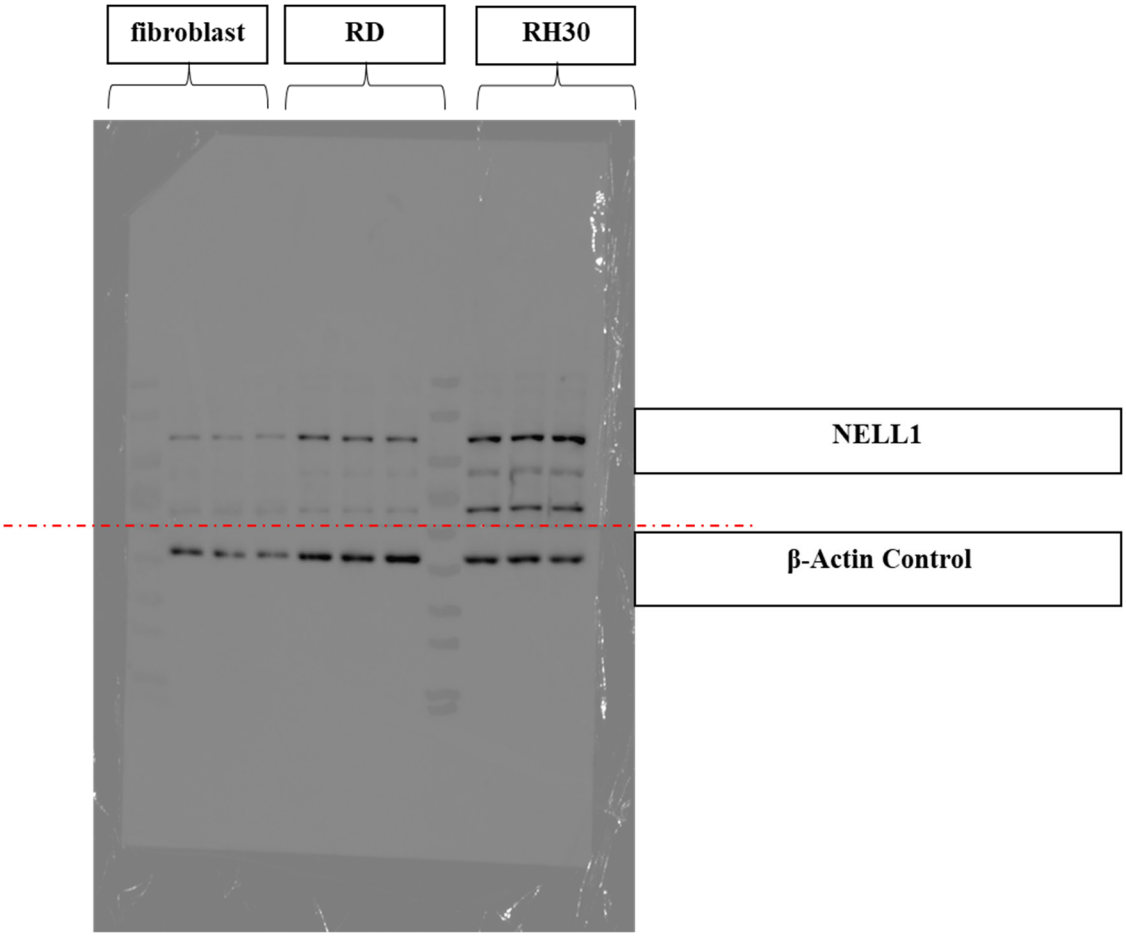

Figure S3 Western blot showing the expression levels of NELL1 expression levels of fibroblasts, RD and RH30 cells.

Western blotting showing NELL1 expression level of fibroblast, RD and RH30 cells. β-Actin was applied as a housekeeping gene control (loading control for the total protein). The red line shows the cutting position before the separate incubation for β-Actin and NELL1 with different secondary antibodies

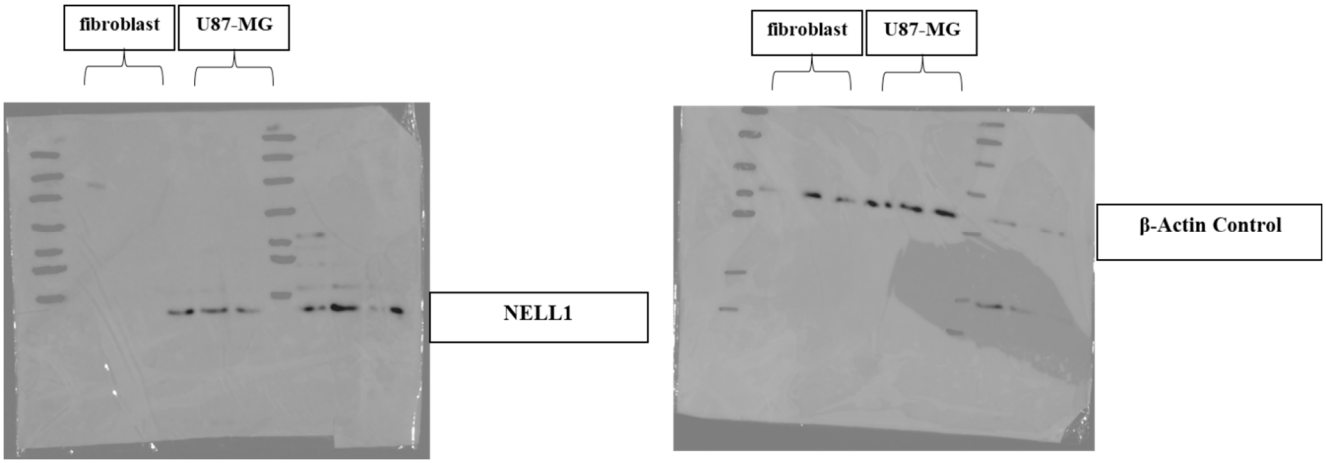

Figure S4 Western blot of NELL1 expression levels of fibroblast, U87-MG and RH30 cells

Western blotting showing NELL1 expression level of fibroblast, RD and RH30 cells. β-Actin was applied as a housekeeping gene control (loading control for the total protein). The blot was cut at the last step for different incubation of secondary antibodies.

Table S1 Measurement of densitometry readings of each β-Actin bands on Western blots of all tested cell lines (Unit: Arbitrary Area Value)

	Fibroblast	U87-MG	RD	RH30
Band 1	21145.61	21629.48	33759.49	32272.44
Band 2	15774.97	20246.51	34191.32	32369.66
Band 3	14053.78	23285.39	44321.97	27870.78

Table S2 Measurement of densitometry readings of each NELL1 bands within Western Blotting of all tested cell lines (Unit: Arbitrary Area Value)

	Fibroblast	U87-MG	RD	RH30
Band 1	2672.962	4205.326	11396.9	19974.44
Band 2	2540.79	3873.326	9929.539	20453.95
Band 3	2424.284	3787.912	9841.489	28318.13

Figure S5 Synthesized PEG-*b*-PAMA in the dialysis bag

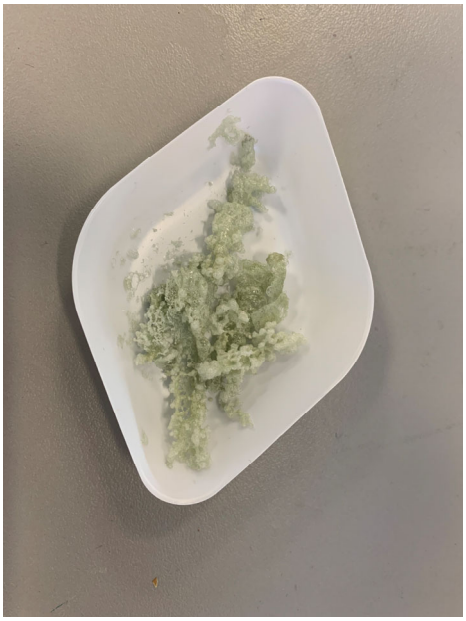

Figure S6 Freeze dried PEG-*b*-PAMA sample

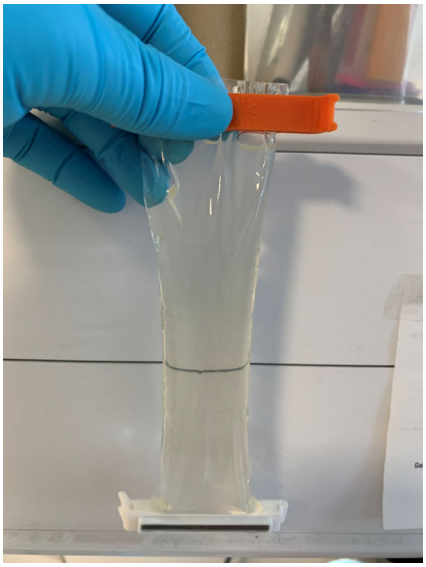

Figure S7 Dialyzed PEG-*b*-PAMA/DMMA

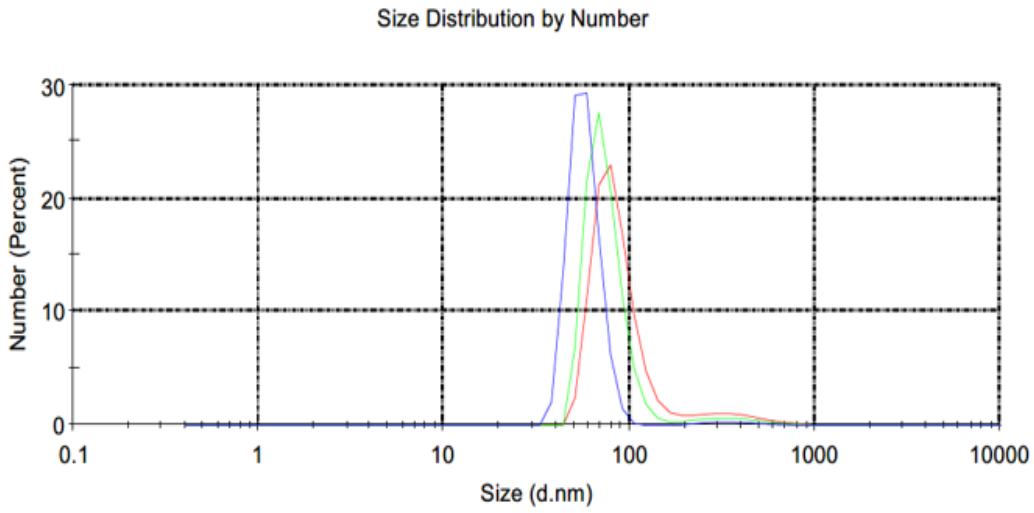

Figure S8 Zeta Size Distribution by number of Synthesized SH-MSNPs

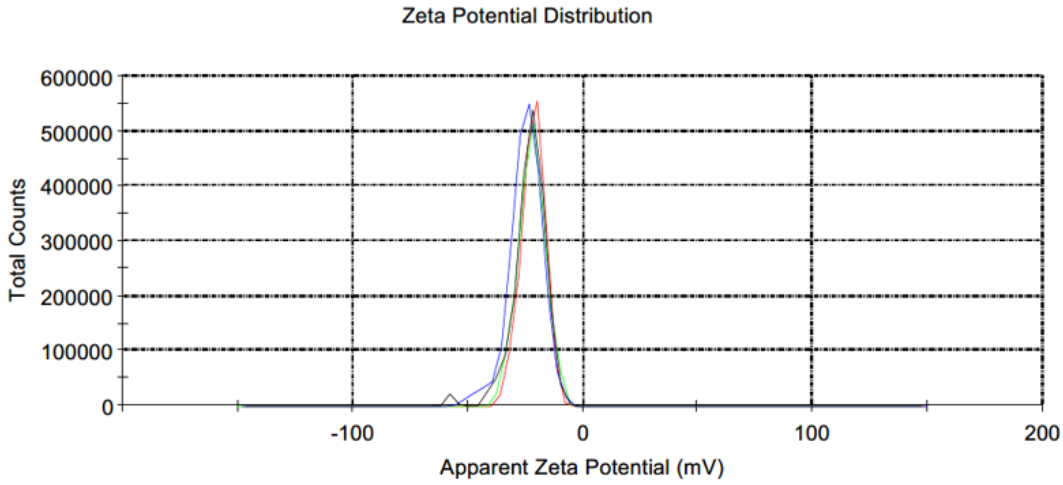

Figure S9 Zeta Potential of Synthesized SH-MSNPs (Neutral pH)

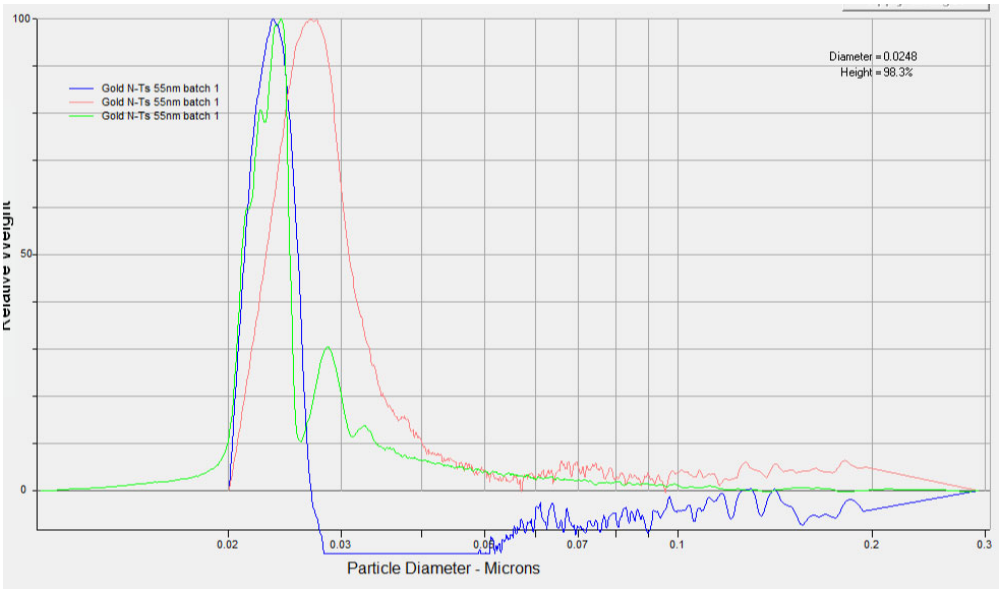

Figure S10 CPS Size Distribution of Synthesized Au NTs

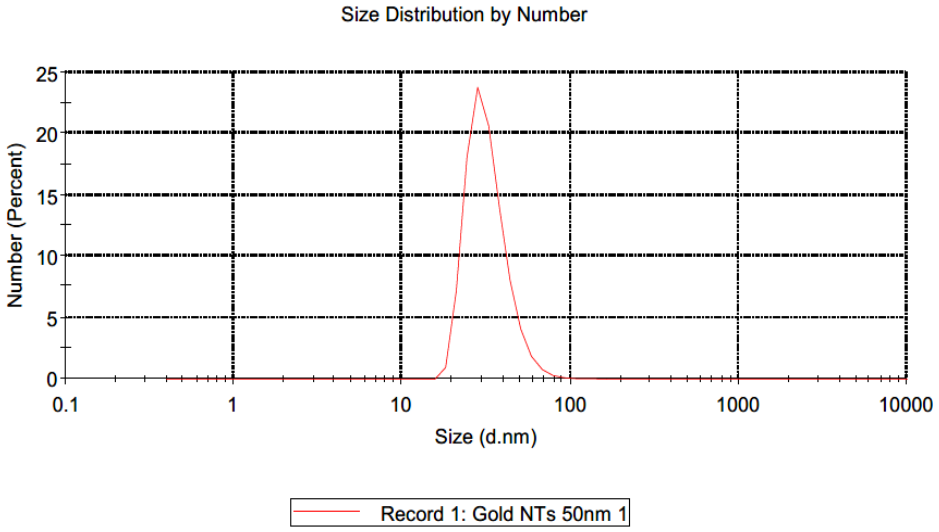

Figure S11 Zeta Size Distribution of Synthesized Au NTs (number mean)

Table S3 Quantification of activated thiol-siRNA concentration, column recovery, and synthesised SH-MSNPs Binding Ratio

Well	ng/µl	µM	Recovery/Binding Ratio
Unbound CRYAB+HSPB2 siRNA after SH-MSNPs incubation (5x dilution)	6.35	0.48	51.41 %

Unbound KRT17 siRNA after SH-MSNPs incubation (5x dilution)	1.8	0.14	49.46 %

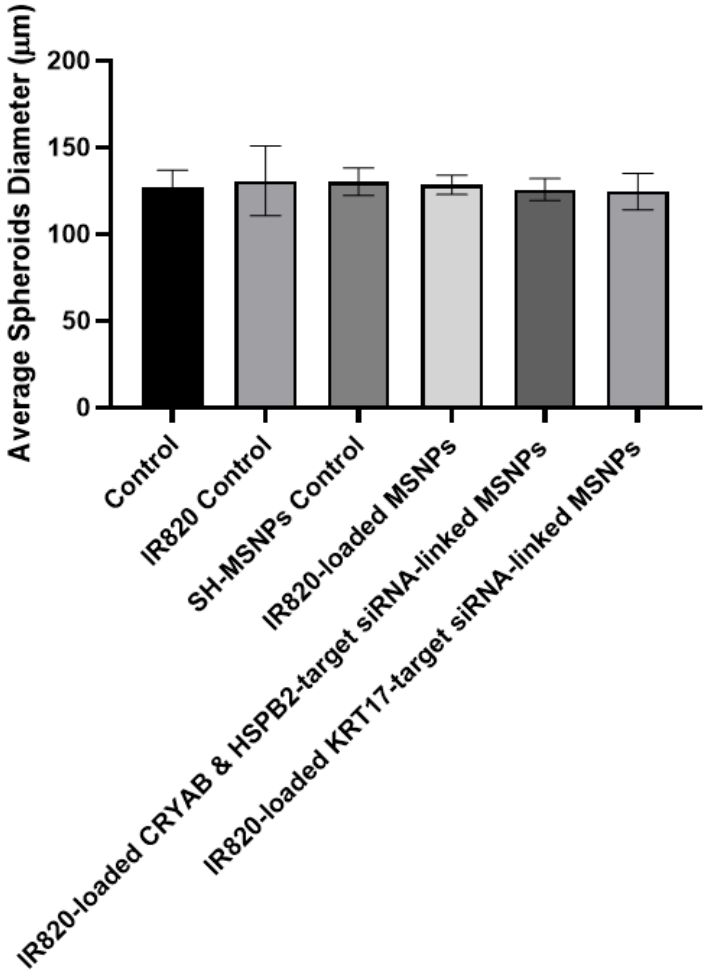

Figure S12 Diameter of RD spheroids after treatment for 72 hours with PBS, unbound IR820, SH-MSNPs, IR820-loaded MSNPs, IR820-loaded CRYAB & HSPB2-target siRNA-linked MSNPs, or IR820-loaded KRT17-target siRNA-linked MSNPs (n=6).

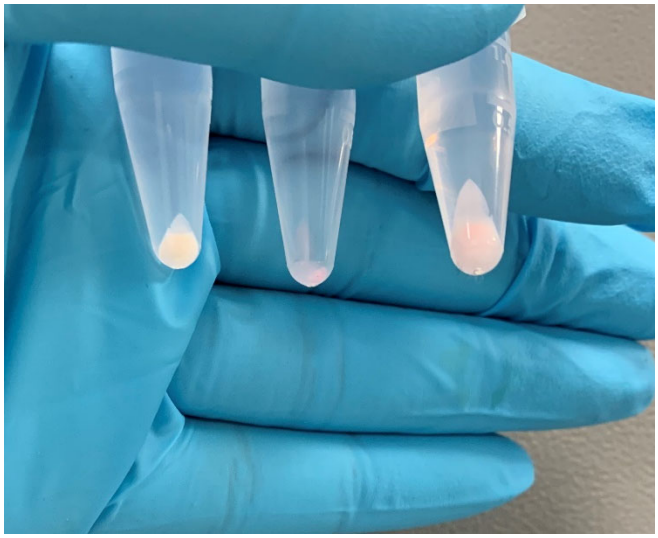

Figure S13 Concentrated samples after binding to PE-labelled aptamers. From left to right: IR820-loaded siRNA-linked MSNPs group, PMPC-PDPA@PEG-*b*-PAMA/DMMA polymer group, PMPC-PDPA@PEG-*b*-PAMA/DMMA coated IR820-loaded siRNA-linked MSNPs group.

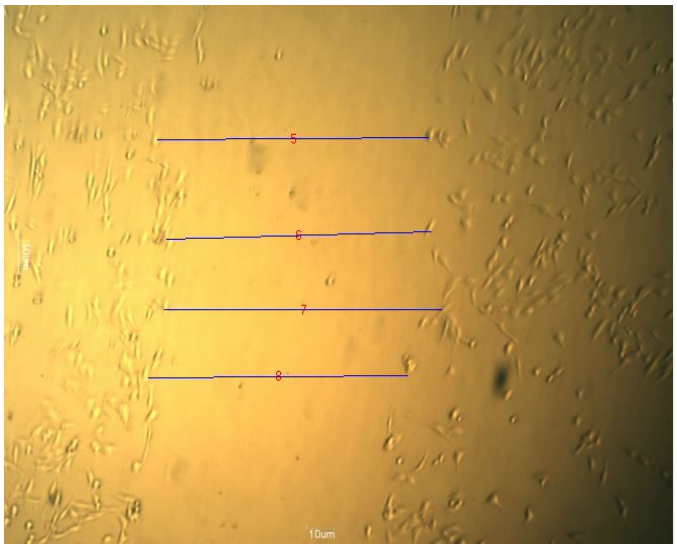

$$\frac{W_{before} - W_{after}}{W_{before}} \times 100\ \%$$

Figure S14 Illustration of scratch assay measurement and equation used for this

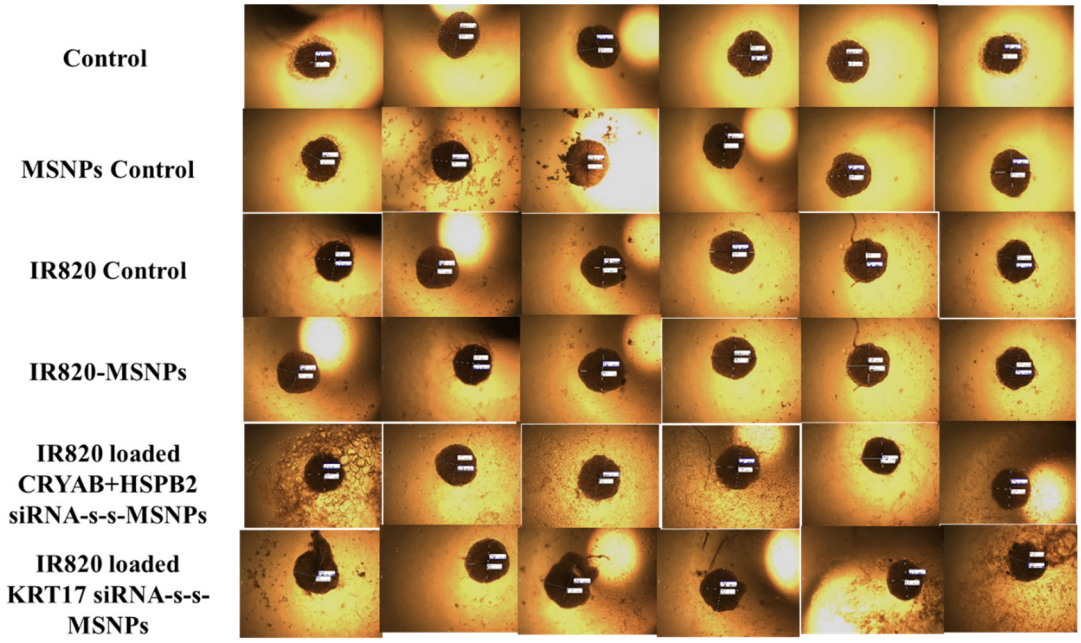

Figure S15 Measurement of RD spheroids treated for 72 hours with PBS, unbound IR820, SH-MSNPs, IR820-loaded MSNPs, IR820-loaded CRYAB & HSPB2-target siRNA-linked MSNPs, or IR820-loaded KRT17-target siRNA-linked MSNP (n=6)

References

Abenhamar Navarro, S., Carrillo, E., Grinan-Lison Carmen and Martin, A., Peran, M., Antonio Marchal, J., & Boulaiz, H. (2016). Cancer suicide gene therapy: a patent review. *EXPERT OPINION ON THERAPEUTIC PATENTS*, *26*(9), 1095–1104. https://doi.org/10.1080/13543776.2016.1211640

Al-Jamal, K. T., Gherardini, L., Bardi, G., Nunes, A., Guo, C., Bussy, C., Herrero, M. A., Bianco, A., Prato, M., Kostarelos, K., & Pizzorusso, T. (2011). Functional motor recovery from brain ischemic insult by carbon nanotube-mediated siRNA silencing. *PROCEEDINGS OF THE NATIONAL ACADEMY OF SCIENCES OF THE UNITED STATES OF*, *108*(27), 10952–10957. https://doi.org/10.1073/pnas.1100930108

Allerson, C. R., Sioufi, N., Jarres, R., Prakash, T. P., Naik, N., Berdeja, A., Wanders, L., Griffey, R. H., Swayze, E. E., & Bhat, B. (2005). Fully 2′-modified oligonucleotide duplexes with improved in vitro potency and stability compared to unmodified small interfering RNA. *JOURNAL OF MEDICINAL CHEMISTRY*, *48*(4), 901–904. https://doi.org/10.1021/JM049167J/SUPPL_FILE/JM049167JSI20041209_020118.PDF

Altanerova, U., Babincova, M., Babinec, P., Benejova, K., Jakubechova, J., Altanerova, V., Zduriencikova, M., Repiska, V., & Altaner, C. (2017). Human mesenchymal stem cell-derived iron oxide exosomes allow targeted ablation of tumor cells via magnetic hyperthermia. *INTERNATIONAL JOURNAL OF NANOMEDICINE*, *12*, 7923.

https://doi.org/10.2147/IJN.S145096
Alvarez-Puebla, R. A., & Liz-Marzán, L. M. (2010). SERS-based diagnosis and biodetection. *SMALL*, *6*(5), 604–610. https://doi.org/10.1002/smll.200901820
Amer, M. H. (2014). Gene therapy for cancer: present status and future perspective. *MOLECULAR AND CELLULAR THERAPIES*, *2*, 27. https://doi.org/10.1186/2052-8426-2-27
Armaghany, T., Wilson, J. D., Chu, Q., & Mills, G. (2012). Genetic Alterations in Colorectal Cancer. *GASTROINTESTINAL CANCER RESEARCH : GCR*, *5*(1), 19. /pmc/articles/PMC3348713/
Arruebo, M., Vilaboa, N., Sáez-Gutierrez, B., Lambea, J., Tres, A., Valladares, M., & González-Fernández, Á. (2011). Assessment of the Evolution of Cancer Treatment Therapies. *CANCERS 2011, Vol. 3, Pages 3279-3330*, *3*(3), 3279–3330. https://doi.org/10.3390/CANCERS3033279
Ars, E., Kruyer, H., Morell, M., Pros, E., Serra, E., Ravella, A., Estivill, X., & Lázaro, C. (2003). Recurrent mutations in the NF1 gene are common among neurofibromatosis type 1 patients. *JOURNAL OF MEDICAL GENETICS*, *40*(6), E82–e82. https://doi.org/10.1136/JMG.40.6.E82
Artiga, A., Serrano-Sevilla, I., de Matteis, L., Mitchell, S. G., & de la Fuente, J. M. (2019). Current status and future perspectives of gold nanoparticle vectors for siRNA delivery. *JOURNAL OF MATERIALS CHEMISTRY B*, *7*(6), 876–896. https://doi.org/10.1039/c8tb02484g
Bacsa, R. R., Laurent, C., Peigney, A., Bacsa, W. S., Vaugien, T., & Rousset, A. (2000). High specific surface area carbon nanotubes from catalytic chemical vapor deposition process. *CHEMICAL PHYSICS LETTERS*, *323*(5–6), 566–571. https://doi.org/10.1016/S0009-2614(00)00558-3
Baek, J. S., & Cho, C. W. (2017). Surface modification of solid lipid nanoparticles for oral delivery of curcumin: Improvement of bioavailability through enhanced cellular uptake, and lymphatic uptake. *EUROPEAN JOURNAL OF PHARMACEUTICS AND BIOPHARMACEUTICS*, *117*, 132–140. https://doi.org/10.1016/J.EJPB.2017.04.013
Basu, A., Persaud, S. D., & Sivaprasad, U. (2008). Chapter 8 Manipulation of PKC Isozymes by RNA Interference and Inducible Expression of PKC Constructs. *METHODS IN ENZYMOLOGY*, *446*, 141–157. https://doi.org/10.1016/S0076-6879(08)01608-X
Benjamin, I. J., Guo, Y., Srinivasan, S., Boudina, S., Taylor, R. P., Rajasekaran, N. S., Gottlieb, R., Wawrousek, E. F., Abel, E. D., & Bolli, R. (2007). CRYAB and HSPB2 deficiency alters cardiac metabolism and paradoxically confers protection against myocardial ischemia in aging mice. *AMERICAN JOURNAL OF PHYSIOLOGY - HEART AND CIRCULATORY PHYSIOLOGY*, *293*(5), 3201–3209. https://doi.org/10.1152/AJPHEART.01363.2006/ASSET/IMAGES/LARGE/ZH401107788000 05.JPEG
Berx, G., & van Roy, F. (2009). Involvement of Members of the Cadherin Superfamily in Cancer. *COLD SPRING HARBOR PERSPECTIVES IN BIOLOGY*, *1*(6), a003129. https://doi.org/10.1101/CSHPERSPECT.A003129
Bhakta, G., Sharma, R. K., Gupta, N., Cool, S., Nurcombe, V., & Maitra, A. (2011). Multifunctional silica nanoparticles with potentials of imaging and gene delivery. *NANOMEDICINE-NANOTECHNOLOGY BIOLOGY AND MEDICINE*, *7*(4), 472–479. https://doi.org/10.1016/j.nano.2010.12.008
Cancer Research UK. (2019). *CANCER IN THE UK 2019*. https://www.cancerresearchuk.org/sites/default/files/state_of_the_nation_april_2019.pdf
Caza, T. N., Hassen, S. I., Dvanajscak, Z., Kuperman, M., Edmondson, R., Herzog, C., Storey, A., Arthur, J., Cossey, L. N., Sharma, S. G., Kenan, D. J., & Larsen, C. P. (2021). NELL1 is a target antigen in malignancy-associated membranous nephropathy. *KIDNEY INTERNATIONAL*, *99*(4), 967–976. https://doi.org/10.1016/J.KINT.2020.07.039
Chabner, B. A., & Roberts, T. G. (2005). Chemotherapy and the war on cancer. *NATURE REVIEWS CANCER 2005 5:1*, *5*(1), 65–72. https://doi.org/10.1038/nrc1529
Chakraborty, S., & Rahman, T. (2012). The difficulties in cancer treatment. *ECANCERMEDICALSCIENCE*, *6*. https://doi.org/10.3332/ECANCER.2012.ED16
Chandradoss, S. D., Haagsma, A. C., Lee, Y. K., Hwang, J. H., Nam, J. M., & Joo, C. (2014). Surface Passivation for Single-molecule Protein Studies. *JOVE (JOURNAL OF VISUALIZED EXPERIMENTS)*, *86*, E50549. https://doi.org/10.3791/50549
Chen, C., Dorado Garcia, H., Scheer, M., & Henssen, A. G. (2019). Current and Future Treatment

Strategies for Rhabdomyosarcoma. *FRONTIERS IN ONCOLOGY*, *9*, 1458. https://doi.org/10.3389/FONC.2019.01458/BIBTEX

Chen, D., Cao, G., Qiao, C., Liu, G., Zhou, H., & Liu, Q. (2018). Alpha B-crystallin promotes the invasion and metastasis of gastric cancer via NF-κB-induced epithelial-mesenchymal transition. *JOURNAL OF CELLULAR AND MOLECULAR MEDICINE*, *22*(6), 3215–3222. https://doi.org/10.1111/JCMM.13602

Chen, J., Guo, Z., Tian, H., & Chen, X. (2016). Production and clinical development of nanoparticles for gene delivery. *MOLECULAR THERAPY-METHODS & CLINICAL DEVELOPMENT*, *3*. https://doi.org/10.1038/mtm.2016.23

Chen, X., Mangala, L. S., Mooberry, L., Bayraktar, E., Dasari, S. K., Ma, S., Ivan, C., Court, K. A., Rodriguez-Aguayo, C., Bayraktar, R., Raut, S., Sabnis, N., Kong, X., Yang, X., Lopez-Berestein, G., Lacko, A. G., & Sood, A. K. (2019). Identifying and targeting angiogenesis-related microRNAs in ovarian cancer. *ONCOGENE*, *38*(33), 6095–6108. https://doi.org/10.1038/s41388-019-0862-y

Chen, X., Zhu, Q., Xu, X., Shen, S., Zhang, Y., & Mo, R. (2019). Sequentially Site-Specific Delivery of Apoptotic Protein and Tumor-Suppressor Gene for Combination Cancer Therapy. *SMALL*, *15*(40). https://doi.org/10.1002/smll.201902998

Chithrani, B. D., Ghazani, A. A., & Chan, W. C. W. (2006). Determining the size and shape dependence of gold nanoparticle uptake into mammalian cells. *NANO LETT.*, *6*. https://doi.org/10.1021/nl052396o

Chivu-Economescu, M., Dragu, D. L., Necula, L. G., Matei, L., Enciu, A. M., Bleotu, C., & Diaconu, C. C. (2017). Knockdown of KRT17 by siRNA induces antitumoral effects on gastric cancer cells. *GASTRIC CANCER*, *20*(6), 948–959. https://doi.org/10.1007/S10120-017-0712-Y/FIGURES/5

Choi, J. Y., Ramasamy, T., Kim, S. Y., Kim, J., Ku, S. K., Youn, Y. S., Kim, J.-R., Jeong, J.-H., Choi, H.-G., Yong, C. S., & Kim, J. O. (2016). PEGylated lipid bilayer-supported mesoporous silica nanoparticle composite for synergistic co-delivery of axitinib and celastrol in multi-targeted cancer therapy. *ACTA BIOMATERIALIA*, *39*, 94–105. https://doi.org/10.1016/j.actbio.2016.05.012

Cowan, C. M., Jiang, X., Hsu, T., Soo, C., Zhang, B., Wang, J. Z., Kuroda, S., Wu, B., Zhang, Z., Zhang, X., & Ting, K. (2007). Synergistic Effects of Nell-1 and BMP-2 on the Osteogenic Differentiation of Myoblasts. *JOURNAL OF BONE AND MINERAL RESEARCH*, *22*(6), 918–930. https://doi.org/10.1359/JBMR.070312

Crisan, M., Yap, S., Casteilla, L., Chen, C. W., Corselli, M., Park, T. S., Andriolo, G., Sun, B., Zheng, B., Zhang, L., Norotte, C., Teng, P. N., Traas, J., Schugar, R., Deasy, B. M., Badylak, S., Buhring, H. J., Giacobino, J. P., Lazzari, L., … Péault, B. (2008). A Perivascular Origin for Mesenchymal Stem Cells in Multiple Human Organs. *CELL STEM CELL*, *3*(3), 301–313. https://doi.org/10.1016/J.STEM.2008.07.003

Crucis, A., Richer, W., Brugières, L., Bergeron, C., Marie-Cardine, A., Stephan, J. L., Girard, P., Corradini, N., Munzer, M., Lacour, B., Minard-Colin, V., Sarnacki, S., Ranchere-Vince, D., Orbach, D., & Bourdeaut, F. (2015). Rhabdomyosarcomas in children with neurofibromatosis type I: A national historical cohort. *PEDIATRIC BLOOD & CANCER*, *62*(10), 1733–1738. https://doi.org/10.1002/PBC.25556

Dai, Z., Song, X.-Z., Cao, J., He, Y., Wen, W., Xu, X., & Tan, Z. (2018). Dual-stimuli-responsive TiOx/DOX nanodrug system for lung cancer synergistic therapy. *RSC ADVANCES*, *8*(39), 21975–21984. https://doi.org/10.1039/c8ra02899k

Dana, H., Mahmoodi Chalbatani, G., Mahmoodzadeh, H., Karimloo, R., Rezaiean, O., Moradzadeh, A., Mehmandoost, N., Moazzen, F., Mazraeh, A., Marmari, V., Ebrahimi, M., Menati Rashno, M., Jan Abadi, S., Gharagouzlo, E., & Mar-mari, V. (2017). Molecular Mechanisms and Biological Functions of siRNA. *International Journal of Biomedical Science : IJBS*, *13*(2), 48. /pmc/articles/PMC5542916/

Davicioni, E., Anderson, M. J., Finckenstein, F. G., Lynch, J. C., Qualman, S. J., Shimada, H., Schofield, D. E., Buckley, J. D., Meyer, W. H., Sorensen, P. H. B., & Triche, T. J. (2009). Molecular Classification of Rhabdomyosarcoma—Genotypic and Phenotypic Determinants of Diagnosis: A Report from the Children's Oncology Group. *THE AMERICAN JOURNAL OF*

PATHOLOGY, *174*(2), 550–564. https://doi.org/10.2353/AJPATH.2009.080631
de Palma, M., Biziato, D., & Petrova, T. v. (2017). Microenvironmental regulation of tumour angiogenesis. *NATURE REVIEWS CANCER*, *17*(8), 457–474. https://doi.org/10.1038/nrc.2017.51
Deisboeck, T. S., Berens, M. E., Kansal, A. R., Torquato, S., Stemmer-Rachamimov, A. O., & Chiocca, E. A. (2001). Pattern of self-organization in tumour systems: complex growth dynamics in a novel brain tumour spheroid model. *CELL PROLIFERATION*, *34*(2), 115–134. https://doi.org/10.1046/J.1365-2184.2001.00202.X
del Pozo-Rodriguez, A., Angeles Solinis, M., & Rodriguez-Gascon, A. (2016). Applications of lipid nanoparticles in gene therapy. *EUROPEAN JOURNAL OF PHARMACEUTICS AND BIOPHARMACEUTICS*, *109*, 184–193. https://doi.org/10.1016/j.ejpb.2016.10.016
Deng, H., Song, K., Zhang, J., Deng, L., Dong, A., & Qin, Z. (2018). Modulating the rigidity of nanoparticles for tumor penetration. *CHEMICAL COMMUNICATIONS*, *54*(24), 3014–3017. https://doi.org/10.1039/c8cc00398j
Depianto, D., Kerns, M. L., Dlugosz, A. A., & Coulombe, P. A. (2010). Keratin 17 promotes epithelial proliferation and tumor growth by polarizing the immune response in skin. *NATURE GENETICS 2010 42:10*, *42*(10), 910–914. https://doi.org/10.1038/ng.665
Devi, G. R. (2006). siRNA-based approaches in cancer therapy. In *CANCER GENE THERAPY* (VOL. 13, ISSUE 9, PP. 819–829). https://doi.org/10.1038/sj.cgt.7700931
Dewi, M. R., Laufersky, G., & Nann, T. (2014). A highly efficient ligand exchange reaction on gold nanoparticles: Preserving their size, shape and colloidal stability. *RSC ADVANCES*, *4*(64), 34217–34220. https://doi.org/10.1039/c4ra05035e
Ding, Y., Jiang, Z., Saha, K., Kim, C. S., Kim, S. T., Landis, R. F., & Rotello, V. M. (2014). Gold nanoparticles for nucleic acid delivery. *MOLECULAR THERAPY*, *22*(6), 1075–1083. https://doi.org/10.1038/mt.2014.30
Dizaj, S. M., Jafari, S., & Khosroushahi, A. Y. (2014). A sight on the current nanoparticle-based gene delivery vectors. *NANOSCALE RESEARCH LETTERS*, *9*. https://doi.org/10.1186/1556-276X-9-252
Dong, Z., Feng, L., Zhu, W., Sun, X., Gao, M., Zhao, H., Chao, Y., & Liu, Z. (2016). CaCO3 nanoparticles as an ultra-sensitive tumor-pH-responsive nanoplatform enabling real-time drug release monitoring and cancer combination therapy. *BIOMATERIALS*, *110*, 60–70. https://doi.org/10.1016/j.biomaterials.2016.09.025
Du, J.-Z., Mao, C.-Q., Yuan, Y.-Y., Yang, X.-Z., & Wang, J. (2014). Tumor extracellular acidity-activated nanoparticles as drug delivery systems for enhanced cancer therapy. *BIOTECHNOLOGY ADVANCES*, *32*(4), 789–803. https://doi.org/10.1016/J.BIOTECHADV.2013.08.002
du Plessis, S. S., Agarwal, A., Mohanty, G., & van der Linde, M. (2015). Oxidative phosphorylation versus glycolysis: what fuel do spermatozoa use? *ASIAN JOURNAL OF ANDROLOGY*, *17*(2), 230. https://doi.org/10.4103/1008-682X.135123
Dunn, M. R., Jimenez, R. M., & Chaput, J. C. (2017). Analysis of aptamer discovery and technology. *NATURE REVIEWS CHEMISTRY 2017 1:10*, *1*(10), 1–16. https://doi.org/10.1038/s41570-017-0076
Durymanov, M., & Reineke, J. (2018). Non-viral Delivery of Nucleic Acids: Insight Into Mechanisms of Overcoming Intracellular Barriers. *FRONTIERS IN PHARMACOLOGY*, *9*. https://doi.org/10.3389/fphar.2018.00971
Duzgunes, N. (2019). Origins of Suicide Gene Therapy. In N. Duzgunes (Ed.), *SUICIDE GENE THERAPY: METHODS AND PROTOCOLS* (Vol. 1895, pp. 1–9). https://doi.org/10.1007/978-1-4939-8922-5_1
Egas-Bejar, D., & Huh, W. W. (2014). Rhabdomyosarcoma in adolescent and young adult patients: current perspectives. *ADOLESCENT HEALTH, MEDICINE AND THERAPEUTICS*, *5*, 115. https://doi.org/10.2147/AHMT.S44582
el Sharkawi, F. Z., Ewais, S. M., Fahmy, R. H., & Rashed, L. A. (2017). PTEN and TRAIL genes loaded zein nanoparticles as potential therapy for hepatocellular carcinoma. *JOURNAL OF DRUG TARGETING*, *25*(6), 513–522. https://doi.org/10.1080/1061186X.2017.1289536
Elbakry, A., Zaky, A., Liebkl, R., Rachel Reinhard and Goepferich, A., & Breunig, M. (2009). Layer-

by-Layer Assembled Gold Nanoparticles for siRNA Delivery. *NANO LETTERS*, *9*(5), 2059–2064. https://doi.org/10.1021/nl9003865

Eloy, J. O., Petrilli, R., & Raspantini Giovanni Loureiro and Lee, R. J. (2018). Targeted Liposomes for siRNA Delivery to Cancer. *CURRENT PHARMACEUTICAL DESIGN*, *24*(23), 2664–2672. https://doi.org/10.2174/1381612824666180807121935

El-Say, K. M., & El-Sawy, H. S. (2017). Polymeric nanoparticles: Promising platform for drug delivery. *INTERNATIONAL JOURNAL OF PHARMACEUTICS*, *528*(1–2), 675–691. https://doi.org/10.1016/j.ijpharm.2017.06.052

Estrela, J. M., Ortega, A., & Obrador, E. (2008). Glutathione in Cancer Biology and Therapy., *43*(2), 143–181. https://doi.org/10.1080/10408360500523878

Fahrenholtz, C. D., Ding, S., Bernish, B. W., Wright, M. L., Zheng, Y., Yang, M., Yao, X., Donati, G. L., Gross, M. D., Bierbach, U., & Singh, R. (2016). Design and cellular studies of a carbon nanotube-based delivery system for a hybrid platinum-acridine anticancer agent. *JOURNAL OF INORGANIC BIOCHEMISTRY*, *165*, 170–180. https://doi.org/10.1016/J.JINORGBIO.2016.07.016

Fang, J., Nakamura, H., & Maeda, H. (2011). The EPR effect: Unique features of tumor blood vessels for drug delivery, factors involved, and limitations and augmentation of the effect. *ADVANCED DRUG DELIVERY REVIEWS*, *63*(3), 136–151. https://doi.org/10.1016/J.ADDR.2010.04.009

Feng, L., Cheng, L., Dong, Z., Tao, D., Barnhart, T. E., Cai, W., Chen, M., & Liu, Z. (2017). Theranostic Liposomes with Hypoxia-Activated Prodrug to Effectively Destruct Hypoxic Tumors Post-Photodynamic Therapy. *ACS NANO*, *11*(1), 927–937. https://doi.org/10.1021/acsnano.6b07525

Feng, Z., Yu, X., Jiang, M., Zhu, L., Zhang, Y., Yang, W., Xi, W., Li, G., & Qian, J. (2019). Excretable IR-820 for in vivo NIR-II fluorescence cerebrovascular imaging and photothermal therapy of subcutaneous tumor. *THERANOSTICS*, *9*(19), 5706. https://doi.org/10.7150/THNO.31332

Fernandes, A. R., & Baptista, P. v. (2017). Gene Silencing Using Multifunctionalized Gold Nanoparticles for Cancer Therapy. In R. Zeineldin (Ed.), *CANCER NANOTECHNOLOGY: METHODS AND PROTOCOLS* (Vol. 1530, pp. 319–336). https://doi.org/10.1007/978-1-4939-6646-2_19

Fialho, L., Araujo, D., Alves, V. D., Roma-Rodrigues, C., Baptista V, P., Fernandes, A. R., Freitas, F., & Reis, M. A. M. (2021). Cation-mediated gelation of the fucose-rich polysaccharide FucoPol: preparation and characterization of hydrogel beads and their cytotoxicity assessment. *INTERNATIONAL JOURNAL OF POLYMERIC MATERIALS AND POLYMERIC BIOMATERIALS*, *70*(2), 90–99. https://doi.org/10.1080/00914037.2019.1695205

Flannery, T., Kano, H., Niranjan, A., Monaco, E. A., Flickinger, J. C., Kofler, J., Lunsford, L. D., & Kondziolka, D. (2010). Gamma Knife Radiosurgery as a Therapeutic Strategy for Intracranial Sarcomatous Metastases. *INTERNATIONAL JOURNAL OF RADIATION ONCOLOGY*BIOLOGY*PHYSICS*, *76*(2), 513–519. https://doi.org/10.1016/J.IJROBP.2009.02.007

Fordham, A. M., Ekert, P. G., & Fleuren, E. D. G. (2021). Precision medicine and phosphoproteomics for the identification of novel targeted therapeutic avenues in sarcomas. *Biochimica et Biophysica Acta (BBA) - REVIEWS ON CANCER*, *1876*(2), 188613. https://doi.org/10.1016/J.BBCAN.2021.188613

Francis, A. P., & Devasena, T. (2018). Toxicity of carbon nanotubes: A review. *TOXICOLOGY AND INDUSTRIAL HEALTH*, *34*(3), 200–210. https://doi.org/10.1177/0748233717747472

Franke, A., Hampe, J., Rosenstiel, P., Becker, C., Wagner, F., Häsler, R., Little, R. D., Huse, K., Ruether, A., Balschun, T., Wittig, M., ElSharawy, A., Mayr, G., Albrecht, M., Prescott, N. J., Onnie, C. M., Fournier, H., Keith, T., Radelof, U., … Schreiber, S. (2007). Systematic Association Mapping Identifies NELL1 as a Novel IBD Disease Gene. *PLOS ONE*, *2*(8), e691. https://doi.org/10.1371/JOURNAL.PONE.0000691

Franzen, C. A., Simms, P. E., van Huis, A. F., Foreman, K. E., Kuo, P. C., & Gupta, G. N. (2014). Characterization of Uptake and Internalization of Exosomes by Bladder Cancer Cells. *BIOMED RESEARCH INTERNATIONAL*, *2014*. https://doi.org/10.1155/2014/619829

Fröhlich, E. (2012). The role of surface charge in cellular uptake and cytotoxicity of medical nanoparticles. *INTERNATIONAL JOURNAL OF NANOMEDICINE*, *7*, 5577. https://doi.org/10.2147/IJN.S36111

Gallego, S., Llort, A., Roma, J., Sabado, C., Gros, L., & Sanchez De Toledo, J. (2006). Detection of bone marrow micrometastasis and microcirculating disease in rhabdomyosarcoma by a real-time RT-PCR assay. *JOURNAL OF CANCER RESEARCH AND CLINICAL ONCOLOGY*, *132*(6), 356–362. https://doi.org/10.1007/S00432-006-0083-Y

Garcia-Pinel, B., Porras-Alcala, C., Ortega-Rodriguez, A., Sarabia, F., Prados, J., & Melguizo Consolacion and Lopez-Romero, J. M. (2019). Lipid-Based Nanoparticles: Application and Recent Advances in Cancer Treatment. *NANOMATERIALS*, *9*(4). https://doi.org/10.3390/nano9040638

Gilligan, K. E., & Dwyer, R. M. (2017). Engineering Exosomes for Cancer Therapy. *INTERNATIONAL JOURNAL OF MOLECULAR SCIENCES*, *18*(6). https://doi.org/10.3390/ijms18061122

Glunde, K., Guggino, S. E., Solaiyappan, M., Pathak, A. P., Ichikawa, Y., & Bhujwalla, Z. M. (2003). Extracellular acidification alters lysosomal trafficking in human breast cancer cells. *NEOPLASIA*, *5*(6), 533–545. https://doi.org/10.1016/S1476-5586(03)80037-4

Gordon, A. T., & McMillan, T. J. (1997). A role for molecular radiobiology in radiotherapy? *CLINICAL ONCOLOGY*, *9*(2), 70–78. https://doi.org/10.1016/S0936-6555(05)80443-1

Gouveia, V. M., Rizzello, L., Nunes, C., Poma, A., Ruiz-Perez, L., Oliveira, A., Reis, S., & Battaglia, G. (2019). Macrophage Targeting pH Responsive Polymersomes for Glucocorticoid Therapy. *PHARMACEUTICS*, *11*(11). https://doi.org/10.3390/PHARMACEUTICS11110614

Grieger, J. C., & Samulski, R. J. (2005). Packaging Capacity of Adeno-Associated Virus Serotypes: Impact of Larger Genomes on Infectivity and Postentry Steps. *JOURNAL OF VIROLOGY*, *79*(15), 9933–9944. https://doi.org/10.1128/JVI.79.15.9933-9944.2005/ASSET/A4E972C0-D213-4C0D-8237-C32F389EC818/ASSETS/GRAPHIC/ZJV0150565900008.JPEG

Grinnell, F. (1994). Fibroblasts, myofibroblasts, and wound contraction. In *JOURNAL OF CELL BIOLOGY* (Vol. 124, Issue 4, pp. 401–404). Rockefeller University Press. https://doi.org/10.1083/jcb.124.4.401

Griset, A. P., Walpole, J., Liu, R., Gaffey, A., Colson, Y. L., & Grinstaff, M. W. (2009). Expansile Nanoparticles: Synthesis, Characterization, and in Vivo Efficacy of an Acid-Responsive Polymeric Drug Delivery System. *JOURNAL OF THE AMERICAN CHEMICAL SOCIETY*, *131*(7), 2469+. https://doi.org/10.1021/ja807416t

Grivennikov, S. I., Greten, F. R., & Karin, M. (2010). Immunity, Inflammation, and Cancer. *CELL*, *140*(6), 883. https://doi.org/10.1016/J.CELL.2010.01.025

Grose, J. H., Langston, K., Wang, X., Squires, S., Mustafi, S. B., Hayes, W., Neubert, J., Fischer, S. K., Fasano, M., Saunders, G. M., Dai, Q., Christians, E., Lewandowski, E. D., Ping, P., & Benjamin, I. J. (2015). Characterization of the cardiac overexpression of HSPB2 reveals mitochondrial and myogenic roles supported by a cardiac HspB2 interactome. *PLOS ONE*, *10*(10). https://doi.org/10.1371/JOURNAL.PONE.0133994

Guan, X. (2015). Cancer metastases: challenges and opportunities. *ACTA PHARMACEUTICA SINICA B*, *5*(5), 402–418. https://doi.org/10.1016/J.APSB.2015.07.005

Guo, Y., Zhao, S., Qiu, H., Wang, T., Zhao, Y., Han, M., Dong, Z., & Wang, X. (2018). Shape of Nanoparticles as a Design Parameter to Improve Docetaxel Antitumor Efficacy. *BIOCONJUGATE CHEMISTRY*, *29*(4), 1302–1311. https://doi.org/10.1021/acs.bioconjchem.8b00059

Hasebe, A., Nakamura, Y., Tashima, H., Takahashi, K., Iijima, M., Yoshimoto, N., Ting, K., Kuroda, S., & Niimi, T. (2012). The C-terminal region of NELL1 mediates osteoblastic cell adhesion through integrin α3β1. *FEBS LETTERS*, *586*(16), 2500–2506. https://doi.org/10.1016/J.FEBSLET.2012.06.014

Heske, C. M., & Mascarenhas, L. (2021). Relapsed Rhabdomyosarcoma. *JOURNAL OF CLINICAL MEDICINE*, *10*(4), 1–15. https://doi.org/10.3390/JCM10040804

Hoffmeier, A., Sindermann, J. R., Scheld, H. H., & Martens, S. (2014). Cardiac Tumors—Diagnosis and Surgical Treatment. *DEUTSCHES ÄRZTEBLATT INTERNATIONAL*, *111*(12), 205. https://doi.org/10.3238/ARZTEBL.2014.0205

Hsiang, Y. H., Hertzberg, R., Hecht, S., & Liu, L. F. (1985). Camptothecin induces protein-linked DNA breaks via mammalian DNA topoisomerase I. *JOURNAL OF BIOLOGICAL CHEMISTRY*, *260*(27), 14873–14878. https://doi.org/10.1016/S0021-9258(17)38654-4

Hu, S.-H., Chen, S.-Y., & Gao, X. (2012). Multifunctional Nanocapsules for Simultaneous Encapsulation of Hydrophilic and Hydrophobic Compounds and On-Demand Release. *ACS NANO*, *6*(3), 2558–2565. https://doi.org/10.1021/nn205023w

Huang, X., & Townley, H. (2016). Knock-down of ELMO1 in Paediatric Rhabdomyosarcoma Cells by Nanoparticle Mediated siRNA Delivery. *NANOBIOMEDICINE*, *3*, 4. https://doi.org/10.5772/62690

Huang, X., Young, N. P., & Townley, H. E. (2014). Characterization and Comparison of Mesoporous Silica Particles for Optimized Drug Delivery. *NANOMATERIALS AND NANOTECHNOLOGY*, *4*(Godište 2014), 4–2. https://doi.org/10.5772/58290

Huang, Y.-P., Hung, C.-M., Hsu, Y.-C., Zhong, C.-Y., Wang, W.-R., Chang, C.-C., & Lee, M.-J. (2016). Suppression of Breast Cancer Cell Migration by Small Interfering RNA Delivered by Polyethylenimine-Functionalized Graphene Oxide. *NANOSCALE RESEARCH LETTERS*, *11*. https://doi.org/10.1186/s11671-016-1463-0

Hu-Lieskovan, S., Heidel, J. D., Bartlett, D. W., Davis, M. E., & Triche, T. J. (2005). Sequence-Specific Knockdown of EWS-FLI1 by Targeted, Nonviral Delivery of Small Interfering RNA Inhibits Tumor Growth in a Murine Model of Metastatic Ewing's Sarcoma. *CANCER RESEARCH*, *65*(19), 8984–8992. https://doi.org/10.1158/0008-5472.CAN-05-0565

Hunter, T., & Garrels, J. I. (1977). Characterization of the mRNAs for α-, β- and γ-actin. *CELL*, *12*(3), 767–781. https://doi.org/10.1016/0092-8674(77)90276-8

Hwang, A. A., Lu, J., Tamanoi, F., & Zink, J. I. (2015). Functional Nanovalves on Protein-Coated Nanoparticles for In vitro and In vivo Controlled Drug Delivery. *SMALL*, *11*(3), 319–328. https://doi.org/10.1002/smll.201400765

Ibnat, N., Kamaruzman, N. I., Ashaie, M., & Chowdhury, E. H. (2019). Transfection with p21 and p53 tumor suppressor plasmids suppressed breast tumor growth in syngeneic mouse model. *GENE*, *701*, 32–40. https://doi.org/10.1016/j.gene.2019.02.082

ISO - ISO/TS 80004-2:2015 - NANOTECHNOLOGIES — VOCABULARY — PART 2: NANO-OBJECTS. (n.d.). Retrieved November 7, 2019, from https://www.iso.org/standard/54440.html

Jain, S., Pathak, K., & Vaidya, A. (2018). Molecular therapy using siRNA: Recent trends and advances of multi target inhibition of cancer growth. *INTERNATIONAL JOURNAL OF BIOLOGICAL MACROMOLECULES*, *116*, 880–892. https://doi.org/10.1016/j.ijbiomac.2018.05.077

James, A. W., Pan, A., Chiang, M., Zara, J. N., Zhang, X., Ting, K., & Soo, C. (2011). A new function of Nell-1 protein in repressing adipogenic differentiation. *BIOCHEMICAL AND BIOPHYSICAL RESEARCH COMMUNICATIONS*, *411*(1), 126–131. https://doi.org/10.1016/J.BBRC.2011.06.111

James, A. W., Shen, J., Zhang, X., Asatrian, G., Goyal, R., Kwak, J. H., Jiang, L., Bengs, B., Culiat, C. T., Turner, A. S., Seim, H. B., Wu, B. M., Lyons, K., Adams, J. S., Ting, K., & Soo, C. (2015). NELL-1 in the treatment of osteoporotic bone loss. *NATURE COMMUNICATIONS 2015 6:1*, *6*(1), 1–14. https://doi.org/10.1038/ncomms8362

Janiszewska, M., Primi, M. C., & Izard, T. (2020). Cell adhesion in cancer: Beyond the migration of single cells. *JOURNAL OF BIOLOGICAL CHEMISTRY*, *295*(8), 2495–2505. https://doi.org/10.1074/JBC.REV119.007759

Jones, R. G., & Thompson, C. B. (2009). Tumor suppressors and cell metabolism: a recipe for cancer growth. *GENES & DEVELOPMENT*, *23*(5), 537–548. https://doi.org/10.1101/GAD.1756509

Kaiser, J. (2020). BIOMEDICINE How safe is a popular gene therapy vector? *SCIENCE*, *367*(6474), 131. https://doi.org/10.1126/science.367.6474.131

Kamimura, K., Yokoo, T., Abe, H., & Terai, S. (2019). Gene Therapy for Liver Cancers: Current Status from Basic to Clinics. *CANCERS*, *11*(12). https://doi.org/10.3390/cancers11121865

Karasik, D., Hsu, Y. H., Zhou, Y., Cupples, L. A., Kiel, D. P., & Demissie, S. (2010). Genome-wide pleiotropy of osteoporosis-related phenotypes: The framingham study. *JOURNAL OF BONE AND MINERAL RESEARCH*, *25*(7), 1555–1563. https://doi.org/10.1002/JBMR.38

Keller, M., Rüegg, A., Werner, S., & Beer, H. D. (2008). Active Caspase-1 Is a Regulator of

Unconventional Protein Secretion. *CELL*, *132*(5), 818–831. https://doi.org/10.1016/J.CELL.2007.12.040

Kerr, B., Delrue, M. A., Sigaudy, S., Perveen, R., Marche, M., Burgelin, I., Stef, M., Tang, B., Eden, O. B., O'Sullivan, J., de Sandre-Giovannoli, A., Reardon, W., Brewer, C., Bennett, C., Quarell, O., M'Cann, E., Donnai, D., Stewart, F., Hennekam, R., … Black, G. (2006). Genotype-phenotype correlation in Costello syndrome: HRAS mutation analysis in 43 cases. *JOURNAL OF MEDICAL GENETICS*, *43*(5), 401–405. https://doi.org/10.1136/JMG.2005.040352

Khawar, I. A., Kim, J. H., & Kuh, H. J. (2015). Improving drug delivery to solid tumors: Priming the tumor microenvironment. *JOURNAL OF CONTROLLED RELEASE*, *201*, 78–89. https://doi.org/10.1016/J.JCONREL.2014.12.018

Kim, H. J., Kim, A., Miyata, K., & Kataoka, K. (2016). Recent progress in development of siRNA delivery vehicles for cancer therapy. In *ADVANCED DRUG DELIVERY REVIEWS* (Vol. 104, pp. 61–77). Elsevier B.V. https://doi.org/10.1016/j.addr.2016.06.011

Kim, H., Kim, S., Kang, S., Song, Y., Shin, S., Lee, S., Kang, M., Nam, S. H., & Lee, Y. (2018). Ring Opening Metathesis Polymerization of Bicyclic α,β-Unsaturated Anhydrides for Ready-to-be-grafted Polymers Having Tailored pH-Responsive Degradability. *ANGEWANDTE CHEMIE INTERNATIONAL EDITION*, *57*(38), 12468–12472. https://doi.org/10.1002/ANIE.201806763

Konieczny, P., Sułkowski, M., Badyra, B., Kijowski, J., & Majka, M. (2017). Suicide gene therapy of rhabdomyosarcoma. *INTERNATIONAL JOURNAL OF ONCOLOGY*, *50*(2), 597–605. https://doi.org/10.3892/IJO.2016.3824/HTML

Koscielniak, E., Rodary, C., Flamant, F., Carli, M., Treuner, J., Pinkerton, C. R., & Grotto, P. (1992). Metastatic rhabdomyosarcoma and histologically similar tumors in childhood: A retrospective european multi-center analysis. *MEDICAL AND PEDIATRIC ONCOLOGY*, *20*(3), 209–214. https://doi.org/10.1002/MPO.2950200305

Koten, J. W., Neijt, J. P., Zonnenberg, B. A., & den Otter, W. (1993). The difference between benign and malignant tumours explained with the 4-mutation paradigm for carcinogenesis. *ANTICANCER RESEARCH*, *13*(4), 1179–1182. https://europepmc.org/article/med/8352541

Krock, B. L., Skuli, N., & Simon, M. C. (2011). Hypoxia-Induced Angiogenesis: Good and Evil. *GENES & CANCER*, *2*(12), 1117. https://doi.org/10.1177/1947601911423654

Kumar, P., Huo, P., & Liu, B. (2019). Formulation Strategies for Folate-Targeted Liposomes and Their Biomedical Applications. *PHARMACEUTICS*, *11*(8). https://doi.org/10.3390/pharmaceutics11080381

Kuroda, S., Oyasu, M., Kawakami, M., Kanayama, N., Tanizawa, K., Saito, N., Abe, T., Matsuhashi, S., & Ting, K. (1999). Biochemical characterization and expression analysis of neural thrombospondin-1-like proteins NELL1 and NELL2. *BIOCHEMICAL AND BIOPHYSICAL RESEARCH COMMUNICATIONS*, *265*(1), 79–86. https://doi.org/10.1006/BBRC.1999.1638

Laird, A. K. (1964). Dynamics of Tumour Growth. *BRITISH JOURNAL OF CANCER*, *18*(3), 490. https://doi.org/10.1038/bjc.1964.55

Lauridsen, L. H., Shamaileh, H. A., Edwards, S. L., Taran, E., & Veedu, R. N. (2012). Rapid One-Step Selection Method for Generating Nucleic Acid Aptamers: Development of a DNA Aptamer against α-Bungarotoxin. *PLOS ONE*, *7*(7), e41702. https://doi.org/10.1371/journal.pone.0041702

Lee, J.-M., Yoon, T.-J., & Cho, Y.-S. (2013). Recent Developments in Nanoparticle-Based siRNA Delivery for Cancer Therapy. *BIOMED RESEARCH INTERNATIONAL*, *2013*. https://doi.org/10.1155/2013/782041

Lei, T., Fernandez-Fernandez, A., Manchanda, R., Huang, Y. C., & McGoron, A. J. (2014). Near-infrared dye loaded polymeric nanoparticles for cancer imaging and therapy and cellular response after laser-induced heating. *BEILSTEIN JOURNAL OF NANOTECHNOLOGY 5:35*, *5*(1), 313–322. https://doi.org/10.3762/BJNANO.5.35

Li, D., Ni, X. F., Tang, H., Zhang, J., Zheng, C., Lin, J., Wang, C., Sun, L., & Chen, B. (2020). KRT17 Functions as a Tumor Promoter and Regulates Proliferation, Migration and Invasion in Pancreatic Cancer via mTOR/S6k1 Pathway. *CANCER MANAGEMENT AND RESEARCH*, *12*, 2087. https://doi.org/10.2147/CMAR.S243129

Li, J., Chen, J., Wang, S., Li, P., Zheng, C., Zhou, X., Tao, Y., Chen, X., Sun, L., Wang, A., Cao, K., Tang, S., & Zhou, J. (2019). Blockage of transferred exosome-shuttled miR-494 inhibits

melanoma growth and metastasis. *JOURNAL OF CELLULAR PHYSIOLOGY*, *234*(9), 15763–15774. https://doi.org/10.1002/jcp.28234

Li, L., Hu, S., & Chen, X. (2018). Non-viral delivery systems for CRISPR/Cas9-based genome editing: Challenges and opportunities. *BIOMATERIALS*, *171*, 207–218. https://doi.org/10.1016/j.biomaterials.2018.04.031

Li, S., Zhao, Z., Wu, W., Ding, C., & Li, J. (2016). Dual pH-responsive micelles with both charge-conversional property and hydrophobic–hydrophilic transition for effective cellular uptake and intracellular drug release. *POLYMER CHEMISTRY*, *7*(12), 2202–2208. https://doi.org/10.1039/C6PY00177G

Li, W., Zara, J. N., Siu, R. K., Lee, M., Aghaloo, T., Zhang, X., Wu, B. M., Gertzman, A. A., Ting, K., & Soo, C. (2011). Nell-1 Enhances Bone Regeneration in a Rat Critical-Sized Femoral Segmental Defect Model. *PLASTIC AND RECONSTRUCTIVE SURGERY*, *127*(2), 580. https://doi.org/10.1097/PRS.0B013E3181FED5AE

Limoni, S. K., Moghadam, M. F., Moazzeni, S. M., Gomari, H., & Salimi, F. (2019). Engineered Exosomes for Targeted Transfer of siRNA to HER2 Positive Breast Cancer Cells. *APPLIED BIOCHEMISTRY AND BIOTECHNOLOGY*, *187*(1), 352–364. https://doi.org/10.1007/S12010-018-2813-4/TABLES/1

Lin, E., Kuo, P. H., Liu, Y. L., Yu, Y. W. Y., Yang, A. C., & Tsai, S. J. (2018). A deep learning approach for predicting antidepressant response in major depression using clinical and genetic biomarkers. *FRONTIERS IN PSYCHIATRY*, *9*(JUL), 290. https://doi.org/10.3389/FPSYT.2018.00290/BIBTEX

Liotta, L. A., Steeg, P. S., & Stetler-Stevenson, W. G. (1991). Cancer metastasis and angiogenesis: An imbalance of positive and negative regulation. *CELL*, *64*(2), 327–336. https://doi.org/10.1016/0092-8674(91)90642-C

Liu, H., Rajasekaran, A. K., Moy, P., Xia, Y., Kim, S., Navarro, V., Rahmati, R., & Bander, N. H. (1998). Constitutive and antibody-induced internalization of prostate-specific membrane antigen. *CANCER RESEARCH*, *58*(18), 4055–4060.

Liu, S., Yan, B., Lai, W., Chen, L., Xiao, D., Xi, S., Jiang, Y., Dong, X., An, J., Chen, X., Cao, Y., & Tao, Y. (2014). As a novel p53 direct target, bidirectional gene HspB2/αB-crystallin regulates the ROS level and Warburg effect. *BIOCHIMICA ET BIOPHYSICA ACTA (BBA) - GENE REGULATORY MECHANISMS*, *1839*(7), 592–603. https://doi.org/10.1016/J.BBAGRM.2014.05.017

Liu, T., Zhou, L., Li, D., Andl, T., & Zhang, Y. (2019). Cancer-Associated Fibroblasts Build and Secure the Tumor Microenvironment. *FRONTIERS IN CELL AND DEVELOPMENTAL BIOLOGY*, *7*(APR). https://doi.org/10.3389/FCELL.2019.00060

Llen, E., Apiteijn, K., Arijnen, O. A. M. M., Agtegaal, R. D. N., Teup, I. H. S., Heo, T., Iggers, W., Utten, A. J. T. R., Ars, L., Ahlman, P., Limelius, G., An, J. H., van K Rieken, J. M., Eer, A. W. H. L., Ornelis, C., van de V Elde, J. H., Olorectal, C., Ancer, C., & Roup, G. (2009). Preoperative Radiotherapy Combined with Total Mesorectal Excision for Resectable Rectal Cancer. https://doi.org/10.1056/NEJMOA010580

Lomas, H., Du, J., Canton, I., Madsen, J., Warren, N., Armes, S. P., Lewis, A. L., & Battaglia, G. (2010). Efficient Encapsulation of Plasmid DNA in pH-Sensitive PMPC–PDPA Polymersomes: Study of the Effect of PDPA Block Length on Copolymer–DNA Binding Affinity. *MACROMOLECULAR BIOSCIENCE*, *10*(5), 513–530. https://doi.org/10.1002/MABI.201000083

Lopez-Lazaro, M. (2008). The Warburg Effect: Why and How Do Cancer Cells Activate Glycolysis in the Presence of Oxygen? *ANTI-CANCER AGENTS IN MEDICINAL CHEMISTRY*, *8*(3), 305–312. https://doi.org/10.2174/187152008783961932

Lugano, R., Ramachandran, M., & Dimberg, A. (2020). Tumor angiogenesis: causes, consequences, challenges and opportunities. *CELLULAR AND MOLECULAR LIFE SCIENCES*, *77*(9), 1745–1770. https://doi.org/10.1007/s00018-019-03351-7

Lundstrom, K. (2018). Viral Vectors in Gene Therapy. *DISEASES (Basel, Switzerland)*, *6*(2). https://doi.org/10.3390/diseases6020042

Lychou, S. E., Gustafsson, G. G., & Ljungman, G. E. (2016). Higher rates of metastatic disease may explain the declining trend in Swedish paediatric rhabdomyosarcoma survival rates. *Acta*

PAEDIATRICA (Oslo, Norway : 1992), *105*(1), 74–81. https://doi.org/10.1111/APA.13172
Ma, X., Lee, N.-H., Oh, H.-J., Kim, J.-W., Rhee, C.-K., Park, K.-S., & Kim, S.-J. (2010). Surface modification and characterization of highly dispersed silica nanoparticles by a cationic surfactant. *COLLOIDS AND SURFACES A: PHYSICOCHEMICAL AND ENGINEERING ASPECTS*, *358*(1–3), 172–176. https://doi.org/10.1016/J.COLSURFA.2010.01.051
Maeda, K., Matsuhashi, S., Tabuchi, K., Watanabe, T., Katagiri, T., Oyasu, M., Saito, N., & Kuroda, S. I. (2001). Brain specific human genes, NELL1 and NELL2, are predominantly expressed in neuroblastoma and other embryonal neuroepithelial tumors. *NEUROLOGIA MEDICO-CHIRURGICA*, *41*(12), 582–588. https://doi.org/10.2176/nmc.41.582
Maeder, M. L., & Gersbach, C. A. (2016). Genome-editing Technologies for Gene and Cell Therapy. *MOLECULAR THERAPY*, *24*(3), 430–446. https://doi.org/10.1038/mt.2016.10
Magnusson, S., Gisselsson, D., Wiebe, T., Kristoffersson, U., Borg, Å., & Olsson, H. (2012). Prevalence of germline TP53 mutations and history of Li–Fraumeni syndrome in families with childhood adrenocortical tumors, choroid plexus tumors, and rhabdomyosarcoma: A population-based survey. *PEDIATRIC BLOOD & CANCER*, *59*(5), 846–853. https://doi.org/10.1002/PBC.24223
Magro, M., Martinello, T., Bonaiuto, E., Gomiero, C., Baratella, D., Zoppellaro, G., Cozza, G., Patruno, M., Zboril, R., & Vianello, F. (2017). Covalently bound DNA on naked iron oxide nanoparticles: Intelligent colloidal nano-vector for cell transfection. *BIOCHIMICA ET BIOPHYSICA ACTA-GENERAL SUBJECTS*, *1861*(11, A), 2802–2810. https://doi.org/10.1016/j.bbagen.2017.07.025
Manchun, S., Dass, C. R., & Sriamornsak, P. (2012). Targeted therapy for cancer using pH-responsive nanocarrier systems. In *LIFE SCIENCES* (Vol. 90, Issues 11–12, pp. 381–387). Pergamon. https://doi.org/10.1016/j.lfs.2012.01.008
Marshall, A. D., & Grosveld, G. C. (2012). Alveolar rhabdomyosarcoma - The molecular drivers of PAX3/7-FOXO1-induced tumorigenesis. *Skeletal Muscle*, *2*(1), 1–14. https://doi.org/10.1186/2044-5040-2-25/FIGURES/2
Mashouri, L., Yousefi, H., Aref, A. R., Ahadi, A. M., Molaei, F., & Alahari, S. K. (2019). Exosomes: composition, biogenesis, and mechanisms in cancer metastasis and drug resistance. *MOLECULAR CANCER*, *18*. https://doi.org/10.1186/s12943-019-0991-5
Mathieu, F., Etain, B., Dizier, M. H., Lajnef, M., Lathrop, M., Cabon, C., Leboyer, M., Henry, C., & Bellivier, F. (2015). Genetics of emotional reactivity in bipolar disorders. *JOURNAL OF AFFECTIVE DISORDERS*, *188*, 101–106. https://doi.org/10.1016/J.JAD.2015.08.037
Matsumura, Y., & Maeda, H. (1986). A New Concept for Macromolecular Therapeutics in Cancer Chemotherapy: Mechanism of Tumoritropic Accumulation of Proteins and the Antitumor Agent Smancs1. *CANCER RESEARCH*, *46*(12_Part_1), 6387–6392.
Matyjaszewski, K., & Xia, J. (2001). Atom Transfer Radical Polymerization. *Chemical Reviews*, *101*(9), 2921–2990. https://doi.org/10.1021/CR940534G
McBain, S. C., Yiu, H. H. P., & Dobson, J. (2008). Magnetic nanoparticles for gene and drug delivery. *INTERNATIONAL JOURNAL OF NANOMEDICINE*, *3*(2), 169–180.
McNeish, I. A., Bell, S. J., & Lemoine, N. R. (2004). Gene therapy progress and prospects: cancer gene therapy using tumour suppressor genes. *GENE THERAPY*, *11*(6), 497–503. https://doi.org/10.1038/sj.gt.3302238
Mehta, A., Vedove, E. D., Isert, L., & Merkel, O. M. (2019). Targeting KRAS Mutant Lung Cancer Cells with siRNA-Loaded Bovine Serum Albumin Nanoparticles. *PHARMACEUTICAL RESEARCH*, *36*(9). https://doi.org/10.1007/s11095-019-2665-9
Mi, P., Kokuryo, D., Cabral, H., Wu, H., Terada, Y., Saga, T., Aoki, I., & Nishiyama Nobuhiro and Kataoka, K. (2016). A pH-activatable nanoparticle with signal-amplification capabilities for non-invasive imaging of tumour malignancy. *NATURE NANOTECHNOLOGY*, *11*(8), 724+. https://doi.org/10.1038/NNANO.2016.72
Mishra, V., Bansal, K. K., Verma, A., Yadav Nishika and Thakur, S., Sudhakar, K., & Rosenholm, J. M. (2018). Solid Lipid Nanoparticles: Emerging Colloidal Nano Drug Delivery Systems. *PHARMACEUTICS*, *10*(4). https://doi.org/10.3390/pharmaceutics10040191
Mitkevich, V. A., Burnysheva, K. M., Ilinskaya, O. N., Pace, C. N., & Makarov, A. A. (2014). Cytotoxicity of RNase Sa to the acute myeloid leukemia Kasumi-1 cells depends on the net

charge. *ONCOSCIENCE*, *1*(11), 738. https://doi.org/10.18632/ONCOSCIENCE.97
Mohan, S., Oluwafemi, O. S., Kalarikkal, N., Thomas, S., & Songca, S. P. (2016). Biopolymers - Application in Nanoscience and Nanotechnology. In F. K. Perveen (Ed.), *RECENT ADVANCES IN BIOPOLYMERS* (pp. 47–72). https://doi.org/10.5772/62225
Moisoiu, V., Iancu, S. D., Stefancu, A., Moisoiu, T., Pardini, B., Dragomir, M. P., Crisan, N., Avram, L., Crisan, D., Andras, I., Fodor, D., Leopold, L. F., Socaciu, C., Bálint, Z., Tomuleasa, C., Elec, F., & Leopold, N. (2021). SERS liquid biopsy: An emerging tool for medical diagnosis. *COLLOIDS AND SURFACES B: BIOINTERFACES*, *208*, 112064. https://doi.org/10.1016/J.COLSURFB.2021.112064
Moll, R., Divo, M., & Langbein, L. (2008). The human keratins: Biology and pathology. *HISTOCHEMISTRY AND CELL BIOLOGY*, *129*(6), 705–733. https://doi.org/10.1007/S00418-008-0435-6/FIGURES/6
Möller, K., Müller, K., Engelke, H., Bräuchle, C., Wagner, E., & Bein, T. (2016). Highly efficient siRNA delivery from core–shell mesoporous silica nanoparticles with multifunctional polymer caps. *NANOSCALE*, *8*(7), 4007–4019. https://doi.org/10.1039/C5NR06246B
Moolgavkar, S. H. (1993). Cell proliferation and carcinogenesis models: general principles with illustrations from the rodent liver system. *ENVIRONMENTAL HEALTH PERSPECTIVES*, *101*(Suppl 5), 91. https://doi.org/10.1289/EHP.93101S591
Moon, S. bin, Kim, D. Y., Ko, J.-H., & Kim, Y.-S. (2019). Recent advances in the CRISPR genome editing tool set. *EXPERIMENTAL AND MOLECULAR MEDICINE*, *51*. https://doi.org/10.1038/s12276-019-0339-7
Moore, E. C., Sun, L., Clavijo, P. E., Friedman Jay and Harford, J. B., Saleh, A. D., van Waes, C., Chang, E. H., & Allen, C. T. (2018). Nanocomplex-based TP53 gene therapy promotes anti-tumor immunity through TP53-and STING-dependent mechanisms. *ONCOIMMUNOLOGY*, *7*(7). https://doi.org/10.1080/2162402X.2017.1404216
Muniswamy, V. J., Raval, N., Gondaliya, P., Tambe, V., Kalia, K., & Tekade, R. K. (2019). `Dendrimer-Cationized-Albumin' encrusted polymeric nanoparticle improves BBB penetration and anticancer activity of doxorubicin. *INTERNATIONAL JOURNAL OF PHARMACEUTICS*, *555*, 77–99. https://doi.org/10.1016/j.ijpharm.2018.11.035
Mura, S., Nicolas, J., & Couvreur, P. (2013). Stimuli-responsive nanocarriers for drug delivery. *NATURE MATERIALS*, *12*(11), 991–1003. https://doi.org/10.1038/nmat3776
Murugadoss, S., Lison, D., Godderis, L., Van den Brule, S., Mast, J., Brassinne, F., Sebaihi, N., & Hoet, P. H. (2017). Toxicology of silica nanoparticles: an update. *ARCHIVES OF TOXICOLOGY*, *91*(9), 2967–3010. https://doi.org/10.1007/s00204-017-1993-y
Na, H. K., Kim, M. H., Park, K., Ryoo, S. R., Lee, K. E., Jeon, H., Ryoo, R., Hyeon, C., & Min, D. H. (2012). Efficient Functional Delivery of siRNA using Mesoporous Silica Nanoparticles with Ultralarge Pores. *SMALL*, *8*(11), 1752–1761. https://doi.org/10.1002/SMLL.201200028
Nakamura, Y., Mochida, A., Choyke, P. L., & Kobayashi, H. (2016). Nanodrug Delivery: Is the Enhanced Permeability and Retention Effect Sufficient for Curing Cancer? *BIOCONJUGATE CHEMISTRY*, *27*(10), 2225–2238. https://doi.org/10.1021/ACS.BIOCONJCHEM.6B00437/ASSET/IMAGES/ACS.BIOCONJCHEM.6B00437.SOCIAL.JPEG_V03
Nam, H. Y., Kwon, S. M., Chung, H., Lee, S. Y., Kwon, S. H., Jeon, H., Kim, Y., Park, J. H., Kim, J., Her, S., Oh, Y. K., Kwon, I. C., Kim, K., & Jeong, S. Y. (2009). Cellular uptake mechanism and intracellular fate of hydrophobically modified glycol chitosan nanoparticles. *JOURNAL OF CONTROLLED RELEASE*, *135*(3), 259–267. https://doi.org/10.1016/J.JCONREL.2009.01.018
Nandiyanto, A. B. D., Kim, S. G., Iskandar, F., & Okuyama, K. (2009). Synthesis of spherical mesoporous silica nanoparticles with nanometer-size controllable pores and outer diameters. *MICROPOROUS AND MESOPOROUS MATERIALS*, *120*(3), 447–453. https://doi.org/10.1016/J.MICROMESO.2008.12.019
Navarro, G., Sawant, R. R., Biswas, S., Essex, S., de Ilarduya, C., & Torchilin, V. P. (2012). P-glycoprotein silencing with siRNA delivered by DOPE-modified PEI overcomes doxorubicin resistance in breast cancer cells. *NANOMEDICINE*, *7*(1), 65–78. https://doi.org/10.2217/NNM.11.93
Ngamcherdtrakul, W., Morry, J., Gu, S., Castro, D. J., Goodyear, S. M., Sangvanich, T., Reda, M.

M., Lee, R., Mihelic, S. A., Beckman, B. L., Hu, Z., Gray, J. W., & Yantasee, W. (2015). Cationic Polymer Modified Mesoporous Silica Nanoparticles for Targeted siRNA Delivery to HER2+ Breast Cancer. *ADVANCED FUNCTIONAL MATERIALS*, *25*(18), 2646–2659. https://doi.org/10.1002/ADFM.201404629

Nitta, S. K., & Numata, K. (2013). Biopolymer-Based Nanoparticles for Drug/Gene Delivery and Tissue Engineering. *INTERNATIONAL JOURNAL OF MOLECULAR SCIENCES*, *14*(1), 1629–1654. https://doi.org/10.3390/ijms14011629

Nizardo, N. M., Schanzenbach, D., Schönemann, E., & Laschewsky, A. (2018). Exploring Poly(ethylene glycol)-Polyzwitterion Diblock Copolymers as Biocompatible Smart Macrosurfactants Featuring UCST-Phase Behavior in Normal Saline Solution. *POLYMERS 2018, Vol. 10, Page 325*, *10*(3), 325. https://doi.org/10.3390/POLYM10030325

Nur, U., Quaresma, M., de Stavola, B., Peake, M., & Rachet, B. (2015). Inequalities in non-small cell lung cancer treatment and mortality. *J EPIDEMIOL COMMUNITY HEALTH*, *69*(10), 985–992. https://doi.org/10.1136/JECH-2014-205309

Ognjanovic, S., Linabery, A. M., Charbonneau, B., & Ross, J. A. (2009). Trends in Childhood Rhabdomyosarcoma Incidence and Survival in the United States (1975–2005). *CANCER*, *115*(18), 4218. https://doi.org/10.1002/CNCR.24465

Okada, H., & Mak, T. W. (2004). Pathways of apoptotic and non-apoptotic death in tumour cells. *NATURE REVIEWS CANCER 2004 4:8*, *4*(8), 592–603. https://doi.org/10.1038/nrc1412

Ou, L., Song, B., Liang, H., Liu, J., Feng, X., Deng, B., Sun, T., & Shao, L. (2016). Toxicity of graphene-family nanoparticles: a general review of the origins and mechanisms. *PARTICLE AND FIBRE TOXICOLOGY 2016 13:1*, *13*(1), 1–24. https://doi.org/10.1186/S12989-016-0168-Y

Pan, L., He, Q., Liu, J., Chen, Y., Ma, M., Zhang, L., & Shi, J. (2012). Nuclear-targeted drug delivery of tat peptide-conjugated monodisperse mesoporous silica nanoparticles. *JOURNAL OF THE AMERICAN CHEMICAL SOCIETY*, *134*(13), 5722–5725. https://doi.org/10.1021/ja211035w

Pang, S., Shen, J., Liu, Y., Chen, F., Zheng, Z., James, A. W., Hsu, C. Y., Zhang, H., Lee, K. S., Wang, C., Li, C., Chen, X., Jia, H., Zhang, X., Soo, C., & Ting, K. (2015). Proliferation and osteogenic differentiation of mesenchymal stem cells induced by a short isoform of NELL-1. *STEM CELLS*, *33*(3), 904–915. https://doi.org/10.1002/stem.1884

Panzarasa, G., Soliveri, G., & Pifferi, V. (2015). Tuning the electrochemical properties of silicon wafer by grafted-from micropatterned polymer brushes. *JOURNAL OF MATERIALS CHEMISTRY C*, *4*(2), 340–347. https://doi.org/10.1039/C5TC03367E

Pappo, A. S., Shapiro, D. N., & Crist, W. M. (1997). RHABDOMYOSARCOMA: Biology and Treatment. *PEDIATRIC CLINICS OF NORTH AMERICA*, *44*(4), 953–972. https://doi.org/10.1016/S0031-3955(05)70539-3

Parham, D. M., & Barr, F. G. (2013). Classification of Rhabdomyosarcoma and Its Molecular Basis. *ADVANCES IN ANATOMIC PATHOLOGY*, *20*(6), 387. https://doi.org/10.1097/PAP.0B013E3182A92D0D

Patil, S., Gao, Y.-G., Lin, X., Li, Y., Dang, K., Tian, Y., Zhang, W.-J., Jiang, S.-F., Qadir, A., & Qian, A.-R. (2019). The Development of Functional Non-Viral Vectors for Gene Delivery. *INTERNATIONAL JOURNAL OF MOLECULAR SCIENCES*, *20*(21). https://doi.org/10.3390/ijms20215491

Pegoraro, C., Cecchin, D., Gracia, L. S., Warren, N., Madsen, J., Armes, S. P., Lewis, A., MacNeil, S., & Battaglia, G. (2013). Enhanced drug delivery to melanoma cells using PMPC-PDPA polymersomes. *CANCER LETTERS*, *334*(2), 328–337. https://doi.org/10.1016/J.CANLET.2013.02.007

Peng, J., & Liang, X. (2019). Progress in research on gold nanoparticles in cancer management. *MEDICINE*, *98*(18). https://doi.org/10.1097/MD.0000000000015311

Peng, L.-H., Huang, Y.-F., Zhang, C.-Z., Niu, J., Chen, Y., Chu, Y., Jiang, Z.-H., Gao, J.-Q., & Mao, Z.-W. (2016). Integration of antimicrobial peptides with gold nanoparticles as unique non-viral vectors for gene delivery to mesenchymal stem cells with antibacterial activity. *BIOMATERIALS*, *103*, 137–149. https://doi.org/10.1016/j.biomaterials.2016.06.057

Peng, X.-H., Qian, X., Mao, H., Wang, A. Y., Chen, Z. (Georgia), Nie, S., & Shin, D. M. (2008). Targeted magnetic iron oxide nanoparticles for tumor imaging and therapy. *INTERNATIONAL*

JOURNAL OF NANOMEDICINE, *3*(3), 311–321.
Potter, M., Newport, E., & Morten, K. J. (2016). The Warburg effect: 80 years on. *BIOCHEMICAL SOCIETY TRANSACTIONS*, *44*(5), 1499–1505. https://doi.org/10.1042/BST20160094
Pozzo, E., Giarratana, N., Sassi, G., Elmastas, M., Killian, T., Wang, C. C., Marini, V., Ronzoni, F., Yustein, J., Uyttebroeck, A., & Sampaolesi, M. (2021). Upregulation of miR181a/miR212 Improves Myogenic Commitment in Murine Fusion-Negative Rhabdomyosarcoma. *FRONTIERS IN PHYSIOLOGY*, *12*, 1146. https://doi.org/10.3389/FPHYS.2021.701354/BIBTEX
Pucci, C., Martinelli, C., & Ciofani, G. (2019). Innovative approaches for cancer treatment: current perspectives and new challenges. *ECANCERMEDICALSCIENCE*, *13*. https://doi.org/10.3332/ECANCER.2019.961
Putz, A.-M., Cecilia, S., Ianasi, C., Dudas Zoltan and Szekely, K. N., Plocek, J., Sfarloaga, P., Sacarescu, L., & Almasy, L. (2015). Pore ordering in mesoporous matrices induced by different directing agents. *JOURNAL OF POROUS MATERIALS*, *22*(2), 321–331. https://doi.org/10.1007/s10934-014-9899-z
Qiu, M., Wang, D., Liang, W., Liu, L., Zhang, Y., Chen, X., Sang, D. K., Xing, C., Li, Z., Dong, B., Xing, F., Fan, D., Bao, S., Zhang, H., & Cao, Y. (2018). Novel concept of the smart NIR-light-controlled drug release of black phosphorus nanostructure for cancer therapy. *PROCEEDINGS OF THE NATIONAL ACADEMY OF SCIENCES OF THE UNITED STATES OFAMERICA*, *115*(3), 501–506. https://doi.org/10.1073/pnas.1714421115
Quail, D. F., & Joyce, J. A. (2013). Microenvironmental regulation of tumor progression and metastasis. *NATURE MEDICINE*, *19*(11), 1423. https://doi.org/10.1038/NM.3394
Rapa, E., Hill, S. K., Morten, K. J., Potter, M., & Mitchell, C. (2012). The over-expression of cell migratory genes in alveolar rhabdomyosarcoma could contribute to metastatic spread. *CLINICAL AND EXPERIMENTAL METASTASIS*, *29*(5), 419–429. https://doi.org/10.1007/S10585-012-9460-X/FIGURES/7
Ray, S. C., Saha, A., Jana, N. R., & Sarkar, R. (2009). Fluorescent Carbon Nanoparticles: Synthesis, Characterization, and Bioimaging Application. *THE JOURNAL OF PHYSICAL CHEMISTRY C*, *113*(43), 18546–18551. https://doi.org/10.1021/jp905912n
Roma-Rodrigues, C., Fernandes, A. R., & Baptista, P. V. (2014). Exosome in Tumour Microenvironment: Overview of the Crosstalk between Normal and Cancer Cells. *BIOMED RESEARCH INTERNATIONAL*, *2014*. https://doi.org/10.1155/2014/179486
Roma-rodrigues, C., Rivas-garcía, L., Baptista, P. v., & Fernandes, A. R. (2020). Gene Therapy in Cancer Treatment: Why Go Nano? *PHARMACEUTICS 2020, VOL. 12, Page 233*, *12*(3), 233. https://doi.org/10.3390/PHARMACEUTICS12030233
Rossi, G. R., Trindade, E. S., & Souza-Fonseca-Guimaraes, F. (2020). Tumor Microenvironment-Associated Extracellular Matrix Components Regulate NK Cell Function. *FRONTIERS IN IMMUNOLOGY*, *11*, 73. https://doi.org/10.3389/FIMMU.2020.00073
Rudzinski, E. R., Anderson, J. R., Hawkins, D. S., Skapek, S. X., Parham, D. M., & Teot, L. A. (2015). The World Health Organization Classification of Skeletal Muscle Tumors in Pediatric Rhabdomyosarcoma: A Report From the Children's Oncology Group. *ARCHIVES OF PATHOLOGY & LABORATORY MEDICINE*, *139*(10), 1281. https://doi.org/10.5858/ARPA.2014-0475-OA
Ryou, S.-M., Kim, J.-M., Yeom, J.-H., Hyun Seogang and Kim, S., Han, M. S., Kim, S. W., Bae, J., Rhee, S., & Lee, K. (2011). Gold nanoparticle-assisted delivery of small, highly structured RNA into the nuclei of human cells. *BIOCHEMICAL AND BIOPHYSICAL RESEARCH COMMUNICATIONS*, *416*(1–2), 178–183. https://doi.org/10.1016/j.bbrc.2011.11.020
Sankar, S., Tanner, J. M., Bell, R., Chaturvedi, A., Randall, R. L., Beckerle, M. C., & Lessnick, S. L. (2013). A Novel Role for Keratin 17 in Coordinating Oncogenic Transformation and Cellular Adhesion in Ewing Sarcoma. *MOLECULAR AND CELLULAR BIOLOGY*, *33*(22), 4448–4460. https://doi.org/10.1128/MCB.00241-13/SUPPL_FILE/ZMB999100193SO1.PDF
Santo, D., Mendonca, P. v, Lima, M. S., Cordeiro, R. A., Cabanas, L., Serra, A., Coelho, J. F. J., & Faneca, H. (2019). Poly(ethylene glycol)-block-poly(2-aminoethyl methacrylate hydrochloride)-Based Polyplexes as Serum-Tolerant Nanosystems for Enhanced Gene Delivery. *MOLECULAR PHARMACEUTICS*, *16*(5), 2129–2141.

https://doi.org/10.1021/acs.molpharmaceut.9b00101
Santos-Carballal, B., Aaldering, L. J., Ritzefeld, M., Pereira, S., Sewald, N., Moerschbacher, B. M., Götte, M., & Goycoolea, F. M. (2015). Physicochemical and biological characterization of chitosan-microRNA nanocomplexes for gene delivery to MCF-7 breast cancer cells. *SCIENTIFIC REPORTS 2015 5:1*, *5*(1), 1–15. https://doi.org/10.1038/srep13567
Scarabelli, L., Coronado-Puchau, M., Giner-Casares, J. J., Langer, J., & Liz-Marzán, L. M. (2014a). Monodisperse Gold Nanotriangles: Size Control, Large-Scale Self-Assembly, and Performance in Surface-Enhanced Raman Scattering. *ACS NANO*, *8*(6), 5833–5842. https://doi.org/10.1021/nn500727w
Schiliro, C., & Firestein, B. L. (2021). Mechanisms of Metabolic Reprogramming in Cancer Cells Supporting Enhanced Growth and Proliferation. *CELLS*, *10*(5). https://doi.org/10.3390/CELLS10051056
Sears, R. C., & Nevins, J. R. (2002). Signaling Networks That Link Cell Proliferation and Cell Fate *. *JOURNAL OF BIOLOGICAL CHEMISTRY*, *277*(14), 11617–11620. https://doi.org/10.1074/JBC.R100063200
Senapati, D., Patra, B. C., Kar, A., Chini, D. S., Ghosh, S., Patra, S., & Bhattacharya, M. (2019). Promising approaches of small interfering RNAs (siRNAs) mediated cancer gene therapy. *GENE*, *719*. https://doi.org/10.1016/j.gene.2019.144071
Setten, R. L., Rossi, J. J., & Han, S. (2019). The current state and future directions of RNAi-based therapeutics. *NATURE REVIEWS DRUG DISCOVERY*, *18*(6), 421–446. https://doi.org/10.1038/s41573-019-0017-4
Shao, L., Kahraman, N., Yan, G., Wang, J., Ozpolat, B., & Ittmann, M. (2020). Targeting the TMPRSS2/ERG fusion mRNA using liposomal nanovectors enhances docetaxel treatment in prostate cancer. *PROSTATE*, *80*(1), 65–73. https://doi.org/10.1002/pros.23918
Shao, Y.-T., Ma, L., Zhang, T.-H., Xu, T.-R., Ye, Y.-C., & Liu, Y. (2019). The Application of the RNA Interference Technologies for KRAS: Current Status, Future Perspective and Associated Challenges. *CURRENT TOPICS IN MEDICINAL CHEMISTRY*, *19*(23), 2143–2157. https://doi.org/10.2174/1568026619666190828162217
Shen, J., James, A. W., Zhang, X., Pang, S., Zara, J. N., Asatrian, G., Chiang, M., Lee, M., Khadarian, K., Nguyen, A., Lee, K. S., Siu, R. K., Tetradis, S., Ting, K., & Soo, C. (2016). Novel Wnt Regulator NEL-Like Molecule-1 Antagonizes Adipogenesis and Augments Osteogenesis Induced by Bone Morphogenetic Protein 2. *THE AMERICAN JOURNAL OF PATHOLOGY*, *186*(2), 419–434. https://doi.org/10.1016/J.AJPATH.2015.10.011
Shen, J., Kim, H. C., Su, H., Wang, F., Wolfram, J., Kirui, D., Mai, J., Mu, C., Ji, L. N., Mao, Z. W., & Shen, H. (2014). Cyclodextrin and Polyethylenimine Functionalized Mesoporous Silica Nanoparticles for Delivery of siRNA Cancer Therapeutics. *THERANOSTICS*, *4*(5), 487. https://doi.org/10.7150/THNO.8263
Sheoran, R., Khokra, S. L., Chawla, V., & Dureja, H. (2019). Recent Patents, Formulation Techniques, Classification and Characterization of Liposomes. *RECENT PATENTS ON NANOTECHNOLOGY*, *13*(1), 17–27. https://doi.org/10.2174/1872210513666181127110413
Shern, J. F., Chen, L., Chmielecki, J., Wei, J. S., Patidar, R., Rosenberg, M., Ambrogio, L., Auclair, D., Wang, J., Song, Y. K., Tolman, C., Hurd, L., Liao, H., Zhang, S., Bogen, D., Brohl, A. S., Sindiri, S., Catchpoole, D., Badgett, T., … Khan, J. (2014). Comprehensive genomic analysis of rhabdomyosarcoma reveals a landscape of alterations affecting a common genetic axis in fusion-positive and fusion-negative tumors. *CANCER DISCOVERY*, *4*(2), 216. https://doi.org/10.1158/2159-8290.CD-13-0639
Sherwood, L. M., Parris, E. E., & Folkman, J. (1971). Tumor angiogenesis: therapeutic implications. *THE NEW ENGLAND JOURNAL OF MEDICINE*, *285*(21), 1182–1186. https://doi.org/10.1056/NEJM197111182852108
Shi, J., Kantoff, P. W., Wooster, R., & Farokhzad, O. C. (2017). Cancer nanomedicine: progress, challenges and opportunities. *NATURE REVIEWS CANCER*, *17*(1), 20–37. https://doi.org/10.1038/nrc.2016.108
Shum, K. T., Lui, E. L. H., Wong, S. C. K., Yeung, P., Sam, L., Wang, Y., Watt, R. M., & Tanner, J. A. (2011). Aptamer-mediated inhibition of mycobacterium tuberculosis polyphosphate kinase 2. *Biochemistry*, *50*(15), 3261–3271.

https://doi.org/10.1021/BI2001455/SUPPL_FILE/BI2001455_SI_001.PDF
Singh, A., Trivedi, P., & Jain, N. K. (2018). Advances in siRNA delivery in cancer therapy. *ARTIFICIAL CELLS NANOMEDICINE AND BIOTECHNOLOGY*, *46*(2), 274–283. https://doi.org/10.1080/21691401.2017.1307210
Sivakumar, P., Kim, S., Kang, H. C., & Shim, M. S. (n.d.). Targeted siRNA delivery using aptamer-siRNA chimeras and aptamer-conjugated nanoparticles. *WILEY INTERDISCIPLINARY REVIEWS: NANOMEDICINE AND NANOBIOTECHNOLOGY*, *11*(3), e1543. Retrieved December 14, 2018, from https://onlinelibrary.wiley.com/doi/full/10.1002/wnan.1543
Skapek, S. X., Ferrari, A., Gupta, A. A., Lupo, P. J., Butler, E., Shipley, J., Barr, F. G., & Hawkins, D. S. (2019). Rhabdomyosarcoma. *NATURE REVIEWS DISEASE PRIMERS 2018 5:1*, *5*(1), 1–19. https://doi.org/10.1038/s41572-018-0051-2
Slowing, I. I., Vivero-Escoto, J. L., Wu, C. W., & Lin, V. S. Y. (2008). Mesoporous silica nanoparticles as controlled release drug delivery and gene transfection carriers. *ADVANCED DRUG DELIVERY REVIEWS*, *60*(11), 1278–1288. https://doi.org/10.1016/J.ADDR.2008.03.012
Smeitink, J., van den Heuvel, L., & DiMauro, S. (2001). The genetics and pathology of oxidative phosphorylation. *NATURE REVIEWS GENETICS 2001 2:5*, *2*(5), 342–352. https://doi.org/10.1038/35072063
Stanley, S. A., Gagner, J. E., Damanpour, S., Yoshida, M., Dordick, J. S., & Friedman, J. M. (2012). Radio-Wave Heating of Iron Oxide Nanoparticles Can Regulate Plasma Glucose in Mice. *SCIENCE*, *336*(6081), 604–608. https://doi.org/10.1126/science.1216753
Strand, M. S., Krasnick, B. A., Pan, H., Zhang Xiuli and Bi, Y., Brooks, C., Wetzel, C., Sankpal, N., Fleming, T., Goedegebuure, S. P., DeNardo, D. G., Gillanders, W. E., Hawkins, W. G., Wickline, S. A., & Fields, R. C. (2019). Precision delivery of RAS-inhibiting siRNA to KRAS driven cancer via peptide-based nanoparticles. *ONCOTARGET*, *10*(46), 4761–4775. https://doi.org/10.18632/oncotarget.27109
Stratton, M. R., Campbell, P. J., & Futreal, P. A. (2009). The cancer genome. *NATURE*, *458*(7239), 719. https://doi.org/10.1038/NATURE07943
Su, S. C., Hsieh, M. J., Yang, W. E., Chung, W. H., Reiter, R. J., & Yang, S. F. (2017). Cancer metastasis: Mechanisms of inhibition by melatonin. *JOURNAL OF PINEAL RESEARCH*, *62*(1), E12370. https://doi.org/10.1111/JPI.12370
Su, Y.-L., & Hu, S.-H. (2018). Functional Nanoparticles for Tumor Penetration of Therapeutics. *PHARMACEUTICS*, *10*(4). https://doi.org/10.3390/pharmaceutics10040193
Sullivan, R., Alatise, O. I., Anderson, B. O., Audisio, R., Autier, P., Aggarwal, A., Balch, C., Brennan, M. F., Dare, A., D'Cruz, A., Eggermont, A. M. M., Fleming, K., Gueye, S. M., Hagander, L., Herrera, C. A., Holmer, H., Ilbawi, A. M., Jarnheimer, A., Ji, J. fu, … Purushotham, A. (2015). Global cancer surgery: delivering safe, affordable, and timely cancer surgery. *THE LANCET ONCOLOGY*, *16*(11), 1193–1224. https://doi.org/10.1016/S1470-2045(15)00223-5
Sun, W., Shi, Q., Zhang, H., Yang, K., Ke, Y., Wang, Y., & Qiao, L. (2019). Advances in the Techniques and Methodologies of Cancer Gene Therapy. *DISCOVERY MEDICINE*, *27*(146), 45–55.
Sung, H., Ferlay, J., Siegel, R. L., Laversanne, M., Soerjomataram, I., Jemal, A., & Bray, F. (2021). Global Cancer Statistics 2020: GLOBOCAN Estimates of Incidence and Mortality Worldwide for 36 Cancers in 185 Countries. *CA: A CANCER JOURNAL FOR CLINICIANS*, *71*(3), 209–249. https://doi.org/10.3322/CAAC.21660
Suteewong, T., Sai, H., Lee, J., Bradbury, M., Hyeon, T., Gruner, S. M., & Wiesner, U. (2010). Ordered mesoporous silica nanoparticles with and without embedded iron oxide nanoparticles : structure evolution during synthesis. *JOURNAL OF MATERIALS CHEMISTRY*, *20*(36), 7807–7814. https://doi.org/10.1039/C0JM01002B
Symonds, R. P. (2001). Radiotherapy. *BMJ*, *323*(7321), 1107–1110. https://doi.org/10.1136/BMJ.323.7321.1107
Tan, L., Sha, L., Hou, N., Zhang, M., Ma, Q., & Shi, C. (2019). High α B-crystallin and p53 co-expression is associated with poor prognosis in ovarian cancer. *BIOSCIENCE REPORTS*, *39*(6), 20182407. https://doi.org/10.1042/BSR20182407/219305

Tan, W., Liu, B., Qu, S., Liang, G., & Luo Wei and Gong, C. (2018). MicroRNAs and cancer: Key paradigms in molecular therapy (Review). *ONCOLOGY LETTERS*, *15*(3), 2735–2742. https://doi.org/10.3892/ol.2017.7638

Tang, F., Li, L., Chen, D., Tang, F. Q., Li, L. L., & Chen Beijing Creative Nanophase Hi, D. (2012). Mesoporous Silica Nanoparticles: Synthesis, Biocompatibility and Drug Delivery. *ADVANCED MATERIALS*, *24*(12), 1504–1534. https://doi.org/10.1002/ADMA.201104763

Tatiparti, K., Sau, S., Kashaw, S. K., & Iyer, A. K. (2017). siRNA delivery strategies: A comprehensive review of recent developments. In *NANOMATERIALS* (Vol. 7, Issue 4). MDPI AG. https://doi.org/10.3390/nano7040077

Thapa, R. K., Nguyen, H. T., Gautam, M., Shrestha, A., Lee, E. S., Ku, S. K., Choi, H. G., Yong, C. S., & Kim, J. O. (2017). Hydrophobic binding peptide-conjugated hybrid lipid-mesoporous silica nanoparticles for effective chemo-photothermal therapy of pancreatic cancer. *DRUG DELIVERY*, *24*(1), 1690–1702. https://doi.org/10.1080/10717544.2017.1396382/SUPPL_FILE/IDRD_A_1396382_SM2224.DOCX

Thomson, B., Hawkins, D., Felgenhauer, J., & Radich, J. P. (1999). RT-PCR evaluation of peripheral blood, bone marrow and peripheral blood stem cells in children and adolescents undergoing VACIME chemotherapy for Ewing's sarcoma and alveolar rhabdomyosarcoma. *BONE MARROW TRANSPLANTATION*, *24*(5), 527–533. https://doi.org/10.1038/SJ.BMT.1701939

Tombolan, L., Poli, E., Martini, P., Zin, A., Romualdi, C., Bisogno, G., & Lanfranchi, G. (2017). NELL1, whose high expression correlates with negative outcomes, has different methylation patterns in alveolar and embryonal rhabdomyosarcoma. *ONCOTARGET*, *8*(20), 33086–33099. https://doi.org/10.18632/oncotarget.16526

Tong, S., Moyo, B., Lee, C. M., Leong, K., & Bao, G. (2019). Engineered materials for in vivo delivery of genome-editing machinery. *NATURE REVIEWS MATERIALS*, *4*(11), 726–737. https://doi.org/10.1038/s41578-019-0145-9

Torchilin, V. (2011). Tumor delivery of macromolecular drugs based on the EPR effect. *ADVANCED DRUG DELIVERY REVIEWS*, *63*(3), 131–135. https://doi.org/10.1016/J.ADDR.2010.03.011

Trédan, O., Galmarini, C. M., Patel, K., & Tannock, I. F. (2007). Drug resistance and the solid tumor microenvironment. In *JOURNAL OF THE NATIONAL CANCER INSTITUTE* (Vol. 99, Issue 19, pp. 1441–1454). https://doi.org/10.1093/jnci/djm135

Valente, J. F. A., Queiroz, J. A., & Sousa, F. (2018). p53 as the Focus of Gene Therapy: Past, Present and Future. *CURRENT DRUG TARGETS*, *19*(15), 1801–1817. https://doi.org/10.2174/1389450119666180115165447

Vallet-Regi, M., Rámila, A., del Real, R. P., & Pérez-Pariente, J. (2000). A New Property of MCM-41: Drug Delivery System. *CHEMISTRY OF MATERIALS*, *13*(2), 308–311. https://doi.org/10.1021/CM0011559

van de Rijn, M., Perou, C. M., Tibshirani, R., Haas, P., Kallioniemi, O., Kononen, J., Torhorst, J., Sauter, G., Zuber, M., Köchli, O. R., Mross, F., Dieterich, H., Seitz, R., Ross, D., Botstein, D., & Brown, P. (2002). Expression of Cytokeratins 17 and 5 Identifies a Group of Breast Carcinomas with Poor Clinical Outcome. *THE AMERICAN JOURNAL OF PATHOLOGY*, *161*(6), 1991–1996. HTTPS://DOI.ORG/10.1016/S0002-9440(10)64476-8

van Haasteren, J., Hyde, S. C., & Gill, D. R. (2018). Lessons learned from lung and liver in-vivo gene therapy: implications for the future. *EXPERT OPINION ON BIOLOGICAL THERAPY*, *18*(9), 959–972. https://doi.org/10.1080/14712598.2018.1506761

Vasir, J. K., & Labhasetwar, V. (2008). Quantification of the force of nanoparticle-cell membrane interactions and its influence on intracellular trafficking of nanoparticles. *BIOMATERIALS*, *29*(31), 4244–4252. https://doi.org/10.1016/J.BIOMATERIALS.2008.07.020

Verma, A., & Stellacci, F. (2010). Effect of Surface Properties on Nanoparticle–Cell Interactions. *SMALL*, *6*(1), 12–21. https://doi.org/10.1002/SMLL.200901158

Villar-Alvarez, E., Cambon, A., Pardo, A., Mosquera, V. X., Bouzas-Mosquera, A., Topete, A., Barbosa, S., Taboada, P., & Mosquera, V. (2018). Gold Nanorod-Based Nanohybrids for Combinatorial Therapeutics. *ACS OMEGA*, *3*(10), 12633–12647. https://doi.org/10.1021/acsomega.8b01591

Wang, C. (2012). Childhood Rhabdomyosarcoma: Recent Advances and Prospective Views.

JOURNAL OF DENTAL RESEARCH, *91*(4), 341. https://doi.org/10.1177/0022034511421490
Wang, J., Lu, Z., Wientjes, M. G., & Au, J. L. S. (2010). Delivery of siRNA therapeutics: Barriers and carriers. In *AAPS JOURNAL* (Vol. 12, Issue 4, pp. 492–503). https://doi.org/10.1208/s12248-010-9210-4
Wang, Y. F., Lang, H. Y., Yuan, J., Wang, J., Wang, R., Zhang, X. H., Zhang, J., Zhao, T., Li, Y. R., Liu, J. Y., Zeng, L. H., & Guo, G. Z. (2013). Overexpression of keratin 17 is associated with poor prognosis in epithelial ovarian cancer. *TUMOR BIOLOGY*, *34*(3), 1685–1689. https://doi.org/10.1007/S13277-013-0703-5/TABLES/2
Wang, Y., Rajala, A., & Rajala, R. V. S. (2015). Lipid Nanoparticles for Ocular Gene Delivery. *JOURNAL OF FUNCTIONAL BIOMATERIALS*, *6*(2), 379–394. https://doi.org/10.3390/jfb6020379
Warburg, O. (1956). On the origin of cancer cells. *SCIENCE*, *123*(3191), 309–314. https://doi.org/10.1126/SCIENCE.123.3191.309/ASSET/A8D38B53-799F-4009-AAD3-E77CEF33D301/ASSETS/SCIENCE.123.3191.309.FP.PNG
Warburg, O., Wind, F., & Negelein, E. (1927). THE METABOLISM OF TUMORS IN THE BODY. *THE JOURNAL OF GENERAL PHYSIOLOGY*, *8*(6), 519. https://doi.org/10.1085/JGP.8.6.519
Ward, E., Desantis, C., Robbins, ; Anthony, Kohler, B., & Jemal, A. (2014). Childhood and adolescent cancer statistics, 2014. *CA: A CANCER JOURNAL FOR CLINICIANS*, *64*(2), 83–103. https://doi.org/10.3322/CAAC.21219
Weidner, N., Semple, J. P., Welch, W. R., & Folkman, J. (2010). Tumor Angiogenesis and Metastasis — Correlation in Invasive Breast Carcinoma. https://doi.org/10.1056/NEJM199101033240101
Weiss, J. N., Korge, P., Honda, H. M., & Ping, P. (2003). Role of the mitochondrial permeability transition in myocardial disease. *CIRCULATION RESEARCH*, *93*(4), 292–301. https://doi.org/10.1161/01.RES.0000087542.26971.D4
White, B. D., Duan, C., & Townley, H. E. (2019). Nanoparticle Activation Methods in Cancer Treatment. *BIOMOLECULES 2019, Vol. 9, Page 202*, *9*(5), 202. https://doi.org/10.3390/BIOM9050202
Witsch, E., Sela, M., & Yarden, Y. (2010). Roles for Growth Factors in Cancer Progression. *PHYSIOLOGY*, *25*(2), 85–101. https://doi.org/10.1152/PHYSIOL.00045.2009/ASSET/IMAGES/LARGE/PHY0021000080004.JPEG
Wu, W., Luo, L., Wang, Y., Wu, Q., Dai, H. bin, Li, J. S., Durkan, C., Wang, N., & Wang, G. X. (2018). Endogenous pH-responsive nanoparticles with programmable size changes for targeted tumor therapy and imaging applications. *THERANOSTICS*, *8*(11), 3038–3058. https://doi.org/10.7150/THNO.23459
Xia, B., Wang, B., Chen, Z., Zhang, Q., Shi Xia, J. B., Chen, Z., Shi, J., Xia, B., Wang, B., & Zhang, Q. (2016). Near-Infrared Light-Triggered Intracellular Delivery of Anticancer Drugs Using Porous Silicon Nanoparticles Conjugated with IR820 Dyes. *ADVANCED MATERIALS INTERFACES*, *3*(4), 1500715. https://doi.org/10.1002/ADMI.201500715
Xia, S. J., Pressey, J. G., & Barr, F. G. (2002). Molecular Pathogenesis of Rhabdomyosarcoma. *Http://Dx.Doi.Org/10.4161/Cbt.51*, *1*(2), 97–104. https://doi.org/10.4161/CBT.51
Xie, X., Liao, J., Shao, X., Li, Q., & Lin, Y. (2017). The Effect of shape on Cellular Uptake of Gold Nanoparticles in the forms of Stars, Rods, and Triangles. *SCIENTIFIC REPORTS*, *7*(1). https://doi.org/10.1038/s41598-017-04229-z
Xin, Y., Huang, M., Guo, W. W., Huang, Q., Zhang, L. zhen, & Jiang, G. (2017). Nano-based delivery of RNAi in cancer therapy. *MOLECULAR CANCER*, *16*. https://doi.org/10.1186/s12943-017-0683-y
Xing, H., & Meng, L. (2020). CRISPR-cas9: a powerful tool towards precision medicine in cancer treatment. *ACTA PHARMACOLOGICA SINICA*, *41*(5), 583–587. https://doi.org/10.1038/s41401-019-0322-9
Xiong, L., Du, X., Kleitz, F., & Zhang Qiao, S. (n.d.). *Cancer-Cell-Specific Nuclear-Targeted Drug Delivery by Dual-Ligand-Modified Mesoporous Silica Nanoparticles*. https://doi.org/10.1002/smll.201501056
Xu, X., Wan, T., Xin, H., Li, D., Pan, H., Wu, J., & Ping, Y. (2019). Delivery of CRISPR/Cas9 for

therapeutic genome editing. *JOURNAL OF GENE MEDICINE*, *21*(7, SI). https://doi.org/10.1002/jgm.3107
Xu, X., Wu, J., Liu, Y., Yu, M., Zhao Lili and Zhu, X., Bhasin, S., Li, Q., Ha, E., Shi, J., & Farokhzad, O. C. (2016). Ultra-pH-Responsive and Tumor-Penetrating Nanoplatform for Targeted siRNA Delivery with Robust Anti-Cancer Efficacy. *ANGEWANDTE CHEMIE-INTERNATIONAL EDITION*, *55*(25), 7091–7094. https://doi.org/10.1002/anie.201601273
Xu, Z. P., Zeng, Q. H., Lu, G. Q., & Yu, A. B. (2006). Inorganic nanoparticles as carriers for efficient cellular delivery. *CHEMICAL ENGINEERING SCIENCE*, *61*(3), 1027–1040. https://doi.org/10.1016/j.ces.2005.06.019
Xue, J., Yang, J., Luo, M., Cho, W. C., & Liu, X. (2017). MicroRNA-targeted therapeutics for lung cancer treatment. *EXPERT OPINION ON DRUG DISCOVERY*, *12*(2), 141–157. https://doi.org/10.1080/17460441.2017.1263298
Yamamoto, Y., & Gerbi, S. A. (2018). Making ends meet: targeted integration of DNA fragments by genome editing. *CHROMOSOMA*, *127*(4), 405–420. https://doi.org/10.1007/s00412-018-0677-6
Yan, X., Yang, C., Hu, W., Chen, T., Wang, Q., Pan, F., Qiu, B., & Tang, B. (2020). Knockdown of KRT17 decreases osteosarcoma cell proliferation and the Warburg effect via the AKT/mTOR/HIF1α pathway. *ONCOLOGY REPORTS*, *44*(1), 103–114. https://doi.org/10.3892/OR.2020.7611/HTML
Yanagisawa, T., Shimizu, T., Kuroda, K., & Kato, C. (2006). The Preparation of Alkyltrimethylammonium–Kanemite Complexes and Their Conversion to Microporous Materials. https://doi.org/10.1246/BCSJ.63.988
Yang, H. Y., Jang, M. S., Li, Y., Fu, Y., Wu, T. P., Lee, J. H., & Lee, D. S. (2019). Hierarchical tumor acidity-responsive self-assembled magnetic nanotheranostics for bimodal bioimaging and photodynamic therapy. *JOURNAL OF CONTROLLED RELEASE*, *301*, 157–165. https://doi.org/10.1016/J.JCONREL.2019.03.019
Yang, L., Zhang, S., & Wang, G. (2019). Keratin 17 in disease pathogenesis: from cancer to dermatoses. *The Journal of Pathology*, *247*(2), 158–165. https://doi.org/10.1002/PATH.5178
Yang, N. (2015). An overview of viral and nonviral delivery systems for microRNA. *INTERNATIONAL JOURNAL OF PHARMACEUTICAL INVESTIGATION*, *5*(4), 179. https://doi.org/10.4103/2230-973X.167646
Yang, Y., Wan, J., Niu, Y., Gu, Z., Zhang, J., Yu, M., & Yu, C. (2016). Structure-Dependent and Glutathione-Responsive Biodegradable Dendritic Mesoporous Organosilica Nanoparticles for Safe Protein Delivery. *CHEMISTRY OF MATERIALS*, *28*(24), 9008–9016. https://doi.org/10.1021/acs.chemmater.6b03896
Yeh, C. D., Richardson, C. D., & Corn, J. E. (2019). Advances in genome editing through control of DNA repair pathways. *NATURE CELL BIOLOGY*, *21*(12), 1468–1478. https://doi.org/10.1038/s41556-019-0425-z
Yeo, C. I., Ooi, K. K., & Tiekink, E. R. T. (2018). Gold-Based Medicine: A Paradigm Shift in Anti-Cancer Therapy? *MOLECULES*, *23*(6). https://doi.org/10.3390/molecules23061410
Yin, H., Xue, W., & Anderson, D. G. (2019). CRISPR-Cas: a tool for cancer research and therapeutics. *NATURE REVIEWS CLINICAL ONCOLOGY*, *16*(5), 281–295. https://doi.org/10.1038/s41571-019-0166-8
Yonezawa, S., Koide, H., & Asai, T. (2020). Recent advances in siRNA delivery mediated by lipid-based nanoparticles. *ADVANCED DRUG DELIVERY REVIEWS*, *154–155*, 64–78. https://doi.org/10.1016/J.ADDR.2020.07.022
Yue, Z.-G., Wei, W., You, Z.-X., Yang, Q.-Z., Yue, H., Su, Z.-G., & Ma, G.-H. (2011). Iron Oxide Nanotubes for Magnetically Guided Delivery and pH-Activated Release of Insoluble Anticancer Drugs. *ADVANCED FUNCTIONAL MATERIALS*, *21*(18), 3446–3453. https://doi.org/10.1002/adfm.201100510
Zhang, H., Wang, P., Lu, M., Zhang, S., & Zheng, L. (2019). c-Myc maintains the self-renewal and chemoresistance properties of colon cancer stem cells. *ONCOLOGY LETTERS*, *17*(5), 4487–4493. https://doi.org/10.3892/ol.2019.10081
Zhang, P., Chen, D., Li, L., & Sun, K. (2022a). Charge reversal nano-systems for tumor therapy. *JOURNAL OF NANOBIOTECHNOLOGY*, *20*(1), 1–27. https://doi.org/10.1186/S12951-021-

01221-8/TABLES/3
Zhao, S., Xu, M., Cao, C., Yu, Q., Zhou, Y., & Liu, J. (2017). A redox-responsive strategy using mesoporous silica nanoparticles for co-delivery of siRNA and doxorubicin. *JOURNAL OF MATERIALS CHEMISTRY B*, *5*(33), 6908–6919. https://doi.org/10.1039/C7TB00613F
Zhou, Z., Shen, Y., Tang, J., Fan, M., van Kirk, E. A., Murdoch, W. J., & Radosz, M. (2009). Charge-Reversal Drug Conjugate for Targeted Cancer Cell Nuclear Drug Delivery. *ADVANCED FUNCTIONAL MATERIALS*, *19*(22), 3580–3589. https://doi.org/10.1002/ADFM.200900825
Zhu, L., Wang, T., Perche, F., Taigind, A., & Torchilin, V. P. (2013). Enhanced anticancer activity of nanopreparation containing an MMP2-sensitive PEG-drug conjugate and cell-penetrating moiety. *PROCEEDINGS OF THE NATIONAL ACADEMY OF SCIENCES OF THE UNITED STATES OF AMERICA*, *110*(42), 17047–17052. https://doi.org/10.1073/PNAS.1304987110
Zuker, M. (2003). Mfold web server for nucleic acid folding and hybridization prediction. *NUCLEIC ACIDS RESEARCH*, *31*(13), 3406–3415. https://doi.org/10.1093/NAR/GKG595
Zuo, L., Zhang, F., & Xu, Y. (2019). Anti-EGF antibody cationic polymeric liposomes for delivery of the p53 gene for ovarian carcinoma therapy. *INTERNATIONAL JOURNAL OF CLINICAL AND EXPERIMENTAL PATHOLOGY*, *12*(1), 205–211.
Zylberberg, C., Gaskill, K., Pasley, S., & Matosevic, S. (2017). Engineering liposomal nanoparticles for targeted gene therapy. *GENE THERAPY*, *24*(8), 441–452. https://doi.org/10.1038/gt.2017.41